Search for Dark Matter in Invisible Higgs Boson Decays with the ATLAS Detector at the LHC

Dissertation
zur Erlangung des Doktorgrades
an der Fakultät für Mathematik, Informatik und Naturwissenschaften
Fachbereich Physik
der Universität Hamburg

vorgelegt von
Arthur Linß

Hamburg, 2021

Gutachter der Dissertation:	Dr. Christian Sander
	Prof. Dr. Johannes Haller
Zusammensetzung der Prüfungskommission:	Dr. Christian Sander
	Prof. Dr. Johannes Haller
	Prof. Dr. Dieter Horns
	Prof. Dr. Kerstin Tackmann
	Prof. Dr. Gudrid Moortgat-Pick
Vorsitzender der Prüfungskommission:	Prof. Dr. Dieter Horns
Datum der Disputation:	14.12.2021
Vorsitzender Fach-Promotionsausschuss Physik:	Prof. Dr. Wolfgang Hansen
Leiter des Fachbereichs Physik:	Prof. Dr. Günter H. W. Sigl
Dekan der Fakultät MIN:	Prof. Dr. Heinrich Graener

Abstract

The nature of dark matter is one of the biggest open questions in modern physics. While dark matter accounts for roughly 25 % of the energy density in the Universe, its particle nature remains unknown so far. In this thesis a search for dark matter at the Large Hadron Collider with the ATLAS experiment is presented using proton-proton collision data collected at a center-of-mass energy of $\sqrt{s} = 13\,\text{TeV}$. Furthermore, the absolute Monte Carlo based jet energy scale calibration of particle flow jets is presented.

The dark matter search targets vector boson fusion Higgs boson production, which is expected to be the most sensitive channel. For the full Run II data set, the background estimates with a focus on multijet processes, the event categorisation, limit setting as well as the interpretation of the result are presented.

In absence of a signal excess over the background-only hypothesis, an upper limit is set on the invisible Higgs boson branching fraction. The observed (expected) 95 % CL limit is 0.145 (0.103), which is the best limit ever achieved so far for invisible Higgs boson decays.

The result is interpreted in terms of Higgs portal models to set upper limits on the WIMP-nucleon cross section. Moreover, also limits on potential other scalar mediators than the Higgs boson of the Standard Model are set.

Zusammenfassung

Die Natur der dunklen Materie ist eine der wichtigsten offenen Fragen der modernen Physik. Dunkle Materie macht ungefähr 25 % der Energiedichte des Universums aus, ihre Teilchennatur ist jedoch bisher unbekannt. In dieser Arbeit wird eine Suche nach dunkler Materie am Large Hadron Collider mit dem ATLAS-Experiment präsentiert, die auf Proton-Proton Kollisionsdaten gemessen bei Schwerpunktsenergien von $\sqrt{s} = 13\,\text{TeV}$ basiert. Zusätzlich wird die absolute Monte Carlo-basierte Jet-Energie-Kalibration von Particle Flow Jets präsentiert.

Die Suche nach dunkler Materie zielt auf Higgs-Bosonen die in Vektorboson-Fusion produziert werden, welcher zugleich der sensitivste Kanal ist. Für den vollständigen Run II Datensatz werden die Untergrundabschätzungen mit einem Fokus auf Multijet-Prozessen, die Event-Kategorisierung, die Limitextraktion und die Interpretation der Resultate vorgestellt.

In Abwesenheit eines Signalüberschusses über der reinen Untergrund-Hypothese wird ein oberes Limit auf die unsichtbare Higgs-Boson Zerfallsrate gesetzt. Das beobachtete (erwartete) 95 % CL Limit für unsichtbare Higgs-Boson-Zerfälle ist 0.145 (0.103), welches das bisher beste Limit für unsichtbare Higgs-Boson-Zerfälle ist.

Das Resultat wird im Rahmen von Higgs-Portal-Modellen interpretiert, um Limits auf den WIMP-Nukleon Wirkungsquerschnitt zu setzen. Außerdem werden auch Limits auf andere potenzielle skalare Mediatoren als das Standardmodell Higgs-Boson gesetzt.

Contents

CHAPTER 1

Introduction

The physics program of the world's largest and most powerful hadron collider, the LHC, culminated in 2012 in the discovery of the Higgs boson, which was the last missing particle of the Standard Model of particle physics (SM). By today, all measured Higgs boson characteristics such as spin, parity and couplings to both bosons and fermions are compatible with predictions from the SM. Despite all its successes, the SM cannot explain an invisible form of matter –dark matter– which is observed in a variety of astrophysical measurements. The nature of dark matter is one of the greatest mysteries in modern physics and its explanation is one of the main targets of many experiments at CERN. A search for dark matter with the ATLAS experiment is presented based on Higgs portal models suggesting that the Higgs boson might couple to dark matter candidates, for example the weakly interacting massive particles (WIMPs). The target processes is an invisibly decaying Higgs boson produced in vector boson fusion, which is the most sensitive Higgs boson production channel since it allows for effective background suppression. Major improvements of the presented analysis with respect to the previous analysis iterations [1] are the inclusion of pile-up tagging in the forward detector region, optimised control region selections, improved background estimation strategies, reduction of statistical uncertainties with phase space optimised simulations, reduction of systematic uncertainties as well as optimising the event categorisation and selection to increase the signal sensitivity. Further, the analysis benefited from the large data set collected between 2015 and 2018 during Run II of the LHC. A special focus of this thesis is the multijet background estimation for which different strategies are developed and presented in detail.

The thesis is organised as follows: In Chapter 2 a theoretical overview of the SM and the foundations of dark matter are given. In Chapter 3 the experimental apparatus is described, followed by a description of physics objects and their experimental reconstruction in Chapter 4. The correction of particle flow jet measurements with a focus on the absolute Monte Carlo (MC) jet energy scale calibration is given in Chapter 5. The analysis strategy of the Higgs boson to invisible dark matter search is presented in Chapter 6. The "Rebalance and Smear" (RnS) technique for the multijet background estimation is presented in Chapter 7, followed by the general background estimations in Chapter 8. The analysis fit model is presented in Chapter 9, followed by the results and their interpretation in Chapter 10. Chapter 11 gives a summary and an outlook.

The presented thesis emerged from many years of work from thousands of scientists and engineers of the ATLAS collaboration, CERN and the associated institutes from all over the world who strongly collaborate to explore the phenomena of our Universe. The author of this thesis is the main developer of the modified RnS technique used for the estimation of the multijet background for the full Run II vector boson fusion Higgs boson to invisible search. In addition to modified data-driven RnS versions, novel MC-based RnS techniques are developed and a variety of methods are invented to increase the effective statistics of the multijet background prediction and to reduce uncertainties both statistical and systematical. The obtained RnS multijet background estimate is a cornerstone for the high sensitivity of the presented analysis. Together with another student [2], the author is responsible for the RnS multijet background prediction finalisation, validation, the evaluation of the systematic

uncertainties and the combination with the independent and novel pile-up control region method.

Further, the author is the main responsible for running and improving the absolute MC based jet energy calibration for small-R particle flow jets for the new Run II precision recommendations used by almost all physics analysers in ATLAS. It is his task to push the p_{T} limit of the jet calibration of particle flow jets to previous unattained values by improving the fitting strategy, the input jet collection and the calibration performance metric. In this context, the author implemented a penalised spline technique for fitting the jet response in the ATLAS analysis and calibration framework.

From the presented thesis, the following publication emerged so far or will be published soon:

- Search for invisible Higgs boson decays with vector boson fusion signatures with the ATLAS detector using an integrated luminosity of $139\,\mathrm{fb}^{-1}$ [3].
- Search for invisibly decaying Higgs bosons with the VBF+MET signature [4].

Throughout this thesis, Einstein's summation convention and natural units with $\hbar = c = 1$ are used, where $\hbar$ is the reduced Planck's constant and c the vacuum speed of light. Further, the following convention for Feynman diagrams is used: time flows from left to right and the space-dimensions from top to bottom or vice versa. To simplify notation, antiparticles as well as a off-shell particles are not explicitly highlighted.

CHAPTER 2

Theoretical overview

In this chapter the fundamentals of the SM and the phenomenon of dark matter are explained.

2.1 The Standard Model of Elementary Particle Physics

Physics was revolutionised by Einstein's theory of relativity [5] and the developments in quantum mechanics (QM) in the first half of the 20th century. Based on this, the theory known as the SM was developed in the 1960s and 1970s driven by work of the pioneers Glashow, Salam and Weinberg [6–10]. The SM successfully describes in a relativistic quantum field theory (QFT) three of the four fundamental forces of the Universe, the electromagnetic (EM) force, the weak force and the strong force. QFTs provide the mathematical framework for the SM based on symmetry principles of local gauge-invariance and Lorentz-invariance. The dynamics of quantum fields are described by Lagrangian densities $\mathcal{L}$, which define the action $\mathcal{S}$ by

$$\mathcal{S} = \int \mathcal{L} \, \mathrm{d}^4 x, \tag{2.1}$$

where d^4x is the infinitesimal four-dimensional space-time interval. According to Hamilton's principle [11, 12],

$$\delta \mathcal{S} = 0, \tag{2.2}$$

the evolution of a system is determined by the action $\mathcal{S}$. This principle of stationary action also applies in a more general context in QFT as used in Feynman's path integral approach [13]. In terms of the second quantisation [14], the excitations of fundamental quantum fields correspond to elementary particles, both fermions and bosons. The force carriers are bosons, while fermions are the building blocks of matter. The separation of these two fundamental different classes of particles is based on the spin quantum number: bosons are particles with integer spin, while fermions are particles with half-integer spin. The fermions are further divided into leptons, light fermions such as the electron, muon, τ lepton and the corresponding neutrinos as well as the quarks, which are fermions carrying colour charge. Fermions underly Pauli's exclusion principle [15] stating that two identical fermions cannot be in the same quantum state (Fermi-Dirac statistics) while this is not the case for bosons (Bose-Einstein statistics). The particle content of the SM is displayed in Figure 2.1, which shows the three fermion generations separated into quarks and leptons, the vector bosons and the scalar Higgs boson. The three forces included in the SM are briefly described with respect to their individual history and characteristics in Section 2.1.1-2.1.3. Based on this, the electroweak (EWK) unification and the full SM Lagrangian density are described in Section 2.1.4. Following that, EWK symmetry breaking and its consequences are described in Section 2.1.5.

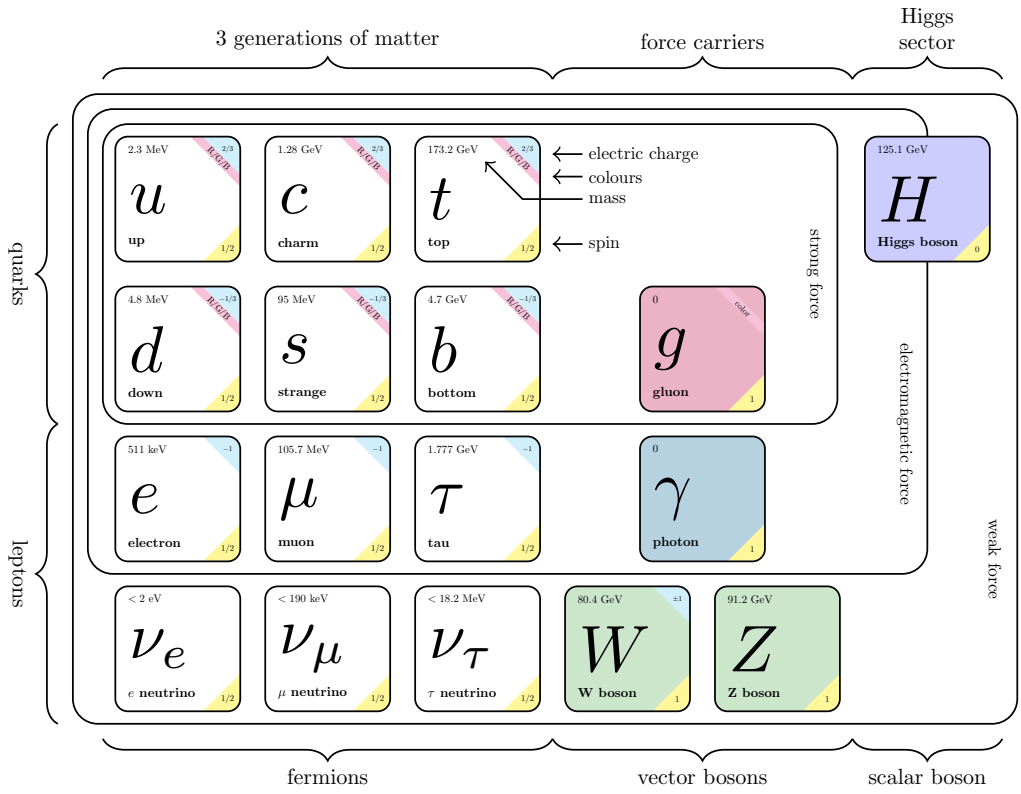

Figure 2.1: Overview of the particle content of the SM (adapted from Ref. [16]).

2.1.1 Quantum Electrodynamics

In classical physics, electromagnetism is described by Maxwell's equations [17], which is historically the first unified description of two apparently different forces - electricity and magnetism. The quantisation of electromagnetism leads to quantum electrodynamics (QED), which was the first successful attempt to use a QFT to describe one of the fundamental forces of nature. The force carrier in QED is the quantum of light, the massless and electrically neutral photon γ. All electrically charged particles underly the electromagnetic force and thus couple to the photon, where the coupling strength is given by the fine-structure constant α_{EM} which gives the electromagnetic unit charge $e = \sqrt{4\pi\alpha_{\text{EM}}}$. QED is an abelian gauge theory based on the unitary group $U(1)$. The Lagrangian for a free fermion field with mass m described by a Dirac spinor ψ can be written as

$$\mathcal{L}_{\text{QED}} = i\bar{\psi}\gamma^{\mu}\partial_{\mu}\psi - m\bar{\psi}\psi, \tag{2.3}$$

where γ^{μ} represent the Dirac γ-matrices with $\mu \in \{0, 1, 2, 3\}$ [18]. By replacing the partial derivative ∂_{μ} by the gauge covariant derivative $D_{\mu} = \partial_{\mu} + ieA_{\mu}$, where A_{μ} is the gauge field of QED, i.e the photon, which transforms as $A_{\mu} \rightarrow A_{\mu} - \partial_{\mu}\xi$, the Lagrangian $\mathcal{L}_{\text{QED}}$ is transformed to a local gauge-invariant Lagrangian, given by

$$\mathcal{L}_{\text{QED}} = i\bar{\psi}\gamma^{\mu}\partial_{\mu}\psi - m\bar{\psi}\psi - e\bar{\psi}A_{\mu}\psi - \frac{1}{4}F^{\mu\nu}F_{\mu\nu}, \tag{2.4}$$

where $F_{\mu\nu} = \partial_\mu A_\nu - \partial_\nu A_\mu$ represents the field strength tensor of the field A_μ. The extension of the global gauge-invariant QED Lagrangian into a local gauge-invariant generates an interaction term of the massless gauge field A_μ and the massive spinor field ψ. An additional mass term associated with the field A_μ would spoil the local gauge invariance of $\mathcal{L}_{\text{QED}}$ and therefore the photon remains massless, which is in accordance with experiments.

2.1.2 Quantum Chromodynamics

The description of strong interactions emerged from the question of how atomic nuclei are bound together. In 1964, Gell-Mann [19] and Zweig [20] developed a model stating that hadrons are made of subparticles - the quarks. That was the basis for the theory describing the strong nuclear force, called Quantum Chromodynamics (QCD) [21–23]. QCD is based on the gauge group $SU(3)_C$, corresponding to three different colour states, often termed as red, green and blue, so a quark field ψ_f of flavour f can be written as a colour triplet

$$\psi_f = \begin{bmatrix} \psi_f^{\text{red}} \\ \psi_f^{\text{green}} \\ \psi_f^{\text{blue}} \end{bmatrix}. \tag{2.5}$$

The force carrier of QCD are massless gluons representing different linear independent combinations of two colour states. All colour-charged elementary particles, the quarks and the gluons, underly the strong force and thus interact with gluons. Since gluons carry colour-charge themselves, there is a gluon self-interaction, which is mathematically mirrored by the non-abelian group $SU(3)_C$, leading to three- and four-point gluon-self-interactions. Typical QCD interactions are sketched in Figure 2.2. The gauge-invariant QCD Lagrangian $\mathcal{L}_{\text{QCD}}$

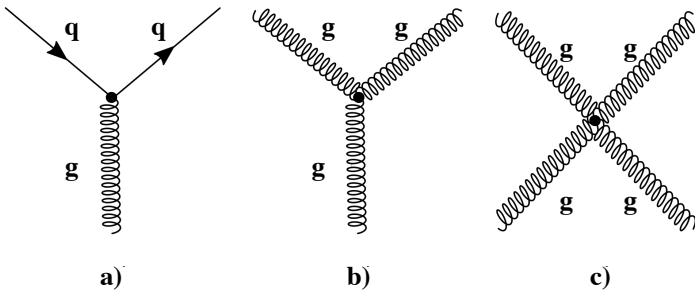

Figure 2.2: Feynman diagram of typical QCD interactions: a) quark-gluon coupling, b) three-point gluon coupling, c) four-point gluon coupling.

is given by

$$\mathcal{L}_{\text{QCD}} = i\overline{\psi}_\alpha \left(\gamma^\mu D_\mu - m\right)_{\alpha\beta} \psi_\beta - \frac{1}{4} G^a_{\mu\nu} G^{\mu\nu}_a, \tag{2.6}$$

with quark spinor fields ψ and gauge covariant derivative

$$D_\mu = \partial_\mu + i g_s \frac{\lambda_i}{2} G^i_\mu, \tag{2.7}$$

where $G^i_{\mu\nu}$ is the gluon gauge field tensor

$$G^i_{\mu\nu} = \partial_\mu G^i_\nu - \partial_\nu G^i_\mu - g_s f^i_{jk} G^j_\mu G^k_\nu, \tag{2.8}$$

f^{ijk} denotes the antisymmetric structure constants of $SU(3)_C$ and λ_i are the eight Gell-Mann matrices fulfilling $[\lambda^i, \lambda^j] = 2if_{ijk}\lambda^k$. The indices α and β denote the flavour of the quark spinor field in the fundamental representation of $SU(3)_C$. While the gluon gauge field tensor is gauge invariant regarding $SU(3)_C$ transformations, the gluon gauge field transforms under local $SU(3)_C$ gauge transformations of the form $a \rightarrow \exp(i\alpha(x)\frac{\lambda_a}{2})a$ via

$$G^a_\mu \rightarrow G^a_\mu + \partial_\mu \alpha^a - f^a_{bc}\alpha^b G^c_\mu. \tag{2.9}$$

There is no gluon mass term in the QCD Lagrangian, which would spoil the $SU(3)_C$ gauge symmetry. The gauge bosons of the strong force, the massless gluons, were discovered in three-jet-events produced in e^+e^- annihilation at DESY in 1979 [24, 25]. As a running renormalisation coupling constant, α_S depends on the energy scale or rather the momentum transfer Q of the process under consideration, parametrised with the β-function of the renormalisation group by

$$\alpha_s(Q^2) = \frac{\alpha_S\left(\mu^2\right)}{1 + \frac{\alpha_S\left(\mu^2\right)}{12\pi}(33 - 2n_f)\log\left(\frac{Q^2}{\mu^2}\right)}, \tag{2.10}$$

where $n_f \leq 6$ denotes the number of quark flavours which are active in quark pair production and μ is the renormalisation factor with the dimension of mass. Hence, α_s decreases logarithmically with increasing Q^2. The energy dependence of the strong coupling constant α_s corresponds to the phenomena of asymptotic freedom and confinement in QCD. Since the strength of QCD decreases asymptotically as the energy scale increases, QCD becomes asymptotically free at short length scales. In this case (as long as $\alpha_s < 1$) perturbative expansions in QCD are possible. In contrast, at low energies or rather larger distances the strong interactions becomes strong, leading to color confinement in QCD. Therefore, color-charged particles cannot be isolated but rather hadronise and form baryons and mesons. Baryons are bound state of three quarks, while mesons are bound states of quark-antiquark pairs. The hadronisation process is theoretically not fully understood yet and phenomenological models are used for its description. Experimentally, α_s can be measured for example by measuring the number of three jet events in e^+e^- collisions with hadronic final states, where the probability of observing a third jet is proportional to α_s.

2.1.3 Weak Interactions

The weak interaction is the fundamental force responsible for radioactive decays, for example the β^--decay. In contrast to the massless gauge bosons in QED and QCD, the mediators of the weak interaction, the W and the Z bosons, are massive, explained within the SM via the Higgs mechanism. The behaviour of particles in weak interactions is described by the weak isospin I, where particles are placed in chiral multiplets, which have a different behaviour under $SU(2)_I$ gauge transformations. Left-handed fermions are placed in weak isospin doublets, with $I^3 = \frac{1}{2}$ for the upper component and $I^3 = -\frac{1}{2}$ for the lower component, while right-handed fermions are placed in weak isospin singlets with $I = 0$, whereby the weak eigenstates of the d, s and b quarks are not equal to the mass eigenstates but mixtures of them. This is the reason that the weak interactions allows for a flavour-change of participating quarks. The most important characteristic of charged weak interaction is its chiral nature. The chiral components for fermions are defined as

$$\psi_{R,L} = \frac{1}{2}\left(1 \pm \gamma^5\right)\psi, \tag{2.11}$$

where $\gamma^5 = i\gamma^0\gamma^1\gamma^2\gamma^3$ is the fifth γ matrix and ψ a spinor field. With this, the kinetic energy term for Dirac fermions can be splitted into a left-handed and a right-handed term via

$$i\bar{\psi}\gamma^\mu\partial_\mu\psi = i\bar{\psi}\gamma^\mu\partial_\mu\psi = i\left(\bar{\psi}_L\gamma^\mu\partial_\mu\psi_L + \bar{\psi}_R\gamma^\mu\partial_\mu\psi_R\right). \tag{2.12}$$

Due to the vector minus axial-vector structure of the charged weak currents only the left-handed term for particles interacts weakly and only the right-handed term for antiparticles. That is, the weak interaction is the only force in the SM allowing for parity violation, as observed by Wu et al. in 1956 [26]. In addition the CP symmetry is violated as discovered by Christenson, Fitch, Cronin and Turlay in 1964 in Kaon decays [27]. In the SM, CP violation in the quark sector is explained with a non-zero complex phase in the unitary Cabibbo-Kobayashi-Maskawa (CKM) quark-mixing matrix, introduced in 1973 [28]. The CKM matrix describes the mixing of three generations of quarks as an extension of the Cabibbo matrix [29] via

$$\begin{bmatrix} d' \\ s' \\ b' \end{bmatrix} = \begin{bmatrix} V_{ud} & V_{us} & V_{ub} \\ V_{cd} & V_{cs} & V_{cb} \\ V_{td} & V_{ts} & V_{tb} \end{bmatrix} \begin{bmatrix} d \\ s \\ b \end{bmatrix}, \tag{2.13}$$

where the elements V_{ij} describe the transition probability $|V_{ij}|$ from quark flavour i to j, thus $\sum_k |V_{ik}|^2 = 1$.

The neutral and charged weak currents were discovered at CERN by the UA1 and UA2 experiments with the SPS collider [30]. The masses of the W and Z [31] are determined to

$$\begin{aligned} m_Z &= 91.188 \pm 0.002\,\text{GeV} \\ m_W &= 80.379 \pm 0.012\,\text{GeV}. \end{aligned}$$

The discovery of the weak vector bosons and the accompanying development of stochastic cooling [32] to reduce the energy spread and angular divergence of charged particle beams was awarded with Nobel prizes for Rubbia and van der Meer. The Z boson is an electrically neutral vector boson, while the W boson is an electrically charged vector boson with charge $q = \pm 1e$. The branching fractions of the Z and W boson are sketched in Figure 2.3.

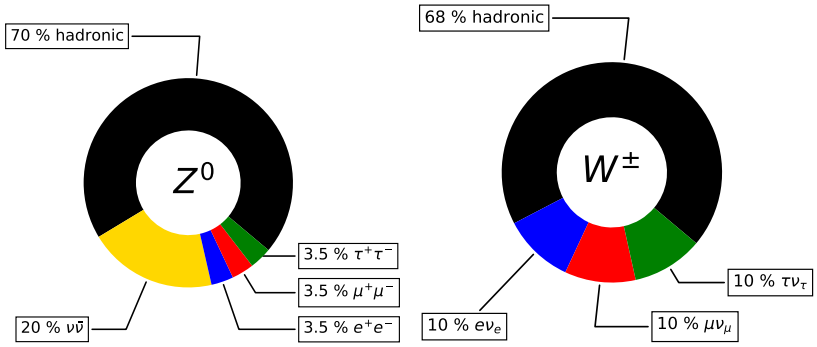

Figure 2.3: Main decay modes of the Z boson (left) and W boson (right).

2.1.4 Electroweak Unification and Standard Model Lagrangian

The EWK unification includes two forces, weak and EM interactions, and emerged historically from attempts to obtain a renormalisable theory of the weak interactions. The EWK gauge group is $SU(2)_I \times U(1)_Y$ with the generators weak isospin I and weak hypercharge Y, respectively, leading to three initially massless W boson

fields of $SU(2)_I$, W^a ($a \in \{1,2,3\}$), and one B boson field of $U(1)_Y$. The electric charge q follows from a combination of weak hypercharge Y and third isospin component I^3 via

$$q = I^3 + \frac{Y}{2}. \tag{2.14}$$

Adding the gauge group of QCD to the one of EWK unification, the SM is based on the symmetry group $SU(3)_C \times SU(2)_I \times U(1)_Y$. The Lagrangian density $\mathcal{L}_{\text{SM}}$ of the SM, before EWK symmetry breaking, can be decomposed into the strong part $\mathcal{L}_{\text{QCD}}$ and the EWK part $\mathcal{L}_{\text{EW}}$ by

$$\mathcal{L}_{\text{SM}} = \mathcal{L}_{\text{QCD}} + \mathcal{L}_{\text{EW}}. \tag{2.15}$$

The strong part is given in Equation 2.6. The EWK part $\mathcal{L}_{\text{EW}}$ can be written as

$$\mathcal{L}_{\text{EW}} = \mathcal{L}_{\text{gauge}} + \mathcal{L}_f + \mathcal{L}_\phi + \mathcal{L}_{\text{Yukawa}} \tag{2.16}$$

with the gauge term $\mathcal{L}_{\text{gauge}}$, the Higgs field term $\mathcal{L}_\phi$, the fermionic term $\mathcal{L}_f$ and the Yukawa term $\mathcal{L}_{\text{Yukawa}}$. The gauge term describes the interaction of the gauge boson fields W_a and B described with their field strength tensors $W_a^{\mu\nu}$ and $B^{\mu\nu}$ via

$$\mathcal{L}_{\text{gauge}} = -\frac{1}{4}\left(W_a^{\mu\nu} W^a_{\mu\nu} + B^{\mu\nu} B_{\mu\nu}\right). \tag{2.17}$$

The fermion term describes the interaction of the gauge bosons and fermions via

$$\mathcal{L}_{\text{f}} = -i\bar{\psi}_q^I \gamma^\mu D_\mu \psi_q^I + i\bar{\psi}_l^I \gamma^\mu D_\mu \psi_l^I, \tag{2.18}$$

where ψ_q^I is the short-hand notation for the spinor of left-handed doublet, right-handed singlet up and right-handed singlet down quark fields and ψ_e^I a short-hand notation for left-handed doublet and right-handed singlet fermion fields. Note that the chiral weak isospin doublets are constructed from the weak eigenstates. Further, the covariant derivative

$$D_\mu = \partial_\mu + i g_W T_a \cdot W_\mu^a + \frac{i g'}{2} B_\mu \tag{2.19}$$

is used, where W_μ^a and B^μ are the gauge fields of the $SU(2)_I \times U(1)_Y$ gauge symmetry, $T^a = \frac{1}{2}\sigma^a$ are the generators of the $SU(2)_I$ symmetry group, σ^a are the Pauli matrices, and g_W as well as g' are dimensionless coupling parameters. The Higgs term $\mathcal{L}_\phi$ describes the Higgs field and due to the gauge covariant derivative also interactions with gauge bosons. To ensure gauge invariance, the particles in the SM are initially massless but acquire mass through the Brout-Englert-Higgs mechanism, often simply called Higgs-mechanism. In the Higgs-mechanism, the EWK gauge symmetry is spontaneously broken, described in more detail in Section 2.1.5. The Yukawa term $\mathcal{L}_{\text{Yukawa}}$ leads to the generation of fermion masses after EWK symmetry breaking. As proven by t'Hooft and Veltman, the SM, as a Yang-Mills theory with spontaneously broken symmetry, is fully renormalisable [33, 34].

2.1.5 Electroweak Symmetry Breaking

A mass term of the quantum fields in the Lagrangian density $\mathcal{L}_{\text{SM}}$ would spoil the local gauge invariance of the SM, therefore the gauge symmetry of the SM requires the gauge bosons and fermions to be massless. In contrast, many experiments showed that many of the elementary particles are actually massive [31, 35]. A solution to this objection was given in 1964 by Brout and Englert [36], Higgs [37] as well as Guralnik, Hagen and Kibble [38], using the concept of spontaneous symmetry breaking (SSB), which was previously introduced in solid state physics by Nambu [39] and Goldstone [40]. In context of the EWK unification SSB is called the Higgs mechanism, in which a scalar field, the Higgs field ϕ, is added to the EWK part of the Lagrangian density $\mathcal{L}_{EW}$ as written in Equation 2.16. Below the EWK scale at a temperature around $T = 200\,\text{GeV}$ the Higgs field

acquires a non-zero vacuum expectation value (VEV) breaking the EWK symmetry. The non-zero VEV v results in an additional, massive scalar boson within the SM: the Higgs boson. This mechanism is outlined in the following. In order to generate mass terms for the weak gauge bosons as it is realised in nature, a complex scalar field doublet ϕ is introduced, defined by

$$\phi = \begin{pmatrix} \phi^+ \\ \phi^0 \end{pmatrix} = \frac{1}{\sqrt{2}} \begin{pmatrix} \phi_1 + i\phi_2 \\ \phi_3 + i\phi_4 \end{pmatrix}. \tag{2.20}$$

The corresponding Lagrangian density associated with ϕ is given by

$$\mathcal{L}_\phi = (D_\mu \phi^\dagger)(D^\mu \phi) - V(\phi) \tag{2.21}$$

where the Higgs potential $V(\phi)$ is defined as

$$V(\phi) = \mu^2 \phi^\dagger \phi + \lambda (\phi^\dagger \phi)^2, \tag{2.22}$$

where $\lambda > 0$ is a real self-coupling parameter and $\mu < 0$ is a real parameter of mass-dimension one. The potential $V(\phi)$ is restricted to this form by the EWK gauge symmetry and the renormalisability condition. Vacuum stability requires $\lambda > 0$, corresponding to a potential $V(\phi)$ which is bounded from below. For $\mu^2 \geq 0$ the potential $V(\phi)$ has a minimum at $\phi = 0$. In contrast, for $\mu^2 < 0$, the potential $V(\phi)$ has a local maximum at $\phi = 0$ and an infinite set of minima determined by $\phi^\dagger \phi = -\frac{\mu^2}{2\lambda} = \frac{v^2}{2}$, where v is the vacuum expectation value of the Higgs field given by

$$v^2 = -\frac{\mu^2}{\lambda}. \tag{2.23}$$

The ground state of the Higgs field is not unique due to the internal symmetry (which leads according to Goldstone's theorem after explicit and spontaneous symmetry breaking to massive spinless bosons). The Higgs potential $V(\phi)$ is plotted in Figure 2.4, The scalar field ϕ with weak hypercharge $Y = 1$ and isospin $I = \frac{1}{2}$

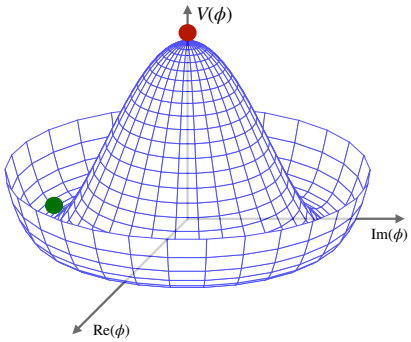

Figure 2.4: Sketch of the Mexican hat potential $V(\phi)$ of the Higgs field. The red dot marks the configuration before EWSB - the position is a metastable local maximum at $\mathrm{Re}(\phi) = \mathrm{Im}(\phi) = 0$ with perfect symmetry. In contrast, the green dot marks the configuration after EWSB - the vacuum state is degenerate.

transforms as a doublet under $SU(2)_I$ gauge transformations. The covariant derivative D_μ, given in Equation 2.19, ensures that the Lagrangian $\mathcal{L}_\phi$ respects local gauge invariance. The VEV v is in the neutral component of the scalar field doublet

$$\langle 0|\phi|0\rangle = \frac{1}{\sqrt{2}} \begin{pmatrix} 0 \\ v \end{pmatrix}. \tag{2.24}$$

This special choice of the vacuum state breaks the $SU(2)_I \times U(1)_Y$ symmetry but results in a massless photon γ. By expanding the scalar field ϕ about the VEV v, setting $\phi_3(x) = v + h(x)$ and using, without loss of generality,

the unitary gauge, the Lagrangian $\mathcal{L}_\phi$ offers different mass and coupling terms of the physical fields. The mass terms of the W boson is

$$\frac{1}{2} m_W^2 W_\mu^{(1,2)} W^{(1,2)\mu}, \tag{2.25}$$

implying the mass of the W boson $m_W = \frac{1}{2} g_W v$, where the physical W boson fields are given by a linear combination of the fields $W^{(1,2)}$:

$$W_\mu = \frac{1}{\sqrt{2}} (W_\mu^{(1)} \mp i W_\mu^{(2)}). \tag{2.26}$$

The masses of the Z boson and the photon γ, corresponding to the physical fields Z_μ and A_μ, respectively, are given by

$$m_A = 0 \text{ and } m_Z = \frac{v}{2} \sqrt{g_W^2 + g'^2}, \tag{2.27}$$

where the fields Z_μ and A_μ are combinations of the gauge fields $W_\mu^{(3)}$ and B_μ, given by a rotation via

$$\begin{pmatrix} Z_\mu \\ A_\mu \end{pmatrix} = \begin{pmatrix} \cos\theta_W & -\sin\theta_W \\ \sin\theta_W & \cos\theta_W \end{pmatrix} \begin{pmatrix} W_\mu^{(3)} \\ B_\mu \end{pmatrix}, \tag{2.28}$$

where the weak mixing angle θ_W (Weinberg angle) is introduced, defined by

$$\cos\theta_W = \frac{g_W}{\sqrt{g_W^2 + g'^2}} = \frac{g_W}{g_Z}, \tag{2.29}$$

which relates the W boson mass and the mass of the Z boson by

$$m_W = m_Z \cos(\theta_W). \tag{2.30}$$

After symmetry breaking, the part of $\mathcal{L}_\phi$ containing the Higgs field offers a mass-term and self-interaction terms of the Higgs boson. The mass of the Higgs boson is given by

$$m_H = \sqrt{2\lambda} v. \tag{2.31}$$

From measurements of m_W and g_W, the VEV v of the Higgs field is determined to $v = 246$ GeV. Since the self-coupling parameter λ of the field ϕ is unknown, there is no theoretical prediction for the mass of the Higgs boson m_H. Beside the mass terms for the vector bosons, the EWSB comes along with interaction terms of the vector bosons and the Higgs boson:

- three- and four-point self-interactions of the Higgs boson
- direct Higgs boson couplings to the weak gauge bosons W and Z
- three- and four-point (self-)interactions of the gauge bosons W, Z and the photon γ.

While the Higgs mechanism in the first place described the mass generation of the EWK vector bosons, the mass generation for electrically charged fermions within the SM is described by Yukawa interactions. A coupling between the Higgs doublet ϕ, the left-handed fermion doublets ψ_L and the right-handed fermion singlets ψ_R is introduced. The Yukawa term after EWK symmetry breaking can be written in the unitary gauge as

$$\mathcal{L}_f = -\frac{g_f v}{\sqrt{2}} \left(\bar{\psi}_L \psi_R + \bar{\psi}_R \psi_L \right) - \frac{g_f h}{\sqrt{2}} \left(\bar{\psi}_L \psi_R + \bar{\psi}_R \psi_L \right). \tag{2.32}$$

The first term in $\mathcal{L}_f$ can be identified as the mass term of the fermions, described by the coupling of the chiral fermions to the Higgs field, where

$$m_f = \frac{g_f v}{\sqrt{2}} \tag{2.33}$$

determines the mass of the fermions. The second term in Equation 2.32 describes the coupling of the fermions to the Higgs boson. This coupling is proportional to the mass of the fermion m_f. This mechanism can only explain the masses of the lower components of the fermion isospin doublets, which can be solved by defining a conjugate Higgs doublet ϕ_C, given by

$$\phi_C = \begin{pmatrix} -\phi^{0*} \\ \phi^- \end{pmatrix} \tag{2.34}$$

with hypercharge $Y = -1$. In an analogous way, the mass terms of the fermions in the upper components of the isospin doublets can be constructed. In conclusion, the framework of the Higgs mechanism within the SM is able to generate the masses of both the vector bosons and the electrically charged fermions using one Higgs doublet ϕ in a gauge invariant way. Note that the majority of the hadron masses which can be measured is not caused by the Higgs mechanism but due to binding energy in the nucleus from QCD interactions.

2.1.6 Higgs Boson Phenomenology

The Higgs boson plays a special role in the presented analysis and is discussed in more detail in this section. The theoretical framework of the SM allows to calculate the production cross sections σ and branching ratios $\mathcal{B}$ of the Higgs boson as a function of its mass m_H, which is a free parameter in the SM. The following discussion refers to the SM Higgs boson, as discovered in 2012 [41, 42], with a mass of $m_H = 125\,\text{GeV}$.

Production Modes

The SM Higgs boson can be produced in different mechanisms, which are summarised in Table 2.1. Gluon gluon fusion (ggF) corresponds to the largest Higgs boson production rate at the LHC at $\sqrt{s} = 13$ TeV ($\sim$ 44 pb), followed by vector boson fusion (VBF). The ggF process is principally mediated by virtual top quarks. The Higgs boson production in VBF is the channel with the second highest production cross section at the LHC ($\sim$ 3.78 pb) but it the most sensitive one since it allows for more background suppression than ggF, in particular regarding background multijet processes. In VBF, two incoming quarks, mostly the up- and down valence quarks of the colliding protons, radiate a weak vector boson $V = W, Z$ which fuse to form a Higgs boson. The two incoming quarks emerge as two high-energetic jets (tagging jets) with a high invariant mass m_{jj}. In contrast to the tagging jets, the Higgs boson decay products are expected to be found in the central detector. In addition, gluon radiation from the central region is heavily suppressed due to the colour-singlet nature of the weak bosons V. Other production mechanisms are associated production with weak vector bosons VH with production cross section at $\sqrt{s} = 13$ TeV of ~ 1.37 pb for WH and ~ 0.88 pb for ZH or associated production with top quarks $t\bar{t}H$ with a production cross section of ~ 0.5 pb. Minor Higgs boson production channels are in association with single top quarks, associated production with $b\bar{b}$. Further, the Higgs potential $V(\phi)$ includes triple and quartic Higgs boson self-coupling terms which allow for di-Higgs boson and tri-Higgs boson production (dominantly in ggF).

Table 2.1: Essential SM Higgs boson production cross sections σ with relative uncertainties at $\sqrt{s} = 13$ TeV in proton-proton collisions based on state-of-the-art theoretical calculations [31].

channel	σ [pb]
ggF	$48.6^{+4.6\,\%}_{-6.7\,\%}$
VBF	$3.78 \pm 2.2\,\%$
WH	$1.37 \pm 2.6\,\%$
ZH	$0.88^{+4.1\,\%}_{-3.5\,\%}$
$t\bar{t}H$	$0.50^{+6.9\,\%}_{-9.8\,\%}$

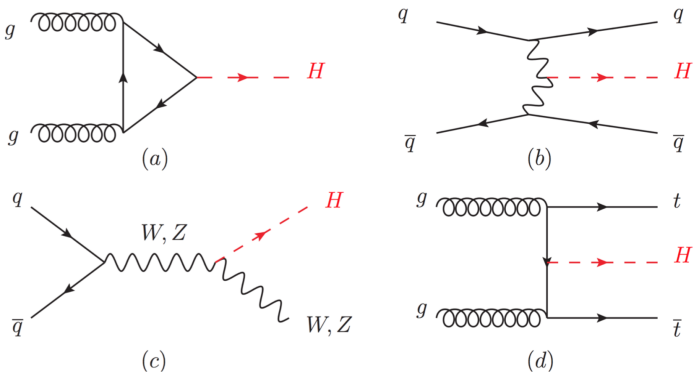

Figure 2.5: Representative Feynman diagrams for the dominant SM Higgs boson production mechanisms at the LHC: gluon gluons fusion (a), vector boson fusion (b), VH production (c) and associated production with top quarks (d) [43].

Decay Modes

Due to its short life time, the Higgs boson can only be detected via its decay products. The leading decay mode of the Higgs boson is $H \to b\bar{b}$ due to the large Yukawa coupling of the heavy bottom quark b to the Higgs boson. In contrast, the top quark t is more massive than the Higgs boson, so the decay $H \to t\bar{t}$ is kinematically forbidden due to energy conservation. Another dominant decay mode is the decay into two vector bosons $H \to VV$ with $V = W, Z$. In addition, the Higgs boson can also decay next-to-leading order (NLO) into massless particles such as gluons g, $H \to gg$ mainly mediated via top quark loops, and photons γ, $H \to \gamma\gamma$ mostly mediated by W boson and top quark loops. Another important Higgs boson decay channel is $H \to \gamma Z$ via virtual W boson loops. The decay modes are summarised in Figure 2.6. Cumulative measurements of the branching ratio $\mathcal{B}$ of the Higgs boson still let room for invisible BSM Higgs boson decay modes, e.g. into dark matter candidates.

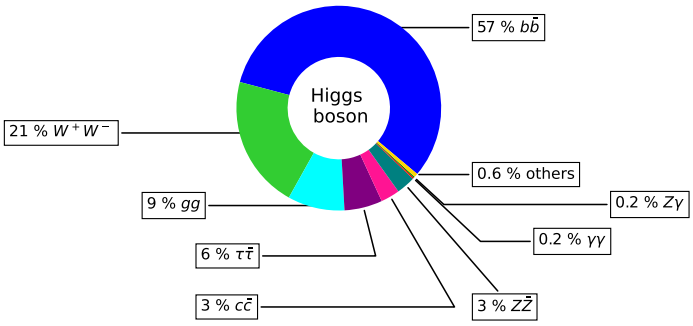

Figure 2.6: Main decay modes of the Higgs boson.

Discovery and Status

After searches for the Higgs boson at LEP [44] and TEVATRON [45, 46], which yielded in exclusion limits, the discovery of a new particle was announced on the 4th of July, 2012 at CERN by the ATLAS [41] and CMS [42] collaborations after roughly two years of data taking at $\sqrt{s} = 7$ and 8 TeV at the LHC. Since the new particle has been observed in the diphoton decay channel and also in decays with two vector bosons, it has to be a new boson. Due to the Landau-Young theorem [47], the diphoton decay channel indicates that the new boson is not

of spin 1. This observation and further precision measurements of the newly observed boson determine the particle's mass to $m_H = 125\,\text{GeV}$. Also the scalar spin property, branching ratios and production cross section of the new boson were established and all measurements agree with the SM prediction of the characteristics of the Higgs boson. The VBF Higgs boson production channel was for instance used to confirm the even CP nature of the Higgs boson [48] as predicted by the SM. A summary of ATLAS Higgs boson measurements in various production and decay channels is presented in Figure 2.7, which are overall compatible with SM expectations.

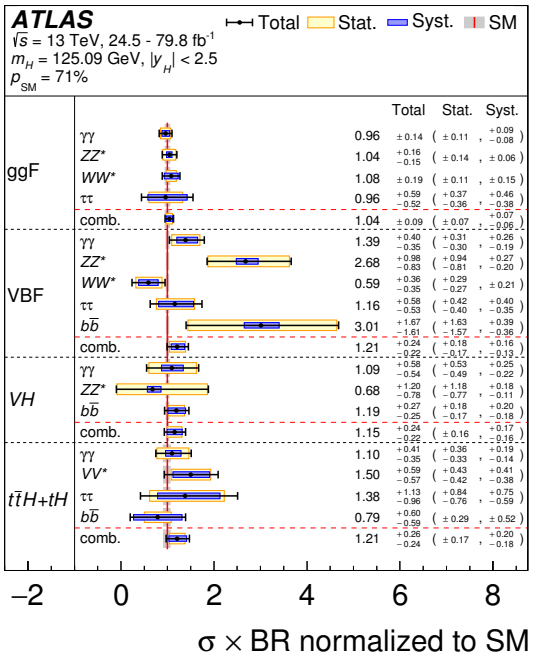

Figure 2.7: Summary of ATLAS measurements of the cross section times branching fraction normalised to SM expectations [31].

2.1.7 Successes and Limitations

The SM describes many of the observed processes in the Universe. It has even predicted many phenomena before they were experimentally confirmed such as the existence of the W and Z bosons and their mass ratio, given by Equation 2.30. The great success of the SM recently culminated in the discovery of the Higgs boson in 2012 at the LHC, roughly 50 years after its theoretical prediction to explain the generation of mass of elementary particles within the mathematical framework of the SM. Apart from that, one of the most promising predictions of the SM refers to the g-factor of the electron which is measured with extraordinary precision [49]. However, the SM has several aesthetical as well as fundamental shortcomings and thus it is widely believed that the SM is a low-energy limit of a yet unknown, bigger theory. The most important limitations of the SM are briefly described in the following.

The SM does not include gravity, which is a fundamental force. In fact, this is not an issue for the description of particle physics processes due to the low strength of gravity in comparison to the other three fundamental forces. Nevertheless, a theory of everything should include quantum gravity. At least at the Planck scale, $m_{\text{Planck}} \sim \sqrt{Ghc^{-3}} \sim 10^{19}\,\text{GeV}$ with the gravitational constant G, quantum gravitational effects arise. Current

attempts of a unification of QM and general relativity lead to non-renormalisable theories. Associated with this, the SM cannot explain the weakness of gravity relative to the other fundamental forces.

The instability of the Higgs boson mass m_H, termed as the hierarchy problem, is a major problem of the SM. The measured mass m_H of the Higgs boson seems unnatural small when considering the higher-order quantum loop corrections to the Higgs boson propagator of the form

$$m_H^2 = m_{H_0}^2 - \frac{\lambda_f^2 \Lambda^2}{8\pi^2} + \dots \tag{2.35}$$

with the bare Higgs boson mass m_{H_0}, the Yukawa fermion coupling λ_f and Λ is the energy scale where BSM physics is expected. These corrections are quadratically divergent in Λ^2 and thus predict a huge Higgs boson mass compared to the weak energy scale. The observed Higgs boson mass in turn suggests an unnatural fine-tuning through the cancellation of divergent terms in higher-order corrections of m_H.

Further, it is not understood why fermions appear in three generations and why their masses spread over several orders of magnitude. In fact, neutrinos ν are massless within the SM which contradicts the observed neutrino oscillations which imply that at least two neutrinos are massive. Though it is possible to describe the neutrino mass generation within the SM, the magnitude of the Yukawa coupling constants of neutrinos λ_ν remains a mystery.

The SM cannot explain the huge matter-antimatter imbalance, known as the baryon asymmetry, which is measured in the observable Universe. Given that matter and antimatter were produced in equal amounts at the Big Bang 13.8 billion years ago, it seems unnatural that the present Universe is only made of matter. According to Sakharov's theorem [50], the baryon asymmetry can only be produced in baryogenesis if three conditions are fulfilled: First, there is at least one baryon number violating process. Second, C and CP violation do exist and third, baryogenesis takes place out of thermal equilibrium. All of these conditions can be realised in the SM. Within the SM, CP violation is observed in the quark sector and first experimental hints are observed by the T2K experiment that CP is not conserved in the lepton sector [51]. However, all observed CP violating effects are not sufficient to explain the huge observed matter-antimatter asymmetry.

The SM cannot naturally explain the absence of CP violation in QCD, known as the strong CP problem. There are terms in the SM Lagrangian density of the strong interaction breaking the CP symmetry described by a parameter θ. From observation, physicists know that this parameter must be unnatural small, in the order of 10^{-8}. The Peccei-Quinn approach [52] provides a potential solution of the strong CP-problem by introducing a new particle, the axion, emerging from a spontaneous breaking of the Peccei-Quinn $U(1)_{\mathrm{PQ}}$ symmetry. This mechanism enforces $\theta = 0$ and thus gives an explanation for CP conversation in QCD.

Another aesthetical reason to believe that the SM is not a final theory is the large number of free parameters - the SM includes in total 26 free parameters:

- three coupling constants of the fundamental forces g, g' and g_s
- two parameters of the Higgs potential λ and μ (or the VEV v and the Higgs boson mass m_H)
- six quark masses m_{q_i} (or their Yukawa coupling constants)
- six lepton masses m_{l_i} (or their Yukawa coupling constants)
- four parameters of the CKM matrix describing quark mixing
- four parameters of the PMNS matrix describing neutrino mixing
- a QCD phase angle θ

At present, these parameters cannot be derived from theoretical assumptions but must be determined experimentally.

Astrophysical observation strongly suggest the existence of dark matter and dark energy. The issue of dark matter will be addressed in more detail in Chapter 2.2. Dark energy is an unknown form of (vacuum) energy which

forces the Universe to expand accelerated. Further, to explain the cosmological mysteries of the horizon problem, the flatness problem and the magnetic monopole problem, it is assumed, that the Universe expanded exponentially very short time after the big bang - this process is called inflation, which is not understood yet. These astrophysical phenomena, which have a big influence of the structure formation and evolution of the Universe, cannot be explained using the forces and the particle content of the SM.

Recently, Fermilab reported deviations from SM predictions in the muon g-2 experiment [53]. The g-2 experiments probe the gyromagnetic ratio g of muons in an external magnetic field. Since muons are significantly heavier than electrons, they are more sensitive to new types of virtual particles which are eventually created in the vacuum. A polarised muon beam is directed into a storage ring with an external magnetic field in which the muons' spins precess. The difference of the spin precession frequency, which is given by Larmor and Thomas precession, and the cyclotron frequency, measured via the number and energy of final state positrons as a function of time, is directly related to g-2. The measured value of g-2 is larger with $4.2\,\sigma$ than expected from theoretical calculations which confirms strong evidence for new physics from earlier experiments [54] in which muons could couple to yet undiscovered objects or forces. This will be further investigated with improved theoretical calculations and 20-times more data collected in future runs of the muon g-2 experiment at Fermilab.

2.1.8 Physics beyond the Standard Model

After discussing the shortcoming of the SM, potential solutions to these issues are described in this section. There exist several theories which solve some of the SM issues. Supersymmetry (SUSY) is a model based on a proposed symmetry relating the force carriers, the bosons, and the matter particles, the fermions. SUSY is a very promising idea since it potentially solves many shortcomings of the SM at once. Since SUSY predicts a whole bunch on new particles, every SM particle with spin s gets a superpartner with spin $|s - 1/2|$ and vice versa, there are particles which could solve the mysteries of dark matter, dark energy or the strong CP problem. SUSY also provides a solution of the hierarchy problem, since it leads to natural cancellation of fermionic and bosonic loop corrections in the Higgs boson propagator. In addition, SUSY allows for the unification of the coupling constants of the strong, the weak and the electromagnetic force at some higher energy scale of the order $O(10^{16})$ within a grand unified theory (GUT). GUTs are theories to unify the forces of the SM described in one single gauge symmetry such as $SU(5)$ or $SO(10)$. However, if SUSY is realized in nature, the symmetry needs to be broken at low energies since no superpartners of SM particles with equal masses have been found. Despite SUSY has several theoretically appealing and beautiful features from an aesthetic point of view, SUSY searches yielded only exclusion limits yet but there is still room for potential SUSY discoveries at the Lhc in the future.

Other extensions of the SM refer to the neutrino sector. The observed neutrino oscillations [55], theoretically described by the Pontecorvo-Maki-Nakagawa-Sakata (PMNS) matrix [56], indicate that at least two of the SM neutrinos are massive since the probability of a change of the neutrino flavours depends on the squared mass difference of the two involved neutrino flavours.

The Seesaw Mechanism describes the magnitude and relative size of the individual neutrino masses in which for each generation a light neutrino and a yet unobserved neutrino with large Majorana mass is predicted. In this context, also the search for sterile neutrinos is ongoing, which are hypothetical right-handed neutrinos which only interact via gravity and, by construction, do not participate in forces of the SM and thus are dark matter candidates. In addition, sterile neutrinos could explain the origin of matter via a lepton-number violating process called leptogenesis, a process generating a lepton-antilepton-asymmetry in the early Universe.

Other BSM extension predict large extra space dimensions (LEDs), as described by Kaluza [57] and Klein [58] and required by String theory for its mathematical consistency, which could explain the apparent weakness of gravity. The existence of LEDs would correspond to additional particles, where the Lhc signature could be an energetic mono-object plus missing transverse energy [59].

2.2 Dark Matter

> *"Falls sich dies bewahrheiten sollte, würde sich also das überraschende Resultat ergeben, dass dunkle Materie in sehr viel grösserer Dichte vorhanden ist als leuchtende Materie."*
>
> *Fritz Zwicky, 1933*

The visible, baryonic matter only accounts for less than 5 % of the energy density in the observable Universe, as shown in Figure 2.8, while most of the energy in the Universe is provided by dark matter and dark energy as described by the ΛCDM model of cosmology. A brief abstract of the history of dark matter and its experimental evidence is given in Section 2.2.1. Section 2.2.2 summarises hypothesis about the nature of dark matter. Due to its importance for the presented analysis, the Higgs portal model is discussed in more detail in Section 2.2.3. Ongoing searches and strategies are presented in Section 2.2.4.

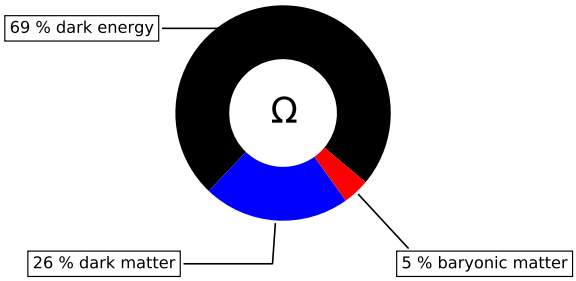

Figure 2.8: Relative contribution of dark matter, dark energy and baryonic matter to the total energy density Ω of the Universe according to the PLANCK experiment [60].

2.2.1 History and Evidence

There is overwhelming observational evidence for the existence of matter beyond the visible one. The first evidence for the existence of non-luminous matter was claimed by the Swiss astronomer Zwicky in 1933 by applying the virial theorem to the Coma galaxy cluster [61, 62]. He observed that the measured velocity dispersion of the galaxies within that cluster is too high to keep the cluster stable. Therefore he deduced that the mean mass density in the Coma cluster must exceed the mass density provided by visible matter, which in turn can be determined from the observed absolute luminosity of that cluster. Similar observations were made a few years later by Smith [63] and Holmberg [64] using measurements from the Virgo galaxy cluster. The potential existence of dark matter was actually taken seriously in the 1970s when Rubin's observation [65] and other measurements of gravitational anomalies provide evidence for dark halos surrounding galaxies. The observation of galactic rotation curves representing the velocity v of stars in a galaxy as a function of their distance to the galaxy center r via a measurement of the 21 cm line of neutral hydrogen strongly suggest the existence of non-luminous matter [66, 67]. The rotational velocity v of an object in an orbit around a galaxy can be described with Newtonian mechanics by

$$v(r) \sim \sqrt{\frac{M(r)}{r}}, \tag{2.36}$$

with the mass $M(r)$ contained inside the orbit of radius r. For radii r which exceed the visible part of the galaxy, the velocity $v(r)$ scales like $v(r) \sim 1/\sqrt{r}$. This contradicts many observations which confirm that $v(r)$

is approximately constant if r is outside of the visible galaxy, strongly implying the existence of dark matter, which dominates the gravitational force outside the visible part of the galaxy. An exemplary measured rotation curve is depicted in Figure 2.9 on the left hand side, showing that the rotational velocity $v(r)$ stays constant with increasing distance r to the spiral galaxy's center. A model with disk and gas cannot fit the data, while adding the dark matter halo leads to a very good description of the observation. The existence of dark matter is also supported by gravitational lensing experiments. Lensing by gravity is the effect, described by general relativity, that light is bent while traversing a gravitational field. From the observational point of view, this bending can lead to circular arranged copies of the image of an object which lies behind the source of the gravitational field. The existence of dark matter is implied since the amount of visible matter between the source of the gravitational field and the observer cannot explain the measured image structure. In this context, the Bullet cluster (1E0657-558) is a key ingredient for observing properties of dark matter, providing especially constraints on the magnitude of dark matter self-interaction. The Bullet cluster actually consists of two colliding galaxy clusters, mainly consisting of baryonic stars and gas as well as the hypothesized dark matter. The key observation in the collision of the two clusters is that the different components, such as stars, gas and dark matter, behave differently as shown by the NASA Chandra X-ray Observatory, displayed in Figure 2.9. The stars in the galaxies, directly visible by the emitted light, are not strongly affected by the collision. In contrast, the main part of the baryonic contribution, the gas, which is visible via X-rays, is influenced much more than the visible stars due to electromagnetic interactions of the gas particles. The matter distribution, observed via gravitational lensing, shows that the majority of mass in the cluster was not braked by the collision [68]. Nowadays, the

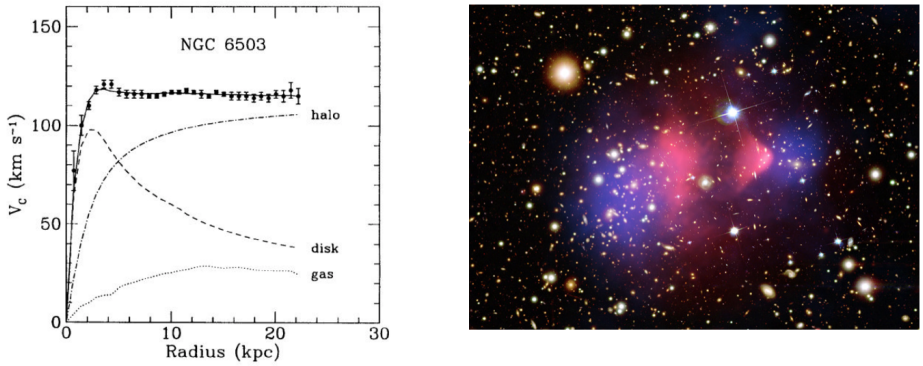

Figure 2.9: Left: Rotation curve of NGC 6503, a dwarf spiral galaxy, showing the baryonic contribution (disk and gas) as well as the halo (dark matter). The black squares with error bars represent the measurement [69]. Right: Picture from the Chandra Observatory of the Bullet cluster showing a X-ray image in pink (which includes most of the baryonic matter as hot gas) superimposed with the calculated matter distribution in blue and the visible light image (credit: NASA/CXC/SAO/STScI).

most important source of information about the amount and properties of dark matter are Cosmic Microwave Background (CMB) radiation observations and the structure formation in the Universe, mainly investigated by the Cobe [70], Wmap [71] and Planck experiments [72]. The CMB is a remnant, nearly isotropic radiation from the early Universe, created roughly 380,000 years after the Big Bang when the temperature dropped below $T = 3 \cdot 10^3$ K so that matter and radiation were decoupled. A Mollweide projection of the CMB is shown in Figure 2.10. In this time of recombination, atoms were formed when atomic cores captured free electrons. These atoms became stable when the universe cooled and the radiation became less energetic and was not able anymore to ionize atoms. The mean free path of photons increased and the Universe became transparent for photons. The CMB was discovered by accident in 1965 by Penzias and Wilson [73]. Since the cosmos expanded after the decoupling, the CMB radiation was redshifted and cooled down. By today, the CMB has an almost perfect thermal black body spectrum with a temperature of $T = 2.72548 \pm 0.00057$ K [74]. It should be noted that the CMB is almost perfectly isotropic even in regions of the universe which are causal disconnected parts. This issue is known as the horizon problem (which may solved by inflation). However, small temperature fluctuations $\Delta T/T$ of the observed CMB in the order of 10^{-5} give rise to important information about the

characteristics of the early universe and the structure formation. The CMB's temperature fluctuations are caused by variations in the density at time of the radiation-matter-decoupling. Considering all relevant effects, in particular a higher redshift in denser regions, denser regions correspond to down-fluctuations in the temperature. The density irregularities in the early Universe are caused by three main effects: baryonic acoustic oscillations, Silk damping [75] and the Sachs-Wolfe-effect [76]. The spherical structure of these temperature or density fluctuations give access to key parameters of the ΛCDM model. The relative temperature fluctuations $\Delta T/T$ can be expanded in spherical harmonics Y_m^l as

$$\frac{\Delta T}{T}(\theta,\phi) = \sum_{l=1}^{\infty}\sum_{m=-l}^{m=l} a_{lm} Y_m^l(\theta,\phi). \tag{2.37}$$

with the azimuthal angle ϕ, polar angle θ and multipole moments a_{lm} with $\langle a_{lm}\rangle = 0$. The multipole coefficients are given by

$$C_l = \frac{1}{2l+1}\sum_m \langle |a_{lm}|^2\rangle. \tag{2.38}$$

The coefficients C_l of the multipole expansion of the fluctuations as a function of the multipole moment l, the so-called angular power spectrum, shows a certain peak structure, displayed in Figure 2.10. For example, the first peak's position provides information on the total density of the Universe and thus on the geometry of the Universe. The height of the first peak corresponds to the matter content. The ratio of the first and second peak is sensitive to the baryonic matter content. The primordial density fluctuations in the CMB are also thought to be the seeds from which the Universe's structure growed through gravitational attraction. The amount of baryonic matter is likely not enough to provide sufficient gravitational attraction indicating that there must be some non-baryonic form of matter. The experiments WMAP, COBE and Planck showed that the temperature power spectrum of the CMB is consistent with a spatially flat Universe as described by the standard model of cosmology. The CMB is one of the most striking evidences for the Big Bang model and dark matter.

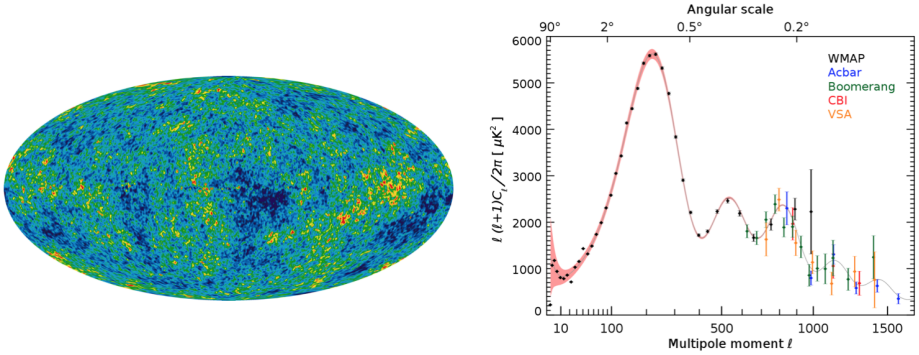

Figure 2.10: Left: CMB combination map as weighted linear combination of five WMAP frequency maps. The colours correspond to a linear scale from -200 to 200 μK showing the CMB anisotropies [71]. Right: Angular power spectrum of the CMB for different experiments (credit: NASA/WMAP).

2.2.2 Dark Matter Candidates

Despite perspicuous evidence for the existence of dark matter from a couple of independent measurements, the fundamental nature of dark matter remains a mystery. Based on observations described in Section 2.2.1, constraints on the properties of dark matter can be summarised as follows:

- massive

- longevity or even stable
- at most weakly self-interacting
- at most weakly interacting with SM objects (electrically neutral and non-coloured)
- likely cold (non-relativistic at matter-radiation decoupling)
- mostly or only non-baryonic

From the observed dark matter properties, models and particle candidates to explain its nature are constructed. However, no particle of the SM fulfils the required properties since these either interact too strongly, are not stable or are too light. In the following, some important dark matter particle candidates are presented:

- **WIMPs**: Many dark matter candidates are classified as weakly interacting massive particles (WIMPs) since these particles are naturally predicted by BSM theories. A WIMP is assumed to be a fundamental particle which is stable over cosmological scales and does not interact with present particle detectors. It is assumed, that WIMPs were produced in the early Universe among with the SM particles and freezed-out at some point of the Universe's evolution. The WIMP hypothesis is in particular interesting due to the WIMP miracle [77]. From the estimated dark matter relic abundance, the dark matter self-annihilation cross section can be calculated, which in turn determines the number density of dark matter within the expansion of the Universe. The quite surprising coincidence is that the observed dark matter relic abundance requires a cross section which corresponds to the order of magnitude of an electroweak interaction, implying that dark matter would have WIMP properties and could be produced at the LHC. Additionally, important experimental support for the WIMP hypothesis is the observation of dark matter in the Bullet cluster as described in Section 2.2.1, while fundamental theoretical support originates from SUSY models.
- **WISPs**: Very weakly interacting slim particles (WISPs) are a class of very light sub-eV dark matter candidates. The most famous candidate is the axion, which is also related to the strong CP problem as predicted in 1978 by the Peccei-Quinn mechanism [52], or hidden-sector photons. The axion is assumed to be a pseudo-scalar boson with a mass between 1 μeV and 1 meV. Theories suggest that axions should be detectable via diphoton decays and by loop-induced conversion to two photons in a strong external magnetic field described by the (inverse) Primakoff effect.
- **Neutrinos**: SM neutrinos were traded as potential dark matter candidates due to their longevity and the neutrality with respect to the electromagnetic and strong interactions. They are candidates for hot dark matter as they were relativistic at time of decoupling. However, neutrinos with masses in the eV-range correspond to a too small relic density parameter to account solely for the total dark matter mass in the Universe. In contrast, potential heavier sterile neutrinos with masses of a few keV and much weaker couplings to SM particles are viable dark matter candidates.
- **Alternatives**: Alternative hypotheses to the existence of particle dark matter is a potential misunderstanding of general relativity on large, galactic scales or of the corresponding dynamical response of particles and thus imply that modifications to general relativity are needed. One of the most famous examples is modified Newton dynamics (MOND) and its relativistic extension TeVeS [78, 79]. The testing of MOND models is ongoing, in particular based on observations of dwarf galaxies. Also the Bullet cluster probes the MOND assumption. Weak lensing observations of the Bullet merger show that the center-of-mass is displaced from the baryonic center-of-mass [68]. This observation is hard to explain by MOND theories and can be seen as an empirical proof that MOND solely cannot explain dark matter. There are also attempts to explain the phenomena of dark matter and dark energy with the SM and general relativity without the need for BSM physics [80].

2.2.3 Dark Matter Models

Theoretical and phenomenological models to describe dark matter can be divided into complete theories, effective field theories (EFTs) and simplified models:

- Complete theories provide full predictions but are less general and come along with a large number of free parameters which may reduced at the cost of ad hoc assumptions. The most prominent example is minimal SUSY. R-parity conserving SUSY theories provide a natural candidate for a dark matter particle, it is the stable lightest supersymmetric particle (LSP), which is typically produced in SUSY decay chains. Thus, a promising cold dark matter candidate of the MSSM is the lightest SUSY neutralino. Neutralinos are assumed to have a mass around the weak scale and coupling characteristics of the weak force, which are WIMP properties as explained in Section 2.2.2
- Simplified models are characterised by a small number of parameters characterising the dark matter properties and couplings. In contrast to EFT dark matter models, simplified models allow for a correct description of the event kinematics.
- EFTs are low-energy limits of some more general (unknown) theories. The SM itself is assumed to be an EFT of some bigger theory. For example, the SM is assumed to be a valid low energy limit of a bigger theory. In general, EFTs are a systematic expansion of new physics around the SM, typically in the form of Lagrangians as

$$\mathcal{L}_{\text{EFT}} = \mathcal{L}_{\text{SM}} + \sum_i \frac{f_i}{\Lambda^2} O_i + \text{ higher order terms} \tag{2.39}$$

  The factors f_i are the Wilson coefficients, Λ is the scale of new physics and O_i are operators, which for example describe the interactions between the SM particles mediated by new physics.

A sketch of these complete or less complete models in given in Figure 2.11. DM theories which are embedded in frameworks that also address other open questions in particle physics such as the hierachy problem, neutrino masses or the strong CP problem are favoured.

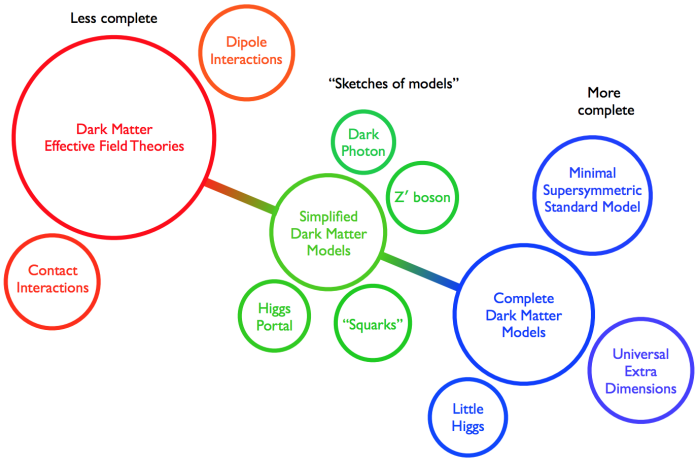

Figure 2.11: Sketch of dark matter models [81].

Since the Higgs portal model has an important role in this thesis, it will be discussed in more detail following Ref. [82–85]. The Higgs portal models are simplified models assuming that the SM Higgs boson, or even a heavier Higgs-like mediator, can act as a portal to the dark sector beyond the SM. The coupling of the Higgs boson to dark matter candidates is well motivated since the Higgs boson naturally couples to massive particles. The Higgs boson or a heavier scalar particle is in this model assumed to be the only mediator to the dark matter candidates, usually assumed to be WIMPs. The simplest, model-independent Higgs portal model assumes the SM Higgs sector, i.e. one single doublet Higgs field ϕ as described in Section 2.1.5, plus one single new dark matter particle which can be a scalar boson, a vector boson or a Dirac or Majorana fermion (a Majorana fermion is a fermion which is its own antiparticle). A new symmetry, dark matter parity, ensures

that dark matter candidates are produced in even numbers in SM particle decays and (the lightest) dark matter particles are stable. The following Lagrangian densities for the different spin scenarios (scalar (S, $s = 0$), vectorial (V, $s = 1$) or fermionic (ψ, $s = 1/2$)) can be written in an effective and model-independent framework as

$$\begin{aligned}
\mathcal{L}_S &= -\frac{1}{2}\left(m_{\chi,S}^2 S^2 + \frac{1}{2}\lambda_S S^4 + \frac{1}{2}\lambda_{HSS}\phi^\dagger\phi S^2\right) \\
\mathcal{L}_V &= \frac{1}{2}\left(m_{\chi,V}^2 V_\mu V^\mu + \frac{1}{2}\lambda_V (V_\mu V^\mu)^2 + \frac{1}{2}\lambda_{HVV}\phi^\dagger\phi V_\mu V^\mu\right) \\
\mathcal{L}_\psi &= -\frac{1}{2}\left(m_{\chi,\psi}\bar{\psi}\psi + \frac{1}{2}\frac{1}{\Lambda}\lambda_{H\psi\psi}\phi^\dagger\phi\bar{\psi}\psi\right),
\end{aligned} \tag{2.40}$$

where Λ represents the scale of new physics. The Higgs portal models come along with a minimal number of new parameters: the coupling of the dark matter particle and the Higgs boson, λ_{HXX} with $X = \{S, V, \psi\}$, as well as the dark matter particle mass m_χ. The dark matter self-interaction terms are not essential for the discussion of Higgs portal models at the LHC so far. The resulting partial Higgs boson decay widths $\Gamma_{\text{H,inv}}$ show especially different dependencies on the Higgs boson mass m_H:

$$\begin{aligned}
\Gamma_{\text{H,inv}}(H \to \chi_S\chi_S) &= \frac{\lambda_{HSS}^2 v^2 \beta_S}{64\pi m_H} \\
\Gamma_{\text{H,inv}}(H \to \chi_V\chi_V) &= \frac{\lambda_{HVV}^2 v^2 \beta_V m_H^3}{256\pi m_H^4}\left(1 - \frac{4m_V^2}{m_H^2} + \frac{12m_V^4}{m_H^4}\right) \\
\Gamma_{\text{H,inv}}(H \to \chi_\psi\chi_\psi) &= \frac{\lambda_{H\psi\psi}^2 v^2 \beta_\psi m_H}{32\pi\Lambda^2}
\end{aligned} \tag{2.41}$$

where $\beta_X = \sqrt{1 - 4(m_X^2 m_H^{-2})}$, v is the VEV of the Higgs field as well as coupling parameters λ_{HSS}, λ_{HVV} and $\lambda_{H\psi\psi}/\Lambda$. In a dark matter search at a collider such as the LHC, the dark matter candidates in the final state emerge as an invisible signature. The branching fractions $\mathcal{B}_{\text{inv.}}$ of invisible Higgs boson decays can be measured from which the maximum allowed decay width to invisible particles can be determined:

$$\Gamma_{\text{H,inv}} = \mathcal{B}_{\text{inv.}} \cdot \Gamma_{\text{H,total}}, \tag{2.42}$$

where $\Gamma_{\text{H,total}}$ is the total Higgs boson decay width. Since the Higgs boson is assumed to be the only mediator to dark matter candidates, the spin-independent dark matter-nucleon scattering cross section σ can be written as:

$$\begin{aligned}
\sigma_{SN} &= \frac{\lambda_{HSS}^2}{16\pi m_H^4}\frac{m_N^4 f_N^2}{(m_N + m_S)^2}, \\
\sigma_{VN} &= \frac{\lambda_{HVV}^2}{16\pi m_H^4}\frac{m_N^4 f_N^2}{(m_N + m_V)^2}, \\
\sigma_{\psi N} &= \frac{\lambda_{H\psi\psi}^2}{4\pi m_H^4\Lambda}\frac{m_\psi^2 m_N^4 f_N^2}{(m_N + m_\psi)^2},
\end{aligned} \tag{2.43}$$

with the nucleon mass $m_N = 939\,\text{MeV}$ and the lattice-QCD form factor f_N parametrising the coupling of the Higgs boson and the nucleon. Different estimations of this parameter range from 0.260 to 0.629 [86]. Due to objections of a non-renormalisable Lagrangian in the vector-like EFT model, it is advisable to use a ultraviolet completion with a dark Higgs boson giving mass to the dark matter candidate via EWSB leading to at least

two additional parameters, the mass of the dark Higgs boson and its mixing angle with the SM Higgs boson [87–89].

2.2.4 Dark Matter Searches

Based on the properties of dark matter candidates and dark matter models, discussed in the Section 2.2.3 and 2.2.4, search strategies for dark matter are developed in strong collaboration of experimental physicists and theorists. The benchmark assumption for dark matter searches is the existence of an interaction between SM particles and a dark matter particle, which is mostly assumed to be WIMP, stable at timescales to be detected and invisible for the detector. Complementarity of search strategies is one of the keys for a successful dark matter search, provided in independent ways via direct, indirect and collider searches, illustrated in Section 2.12 and described in the following:

- Direct dark matter detection is based on elastic scattering of a WIMP with a target atomic nuclei in a high-sensitive detection medium. If a WIMP traverses the detector and scatters off of a recoiling atomic nucleus, it deposits a tiny amount of energy. The interaction rate of WIMPs and the atomic nuclei depends on several parameters, especially the WIMP m_χ and the interaction cross section of WIMPs and nuclei σ_χ. The deposited energy in the WIMP-nucleon-scattering is in the range $1 - 10\,\text{keV}$. So far, various experiments such as DarkSide-50 [90], PandaX-4T [91] Cresst [92] and Xenon1T [93] placed exclusion limits in the plane spanned by the WIMP-nucleon scattering cross section and the WIMP mass.
- Indirect dark matter searches aim for detecting dark matter via an excess in photons, neutrinos or other particles produced in dark matter pair annihilation or particle conversion as for example performed by Fermi LAT [94] or Ams [95]. Experiments such as Any Light Particle Search (ALPS) [96] search for axions and other axion-like particles [97]. The concept of ALPS can be described as a light-shining-through a wall experiment: Light produced by a powerful laser is traversing a magnetic field. In the field, the photons are assumed to be converted into a WISP candidate via axion-photon-mixing in front of a light-blocking barrier and subsequently reconverted into photons behind that barrier, which can be detected.
- Collider searches aim for detecting dark matter by producing it in the laboratory. There are two ways two produce dark matter at colliders - as a mediator or as a final state particle - giving many possibilities for potential dark matter signatures. Due to the properties of dark matter, it is assumed that dark matter particles do not interact with the detector. Therefore, the experimental signature for final state dark matter candidates is the presence of invisible particles, which manifest themselves in missing transverse energy. Typical signatures are $E_{\text{T}}^{\text{miss}} + X$ with $X = V, H, \gamma$ or heavy flavour quarks. It is not expected that different spin scenarios have a significant impact on visible particle kinematics and thus lead to the same phenomenology for collider searches [98]. A collider search for dark matter in the $E_{\text{T}}^{\text{miss}}$+jets channel is presented in this thesis and therefore explained in more detail throughout the following chapters.

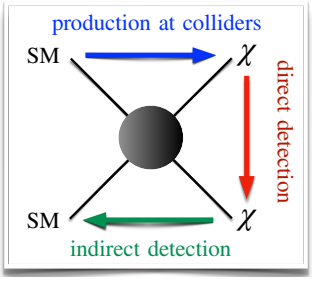

Figure 2.12: Feynman sketch of the dark matter search paradigms.

CHAPTER 3

LHC and the ATLAS experiment

In this chapter the experimental apparatus and proton-proton collision phenomenology are described.

3.1 CERN and LHC

CERN is the European Organization for Nuclear Research established in 1954 and based near Geneva, Switzerland. Many important scientific achievements in modern physics have been made at CERN laboratories. CERN is also the home of the origins of the World Wide Web, developed by Tim Berners-Lee and Robert Cailliau in the 1980s. Most importantly, CERN provides the infrastructure for the largest and most powerful hadron accelerator and collider in the world - the Large Hadron Collider (LHC), providing the highest center-of-mass energy $\sqrt{s}$ worldwide. The LHC lies, protected from cosmic radiation and other disturbances, deep beneath the earth's surface at a depth between 45 m and 170 m in a circular tunnel with a circumference of 26.659 km. The LHC generates proton-proton collisions at four different crossing points of the proton beams, whereby the LHC is the last ring in a chain of several particle accelerators at CERN, sketched in Figure 3.1. The accelerator chain starts with a tank of hydrogen molecules from which the protons are extracted by means of an electric field. A linear accelerator, LINAC 2, accelerates the protons to an energy of 50 MeV with a beam pipe length of 30 m. Then it follows the proton synchrotron booster and the proton synchrotron, further accelerating the protons to 26 GeV, followed by the super proton synchrotron, boosting the energies to 450 GeV. The protons are now ready to be injected into the LHC, boosting and steering protons by means of electromagnetic fields step by step to the final energy. Radiofrequency cavities accelerate the charged particle beams, while the superconducting electromagnets generate magnetic fields with a strength of up to 8.3 T to focus and stabilize the beams and to bend the trajectory of a particle with electric charge q on a circular path due to the Lorentz force

$$\vec{F}_{\text{Lorentz}} = q\left(\vec{E} + \vec{v} \times \vec{B}\right), \tag{3.1}$$

where $\vec{E}$ is the electric field, $\vec{v}$ the particle's velocity and $\vec{B}$ the magnetic field. The curvature of the particle's trajectory with radius R is then given by $R = p_{\text{T}}/(q|\vec{B}|)$. The four main experiments at the LHC, located at the four crossing points of the beam, are ALICE [100], ATLAS [101], CMS [42] and LHCB [102]. The main focus of the ATLAS and CMS physics program is on Higgs boson and top quark physics, establishing the SM of particle physics and searching for BSM physics, e.g. supersymmetric or DM particles and other exotic phenomena such as extra dimensions or dark energy. The ALICE experiment focuses on studying the quark-gluon plasma in heavy-ion collisions, while the LHCB experiment mainly investigates bottom quark physics with a focus on CP violation and the baryon asymmetry. The operation time of the LHC is divided into several runs, which are separated by long-shutdowns (LS) where the machine and the detectors undergo upgrades and rectifications,

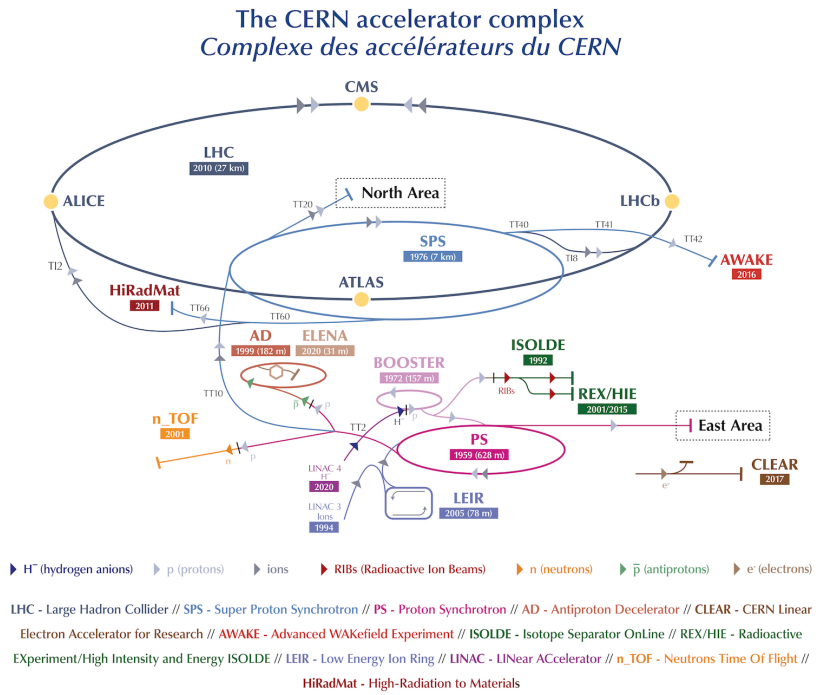

Figure 3.1: LHC accelerator complex providing several accelerators and boosting chains for various experiments [99].

see Table 3.1. The first research run from 2009 to 2013 (Run I) was performed at a nominal center-of-mass energy (CME) $\sqrt{s}$ of 7 TeV until 2011 and 8 TeV from 2012, culminating in the discovery of the Higgs boson, announced on July, 4 2012 [103, 104]. After an upgrade from 2013 to 2015, the LHC was operating in Run II with an increased CME of $\sqrt{s} = 13$ TeV from 2015 til 2018. In Run II, each proton beam contained 2808 bunches with $1.2 \cdot 10^{11}$ protons each, providing a billion collisions per second at an operating temperature of 1.9 K. The switch from Run I to Run II also included several changes related to the beam conditions, the detector system, the MC simulation procedure, and the object reconstruction. At the end of Run III, 300 fb^{-1} of data will be collected. In 2028, the high-luminosity LHC (HL-LHC) [105] is planned to operate at highly increased luminosities, see Section 3.3.2, and will give access to high-sensitivty measurements of rare processes such as $H \to \mu\mu$ or di-Higgs boson production.

Table 3.1: Center-of-mass energy $\sqrt{s}$ and integrated luminosity $\mathcal{L}$ per data-taking periods corresponding to the first three runs of the LHC and the future HL-LHC [105].

Run	Period	$\sqrt{s}$ [GeV]	$\mathcal{L}$ [fb^{-1}]
I	2009 – 2013	7, 8	30
II	2015 – 2018	13	140
III	2022 – 2025	13	300
HL-LHC	> 2028	14	3000

3.2 ATLAS

The ATLAS (A Toroidal LHC Apparatus) experiment is one of the four major experiments located around the LHC at CERN. The ATLAS collaboration consists of roughly 3000 physicists from all over the world working

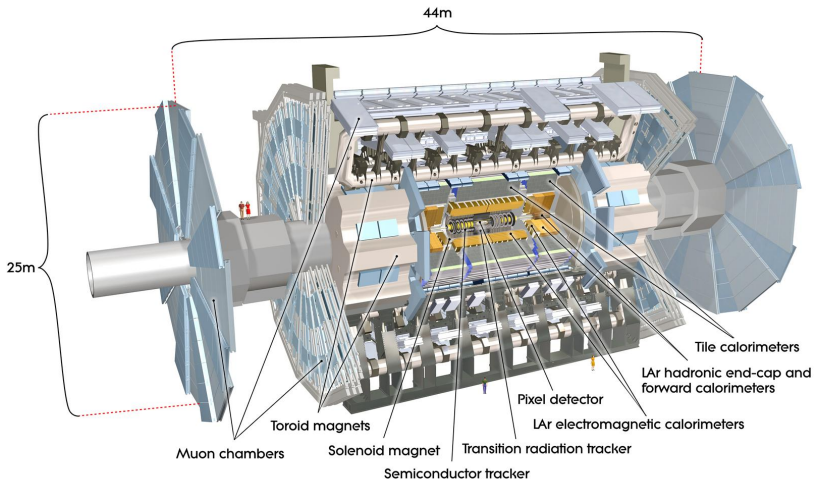

Figure 3.2: ATLAS detector with its subcomponents [106].

on the detector development, computing infrastructure, the collection of data and their analysis as well as the corresponding publications. The ATLAS detector, depicted in Figure 3.2, is a multi-purpose detector with a total height of 25 m, a length of 44 m and a weight of $7 \cdot 10^3$ tonnes. It is designed with a forward–backward symmetric cylindrical geometry and with almost a 4π coverage in solid angle. The detector consists of multiple independent subcomponents to achieve the best possible measurement and identification of various kinds of particles and their properties. The superior subcomponents of the ATLAS detector are the inner detector (ID), the calorimeter system based on an electromagnetic (ECal) as well as a hadronic calorimeter (HCal) and the muon spectrometer (MS). Also, an online and offline trigger system is installed. These components are described in more detail in the following.

3.2.1 Coordinate System

ATLAS uses a right-handed coordinate system for the description of events, sketched in Figure 3.3. The interaction point defines the origin of the coordinate system. The anti-clockwise beam direction corresponds to the z-axis, the x-axis points from the interaction point to the center of the LHC and the y-axis points upwards. In spherical coordinates, the azimuthal angle ϕ is measured around the beam axis with $\phi = 0$ along the x-axis and the polar angle θ is measured with respect to the z-axis, i.e. $\theta = 0$ along the beam pipe. The rapidity y is defined as

$$y = \frac{1}{2} \ln \left(\frac{E + p_z}{E - p_z} \right), \tag{3.2}$$

where E is the energy of the object and p_z is the z-component of the momentum. Using the polar angle θ, the pseudorapidity η ($\eta = 0$ if $\theta = 90^\circ$, $\eta = \infty$ if $\theta = 0^\circ$) can be defined as

$$\eta = -\ln \left(\tan \left(\frac{\theta}{2} \right) \right), \tag{3.3}$$

whereby for $p \gg m$ it holds $\eta = y$, where m is the mass of the object, while for massive jets it holds $|y| < |\eta|$. The transverse momentum p_T in the x-y-plane is given by $p_\mathrm{T} = \sqrt{p_x^2 + p_y^2} = |\vec{p}| \sin(\theta)$. Further, the transverse

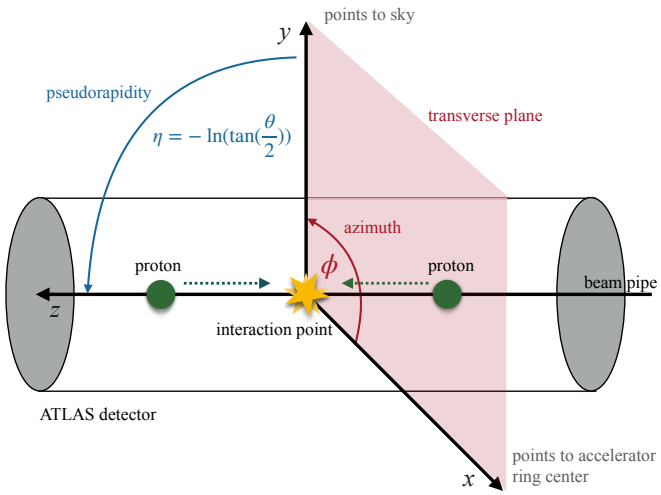

Figure 3.3: Sketch of the ATLAS coordinate system.

momentum p_T and energy E are related by

$$p_T = \frac{\sqrt{E^2 - m^2}}{\cosh(\eta)}, \tag{3.4}$$

which reduces for negligible mass to $p_T = E/\cosh(\eta)$. An important distance measure is ΔR, which defined in the ϕ-η-space by

$$\Delta R = \sqrt{(\Delta\phi)^2 + (\Delta\eta)^2}. \tag{3.5}$$

3.2.2 Inner Detector

The ID is the tracking system in the core of the ATLAS detector, designed to measure the p_T and electric charge of particles. A sketch of the ID and its subcomponents is shown in Figure 3.4 and 3.5. It consists of a cylindrical barrel region covering $|\eta| < 1.5$ and two end-caps disks which are placed orthographic to the beam covering the range $1.5 < |\eta| < 2.5$. The ID is arranged around the beam pipe and covers a range in pseudorapidity of $|\eta| < 2.5$ and it provides a complete cylindrical coverage in azimuthal direction ϕ. To bend the trajectories of charged particles in the r-ϕ-plane, the ID is immersed in an uniform axial-symmetric magnetic field of field strength 2 T provided by a superconducting solenoid magnet, placed between the ID and the ECal. The ID consists of the following components:

- an insertable B-layer (IBL) detector
- a compact and sensitive pixel detector (PXD)
- a semiconductor tracker (SCT)
- a transition radiation tracker (TRT)

In the first layer of the ID, the IBL detector [107], located just a few centimeters from the beam pipe, is installed in order to improve the vertex identification and b-quark tagging. The IBL is based on 14 staves with 20 chip modules on each stave. The pixels of the IBL have a size of $50 \times 250\ \mu m^2$.

In the next layer of the ID, the PXD is located with three barrel layers in the central part and three end-cap discs.

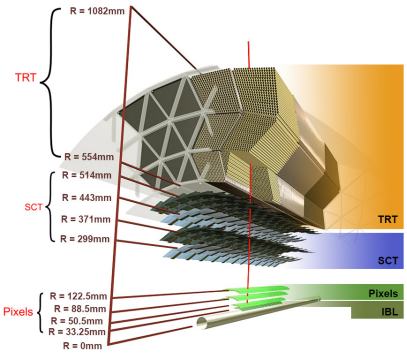

Figure 3.4: Side-view on the ATLAS ID with its subcomponents [110].

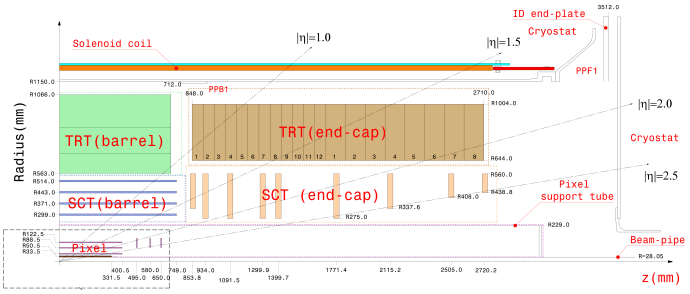

Figure 3.5: Side-view on the ATLAS ID with its subcomponents with a focus on the η-coverage [111]. The PXD and SCT cover $|\eta| < 2.5$, respectively, and the TRT covers $|\eta| < 2.0$.

It is built from small, identical modules with a size of $50 \times 400\,\mu\text{m}^2$ in azimuthal direction with 46,080 pixels each with an independent read-out channels.

The SCT is placed in the middle of the ID. The SCT consists of four double strip layers at radii of 299 mm to 514 mm in the barrel, covering a range of $|\eta| < 1.5$, and nine end-caps disks with a coverage of $|\eta| < 2.5$.

The TRT is the largest subcomponent of the ID enclosing the SCT (at radii between 554 mm and 1082 mm) and is build up of $50 \cdot 10^3$ straw drift tubes in 73 layers in the barrel and $250 \cdot 10^3$ straw drift tubes in the end-caps. The tubes a filled with a gas mixture, mainly consisting of Xenon and CO_2. Charged particles traversing the TRT ionise the gas mixture. With an electric potential, the ions and the electrons can be split and transformed into an electric signal. It provides roughly 34 hits per track. One of the strengths of TRT is the discrimination between particles based on transition radiation [108], which is emitted when a particle crosses the boundary of two materials with different dielectrical properties. The intensity I_{TR} of this radiation scales like $I_{\text{TR}} \sim \gamma^4$, where γ is the Lorentz factor of the particle, which can be written as $\gamma = (1 + (p/m)^2)^{1/2}$. Thus, the intensity I of the transition radiation of particles with same momentum p depend on their rest mass m. This is used to efficiently discriminate electrons and pions $\pi^{\pm}$. The coverage of the TRT in pseudorapidity is $|\eta| < 2$.

The relative p_{T} resolution of tracks with $p_{\text{T}} < 100\,\text{GeV}$ ranges from approximately $2 - 12\,\%$, depending on the track's p_{T} and η position [109] and can be parametrised as

$$\frac{\sigma(p_{\text{T}})}{p_{\text{T}}} = \left(\left(0.05\,\% \cdot \left(\frac{p_{\text{T}}}{\text{GeV}} \right) \right)^2 + (1\,\%)^2 \right)^{1/2} . \tag{3.6}$$

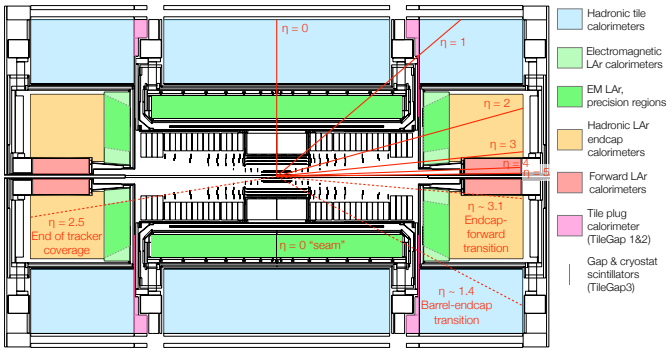

Figure 3.6: Side-view on the ATLAS calorimeter system showing also the different subcomponents [112].

3.2.3 Calorimeter System

The calorimeter system is designed to measure the energy of incoming particles which interact with the detector material either electromagnetically or hadronically and produce particle showers. The particle shower initiates a signal in the active material. The calorimeter system consists of two subsystems: the EM calorimeter (ECal) and the hadronic calorimeter (HCal). Geometrically, the calorimeter system is divided into the barrel region (a long barrel and two extended barrels), the end-caps and the forward part with a total coverage of $|\eta| \leq 4.9$. The three-dimensional segmentation of the calorimeter system allows a full reconstruction of particle showers. A side-view of the ATLAS calorimetry is shown in Figure 3.6. The coverage of the subsystems are summarised in Table 3.3 and the utilised materials in Table 3.2.

Table 3.2: Material of the ECal and HCal.

		Barrel	End-caps	Forward
ECal	active material absorber	liquid argon lead	liquid argon lead	
HCal	active material absorber	scintillating tiles steel	liquid argon copper	
FCal	active material absorber			liquid argon copper/tungsten

Table 3.3: Coverage in pseudorapidity η of the calorimeter subsystems [113].

System	Barrel	End-cap	Forward
ECal	$\lvert\eta\rvert < 1.5$	$1.4 < \lvert\eta\rvert < 3.2$	
TilCal	$\lvert\eta\rvert < 1$	$0.9 < \lvert\eta\rvert < 1.7$	
HEC		$1.5 < \lvert\eta\rvert < 3.2$	
FCal			$3.1 < \lvert\eta\rvert < 4.9$

The ECal is a liquid-argon (LAr) sampling calorimeter [114] and measures particles which interact electromagnetically. As a sampling calorimeter, it is build of alternating layers of absorber and active material. The absorber consists of dense material plates, lead, in which an incoming particle initiates a EM particle shower. The lead plates are constructed with an accordion-like geometry equipped with read-out electrodes and provide a full coverage in ϕ. The particle showers are initiated via EM interactions such as bremsstrahlung or pair-creation, if a photon, an electron or a positron enters the ECal. An EM barrel calorimeter module circumvents three layers

with decreasing granularity for position measurements and particle absorption. The depth of the calorimeter layers is parametrised in terms of the radiation length X_0 in the absorbing medium, which is defined as the mean length to reduce the energy of an particle in an EM cascade by a factor of $1/e$, where e denotes Euler's number (i.e. on average the particle loses 63.2 % of its energy). In terms of material parameters, X_0 is approximately given by

$$X_0 = \left(4\alpha n Z^2 r_e^2 \ln\left(287/\sqrt{Z}\right)\right)^{-1}, \tag{3.7}$$

with the atomic number of the material Z, which for lead is 82, $r_e = 2.8 \cdot 10^{-15}$ and n is the nuclear density. Using dense materials with large Z helps to keep X_0 small and thus the calorimetry compact. The ECAL is between 24 and 27 radiation lengths deep. The particle showers are detected within the active material - liquid argon, which needs to be cooled down to 87 K to be in a liquid state. The signals in the active material, created by ionization, are proportional to the energy of the incoming particle. The ECal barrel covers $0 < |\eta| < 1.5$ and the two end-caps cover $1.4 < |\eta| < 3.2$. The end-cap is divided into two coaxial wheels, where the first covers $1.4 < |\eta| < 2.5$ and the second $2.5 < |\eta| < 3.2$. The HCal surrounds the ECal and consists of the tile calorimeter (TilCal) and the liquid-argon hadronic end-cap calorimeter (HEC). Its designed to measure particles which interact hadronically. The TilCal is the central hadronic calorimeter covering in total $|\eta| < 1.7$, where the two parts, the central barrel and the two extended barrels cover a range of $|\eta| < 1$ and $0.9 < |\eta| < 1.7$, respectively. It is a sampling calorimeter based on steel as absorber and scintillating plastic tiles as active material. In the pseudorapidity range $\eta \in [1.5, 3.2]$, the HEC is built with copper with $Z = 29$ as absorbing material and liquid argon as active medium. Since the hadronic cascades production is mainly driven by QCD, the hadron showers are broader and longer the EM showers. Further, the HCal is non-compensating, i.e. it does not account for energy loss in nuclear break-up and other lost energy due to long-lived particles or secondary muons. In the forward directions the calorimeter system is completed by the forward calorimeter (FCal) covering $|\eta| \in [3.1, 4.9]$. The FCal consists of three layers. In the first layer, copper is used as absorber and liquid argon as active medium. The second and third layer use tungsten with $Z = 74$ as absorber. The relative resolution of the calorimeters is parametrised as

$$\frac{\sigma_E}{E} = \underbrace{\frac{a}{\sqrt{E}}}_{\text{stochastic}} \oplus \underbrace{b}_{\text{constant}} \oplus \underbrace{\frac{c}{E}}_{\text{noise term}}, \tag{3.8}$$

with parameters a, b, c and energy E [GeV]. The three terms in Equation 3.8 are added in quadrature. The noise term reflects electronic noise in the calorimeter. The stochastic term parametrises fluctuations in the energy shower and the constant term non-uniformities in the detector. For high-energy collisions, the noise term parametrised by c is usually negligible and the resolution is paramterised as $\sigma_E/E = a/\sqrt{E} \oplus b$. The fractional resolution σ_E/E of the calorimeter subsystems is summarised in Table 3.4.

Table 3.4: Fractional resolution of the calorimeter subsystems in terms of the parametrisation $\sigma_E/E = a/\sqrt{E} \oplus b$ [114, 115].

System	a [% $\sqrt{\text{GeV}}$]	b [%]
ECal barrel	10	0.2
ECal end-cap	12	0.4
TilCal	52	3.0
HEC	70	5.8
FCal	100	10

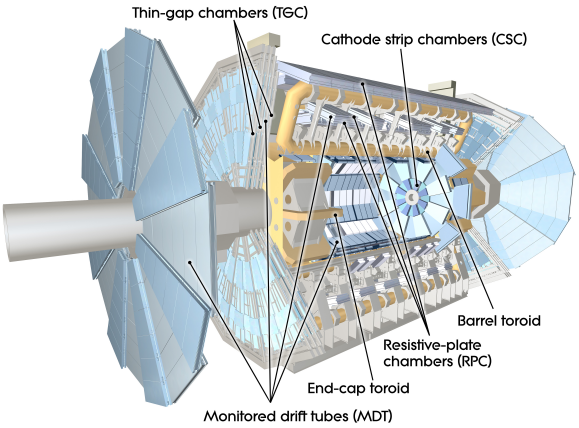

Figure 3.7: Side-view on the ATLAS MS with its subcomponents [117].

3.2.4 Muon Spectrometer

The muon spectrometer (MS) [116] is designed to measure muons μ, which pass through the ID and the calorimetry, in the outermost layer of the ATLAS detector. Trajectories of muons are bend in the r-z-plane with strong magnetic fields provided by three massive superconducting air-core toroidal magnets. The MS includes a trigger system and tracking chambers. The pseudorapidity region $|\eta| < 2.7$ is covered by precision chambers with three layers of monitored drift tube (MDT) chambers, allowing for a measurement of the muon tracks. To account for higher background in the more forward region of $|\eta| > 2$, the first MDT station is replaced with more sensitive cathode-strip chambers (CSCs). The separate muon trigger system covers the range $|\eta| < 2.4$, separated into the barrel ($|\eta| < 1.05$) and the end-caps ($|\eta| \in [1.0, 2.4]$). Three doublet-layers of resistive-plate chambers (RPCs) are used in the barrel, while thin-gap chambers (TGCs) are used in the end-caps. The RPCs and TGCs also provide track measurements in addition to the precision chambers.

The resolution of the MS is mainly driven by the spatial resolution of the MDT precision chambers. The aimed relative p_{T} resolution $\sigma_{p_{\mathrm{T}}}/p_{\mathrm{T}}$ of the MS for muons with $p_{\mathrm{T}} \sim 1\,\mathrm{TeV}$ is 10 % and for $p_{\mathrm{T}} \sim 0.1\,\mathrm{TeV}$ it is 3 % [116].

3.2.5 Trigger System and Data Processing

The ATLAS data acquisition (DAQ) [118] system collects the data from the detector systems and subsequently converts and saves it in a usable format. Due to the size of the experiment and the large amount of collisions at the LHC with a nominal bunch crossing rate in the order of 40 MHz not each event can be stored. Therefore a two-level hardware and software-based trigger system is installed. The trigger system aims to select and save events where potential interesting physics happened with a high efficiency and without introducing a bias, triggering down the event rate to approximately 1 kHz of interesting events.

The trigger module received a major upgrade for Run II to handle the increased CME and luminosity. The Run II trigger system consists of two independent levels, the hardware-based level-1 (L1) trigger and the software-based high level trigger (HLT) system, visualized in Figure 3.8. The L1 trigger is based on muon trigger chamber and calorimeter signals for a preliminary event selection and identification of Regions of Interest (RoI). L1 reduces the event rate from 40 MHz to the order of 100 kHz. The HLT is based on offline algorithms selecting events in the RoI. The HLT reduces the recorded bunch-crossing rate from 100 kHz to roughly 1 kHz. The data quality acceptance in the full Run II data set is in the order of 95 %.

ATLAS uses a worldwide computing grid with a four-level hierarchical "Tier" computing infrastructure to store and analyse data. Tier 0 is the CERN data centre responsible for data read-out as well as first reconstruction. The data is distributed to thirteen Tier 1 computer centers for storing raw and reconstructed data. At Tier 1 also large-scale reprocessing is performed which is distributed to the Tier 2 stage. Finally, the Tier 3 stage represent local computing resources on which data analysis is performed. For collected data, the ATLAS data processing chain includes the triggering, reconstruction and derivation: After data triggering, the raw, collected data (RAW) is saved. The reconstruction transforms the RAW to analysis object data (AOD/xAOD). The derivation transforms the AOD to derived analysis object data (DAOD) in order to reduce the data size according to the need of the physics analysis. By this data processing chain, including the skimming of events, objects and variables in the data, the size of the data to be analyzed can be reduced from $\sim$ PB to $\sim$ GB. For simulated events, the event generator output (EVNT) is passed through the simulation process to emulate the interaction with the detector (HITS). The digitization transforms this to simulated detector output (RDO). The RDO is then reconstructed and passed through the derivation to get the DAOD. The full chain is usually processed with ATHENA [119], which is the central ATLAS software framework.

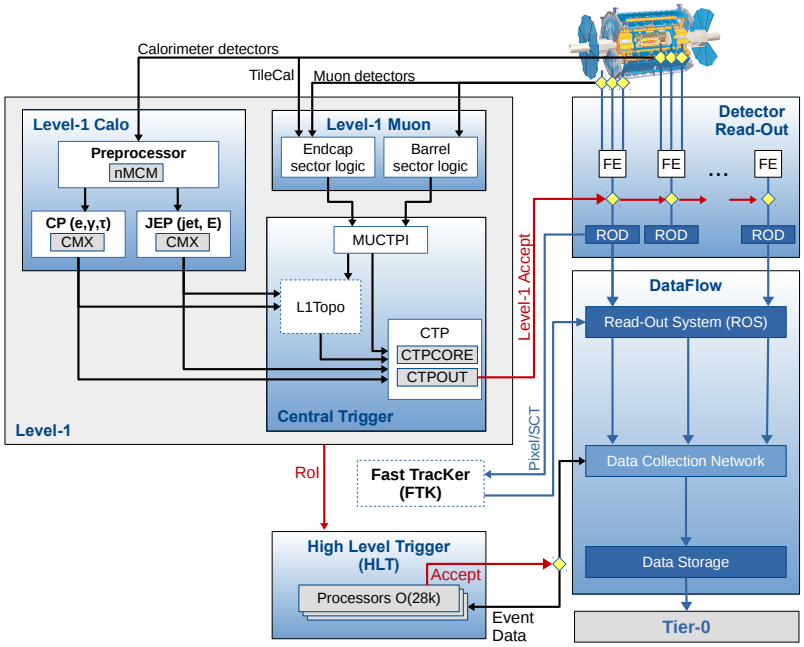

Figure 3.8: Trigger system in Run II consisting of a hardware-based firstlevel trigger and a software-based high-level trigger. [120].

3.3 High-Energy Physics in Hadron Collisons

3.3.1 Center-of-mass Energy

The first Lorentz-invariant Mandelstam variable [121] is defined as $s = (p_1 + p_2)^2$, where p_1 and p_2 are the four-momenta of two colliding particles defined as $p = (E, \vec{p})$, where energy E and momentum $\vec{p}$ are related by the relativistic dispersion relation

$$E^2 = \vec{p}^2 + m^2. \tag{3.9}$$

At the LHC, the incoming particles are collided heads-on with equal energy E and opposite momentum $\pm\vec{p}_z$, resulting in

$$s = 4E^2. \tag{3.10}$$

The quantity $\sqrt{s} = 2E$, where E refers to the energy of the incoming protons, is therefore named the center-of-mass system energy (CME). While in 2012 the LHC operated at beam energies of $E = 4\,\text{TeV}$, the beam energies increased to 6.5 for Run II, giving a center-of-mass energy of $\sqrt{s} = 13\,\text{TeV}$.

3.3.2 Luminosity

An central quantity describing the event rate at particle colliders is the instantaneous luminosity $\mathcal{L}_{\text{inst}}$, defined by

$$\frac{\mathrm{d}N}{\mathrm{d}t} = \mathcal{L}_{\text{inst}}\sigma, \tag{3.11}$$

with the rate of proton bunch collisions $\mathrm{d}N/\mathrm{d}t$ occurring in the collider and the total cross section σ of the physics process. The luminosity $\mathcal{L}$ can be calculated for head-on proton-proton collisions using beam parameters by

$$\mathcal{L}_{\text{inst}} = \frac{N_b^2 n_b f \gamma F}{4\pi\epsilon\beta^*}, \tag{3.12}$$

where N_b is the number of particles per proton bunch, n_b is the number of proton bunches per beam, f is the revolution frequency, γ the relativistic factor, F the geometric luminosity reduction factor, ϵ is the transverse beam emittance and β^* is the collison point's betatron function describing the beam focusing or rather the transverse beam size. The time-integrated luminosity is defined as

$$\mathcal{L} = \int \mathcal{L}_{\text{inst}}(t)\,\mathrm{d}t \tag{3.13}$$

A correlated quantity of the luminosity at the LHC is $\langle\mu\rangle$, the measure of how many proton-proton collisions are expected on average per proton-proton bunch crossing. The ATLAS collaboration uses several detector systems, such as the LUCID-2 Cherenkov detector [122], to measure and calibrate the luminosity $\mathcal{L}_{\text{inst}}$. The instaneous luminosty and its uncertainty are determined from the LHC beam parameters, in particular the number of protons per bunch and the convolved beam sized in horizontal and vertical planes. The luminosty calibration, i.e. the translation of the visible interaction rate into a luminosity, relies on van der Meer (vdM) scans [123], performed in special low-μ runs ($\langle\mu\rangle = 0.5$) in each year of Run II in which the relative interaction rates are measured as a function of the transverse beam separation. The vdM scan calibration is then transferred to the LHC running conditions at high μ. The full Run II proton-proton data corresponds to an integrated luminosity $\mathcal{L} = 139\,\text{fb}^{-1}$ with an uncertainty of 1.7 % [124].

3.3.3 Parton Density Functions

Deep-inelastic scattering experiments showed that the proton has an energy-dependent structure. For low-energetic processes, the valence quarks play the important role for the proton's physics, while for higher energies the sea-quarks are contributing, too. The interacting partons i within the proton carry only a fraction of the total momenta of the colliding protons, described by the Bjorken x_i, defined as

$$x_i = \frac{p_{\text{parton}_i}}{p_{\text{proton}}}. \tag{3.14}$$

The probability density functions (PDFs) describing the probability that a parton carries a distinct fraction of the total momentum of the proton is denoted by $f_i(x_i, Q)$, where Q denotes the factorisation scale, which corresponds to the energy of the physics process where the proton is involved. These functions are determined experimentally and cannot be derived from perturbative calculations. Typical PDFs at a fixed momentum transfer Q are sketched in Figure 3.9. The dependence of the parton density functions f_i on the factorisation scale μ_f are described by the Dokshitzer–Gribov–Lipatov–Altarelli–Parisi (DGLAP) equations [125–127]. Using the Bjorken x values of the colliding protons, the effective center-of-mass energy $\sqrt{s}_{\text{eff}}$ is therefore given by

$$\sqrt{s}_{\text{eff}} = \sqrt{x_1 x_2 s}. \tag{3.15}$$

Any prediction of observables at hadron colliders requires knowledge of PDFs, which cannot be calculated from QCD but are measured experimentally.

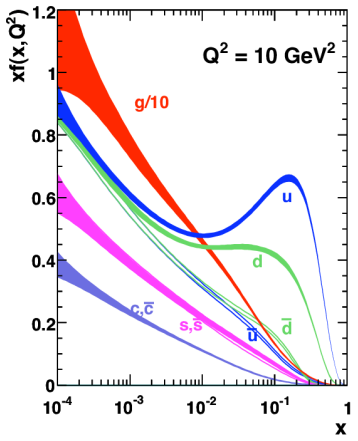

Figure 3.9: Sketch of $x \cdot f_i$ as function of x at 68 % CL. These PDFs describe the probability for finding a parton with a momentum fraction x at a energy scale Q^2. The PDFs are measured by fitting observables to experimental outcomes.

3.3.4 Cross Section

The cross section σ for a process $ij \to X$ with two protons i and j can be calculated from the matrix element $\mathcal{M}$, describing the probability of a process for given initial and final state, with the factorisation theorem

$$\sigma = \int \mathrm{d}x_i \, \mathrm{d}x_j f(x_i, Q^2) f(x_j, Q^2) \sigma_{ij} \tag{3.16}$$

with PDFs $f(x_i, Q^2)$ describing the involved partons in proton i, the partonic cross section $\sigma_{ij} = \int F^{-1} |\mathcal{M}(ij \to X)|^2 \, \mathrm{d}\Omega$ and the particle flux F. The factorisation theorem states that the calculation of the cross section can be factorised into two terms, the partonic cross section term for the short distance interaction which can be described by perturbation theory in QCD (asymptotic freedom) and a non-perturbative long distance term. The partonic cross section term especially depends on the factorisation and renormalisation scales μ_f and μ_r.

In terms of luminosity $\mathcal{L}$, the cross section σ of a process in high-energy physics is given by

$$\sigma = \frac{N}{\mathcal{L}\epsilon}, \tag{3.17}$$

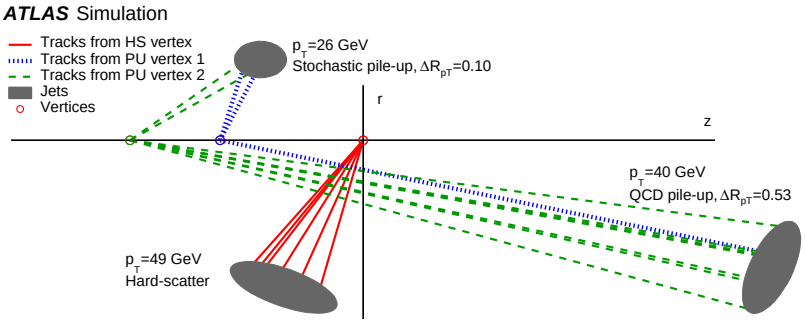

Figure 3.10: Hard-scatter jets, QCD and stochastic pile-up jets in the r-z-plane [128].

where N is the number of events, i.e. the difference of observed and background events, and ϵ is the efficiency (ratio of selected and total events). The cross section σ is usually expressed in a unit called barn b, defined by $1\,\mathrm{b} = 10^{-28}\,\mathrm{m}^2$.

3.3.5 Hard-scatter and Pile-up Processes

The hard-scatter process is the parton interaction where the hard proton-proton collision takes place. It is usually the origin of the interesting and relevant physics. The vertex where the hard-scatter process takes place is called the hard-scatter vertex or primary vertex PV_0. Jets originating from the hard-scatter process are called hard-scatter jets.

Interactions of the rest of the proton except of the hard-scatter process are collectively named the underlying event (UE). The UE can be further divided into beam-beam remnants (BBR) and further multiple parton interactions (MPI) by spectator partons which are not involved in the hard interaction.

Pile-up jets are signals in the detector which originate from multiple proton-proton interactions other than the hard-scattering event. These pile-up effects, which are a big drawback for hadron colliders compared to e^+e^--colliders, can be divided into in-time pile-up and out-of-time pile-up. In-time pile-up means contribution from $\mathrm{PV}_{i>0}$, i.e. from simultaneous collisions in a single event. The amount of in-time pile-up is related to the number of interactions per event. Out-of-time pile-up means contributions to the event from interactions of bunch crossing of the past and the future, which is in particular dependent to the number of collisions in a small time window. In terms of pile-up tagging, one distinguishes QCD and stochastic pile-up jets, which have different properties in terms of jet timing and jet width. QCD (stochastic) pileup jets are produced from single (multiple) vertices as shown in Figure 3.10.

With increasing center-of-mass energy $\sqrt{s}$ and increasing luminosity $\mathcal{L}$ at ATLAS during Run I and Run II, the contribution of pile-up events also increased. In Run II, the average number of pile-up interactions per bunch crossing, $\langle\mu\rangle$, increased from 14 in 2015 to 34 in 2018, see Figure 3.11, and will increase further to ~ 60 in Run III. Using the luminosity $\mathcal{L}$, the total inelastic cross section σ of the proton-proton collisions and the mean frequency of bunch crossings, given by the product of number of proton bunches N_{bunch} and the frequency of collisions f_{LHC}, the mean interactions per bunch-crossing is given by

$$\langle\mu\rangle = \frac{\mathcal{L}\cdot\sigma}{N_{\mathrm{bunch}}\cdot f_{\mathrm{LHC}}}. \tag{3.18}$$

Pile-up events introduce higher charged particle multiplicities in the detector, leading to more tracks and a higher vertex multiplicity N_{PV}. Furthermore, pile-up activity also has an impact on the jet reconstruction itself since pile-up events typically produce a number of soft jets, mostly in form of dijet pairs. Therefore, pile-up

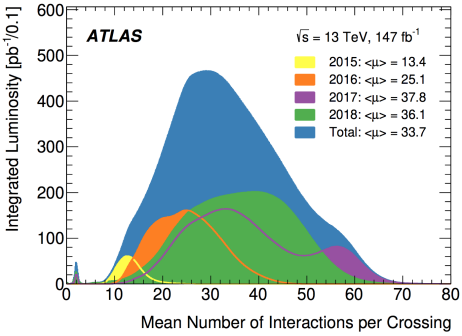

Figure 3.11: Distribution of the luminosity-weighted mean number of interactions per LHC bunch crossing $\langle\mu\rangle$ for different data-taking years in Run II [130].

jets are usually less energetic than hard-scatter jets and are characterised by a topology that both jets are in the same hemisphere of the detector (low invariant dijet mass) as well as tend to be back-to-back in the transverse plane.

Different strategies are used in ATLAS to mitigate pile-up effects [129]. Pile-up subtraction strategies are used in the jet clustering, jet calibration and event reconstruction in which a pile-up removal is performed via sophisticated algorithms based on vertex and tracking information, described in Section 4.7, 5.1 and 7.6.

CHAPTER 4

Object and Event Reconstruction

The ATLAS experiment measures proton-proton collisions provided by the LHC. The direct observables in form of detector signals are particle trajectories in tracking detectors and energy deposits in the calorimetry systems from which physics objects such as leptons, photons or jets are built, which in turn give access to the underlying physics. As a first step, events are directly reconstructed during data-taking to evaluate if the event is interesting and should be recorded, see Section 3.2.5. After this online reconstruction, a detailed offline event and object reconstruction is performed. This chapter presents the idea, challenges and issues of the reconstruction and identification of important physics objects, observables and event quantities based on detector signatures in context of the presented analyses.

4.1 Tracks

Tracks are reconstructed charged particle trajectories and are a central part for reconstructing and identifying several objects such as electrons, jets or primary vertices. In general, tracks are reconstructed from individual aligned hits, which are energy deposits from particles in the different layers of the ID [131]. A sequence of algorithms [132] is used to build tracks from these hits. The track reconstruction procedure starts with an inside-out procedure followed by an outside-in reconstruction. Starting point of the track reconstruction are three hits in the silicon detectors, where a hit is defined as a point where a charged particle traversed the active material of the PXD or SCT detectors. Track candidates are formed from seeds with a combinatorial Kalman filter where additional hits from the other PXD and SCT layers, which are compatible with the provisional trajectory, are added. The track candidates are evaluated with ambiguity-solving algorithms based on a track quality score, derived from a couple of track properties such as p_{T} or the number of hits in the PXD and SCT. Remaining track candidates are extrapolated to the TRT in which compatible TRT hits are associated to the tracks. The extrapolation quality is evaluated with a χ^2 fit and a track score. Also tracks from the PXD detectors which could not be (reliably) extrapolated are kept since tracks with large $|\eta|$-values may not deposit hits in the TRT. It follows the outside-in reconstruction, aiming to built tracks for secondary particles, e.g. products from photon conversion or particle decays. Stand-alone TRT track segments are extrapolated back to the silicon detectors and eventually associated to hits which are not already used in the first inside-out track reconstruction pass. The amount of tracks from the inside-out and outside-in pass form the track collection. All tracks can be parametrised by five parameters, $(d_0, z_0, \phi, \theta, q/p_{\mathrm{T}})$, where d_0 and z_0 are the transverse and the longitudinal impact parameters, respectively, ϕ and θ are the azimuthal and the polar angle of the tracks and q/p_{T} is the ratio of the charge and transverse momentum. According to the ambiguity-solving algorithm, tracks are reconstructed for $p_{\mathrm{T}} > 400\,\mathrm{MeV}$ and the coverage of the ID $|\eta| < 2.5$. Additional quality criteria with respect to the number of (shared) clusters and holes in the PXD detector and SCT as well as geometrical conditions are applied. The

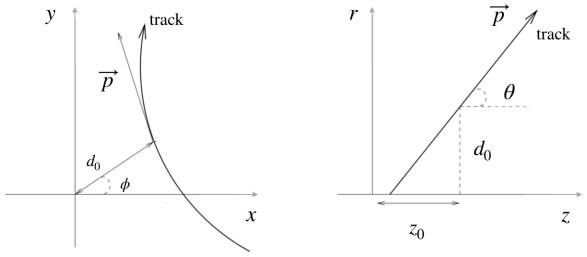

Figure 4.1: Geometrical sketch of the track impact variables d_0 and z_0. The left figure shows the transverse r-ϕ-plane, the right figure the r-z plane.

transverse and longitudinal impact parameters, see Figure 4.1, are used to characterise tracks with respect to the beamspot position. The transverse impact parameter d_0 is defined as the signed minimum distance in the r-ϕ-plane of the track to the point of closest approach to the z-axis. The longitudinal impact parameter z_0 is the z-coordinate of the track at the point where d_0 is defined. The polar angle θ is the angle of the track at the point of closest approach with respect to the transverse plane. Small values of d_0 and z_0 in general correspond to particles produced near the PV_0. It is required that $d_0 < 2\,\text{mm}$ and $z_0 \sin(\theta) < 3\,\text{mm}$. The measured fraction of tracks that fail to be reconstructed is roughly 6 % for jet momenta of $p_\text{T} \in [200, 400]\,\text{GeV}$ and roughly 9 % for jet momenta of $p_\text{T} \in [1400, 1600]\,\text{GeV}$ [131].

4.2 Vertices

Primary vertices PV_i define points where proton-proton collisions occur and are characterized by the sum of the squared track transverse momenta p_T which are associated with the individual vertices. The PV_i reconstruction is based on a subset of all measured tracks. Strict requirements are applied to reach a low rate of fake tracks. First, a track-vertex association is performed. A collection of PV_i candidates is defined by seeding the vertex position from the maximum of the z-coordinate using the tracks fulfiling the quality requirements. The vertex-track matching and the determination of the vertex position is based on an adaptive χ^2-based vertex fitting algorithm [133] in which a model of a charged particle trajectory is fitted to the hit measurements in the layers of the ID. Tracks which are not compatible within $7\,\sigma$ with the reconstructed vertex are removed and eventually used to built another vertex. This process is repeated iteratively until all tracks are associated to a vertex or no new PV_i can be defined. The primary vertex (hard-scatter vertex), PV_i, is defined by the maximal value of $\sum_{i,\text{track}} (p_{T,i}^{\text{track}})^2$, where the sum runs over the associated tracks for each vertex i. The measured number of reconstructed vertices N_PV is smaller than the expected average number of bunch crossings $\langle\mu\rangle$, i.e. not all vertices can be reconstructed due to a variety of reasons:

- the associated tracks are too low in p_T
- no charged particle located in the tracker acceptance
- merging of vertices.

The vertex reconstruction efficiency is $\sim 60\,\%$. In particular in analyses using mostly forward jets it is likely that jets are located in the forward region without tracking information so that often a wrong vertex, a pile-up vertex, is identified as the vertex of the hard-scatter process. The observation of long-lived particles, especially b-quarks, relies on the identification of secondary vertices SV_i. The reconstruction of SV_i is based on a collection of tracks fulfiling different requirements than that of the PV_i, namely that the track has not been used for PV_i reconstruction, $p_\text{T} > 1\,\text{GeV}$ and the number of measured hits in the TRT must be larger than two. A complex multistage algorithm [134] is used to identify the secondary vertices based on this track selection.

4.3 Topological Clusters

Topological clusters (topo-clusters) are noise-suppressed three-dimensional energy deposits in the calorimeters used to identify objects such as jets and electrons. These three-dimensional energy deposits are caused by cell signals from individual or close-by particle showers and are grouped to form topo-clusters with a growing algorithm based on seed, growth and envelope control, given by

- seed control: $|E^{\mathrm{EM}}_{\mathrm{cell}}| > S \cdot \sigma^{\mathrm{EM}}_{\mathrm{noise,cell}}$
- growth control: $|E^{\mathrm{EM}}_{\mathrm{cell}}| > N \cdot \sigma^{\mathrm{EM}}_{\mathrm{noise,cell}}$
- envelope control: $|E^{\mathrm{EM}}_{\mathrm{cell}}| > P \cdot \sigma^{\mathrm{EM}}_{\mathrm{noise,cell}}$

where $E^{\mathrm{EM}}_{\mathrm{cell}}$ denotes the cell energy measured at the EM scale and $\sigma_{\mathrm{noise,cell}}$ is the expected amount of cell noise. Default configuration values for seed, growth and envelop control are $S = 4$ (primary seed threshold), $N = 2$ (growth control threshold) and $P = 0$ (principal cell filter), defining the $4 - 2 - 0$ topo-cluster formation algorithm [135]. The topo-cluster formation is sketched in Figure 4.2. It begins with selecting seed cells with energies significantly above the noise threshold as given by the seed control condition. According to $S = 4$, the absolute energy measurement $|E^{\mathrm{EM}}_{\mathrm{cell}}|$ needs to exceed the expected noise of a cell $\sigma_{\mathrm{noise,cell}}$ by four times. Also, negative cell signals originating from fluctuations caused by pile-up and electronic noise are included. The seed cells define the proto-clusters, which are subsequently expanded both laterally and longitudinally in the calorimeter. Neighboured cells fulfiling the growth control thresholds and the cell filter requirement are associated to the proto-cluster. Any cell which has a neighbouring cell fulfiling $|E^{\mathrm{EM}}_{\mathrm{cell}}| > 2\,\sigma^{\mathrm{EM}}_{\mathrm{noise,cell}}$ are iteratively added to the proto-clusters until no more neighbouring cells fulfiling the growth control condition are found. According to the envelope control, additional neighbouring cells are added to the cluster. Finally, a cluster splitting is performed in which proto-clusters which have more than one local maximum, defined by $E^{\mathrm{EM}}_{\mathrm{cell}} > 500\,\mathrm{MeV}$ in the EM sampling layers, are split between the signal peaks, whereby at most two local energy maxima are divided into separate topo-clusters. Topo-clusters have an individual structure given by its geometry and moments such as energy density or cluster time with respect to the bunch crossing. EM and hadronic clusters are fundamentally different and thus differ in some of their cluster characteristics, e.g. hadronic showers often result in more than one topo-cluster with less signal caused by invisible particles in hadronic showers, while EM showers tend to be more compact with a higher energy density. Topo-clusters are thus either calibrated at the EM scale or the local topo-cluster weighting (LCW) scale, in which a cell weighting scheme is used to calibrate the cluster's energy back to the hadron scale. This is done in two steps - a classification and a calibration: first a probability of being a cluster from an electromagnetic or hadronic shower is derived, then a calibration weighted by that probability is applied. In contrast, for the EM scale, the cluster's energy E_{cluster} is given by the sum of the energy of its associated cells E_{cell} calibrated in situ with well-known control physics samples. Currently, the LC weights are only utilised for large-R jets, while its not applied for EM-scale small-R jets. The angular variables η and ϕ of a cluster are defined as the energy-weighted average of the η and ϕ values of the associated cells and the mass is zero.

4.4 Electrons and Photons

Electrons e were discovered by Thomson in 1897 in cathode ray experiments [136] and are stable, spin-half fermions carrying electric charge. Electrons participate in EM and weak interactions. Therefore electrons typically leave a track signature in the ID and particle showers in the ECal. Due to the low mass of the electron, it looses large parts of its energy via bremsstrahlung processes corresponding to photon production which in turn can convert into electron-positron pairs. As sketched in Figure 4.3, the reconstruction of electrons relies on matching of energy deposits in the ECal and ID tracks [137, 138]. Since photon radiation and pair creation can already occur within the ID multiple tracks can be created in the ID. Photons γ are neutral and massless spin-1 bosons, which couple to particles carrying electric charge. Since they are electrically neutral, photons should

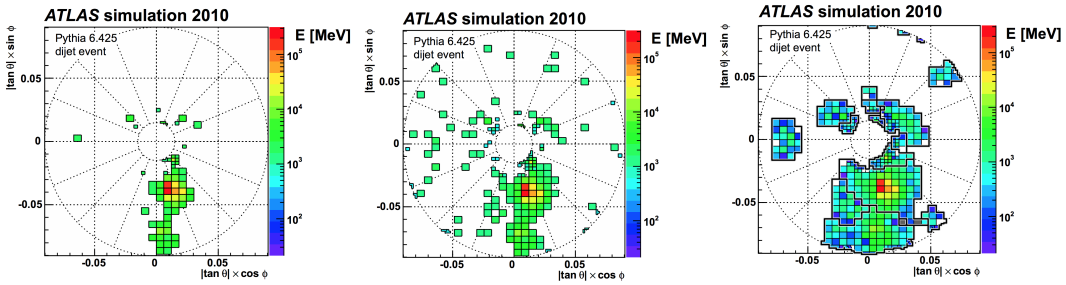

Figure 4.2: Topo-cluster formation in the ATLAS calorimeter: Identification of seed cells (left), growing process (middle) and result of the cluster formation (right) [135]. Pile-up effects are neglected but electronic noise is included.

not leave a track in the ID. However, due to pair creation photons can convert into an electron-positron pair. Hence, the reconstruction and identification of photons is follows closely that of electrons.

The electron and photon reconstruction for $|\eta| < 2.47$ follows the following steps:

- identification of EM calorimeter clusters
- identification of ID tracks
- matching of tracks and EM clusters
- identification of photons and electons

The EM calorimeter is sliced in 200×256 towers in η-ϕ-space with a size of 0.025×0.025 each, in which the EM-scale energy from the different calorimeter layers is summed. Seed clusters of significant and localised energy deposits are identified with a sliding-window algorithm [139] using tower groups with a size of 3×5 in η-ϕ-space. As described in Section 4.1, seed tracks are formed from clusters in the PXD and SCT detector, followed by a pattern recognition, ambiguity resolution and extension into the TRT. Resulting track candidates fulfiling $p_{\mathrm{T}} > 400\,\mathrm{MeV}$ and additional quality criteria are fitted with a global χ^2 track fitter. A matching in η-ϕ-space of the found ID tracks and calorimeter seed clusters is performed to identify electron candidates. Depending on the track characteristics, i.e. in which layers of the ID signals are found, to which PV_i the track is matched or the presence of double-track vertex signatures, the candidate is classified as an electron or a (converted) photon. For example, if the track is matched to a secondary vertex without hits in the pixel detector, the object is a classified as a photon candidate.

A likelihood (LH) discriminator based on both track and cluster information is used to identify prompt electrons for $|\eta| < 2.47$. There are different particles which can lead to similar detector signatures as electrons. Since jets consist of neutral and charged mesons with electron-like detector signatures, it is challenging to distinguish jets and electron candidates. Also photon conversion or photons produced via muon bremsstrahlung can lead to a track in the ID and energy deposited in the ECal from particle showers. To discriminate electrons and electron fakes such as jets and photons different LH operating working points with different energy-dependent signal efficiency and background rejection are defined. At $E_{\mathrm{T}} = 40\,\mathrm{GeV}$, the prompt electron selection efficiency is given by 93 %, 88 % and 80 % for the loose, medium and tight operating points. The reconstruction efficiency is shown in Figure 4.4.

Photon identification and discrimination against photon fakes is based on a rectangular selection using calorimetric variables. Fake photons may result from non-prompt photons arising from hadron decays in jets or from jets with a large ECal energy fraction. Two inclusive identification working points, loose and tight, are defined for photons with different selection efficiency and purity. The photon identification efficiency depends on E_{T}, being almost fully efficient for transverse energies of $E_{\mathrm{T}} > 100\,\mathrm{GeV}$, while for $E_{\mathrm{T}} \sim 10\,\mathrm{GeV}$ the efficiency varies for unconverted (converted) photons between $50 - 65$ % ($45 - 55$ %) [140].

Track- and calorimeter-based isolation criteria are defined to distinguish leptons and photons from background

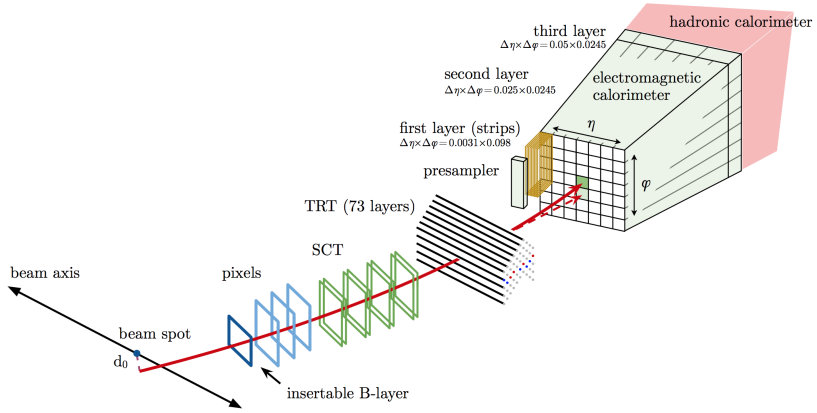

Figure 4.3: Trajectory of an electron in the ATLAS detector. The red line illustrates the electron's path through the ID and the ECal. The dashed red line represents a photon produced in the ID by interactions of the electron and the detector material [138].

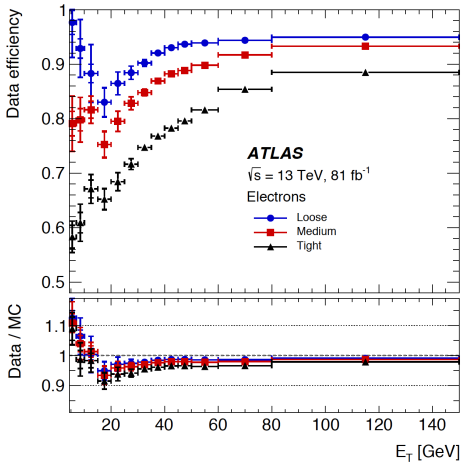

Figure 4.4: Electron reconstruction efficiency as a function of energy for different working points [141].

processes such as semi-leptonic heavy-flavour decays, lepton and photons fakes or photon conversion based on additional activity in η-ϕ-space around the object of interest. The first isolation requirement is based on the deposited energy in the ECal. A cone of size $\Delta R = 0.2$ around the electron candidate's noise-suppressed EM-scale topo-cluster position is built as isolation requirement. In addition, there are track-based isolation conditions based on the shower shape and additional track activity in the vicinity of the matched track of $\Delta R = \min(0.2, 10\,\text{GeV}/p_{\text{T}}\,[\text{GeV}])$. Electron efficiencies and corrections due trigger thresholds, reconstruction as well as identification efficiencies and isolation requirements are obtained with tag and probe measurements in data using well-known $Z \to ee$ and $J/\psi \to ee$ events, which provide large statistics for calibration.

4.5 Muons

Muons, unexpectedly discovered 85 years ago in cosmic rays, are heavier versions of electrons with equal spin and electric properties but higher mass $m_\mu \sim 200 \cdot m_e$. Due the muon's larger mass, muons emit less

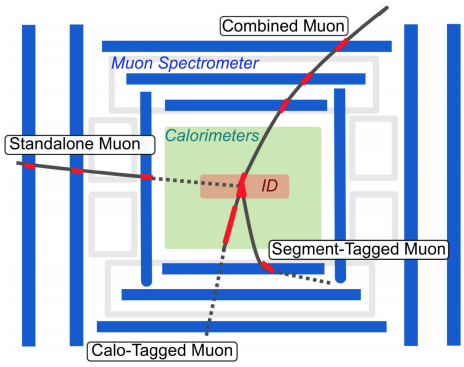

Figure 4.5: Sketch of the four muon reconstruction algorithms [143] in the ATLAS detector with the ID (red), the calorimeter system (green) and the muon spectrometer (blue).

Table 4.1: Standard muon reconstruction working points with selection efficiencies for $5 < p_{\mathrm{T}} < 100\,\mathrm{GeV}$ [145].

Working point	muons	efficiency [%]	comment
Loose	CB, ST, CT, ME	98-99	high efficiency
Medium	CB (ME, ST)	97	ATLAS default
Tight	CB, ME	90-93	high purity

bremsstrahlung and are slower accelerated in EM fields than electrons. Therefore, muons interact very weak and are usually not stopped by calorimeters but in the MS. The reconstruction of muons is based on the individually tracks measured in the ID, eventually matched to calorimeter energy deposits, and tracks from the MS [142]. The combination of MS and ID signals is done with various algorithms which define four types of muons:

- combined muons (CB): hits measured in the ID and MS are combined in one fit by extrapolating and matching the tracks
- segmet-tagged muons (ST): if the muon only accesses the first layer of the MS, the ID track is matched to one segmet in the MDT/CSC
- calorimeter-tagged muons (CT): in ranges with low acceptance of the MS, a track measured in the ID is matched to a calorimeter energy deposit
- extrapolated muons (ME): Muon candidates with $\eta \in [2.5, 2.7]$ can be measured in the MS but no track in the ID will be available. Muon candidates are built it they cross two layers of the MS and point to the PV_0

A sketch of the four muon reconstruction algorithms is shown in Figure 4.5. Different selection criteria correspond to various working points with different reconstruction efficiencies, summarised in Table 4.1. The reconstruction efficiency is measured in tag and probe measurements in dimuon decays of Z bosons and the J/ψ meson. The reconstruction efficiency of muons is roughly 99 % for $|\eta| < 2.5$ and $p_{\mathrm{T}} > 5\,\mathrm{GeV}$. The central region momentum resolution is determined to be 1.7 % and 2.3 % respectively. For $|\eta| > 2.2$ the resolution is determined with muon decays of the Z to be slightly worse with 2.9 % [144]. As in case of electrons, prompt muons must be distinguished from secondary muons e.g. from hadron decays inside jets. Secondary muons can be distinguished from prompt muons via isolation criteria based on additional activity in the vicinity of the muon candidate in calorimeter energy deposits or tracking chambers. In total, seven muon isolation requirements based on track and calorimeter variables are used to quantify the muon's isolation [144].

4.6 Neutrinos

Neutrinos are very light fermions appearing in three different flavours: electron neutrinos ν_e, muon neutrinos ν_μ and τ neutrinos ν_τ. Neutrinos only interact via the weak interaction and cannot be directly observed with the ATLAS detector. The experimental signature is missing transverse energy as described in Section 4.8. Neutrinos can be pair-produced in Z boson decays and are an irreducible background for the VBF Higgs boson to invisible search. Also neutrinos are produced in leptonic W decays.

4.7 Jets

A jet is a collimated bunch of mesons and baryons, commonly called hadrons, roughly flying in the same direction in the detector. Jets are important objects at hadron colliders and were the key objects for the discovery of the gluon [24, 25] or the top quark [146, 147] as well as play a leading role in searches for new physics. In the following, the nature of jets in simulation and experiment is described with a focus on the particle flow jet definition and the small-R anti-k_t jet reconstruction algorithm, which are the relevant ones for the described physics in this thesis.

The strong force grows in strength with increasing distance, leading to the phenomenon of colour confinement in QCD. Thus, single quarks or gluons cannot be observed but rather get enough energy to form quark-antiquark pairs emerging in colour-neutral hadrons. The detector signature of this parton shower and hadronisation process are jets. The parton showering is a non-perturbative processes and cannot be described by pQCD rather it can for simulation purposes be described by different algorithms such as the Lund string model [148] used in PYTHIA or the cluster hadronisation [149] used in HERWIG. From the experimental point of view, a jet is a complex object and the definition of a jet depends for example on the constituents used for jet reconstruction (tracks and topo-clusters), the clustering methods (e.g. small-R anti-k_t), eventually the pile-up mitigation technique at constituent level (e.g. constituent subtraction) and grooming algorithms. In Run I, jets in ATLAS were either reconstructed using inputs from the calorimeter system (EMTopo jets) which are based on three-dimensional topo-clusters, see Section 4.3, or based on information of the tracker in the ID (Track jets). Particle Flow (PFlow) is a newer algorithm in ATLAS, combining both tracks from the ID and calorimeter energy deposits to built jets. The PFlow algorithm decides on a particle-by-particle level if the energy measurement is better performed by the ID or the calorimeter system. Combining both kind of information has a couple of advantages. The relative p_T tracker resolution [113] in units of GeV is given by

$$\frac{\sigma(p_\mathrm{T})}{p_\mathrm{T}[\mathrm{GeV}]} = 0.036\,\% \cdot p_\mathrm{T}[\mathrm{GeV}] \oplus 1.3\,\%. \tag{4.1}$$

In contrast, the energy resolution $\sigma(E)$ of the central ECal is given by

$$\frac{\sigma(E)}{E[\mathrm{GeV}]} = 50\,\% \cdot \frac{1}{\sqrt{E[\mathrm{GeV}]}} \oplus 3.4\,\% \oplus 1\,\%. \tag{4.2}$$

Thus, the ID has a better energy resolution at low p_T, while the calorimeter has a better resolution at high p_T. Also, the tracker provides the better spatial resolution and allows for an association to the primary vertex but it only reconstructs charged particles while the neutral particles are measured by the calorimeters. Overall, compared to EMTopo jets, (small-R) PFlow jets have an improved angular resolution, hard-scatter jet reconstruction efficiency, pile-up jet suppression, jet energy scale uncertainties in most areas, better jet energy resolution at low p_T, improved $E_\mathrm{T}^\mathrm{miss}$ resolution as well as reconstruction (less fake $E_\mathrm{T}^\mathrm{miss}$) and an improved flavour-tagging performance. Therefore, the ATLAS collaboration implemented a PFlow algorithm to benefit from the complementary measurements of the calorimeters and the tracker. The PFlow algorithm comprises of the following steps, sketched in Figure 4.6 and described in more detail below:

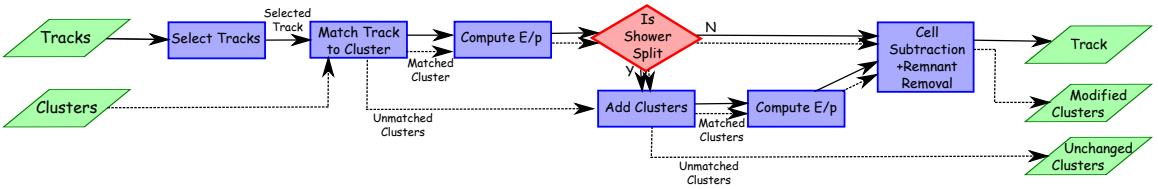

Figure 4.6: Flow chart of the ATLAS PFlow algorithm [112].

- selection of ID tracks and topo-clusters in the calorimeter system
- matching of tracks and topo-cluster
- charged shower subtraction
- shower split recovery
- cluster annihilation
- neutral particle calibration

The PFlow algorithm starts with an object selection, identifying suitable tracks and topo-clusters. Quality criteria are applied for the track selection, selecting tracks for which the momentum measurement by the tracker is expected to be superior to that of the calorimeter. Very soft tracks with $p_{\mathrm{T}} < 500\,\mathrm{MeV}$ are removed to save computing time as well as to remove tracks which are either not expected to reach the calorimeter system or store only cell energy below the noise threshold, see Section 4.3. In addition, an upper cut on the track momentum of $p_{\mathrm{T}} = 40\,\mathrm{GeV}$ is applied. For tracks above that threshold, the energy cascade in the calorimeter cannot be accurately removed due to close-by particles, so the topo-cluster measurement is used in these cases. Tracks matched to electron or muons candidates are not selected. The next step in the PFlow algorithm is the track-topo-cluster matching to allow a removal of the calorimeter energy if a track measurement is utilised. Within the track-cluster-matching, each track is extrapolated to the second layer of the ECal and geometrically matched with a ΔR_σ requirement $\Delta R_\sigma < 1.64$ of the track and cluster position in η-ϕ-space via

$$\Delta R_\sigma = \sqrt{\frac{(\eta_{\mathrm{trk}} - \eta_{\mathrm{cluster}})^2}{\sigma_\eta^2} + \frac{(\phi_{\mathrm{trk}} - \phi_{\mathrm{cluster}})^2}{\sigma_\phi^2}}, \tag{4.3}$$

where angular track variables ϕ_{trk} and η_{trk} are the extrapolated ones and η_{cluster} and ϕ_{cluster} are the angular positions of the calorimeter topo-cluster. $\sigma_{\eta(\phi)}$ denotes the standard deviation of the η (ϕ) coordinates of the topo-cluster cells ensuring that ΔR_σ considers the geometrical size of the topo-cluster. If no matching cluster candidate found, it is assumed that the track did not form a cluster. For now, the used topo-clusters are uncalibrated, i.e. at the EM scale. The special challenge for PFlow algorithms is to avoid double-counting of energy. If a track measurement of a charged particle in the ID is used, the corresponding signal in the calorimeter must be identified and subtracted. In the simplest case, no track was matched to the topo-cluster and the calorimeter measurement is utilised, which was then caused by a electrically neutral particle. If a matching of a track and topo-cluster was successful, a charged shower subtraction is performed. The energy in the calorimeter is removed based on the expected energy in the calorimeter by computing $\omega(\eta) = E/p$, the ratio of the energy E deposited in the calorimeter cells divided by the momentum p of the associated track, estimated with single pion samples. For this, a shower split recovery has to be performed since not every particle deposits all of its energy in a single cluster but splits the energy over different cluster layers. Then a ring-by-ring cell subtraction is done. The selected tracks and the remaining clusters represent the reconstructed event. The clusters only contain the energy from neutral particles, while the track momenta of charged particles are used. Typically, the charged fraction of a jet contributes to $2/3$ of the total energy since jets are dominated by pion production where roughly $2/3$ of pions are charged. It follows a calibration of the remaining calorimeter clusters and a pile-up track suppression based on the impact parameter z_0. A track is tagged as pile-up if $|z_0^{\mathrm{trk}} - z_0^{PV}| > 2\,\mathrm{mm}$.

The PFlow algorithm leads to collection of objects from which a jet reconstruction algorithms can built a jet.

There are various possible ways of reconstructing a jet based on detector inputs. This is usually done with jet algorithms [150] which fulfil certain properties which emerged from the famous "Snowmass standardisation of jet definitions" [151]. A jet reconstruction algorithm needs to be well defined, infrared stable and colinear (IRC) safe, i.e. the jet boundaries have to be well-defined, even if jets overlap, and the reconstructed jets need to be insensitive to low-energy objects and collinear splittings. From the theoretical point of view, soft emission and collinear splitting are associated with divergent tree-level matrix elements. IRC safeness ensures the cancellation of these divergencies in higher-order QCD calculations as described by the Kinoshita–Lee–Nauenberg (KLN) theorem [152, 153], which states that higher-order QCD divergencies cancel in inclusive observables when over all degenerate final states is summed. IRC safeness ensures amongst others that the number of jets per event does not depend on the modelling of parton showers and the hadronisation process. In IRC unsafe algorithms, a collinear splitting leads to a different set of identified jets or even infinite results in the perturbative expansion since cancellation of soft and collinear divergences is not guaranteed. The first developed rigorous jet reconstruction algorithm, the Stermann-Weinberg definition [154], is a naive cone algorithm. A naive cone jet reconstruction algorithm which just sums the p_{T} of all objects within a fixed-size cone in η-ϕ-space is sensitive to non-perturbative QCD effects like hadronisation and thus not IRC safe. The needed reconstruction requirements are amongst others achieved by sequential, longitudinally-invariant recombination jet algorithms such as Cambridge–Aachen [155], k_t and anti-k_t [156, 157]. The Cambridge–Aachen, k_t and anti-k_t algorithm are sequential jet clustering algorithm based on two quantities: the spatial distance d_{ij} between two objects i and j and the distance d_{iB} between an object i and the jet axis (beam) B, which are given by

$$d_{ij} = \min\{k_{ti}^{2p}, k_{tj}^{2p}\} \frac{(y_i - y_j)^2 + (\phi_i - \phi_j)^2}{R^2} \tag{4.4}$$

and $d_{iB} = k_{ti}^{2p}$, where R is the jet radius, corresponding to the size of the jet in the η-ϕ-space. The algorithm begins with a list of objects and searches for the distance minimum d_{ij} for all combinations of objects i and j. If the objects i and j give the minimum of d_{ij}, these objects are merged by summing the momenta and subsequently removed from the list of objects, while the merged object is kept. Otherwise, if d_{iB} is the minimum, the object i is defined as a jet and is removed from the list of objects. This procedure is done for all objects contained in the object list. The value of p defines the jet recombination treatment of soft and hard radiation and can lead to different jet clusters, as visualised in Figure 4.7. In case of Cambridge–Aachen ($p = 0$) the clustering is only based on the angular separation and no p_{T}-dependence is included. So, Cambridge–Aachen provides an approximate angular ordering of the parton shower constituents. The k_t algorithm ($p = 1$) is sensitive to soft radiation and therefore also to contamination from pile-up. It starts building clusters from soft and collinear particles first. The anti-k_t algorithm ($p = -1$), which is nowadays the default jet algorithm used in Atlas (and even at the Lhc), is less sensitive to soft radiation and built from high-p_{T} objects first. Jets can be divided into small-R jets ($R = 0.4$) and large-R jets ($R = 1.0$), where R is the above defined jet radius parameter. EM showers typically generate a single compact topo-cluster while hadronic showers potentially can generate multiple clusters, i.e. a cluster can be at the EM-scale (EM jets, small-R) or the LCW-scale, i.e. hadronic scale (hadronic/LCW jets, large-R). Hadronic jets are brought from the EM scale to the hadron scale using the local hadronic cell weighting (LCW) scheme. Large-R jets typically result from the hadronic decays of massive particles such as Z and W bosons or top quarks t. The maximal opening radius R of hadronic jets is proportional inverse to the transverse momentum p_{T} of the decaying particle, which can be produced with a large Lorentz boost at the current center-of-mass energies. Thus, the hadronic decay products may be identified as a single jet and therefore the jet substructure plays an important role. For example, a feature of hadronic W boson decays, $W \to qq'$ is a two-prong jet substructure. Along the bigger jet radius of large-R jets the contribution of pile-up, contamination from initial state radiation and the underlying event increases, requiring the necessity of so-called grooming algorithms and pile-up mitigation strategies [129, 158].

Tracks are associated to jets by a ghost-association procedure in which all tracks is assigned infinitesimal momentum on which the anti-k_t jet clustering algorithm runs to uniquely associates tracks to jets without changing the jet p_{T} [159].

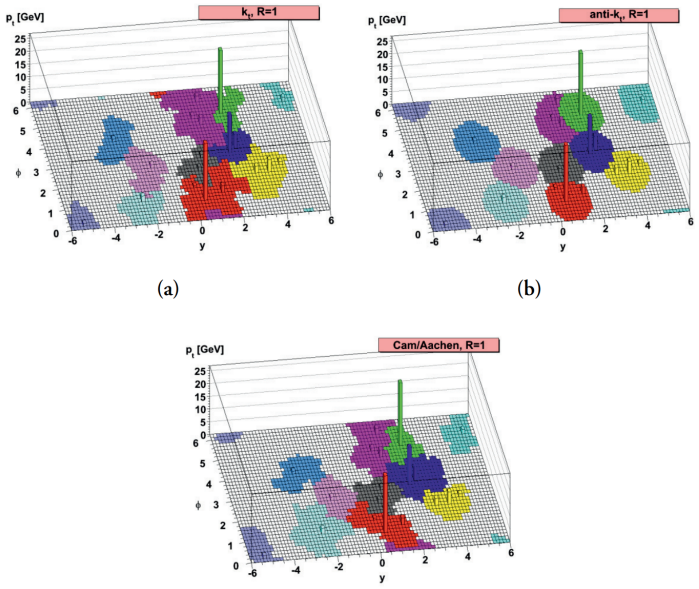

Figure 4.7: Visualisation of the different jet algorithms, k_t (a), anti-k_t (b) and Cambridge–Aachen (c), in the ϕ-y-plane [156].

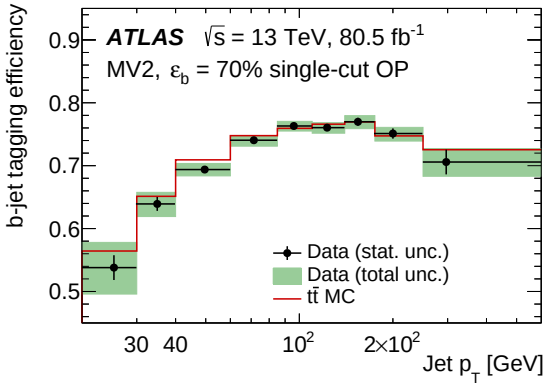

Figure 4.8: Efficiency of the b-jet tagging [161] as a function of jet p_{T} for the 70 % single-cut OP of the MV2 tagger.

Jets initiated from a bottom quark (b-jets) can be distinguished from other jets by a b-tagging method based on that b-jets have a sufficient lifetime that they travel some distance in the detector before decaying into lighter particles. Therefore, the decay vertex is spatially separated from the primary vertex. Since a b-quark is more massive than its decay products, the decay products tend to have high p_{T} which results in wider jets. Sophisticated algorithms based on the impact parameter, the inclusive secondary vertex reconstruction or the decay chain multi-vertex reconstruction are combined into a multivariate discriminator used to identify b-jets [160]. The b-tagging efficiency is displayed in Figure 4.8. The used working point in the analysis has a b-jet efficiency of 77 %, derived with a boosted decision tree based discriminant (mv2c10).

Usually, a pile-up jet removal is performed in analyses with jets. Variables named as JVT [162] and fJVT [128, 163] based on track, vertex, $E_{\mathrm{T}}^{\mathrm{miss}}$ and jets properties are defined and optimised to discriminate hard-scatter jets and pile-up jets. The JVT and fJVT variables are explained in detail in Section 7.6. Two JVT working points are defined for central PFlow jets with $20 < p_{\mathrm{T}} < 60$ GeV, where the Tight (Medium) working point,

corresponding to a cut of 0.2 (0.5) has a hard-scatter efficiency of 97 (96) %.

In general, jets are ordered in decreasing p_{T}, i.e. the jet with the (second) highest p_{T} is often referred to as the (subleading) leading jet.

4.8 Missing Transverse Energy

Missing transverse energy, $E_{\mathrm{T}}^{\mathrm{miss}}$, is one of the most important signatures of the ATLAS physics program, in particular important for searches for BSM physics with invisible particles in the final state. The initial protons, which are accelerated at the LHC along the z-axis, have very small momentum in x- and y-direction. Due to four-momentum conservation, the final state also should have negligible momentum in the transverse plane. Therefore, the vector of $E_{\mathrm{T}}^{\mathrm{miss}}$ is defined as the imbalance in the sum of visible p_{T} in the x-y-plane as

$$\vec{E}_{\mathrm{T}}^{\mathrm{miss}} = -\left(\sum_i \vec{p}_{\mathrm{T},i} + \sum_j \vec{p}_{\mathrm{T},j}\right), \tag{4.5}$$

where i runs over fully calibrated hard objects and j over soft signals. Hard objects are reconstructed and calibrated particles while soft signals are objects which are not associated to any hard objects. The hard objects include electrons, photons, hadronically decaying τ leptons, hard-scatter jets and muons. The hard objects must be found with exclusive detector signals to avoid double-counting of detector signals otherwise an overlap-removal is performed in the order of the particles listed above. Only hard-scatter jets with $p_{\mathrm{T}} > 20\,\mathrm{GeV}$ are included. Soft objects can either be built based on calorimeter energy deposits, calo soft term (CST), or tracks within the ID, which are unassociated with any hard objects, the track soft term (TST). While the CST is more sensitive to pile-up interactions (since no JVT pile-up removal is applied) and considers both charged and neutral objects, the TST is based only on tracks originating from the hard-scatter vertex and also be insensitive to neutral particles. In this thesis, the $E_{\mathrm{T}}^{\mathrm{soft}}$ term refers to the TST and thus it is defined by all reconstructed tracks in the ID, which are matched to the hard-scatter vertex but not geometrically associated with any reconstructed object such as leptons nor ghost-associated with a jet. By this, random pile-up noise is suppressed by using only tracks matched to the hard-scatter vertex. Following Equation 4.5, the magnitude $E_{\mathrm{T}}^{\mathrm{miss}}$ and the azimuthal direction ϕ^{miss} are defined as $E_{\mathrm{T}}^{\mathrm{miss}} = |\vec{E}_T^{\mathrm{miss}}|$ and

$$\phi^{\mathrm{miss}} = \tan^{-1}\left(\frac{E_y^{\mathrm{miss}}}{E_x^{\mathrm{miss}}}\right). \tag{4.6}$$

The scalar p_{T} sum of all objects used in Equation 4.5, denoted as E_{T}, serves as a quantity characterising the transverse hardness of the interaction.

The measurement of $E_{\mathrm{T}}^{\mathrm{miss}}$ is biased by particles which are poorly or not at all reconstructed or outside of the acceptance of the detector. The performance of $E_{\mathrm{T}}^{\mathrm{miss}}$ reconstruction and associated systematic uncertainties for the $E_{\mathrm{T}}^{\mathrm{miss}}$ scale and resolution are measured in comparisons of $Z \to \mu\mu$, $W \to e\nu$ and $t\bar{t}$ data and MC [164]. Different $E_{\mathrm{T}}^{\mathrm{miss}}$ working points are defined. For the loose $E_{\mathrm{T}}^{\mathrm{miss}}$ working point, the $E_{\mathrm{T}}^{\mathrm{miss}}$ is calculated is based on jets with $p_{\mathrm{T}} > 20\,\mathrm{GeV}$ and $|\eta| < 4.5$, while jets with $p_{\mathrm{T}} < 60\,\mathrm{GeV}$ and $|\eta| < 2.4$ tagged as pile-up are not considered. A forward pile-up jet removal is not used for the loose $E_{\mathrm{T}}^{\mathrm{miss}}$ calculation. A tight $E_{\mathrm{T}}^{\mathrm{miss}}$ working point also discards forward jets with $|\eta| > 2.4$ and $20 < p_{\mathrm{T}} < 30\,\mathrm{GeV}$ designed to reduce the pile-up dependence of $E_{\mathrm{T}}^{\mathrm{miss}}$, which however also risks to remove additional hard-scatter jets in the forward region.

Closely related to $E_{\mathrm{T}}^{\mathrm{miss}}$ is the scalar sum of the total hadronic activity, H_{T}, which is a measure of the total jet activity in the transverse plan, defined by

$$H_{\mathrm{T}} = \sum_i p_{\mathrm{T}}^{\mathrm{jet}_i}, \tag{4.7}$$

where i runs over both calibrated hard-scatter and pile-up jets (no pile-up jet removal via JVT or fJVT tagging is applied). The missing hadronic activity $H_{\mathrm{T}}^{\mathrm{miss}}$ is the absolute value of the negative vectorial sum of p_{T} of the hard-scatter and pile-up jets, defined by

$$H_{\mathrm{T}}^{\mathrm{miss}} = -\Big|\sum_i \vec{p}_{\mathrm{T}}^{\,\mathrm{jet}_i}\Big|, \tag{4.8}$$

where i is defined as above. Since no pile-up jet removal with JVT and fJVT is applied, $H_{\mathrm{T}}^{\mathrm{miss}}$ has a larger pile-up dependence than $E_{\mathrm{T}}^{\mathrm{miss}}$. On the other side, $H_{\mathrm{T}}^{\mathrm{miss}}$ is constructed to be insensitive to wrong pile-up jet tagging and serves as an important quantity for the multijet background estimation and rejection, in particular to suppress background multijet processes where the pile-up tagging failed, i.e. either unidentified pile-up jets or jets wrongly tagged as pile-up.

4.9 Dijet Kinematics

The invariant mass m of a system is defined as

$$m^2 = \left(\sum_i E_i\right)^2 - \left(\sum_i \vec{p}_i\right)^2, \tag{4.9}$$

where i runs over the particles within the system. At Atlas, the angular variables ϕ and η as well as the transverse momentum p_{T} are used. The invariant mass of a two-particle system can then be written as

$$m^2 = m_1^2 + m_2^2 + 2\left(E_{\mathrm{T},1}E_{\mathrm{T},2}\cosh(\Delta y) - \vec{p}_{\mathrm{T},1}\vec{p}_{\mathrm{T},2}\right). \tag{4.10}$$

Assuming a dijet system with $m_1 = m_2 = 0$, it follows

$$m_{\mathrm{jj}} = \left(2p_{\mathrm{T},1}p_{\mathrm{T},2}\left(\cosh\left(\Delta\eta_{\mathrm{jj}}\right) - \cos\left(\Delta\phi_{\mathrm{jj}}\right)\right)\right)^{1/2}. \tag{4.11}$$

with the angular separation of the two leading jets in azimuthal direction ϕ and pseudorapidity η defined as $\Delta\phi_{\mathrm{jj}} = |\phi_1 - \phi_2|$ and $\Delta\eta_{\mathrm{jj}} = |\eta_1 - \eta_2|$, where the indices refer to the leading (1) and sub-leading (2) jet. The quantity m_{jj} is called the invariant mass of a dijet system. Note that the term $\cosh(\Delta\eta_{\mathrm{jj}})$ is dominant compared to $\cos(\Delta\phi_{\mathrm{jj}})$ for large values of $\Delta\eta_{\mathrm{jj}}$. QCD dijet events tend to be back-to-back in the transverse plane, i.e. $\Delta\phi_{\mathrm{jj}} \sim \pi$, therefore a cut on $\Delta\phi_{\mathrm{jj}}$ effectively rejects multijet events. Also, dijet topologies involved in a VBF process tend to have a large gap in rapidity corresponding to large m_{jj} and $\Delta\eta_{\mathrm{jj}}$.

CHAPTER 5

Particle Flow Jet Energy Calibration

Jets are key objects in many ATLAS searches and measurements, amongst others in the presented search for invisibly decaying Higgs bosons produced in VBF prcoesses. Two jets in the final state are the only high-level objects present in the final state, in addition to $E_{\mathrm{T}}^{\mathrm{miss}}$ which is basically calculated from the visible objects in the event. Hence, a precise measurement of jets and their properties is essential for precision measurements. The detector measurement of jet energy is affected by several effects:

- calorimeter non-compensations due to different scales of energy measurements from hadronic and EM showers
- energy loss due to inactive detector material
- energy leakage due to showers reaching outer edge of calorimeters (punch-through)
- calorimeter energy deposits below noise threshold
- variation of jet energy responses due to nearby jets (close-by effect) or out-of-cone radiation
- in-time and out-of-time pile-up interactions

To correct the measured jet energy to the energy of the corresponding stable particles, a multi-step jet calibration scheme [112] based on MC simulation and data-driven methods is used in ATLAS to correct for detector, reconstruction and pile-up effects. The absolute MC based jet energy scale (JES) calibration is part of the calibration chain and takes the hadronic jet from the detector scale to the hadron scale, while other calibration steps correct for pile-up contributions, data to simulation differences and other effects. For EMTopo jets, the calibration becomes very challenging for $p_{\mathrm{T}} < 20\,\mathrm{GeV}$ since only a smaller fraction of the jet's energy reaches the calorimeter, which is in addition also often close to the calorimeter's noise level. For PFlow jets the situation is different - tracks in the inner detector of the ATLAS detector can help to calibrate jets with $p_{\mathrm{T}} < 20\,\mathrm{GeV}$ in the central detector region.

This chapter starts with an overview of jet calibration chain with a focus on the absolute MC JES calibration. Then studies to push down the p_{T} threshold of the jet calibration to previously unattained low values using PFlow jets are presented. Subsequently, fit function studies for a performance improvement and a new metric for evaluating the calibration performance are presented. Finally the calibration results for the ATLAS small-R PFlow jet precision recomendations, which are jet corrections and uncertainties used in almost all physics analyses in ATLAS, are shown.

5.1 Jet Calibration

A jet calibration is used to correct for several effects such as pile-up interactions, data-MC differences, dead detector material, jet cone definitions or uncertainties in the calorimeter response. The calibration aims for

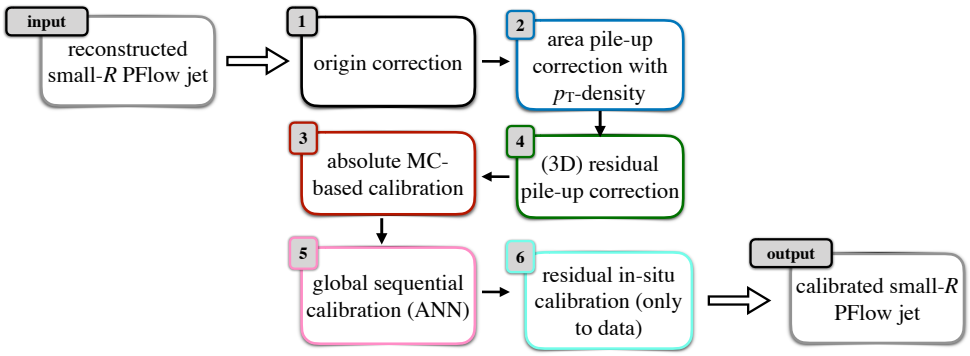

Figure 5.1: Jet energy calibration chain for small-R PFlow jets used in ATLAS as planned to use for the precision recommendations.

correcting the energy scale of the reconstructed jet, the constituent scale, to that of the underlying truth particles. Figure 5.1 shows the small-R jet calibration chain as planned to use for the Run II small-R PFlow jet precision recommendations, which is described in more detail in the following.

5.1.1 Origin Correction

The ATLAS jet calibration starts with a jet origin correction, adjusting the jet's origin from the geometrical center of the cylindrical ATLAS detector to the first reconstructed primary vertex PV_0, obtained from the energy-weighted centroids of the topo-clusters. That modifies in general the four-momentum p^μ of the jet but leaves its energy E constant. This improves the p_T-dependent η-resolution of jets, while the p_T-dependent ϕ-resolution is unchanged since the spread of the beamspot is larger along the beam axis than in the transverse plane [165].

5.1.2 Pile-up Correction

Following the origin correction, a pile-up jet energy correction is applied [166, 167]. The pile-up correction is applied prior to the absolute MC JES calibration to ensure that all jets start at the same pile-up corrected energy scale. The pile-up correction is needed since energy in the calorimeter from pile-up interactions might be added to the jet's energy by the jet clustering algorithm, leading to a jet mis-measurement especially if the pile-up jet is close to a hard-scatter jet. The pile-up subtraction procedure is divided into an area-based and a residual correction. Pile-up energy deposits in the calorimeter tend to be soft and distributed uniformly, leading to a large median energy density distribution per event. The area-based correction subtracts the pile-up contribution to the jet energy E based on the median of the pile-up p_T density distribution ρ of jets reconstructed with a soft-radiation sensitive $k_t(R = 0.4)$ algorithm for $|\eta| < 2$. The median p_T density ρ of an event with jets i is defined on an event-basis by

$$\rho = \text{median}\left(\frac{p_{\text{T,i jet}}}{A_i}\right) \tag{5.1}$$

with the jet area A_i in the $y - \phi$-plane. The jet area A_i is determined by adding thousands of ghost particles with very small energies to the event prior to jet reconstruction. Counting the ghost particles within a jet after the clustering gives an estimate of the jet size. The jet area ρ is calculated from the median of $p^i_{\text{T,i jet}}/A^{\text{jet}}_i$ to suppress a potential bias from high-energetic jets. Distributions of the jet area for different pile-up conditions

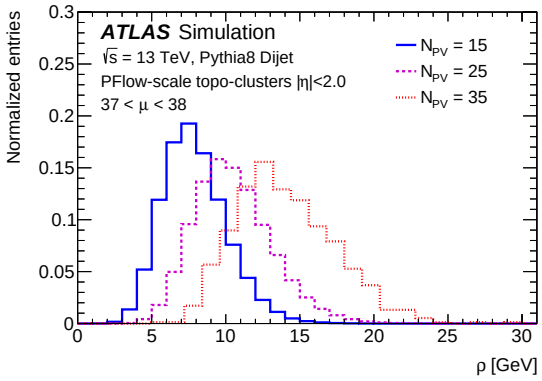

Figure 5.2: MC event median p_{T} density ρ at $N_{\mathrm{PV}} = 15$ (solid), $N_{\mathrm{PV}} = 25$ (long dashed), and $N_{\mathrm{PV}} = 35$ (short dashed) for $\mu \in [37, 38]$ [112].

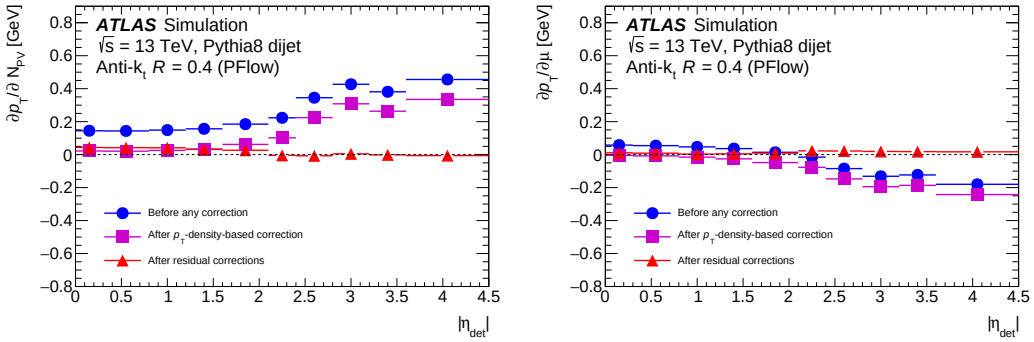

Figure 5.3: Dependence of PFlow jet p_{T} on in-time pile-up (left) and out-of-time pile-up (right) as a function of $|\eta|$ at $p_{\mathrm{T}} = 25\,\mathrm{GeV}$ [112].

are shown in Figure 5.2. To reject a remaining p_{T}-dependence, it follows a residual pile-up p_{T} correction. The one-dimensional residual pile-up correction is parametrised in terms of the average number of interactions per proton bunch crossing $\langle\mu\rangle$ describing out-of-time pile-up effects, and the number of primary vertices in the event N_{PV}, parametrising in-time pile-up effects. The pile-up-subtracted p_{T} after the area-based and residual correction is given by

$$p_{\mathrm{T}}^{\mathrm{corr}} = p_{\mathrm{T}}^{\mathrm{const}} - \rho A \underbrace{-\alpha(N_{\mathrm{PV}} - 1)}_{\text{in-time PU}} \underbrace{-\beta\langle\mu\rangle}_{\text{out-of-time PU}} , \tag{5.2}$$

where $p_{\mathrm{T}}^{\mathrm{const}}$ is the jet transverse momentum at the topo-cluster energy scale and A is the jet area. The product ρA is a measure of the (in-time) pile-up activity in a jet. The parameters α as well as β are MC-derived values obtained from fits of $\partial p_{\mathrm{T}}/\partial N_{\mathrm{PV}}$ at fixed μ for α and $\partial p_{\mathrm{T}}/\partial \mu$ at fixed N_{PV} for β in bins of $p_{\mathrm{T}}^{\mathrm{true}}$ and η. Logarithmic fits are performed in the $p_{\mathrm{T}}^{\mathrm{true}}$ range $[20, 200]\,\mathrm{GeV}$ for each bin in $|\eta|$, where the values at $p_{\mathrm{T}}^{\mathrm{true}} = 25\,\mathrm{GeV}$ (the scale where pile-up effects are important) are taken as the nominal values of α and β. Distributions of the dependence of p_{T} on N_{PV} and μ are shown in Figure 5.3.

5.1.3 Absolute MC Jet Energy Scale Calibration

After the pile-up-correction follows the absolute MC JES calibration aiming for obtaining a calibration function C for the energy depending only on reconstructed quantities such as the reconstructed (reco) jet energy E_{reco}, which are also available in measured data. The absolute MC JES calibration is performed in bins of pseudorapidity η and the true jet energy E_{true}. A binning in η is crucial due to differences in the tracker coverage for PFlow jets and gaps as well as transitions in the calorimeters, which may result in absorbed or undetected particles. The individual jet energy response r is defined for each ΔR-truth-matched jet pair by

$$r = \frac{E_{\text{reco}}}{E_{\text{true}}}, \tag{5.3}$$

where E_{reco} and E_{true} are the reconstructed and the true jet energy, respectively. Usually it holds that $r < 1$, since mostly $E_{\text{reco}} < E_{\text{true}}$ due to several non-linear detector effects. In particular this holds for low p_{T} jets due to an energy cut-off for jet measurements. This is a big challenge for the low p_{T} jet calibration since the jet response gets a non-Gaussian tail leading to a non-trivial bias of the calibration. For each energy E and η bin, the mean jet response can be constructed using a Gaussian fit to the jet response distribution via

$$\mathcal{R} = \text{mode}\left[\frac{E_{\text{reco}}}{E_{\text{true}}}|E_{\text{true}}\right] \tag{5.4}$$

The two important quantities in jet calibrations are the jet energy scale (JES), which is the measure of central tendency of the jet response distribution, and the jet energy resolution (JER), $\sigma_{\mathcal{R}}$, which is the width of the jet response distribution. The absolute MC JES calibration aims for correcting the JES, while no big improvement with respect to the relative JER is expected.

The jet energy correction procedure is described in more detail in the following.

a) Jet Response Evaluation

The first step in the MC JES calibration is the jet response evaluation, which involves several sub-steps namely an optimal energy and η binning, Gaussian fits to the jet response in bins of energy and η as well as fitting the jet response as function of $\log(E)$ with polynomial functions. For all matched-pairs of truth and reconstructed jets, the average jet response $\mathcal{R}$ is obtained by fitting a Gaussian distribution to the distribution obtained by filling a histogram with the individual jet response values r binned in E_{true} and η, where the latter ranges from -4.5 to 4.5 in steps of size 0.1. To obtain the average jet response $\mathcal{R}$ as defined in Equation 5.4, a Gaussian distribution is fitted in an iterative procedure three times to the jet response, called "triple Gaussian fit". The initial fit range is in general set to $\Delta = \langle\mathcal{R}\rangle \pm 1.3 \cdot \sigma_{\mathcal{R}}$ but bounded to $[-0.2, 2.0]$. From the first Gaussian fit, the new mean $\langle\mathcal{R}\rangle'$ and standard deviation σ' are used to define the new fit range Δ' but this time without any boundary condition. This is repeated a third time with the fit range Δ''. The fitting procedure gives in most cases a reasonable estimate of the mode of the underlying distribution. The fitting of the energy jet response is shown in Figure 5.4.

The next step is deriving the average jet response as a function of E_{true} and to model it with fit function F_{calib}, described in more detail in Section 5.2.4.

b) Numerical Inversion

The next step in the JES calibration chain is based on the numerical inversion (NI) technique [168, 169], which is a widely used detector calibration method applied in different parts of the ATLAS jet calibration. The NI procedure is used to derive the energy calibration function in terms of a reconstructed quantity. Directly

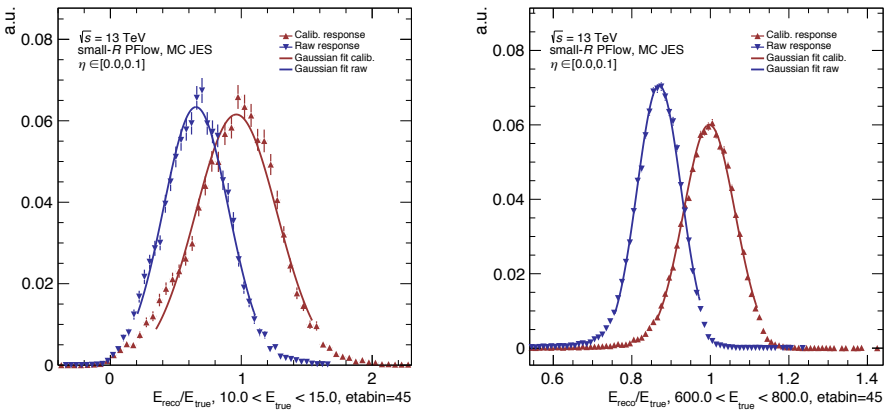

Figure 5.4: Jet response distribution with Gaussian fits before (raw) and after MC JES calibration for $\eta \in [0.0, 0.1]$ for two different E_{true} ranges. The response after the pile-up calibration is plotted in blue, while the response after MC JES calibration is shown in red.

evaluating the jet energy response as a function of E_{reco} is not feasible since, for fixed E_{reco}, the response distribution has a non-Gaussian shape due to the steeply falling jet p_{T} spectrum which corresponds to a migration-trend from low to high p_{T} values, introducing a resolution bias. The approach to make the calibration independent of the underlying energy distribution is the NI: instead using a function $f : E_{\text{reco}} \mapsto E_{\text{true}}$, the NI technique is calibrating E_{reco} using the inversed function $f^{-1}(E_{\text{reco}})$. The NI procedure can be formalised [170]. Define

$$f(x) = \text{mode}\left[E_{\text{reco}}|E_{\text{true}} = x\right] \tag{5.5}$$

and the jet response

$$\mathcal{R}(x) = \text{mode}\left[\frac{E_{\text{reco}}}{x}|E_{\text{true}} = x\right], \tag{5.6}$$

where E_{reco} and E_{true} can be seen as random variables and x is a specific realisation of E_{true}. The distribution $E_{\text{reco}}|E_{\text{true}} = x$ is the distribution of E_{reco} given that E_{true} is realised as x. Let y be in the following a specific value of E_{reco}. Then, the NI procedure consists of three steps:

- obtain $f(x)$ and $\mathcal{R}(x)$
- compute $\mathcal{R}(f^{-1}(y)) = \tilde{\mathcal{R}}(y)$
- apply a jet-by-jet correction via $Y \mapsto Y/\tilde{\mathcal{R}}(Y)$

In these terms the goal of the calibration is determining a function so that $f(x) = \text{mode}[E_{\text{reco}}|E_{\text{true}} = x] = x$ or equivalently

$$\mathcal{R}(x) = \text{mode}\left[\frac{E_{\text{reco}}}{x}|E_{\text{true}} = x\right] = 1. \tag{5.7}$$

Practically, for each bin in true energy E_{true}, the NI energy E_{NI} can be calculated from

$$E_{\text{NI}} = E_{\text{true}} \cdot \mathcal{R}(E_{\text{true}}) \tag{5.8}$$

with the fitted jet response function $\mathcal{R}(E_{\text{true}})$. This gives the response $\mathcal{R}$ as a function of E_{NI}:

$$\mathcal{R} = \text{mode}\left[\frac{E_{\text{reco}}}{E_{\text{true}}}|E_{\text{NI}}\right] \tag{5.9}$$

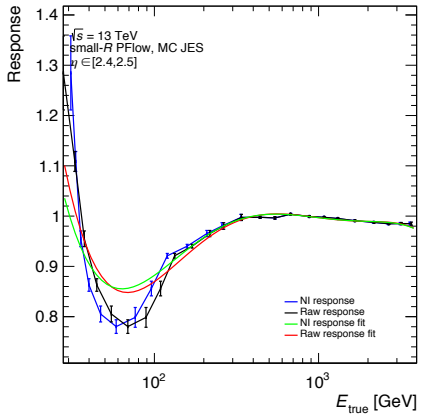

Figure 5.5: Sketch of the NI shift of the response points when transforming the E_{true}-axis to E_{reco} for a given η-bin. The response points $\mathcal{R}$ according to the E_{true} binning are shown in black, while the NI-response is shown in blue. For completeness, the polynomial fits are shown in red and green, respectively. For $\mathcal{R} < 1$, the points are shifted at fixed $\mathcal{R}$ to the left parallel to the x-axis, while for $\mathcal{R} > 1$ the response points are shifted to the right parallel to the x-axis, i.e. at constant $\mathcal{R}$.

Thus the transformation from the truth to reco energy on the x-axis corresponds to a shift of the jet response at their fixed response value $\mathcal{R}(E_{\text{true}}$ to the left for $E_{\text{true}} > E_{\text{reco}}$ and to the right for $E_{\text{true}} > E_{\text{reco}}$ as sketched in Figure 5.5. Subsequently, a polynomial fit is again performed to obtain the response function in dependence of E_{NI}, denoted by $R(E_{\text{NI}})$, which is the inverse of the searched calibration function $C(E_{\text{reco}})$, which in turn follows directly from the definition of the average jet response. For a given measured E_{reco}, the energy is corrected via

$$E_{\text{calib}} = C(E_{\text{reco}}) \cdot E_{\text{reco}} = \frac{E_{\text{reco}}}{\mathcal{R}(E_{\text{NI}})}. \tag{5.10}$$

c) Closure Test

The final step is a closure test showing the performance of the MC JES calibration. The calibration is "closed" if the averaged calibrated jet energy response is given by

$$\mathcal{R}_{\text{calib}} = \text{mode}\left[\frac{E_{\text{calib}}}{E_{\text{true}}}\right] = 1. \tag{5.11}$$

The jet scale of the jet response before and after calibration is shown in Figure 5.6 using the MC JES approach described above, i.e. using polynomial functions for fitting the jet response.

5.1.4 Absolute MC Jet η Calibration

In addition to the jet energy, also the jet pseudorapidity η is calibrated with a similar approach in MC to correct for biases in the η reconstruction which are caused by the transition regions in the calorimeter with respect to technologies and granularity. Significant η-corrections are needed in the barrel–endcap ($|\eta| \sim 1.4$) and forward-endcap ($|\eta| \sim 3.1$) transitions. The η response is defined as $\mathcal{R}_\eta = \langle \eta_{\text{reco}} - \eta_{\text{true}} \rangle$, determined with a Gaussian fit as described in Section 5.1.3, and the correction is performed on a jet-by-jet basis via $\eta_{\text{calib}} = \eta_{\text{reco}} - \mathcal{R}_\eta$. Technically, the η calibration is performed simultaneously with the absolute MC JES

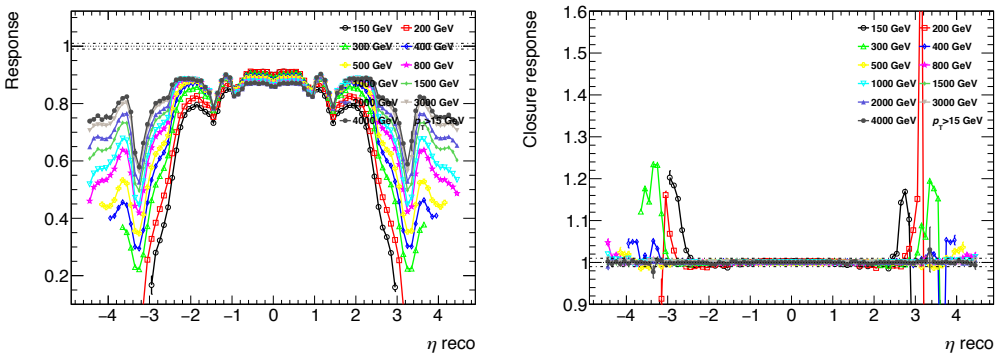

Figure 5.6: Jet response distribution before (left) and after calibration (right) as a function η. The different lines correspond to different energy values in a specific η bin. Only lines for $p_T > 15$ GeV are shown, so low energies are only shown at low $|\eta|$. For the calibration, the "NoPtCut" jet container and the default calibration method from the consolidated Run II recommendations is used, i.e. polynomial fits for fitting the jet response as function of energy. A good closure is observed except of the low energy bins for $|\eta| \sim 3.1$, which are statistically limited and very low in p_T.

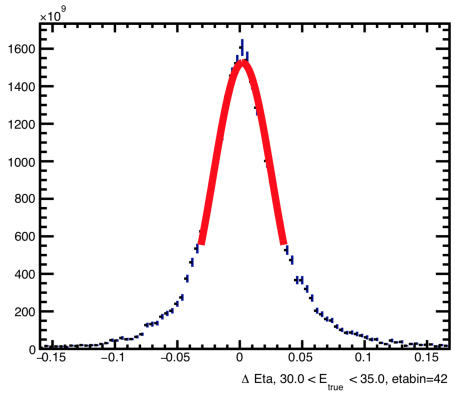

Figure 5.7: Exemplaric Gaussian fit to the η response distribution defined as $\eta_{\text{reco}} - \eta_{\text{true}}$.

calibration, whereby the relative η correction is in general small compared to the energy correction. A typical distribution of the η response is shown in Figure 5.7.

5.1.5 Global Sequential Calibration

After the MC-JES correction follows the global sequential correction (GSC) improving the jet resolution and reducing other uncertainties such as the jet flavour uncertainty [112]. It corrects mainly for differences in the jet energy measurement between quark and gluon initiated jets and for punch-through jets. The jet response is sequentially derived as a function of p_T, η and additional jet properties x_i. In each bin the response $R(x_i)$ as a function of jet property x_i is applied as a correction factor: $p_{T,i}^{\text{corr}} = p_{T,i}/R(x_i)$. The observables x_i are f_{charged}, f_{Tile_0}, f_{LAr_3}, n_{trk}, w_{trk} and n_{segments}. The variable f_{charged} is the charged contribution of the jet energy, f_{Tile_0} is the fraction of the jet energy, which is deposited in the first layer of the hadronic tile calorimeter. f_{LAr_3} is the jet energy fraction, which is measured in the third layer of the electromagnetic calorimeter. The variable n_{trk} represents the number of tracks measured in the ID fulfilling $p_T > 1$ GeV and are associated with the jet. The observable w_{trk} is the defined as the average p_T-weighted distance in the angular $\eta - \phi$ plane between the jet axis and the associated tracks. The fifth variable is the number of associated muon track segments, n_{segments},

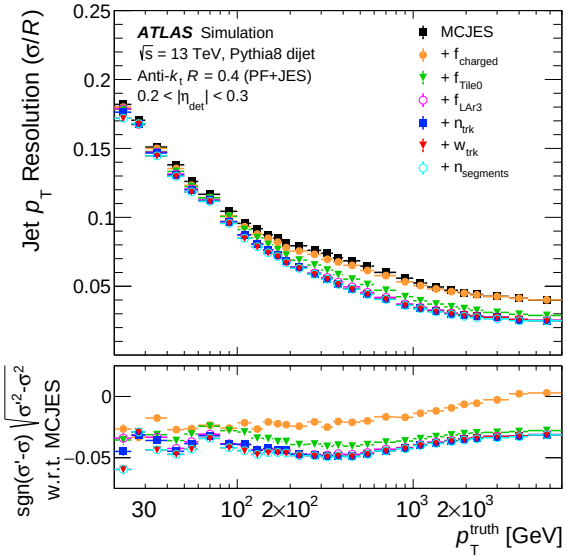

Figure 5.8: Resolution of jets for $\eta \in [0.2, 0.3]$ for each step of the GSC. The lower pad shows the difference in quadrature between the resolution after the MC JES calibration (σ) (before any GSC correction) and after the individual GSC steps (σ') [112].

accounting for punch-through effects. The improvement of the individual GSC steps with respect to the jet resolution is shown in Figure 5.8.

5.1.6 In situ Calibration

The final step in the jet calibration chain is the in situ calibration which is only applied to data and corrects for imperfect simulations of physics processes and detector responses. In the in situ calibration the response in data R_{data} and MC R_{MC} is measured separately and the ratio is taken as the data correction in order to match the simulation:

$$c_{\text{in situ}} = \frac{R_{\text{data}}}{R_{\text{MC}}}, \tag{5.12}$$

where the jet response R is calculated by comparing the jet p_{T} with well-calibrated reference objects such as other jets, Z bosons or photons [171]. The in situ calibration is splitted in three steps:

- dijet η-intercalibration: correcting the JES of forward jets ($0.8 \leq |\eta| < 4.5$) to those of central jets ($|\eta| < 0.8$) via p_{T}-balance in dijet events using the dijet asymmetry
- Z/γ+jet missing-$E_{\text{T}}^{\text{miss}}$ projection fraction: balancing the hadronic recoil against the p_{T} of a well calibrated Z boson or photon
- multijet balance: single high-p_{T} jets are calibrated with a system of well calibrated low-p_{T} jets.

5.2 Absolute Jet Energy Scale Calibration Results

The absolute MC JES and η calibration for small-R PFlow jets uses simulated data for the MC campaigns mc16a, mc16d and mc16e. The generation of the used MC samples and their properties is described in Section 5.2.1. A new metric defining the quality of the calibration is presented in Section 5.2.2, aiming for improving shortcomings of the default closure test. Several studies are performed to improve the MC JES calibration and

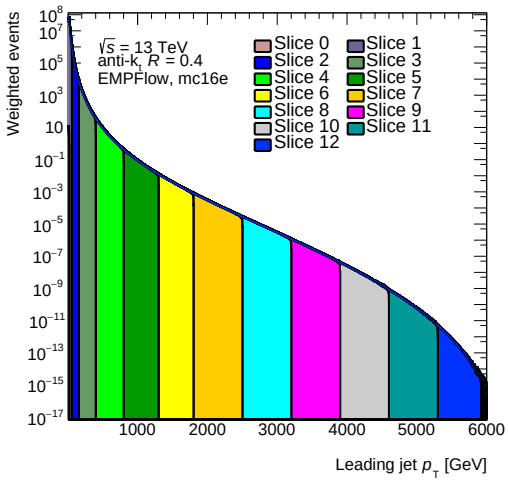

Figure 5.9: Spectrum of the leading truth jet p_{T} of simulated Pythia events with small-R PFlow jets for the MC simulation campaign mc16e at $\sqrt{s}$ = 13 TeV. The 13 p_{T} slices are displayed in different colours.

push the lower p_{T} limitation to lower values. The main result of fixing the reco p_{T} threshold bias of the MC JES calibration is presented in Section 5.2.3. Further, it is extensively studied how different fit functions allow for a potential improvement of the calibration, presented in Section 5.2.4.

5.2.1 Monte Carlo Samples and Selection

Simulated events generated with Pythia8 [172] at $\sqrt{s}$ = 13 TeV and the A14 NNPDF23LO PDF set [173] are used for the absolute MC-based JES and η calibration. The following set of samples is used

mc16_13TeV.3647*.Pythia8EvtGen_A14NNPDF23LO_jetjet_JZ*WithSW.deriv.DAOD_JETM1.e7142_e5984_s3126_r*_p3749,

described in more detail in Table 5.1. A more detailed introduction to MC generators is given in Section 6.2.2. EMTopo as well as PFlow jets with a radius parameter of $R = 0.4$ are generated. These events are simulated in slices in leading jet p_{T} in order to ensure that enough statistics is provided for a wide range in p_{T}. Since the jet p_{T} spectrum is steeply falling, the generated p_{T} slices are subsequently weighted to ensure a smooth, physical p_{T} distribution as shown in Figure 5.9 after applying the event weights for small-R PFlow jets for the MC campaign mc16e. A geometrical matching in the η-ϕ-space of truth and reco jets is performed: reco jets which are found in a cone of $\Delta R < 0.3$ with respect to a truth jet are matched. Further jet isolation criteria are applied to avoid potential ambiguities in the matching: no additional truth jet activity with $p_{\mathrm{T}} > 7$ GeV is present within $2.5 \cdot R = 1$ (with $R = 0.4$) and no additional reco jet activity with $p_{\mathrm{T}} > 7$ GeV is present within $1.5 \cdot R = 0.6$ to ensure a correct matching and excluding bad reconstruction. Truth jets are only generated for $p_{\mathrm{T}} > 7$ GeV and $|\eta| < 5$. The p_{T} threshold for reco jets is discussed in Section 5.2.3. Reco and truth verticies must be close, i.e. the z component of the vertices z_0 needs to be smaller than 0.2 mm. Further criteria refer to the jet multiplicity; at least one truth jet and two reco jets are required. To check against pile-up-only jets the average p_{T} of the two reco jets needs to be smaller than 1.4 of the truth leading jet transverse momentum. After applying these cuts, the jets used for the calibration consist of isolated and matched pairs of reco and truth jets.

Table 5.1: Dijet samples used for the absolute MC-based JES PFlow jet calibration. The samples were produced with PYTHIA8 with the A14 NNPDF23LO generator tune for the MC campaigns mc16a, d and e. Shown is the sample dataset ID (DSID), the corresponding cross section σ and the filter efficiency as provided by the physics modelling group.

DSID	σ	filter eff.
364700	78.10 mb	0.975330
364701	78.10 mb	0.024425
364702	2.43 mb	0.009863
364703	26.50 μb	0.011658
364704	225.00 nb	0.013366
364705	4.55 nb	0.014526
364706	258.00 pb	0.009473
364707	16.20 pb	0.011097
364708	625.00 fb	0.010156
364709	19.60 fb	0.012056
364710	1.20 fb	0.005893
364711	42.30 ab	0.002673
364712	1.04 ab	0.000429

5.2.2 Closure Quality

A closure test as described in Section 5.1.3 is a widely-used figure of merit for evaluating the performance of the absolute MC JES calibration. However, the closure plot has a lack in important information which should be considered when deciding about a calibration strategy. For example, the closure plot does not show if the underlying, calibrated jet response distribution is symmetric and unimodal, which especially is relevant in the low-p_{T} regime. Overall, without knowing the shape of the jet response distribution it may not be sufficient that the calibration closes when comparing different calibration strategies. This issue will be discussed in this section and a potential solution is presented: the closure quality plot. For the following discussion, it is useful to recall the definitions and interpretations of the mean, median and mode of a distribution. The mean is the usual average of a distribution, the median is the middle value, i.e. the value splitting the distribution into two parts of equal size, and the mode is the maximum of a distribution, i.e. the value of the distribution that has the highest probability. As described above, an iterative Gaussian fit is used to determine the mode of the distribution in MC JES calibrations. This choice has a direct impact on the closure plot. In a layman's interpretation, using the mode of a fitted jet response distribution calibrates the jets in the sample so that the largest number of jets is calibrated correctly, accepting that a small number of jets may be calibrated wrongly. Calibrating with respect to the mean can be interpreted that the miscalibrations are distributed so that the sum of all mistakes is close to zero. Calibrating with respect to the median can be interpreted that the number of jets which are under- or over-corrected is balanced. In terms of jet calibration, it is conservative to assume that a consistent and reliable calibration can only be achieved if the jet response distributions, binned in η and E_{true}, can be described and fitted by a Gaussian distribution. A Gaussian distribution is amongst characterised by equality of its mean, median and mode. For a non-Gaussian distribution, mean, median and mode are in general different. Further, just using the mean of a distribution is not sufficient since a double-peak distribution may result in an expected mean but the underlying distribution can still be unphysical. Therefore, the (maximal) difference of the values of mean, median and mode of a jet response distribution provides a metric for its Gaussian character. Another option would be to just use the difference of mean and median as a measure for the non-Gaussian character of a jet response distribution. In principle, there are also other metrics as a measure for the non-Gaussian character of a distribution such as the χ^2 value from a Gaussian fit to the distribution. In the absolute MC JES calibration, the mean and median are directly obtained from the distribution while the mode is obtained from a Gaussian-fit to the $2\,\sigma$-center of the distribution. A contour plot is used to summarise the calibration performance, both the closure and the Gaussian character of the underlying jet response distributions, for all η-bins and the whole p_{T}-range in one single plot. It shows the fraction of the maximal mean/median/mode-difference which is within the n % closure after the JES calibration, where typical values for n are 1, 2 or 5. For example, the 2 % closure

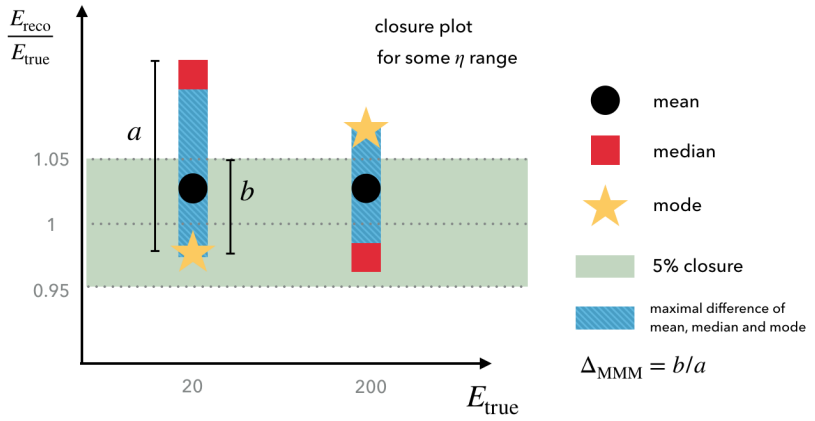

Figure 5.10: Graphical explanation of the closure quality plot.

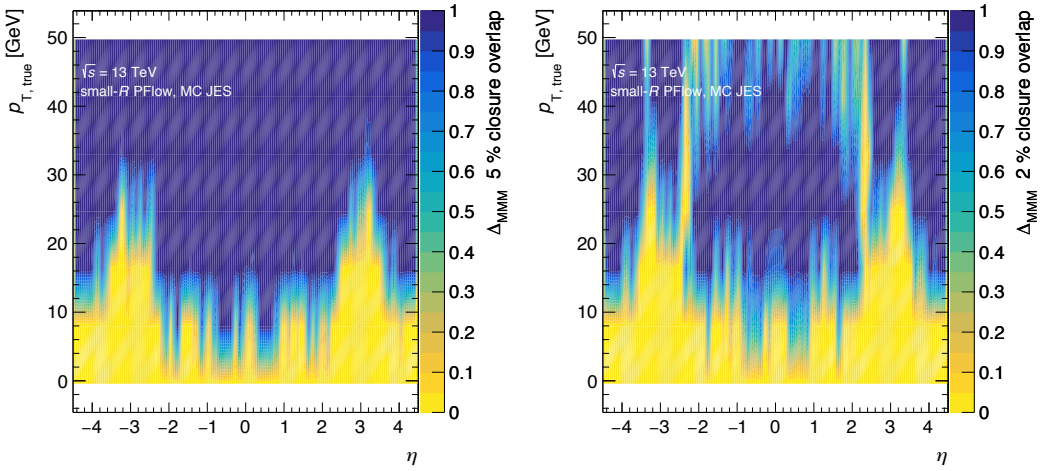

Figure 5.11: Closure quality plot after MC JES calibration for a 5 % (left) and a 2 % (right) closure range. Roughly speaking, the blue coloured region indicates that the calibration performed well in that η-p_{T}-range, while the yellow colour indicates either a calibration non-closure and/or a non-Gaussian calibrated jet response distribution. The forward region and especially the ECal transition regions suffer from a energy miscalibration. In addition, the calibration with polynomial fits produces some non-closure in the central region for $p_{\text{T}} \sim 45\,\text{GeV}$.

corresponds to the jet response range [0.98, 1.02].

It should be further noted that the empircally derived colour scheme used on the z-axis is arbitrary, which should be considered in its interpretation. A graphical explanation of the closure quality plot is shown in Figure 5.10. The closure quality plot for a 5 % and a 2 % closure range is shown in Figure 5.11, based on the jet calibration strategy described above. Although it was described that it is conservative to require a Gaussian jet response distribution for a reliable jet calibration, which is one of the main features displayed in the closure quality contour plot, it may be considered to calibrate the jets anyway. Although some jets are then not correctly calibrated, a majority of jet energy measurements are corrected. Even if a calibration closure is not achieved, quantites such as $E_{\text{T}}^{\text{miss}}$ and $E_{\text{T}}^{\text{soft}}$ can benefit from such a jet energy correction, which might be especially feasible for central low-p_{T} PFlow jets benefting from track measurements.

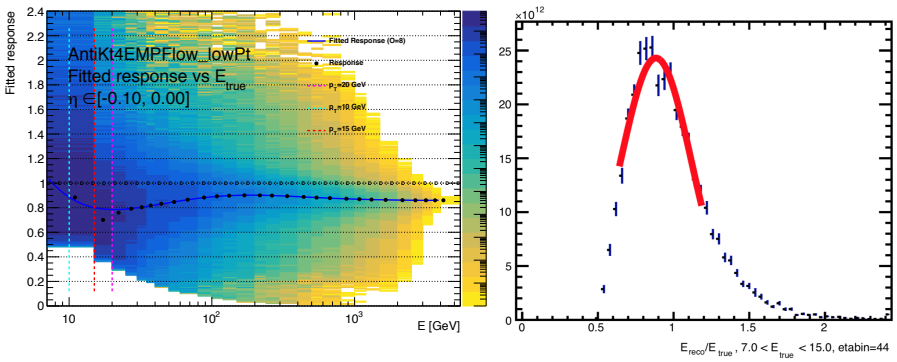

Figure 5.12: Reco p_{T} threshold effect biasing the jet response in the low p_{T} regime. The histogram contains jets after passing through the residual pile-up calibration. The first E_{true} bin ranges from 7 to 15 GeV. Reco jets in the central region are stored down to reco energies of 7 GeV. Thus the minimal jet response which can be obtained with these samples is $r = E_{\mathrm{reco}}/E_{\mathrm{true}} = 7/15 = 0.46$. This threshold is caused by a limitation of the previously used MC samples which in turn limits the calibration performance for $p_{\mathrm{T}} < 20\,\mathrm{GeV}$.

5.2.3 Momentum Threshold Studies

Truth jets down to $p_{\mathrm{T}} = 7\,\mathrm{GeV}$ are generated in simulation, while the reco p_{T} threshold depends on the used jet collection (also called jet container) in the event simulation. The calibration of PFlow jets in the low p_{T} regime can be biased by a jet reconstruction p_{T} threshold. For the "LowPt" jet container this reconstruction threshold is at $p_{\mathrm{T}} = 4\,\mathrm{GeV}$. The jet response $\mathcal{R}$ is biased by this threshold since a jet near the threshold cannot be mis-measured with less energy than the threshold energy, otherwise the jet is not stored in the jet collection. For $p_{\mathrm{T}} < 20\,\mathrm{GeV}$, the bias of the calibration originating from the jet p_{T} reconstruction threshold is visible, as visualised in Figure 5.12. In contrast, for $p_{\mathrm{T}} > 20\,\mathrm{GeV}$, the calibration performs very well.

One note regarding the shape of the response curve: In contrast to the response of EMTopo jets, the PFlow algorithm combines tracks and topo-clusters leading to a higher constituent scale at low p_{T} due to the usage of calibrated tracks. At high p_{T} values, the upper 40 GeV of the track selection means that the scale of PFlow jets reduces to that of EMTopo jets.

The described threshold effect can be tackled by switching to the "NoPtCut" jet container, which contains jets with energies E down to 1 MeV at constituent scale. Further jets with $p_{\mathrm{T}} < 0\,\mathrm{GeV}$ which might occur in the additive and partially event-based pile-up correction are included. For comparison, the jet response distribution as function of energy including reconstructed jets with very low p_{T} is shown in Figure 5.19.

5.2.4 Jet Response Fit

For an improvement of the performance of the MC JES calibration with regard to previous calibrations, different functions to fit the mode of jet response as a function of energy such as higher order polynomial fits, Chebyshev polynomial fits and spline methods are tested and evaluated regarding their performance measured by closure and closure quality plots.

- **Polynomial fits** are defined as a function of $\log(E)$, so that the fit function $\mathcal{F}(E)$ is given as a linear combination of polynomials by

$$\mathcal{F}(E) = \sum_{i=0}^{N_{\mathrm{max}}} \alpha_i \log(E)^i, \tag{5.13}$$

where $N_{\text{max}} = 8$ is the maximal order of the fitted polynomials and $\alpha_i, i \in [0, N_{\text{max}}]$, are free fit parameters. For a given N_{max}, all fit functions with an order $\leq N_{\text{max}}$ are evaluated and the best fitting one is identified by minimising Pearson's χ^2 test, defined by

$$\chi^2 = \sum_i \frac{(\mathcal{R}(E_i) - \mathcal{F}(E_i))^2}{\sigma_{\mathcal{R}(E_i)}}, \tag{5.14}$$

where i runs over the number of energy bins, $\mathcal{R}(E_i)$ is the jet response value of the mean energy E_i in bin i with uncertainty $\sigma_{\mathcal{R}(E_i)}$ and $\mathcal{F}(E_i)$ is the value of the evaluated fit function at energy E_i. The polynomial fitting is performed in the p_{T} range of [5, 5000] GeV due to limited statistics and threshold effects outside of this range. For statistical reasons, the calibration factors are usually freezed at energies beteen 3 and 4 TeV, depending on η, while a linear low-p_{T} extrapolation is performed. For a fixed η, the uncalibrated jet response has a characteristic curve mainly defined by the p_{T} dependent mis-measurement of jets in the detector. Depending on the jet collection, the low p_{T} regime can be biased towards lower jet response values due to the p_{T} threshold effect. The jet response function slightly drops below one at higher energies, which is caused by the η-dependent jet punch-through and calorimeter non-compensations.

It is tested if polynomials with even higher orders up to $N_{\text{max}} = 12$ can improve the MC JES calibration. Higher order polynomials come along the risk of overfitting and suffer from Runge's phenomenon [174]. The latter describes the issue of large oscillations at the fit interval edges leading to non-converging fits. However, this problem can often be solved with a work-around: First, the fit is performed in a limited fit range chosen to be [5, 500] GeV. The resulting fit parameters are set as the start parameters for the second fit, which is performed in the full energy range. This work-around effectively increases the fraction of converging polynomial fits with orders > 8. Nevertheless, the impact on the calibration is negligible and the best polynomial fits in terms of a χ^2-test are found to have an order < 9.

- The **Groom's function** [175, 176] can be understood as a theoretical expectation of the calorimeter's response to jet energy measurements. Groom's function can be parametrised by

$$G(\alpha_i, x) = \alpha_1 \left(1 - \alpha_2 \left(\frac{x}{0.75}\right)^{\alpha_3 - 1}\right) \tag{5.15}$$

with free fit parameters α_i. In general, the Groom's function is not used solely to fit the jet response but alternatively one can use a polynomial fit but using extrapolating points for high and low energies from the Groom's function. Historically, for EMTopo jets the Groom's function $G(\alpha_i, x)$ was used to set additional points to fit the jet response as a function of the energy where the low p_{T} threshold effect biased the fit at low energies. However, the Groom's function cannot be used for PFlow jets in the central detector region, where the tracker is used partially for jet energy measurements and thus the Groom's function is not the correct description for the jet response as a function of energy. However, in the forward detector range, where PFlow jets merely reduce to EMTopo jets, the Groom's function can still be used to support the fitting procedure.

- **Chebyshev polynomials** have appealing features with respect to orthogonality and convergence. The Chebyshev polynomials $T_i(x)$ are defined by

$$\begin{aligned} T_0(x) &= 1 \\ T_1(x) &= x \\ T_{n+1}(x) &= 2x \cdot T_n(x) - T_{n-1}(x). \end{aligned} \tag{5.16}$$

The fit functions are linear combinations of the Chebyshev polynomials $T_{i<12}$. As before, the best-fitting function is identified by minimising Pearson's χ^2 test.

- **Splines** of order n are functions which are defined piece-wise by polynomials of order $n - 1$. The

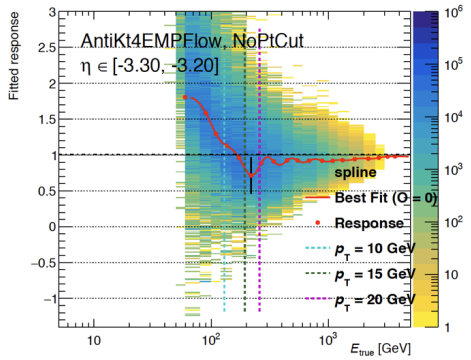

Figure 5.13: Illustration of the overfitting of a cubic spline for a specific η bin.

sub-intervals of the spline meet at points called knots k. A spline can be used to interpolate the jet response $\mathcal{R}$ as function of energy E. However, ordinary cubic splines tend to overfit the data as shown in Figure 5.13, therefore it is tested if penalized splines based on b-splines can avoid those overfitting problems. In general, a spline $S(x) : \mathbb{R} \mapsto \mathbb{R}^n$ is a piecewise polynomial function of degree $n-1$ with knots t in a variable x built from a linear combination from b-spline basis functions $B_i(x,t)$ via

$$S(x) = \sum_i a_i B_i(x,t), \tag{5.17}$$

where $a_i \in \mathbb{R}^n$ are control points weighting the individual basis functions B_i and i runs over the number of b-spline basis functions B_i. The knots t of a b-spline define points where the pieces of polynomials are smoothly added. The b-spline functions can be obtained by help of the Cox–de Boor recursion algorithm [177] where each point on the fitted curve is influenced by a number of its neighbour points. Given the knots t_i, the order-n b-splines are defined as

$$B_{i,n}(x) = \begin{cases} 1, & \text{if } n = 1 \text{ and } t_i \le x \le t_{i+1} \\ 0, & \text{if } n = 1 \text{ and } (x < t_i \text{ or } x > t_{i+1}) \\ w_{i,n} B_{i,n} + (1 - w_{i+1,n}) B_{i+1,n}, & \text{if } n > 1 \end{cases}, \tag{5.18}$$

with $w_{i,n}(x) = (x - t_i)/(t_{i+k} - t_i)$. The spline $S(x)$ is fitted to an unknown function $g(x)$ given at points t by varying the control points so that $S(x) \approx g(x)$ in an optimisation procedure which reduces essentially to a system of linear equations. Since $S(x) = 0$ for x outside of the range defined by the knots, an extrapolation to lower (higher) energy values is added using a linear extrapolation based on the first (last) five points for the low (high) end of the spline is used. Penalized b-splines (p-spline) are spline representations where the fit coefficients are obtained on the one hand by a fit to data and on the other hand by an additional smoothness penalty term which can be used to avoid an overfitting. The p-spline is calculated similar as the b-spline but uses a special regularisation scheme to obtain the best fit results. The p-spline regression model minimises

$$L = \chi^2 + \alpha P = \underbrace{\sum_{i=0}^{n} \big(y_i - S(x_i)\big)^2}_{\text{least squares}} + \underbrace{\alpha \int_a^b \big(S''(x)\big)^2 \, dx}_{\text{penalty}} \tag{5.19}$$

with $a < x_i < b$ and $\alpha \ge 0$ chosen but fixed. The penalty term reduces the sensitivity of the spline to fluctuations. Two extreme penalty cases are $\alpha = 0$ and $\alpha \to \infty$. In the former case, the penalty term

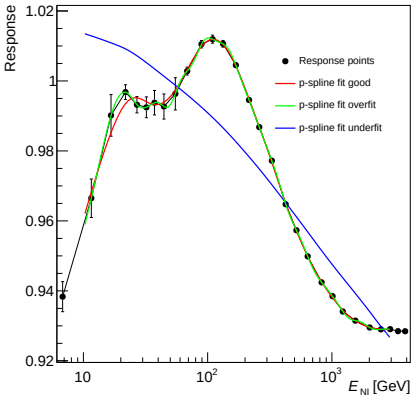

Figure 5.14: P-spline comparison for three different penalisation parameters.

vanishes and there is no restriction on the curvature of $S(x)$. In the latter case the regression is linear. The best value of α needs to consider a trade-off between the curvature penalisation and a reasonable fit of the data as visualised in Figure 5.14. The penalisation parameter is defined dynamically for each η bin as

$$\alpha = \frac{\lambda}{n} \cdot \sum_{i=0}^{n} w_i, \tag{5.20}$$

where i runs over the n data fit points and w_i are the point weights defined as $w = \sigma_y^{-1/2}$, where σ_y is the response fit uncertainty from the iterative Gaussian fit described in Section 5.1.3. By this, the p-spline optimisation procedure considers the uncertainty of the Gaussian fit. The penalisation parameter λ is empirically set to 0.1. To check for a potential overfitting, the calibration and the closure test are performed on statistical independent events by splitting the jet sample into even and odd events, where the one half is used for calibration and the other for closure test.

A comparison of the fitting techniques for different energy values with respect to the MC JES closure is presented in Figures 5.15-5.17 in which only points corresponding to $p_{\mathrm{T}} \geq 20\,\mathrm{GeV}$ are shown, i.e. low energies are only shown at small $|\eta|$. The comparison is shown for jets after the pile-up calibration as it is described in Section 5.2.5. The p-spline can fit the response data best and usually a energy closure within 1 % is achieved with the p-spline which performs especially at low energies better than polynomial fits. Chebyshev polynomials and Groom's function cannot improve the calibration performance. Large closure deviations from 1 in the forward region from low energies correspond to statistical limitations caused by the extreme phase space.

5.2.5 Precision Recommendations

For the Run II precision recommendations for PFlow jets, the pile-up calibration, the MC JES as well as the GSC approach are intensively reviewed and potential modifications and improvements are tested and implemented in the ATLAS software framework. Since the one-dimensional pile-up residual calibration does not take into account correlations between μ and N_{PV}, a three-dimensional (3D) residual pile-up correction is developed in which a correction term $p_{\mathrm{T}}^{\mathrm{residual}}$ is derived in bins of N_{PV}, μ, $p_{\mathrm{T}}^{\mathrm{true}}$ and η via

$$p_{\mathrm{T}}^{\mathrm{corr}} = \underbrace{p_{\mathrm{T}}^{\mathrm{const}} - \rho A}_{p_{\mathrm{T}}^{\mathrm{area}}} \underbrace{- p_{\mathrm{T}}^{\mathrm{3D}}\left(N_{\mathrm{PV}}, \mu, p_{\mathrm{T}}^{\mathrm{true}}, |\eta|\right) + \Delta p_{\mathrm{T}}}_{p_{\mathrm{T}}^{\mathrm{residual,3D}}}, \tag{5.21}$$

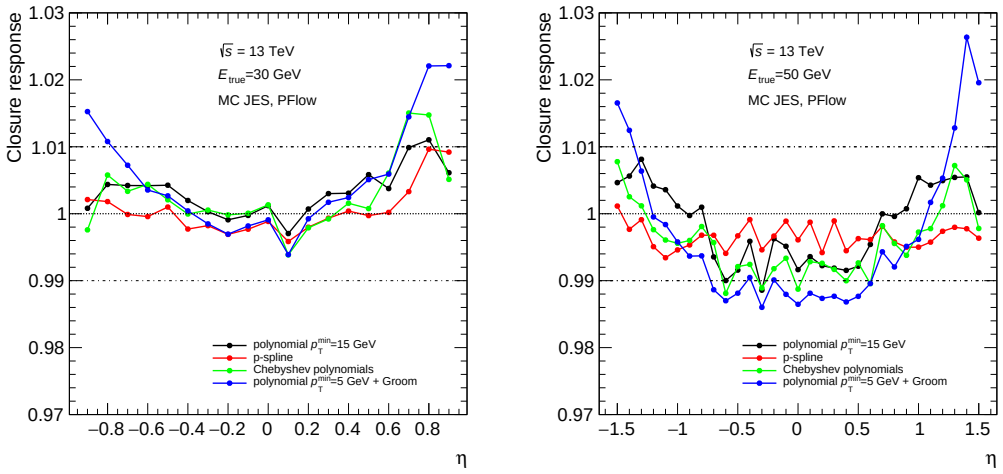

Figure 5.15: Comparison of different fitting techniques for the absolute MC JES calibration with 3D-pile-up calibrated small-R PFlow jets of the "NoPtCut" jet container at fixed energies values $E_{\text{true}} = 30\,\text{GeV}$ and $50\,\text{GeV}$. Shown are calibrations with polynomial fits fitted down to $p_{\text{T}} = 15\,\text{GeV}$ (black), the p-spline calibration (red), Chebyshev polynomial fits (green) and polynomial fit function fitted down to $p_{\text{T}} = 5\,\text{GeV}$ and combined with Groom's function in the forward region (blue). Horizontal dashed lines indicate the 1 % closure range, while the vertical dashed lines show the central detector region.

where p_{T}^{3D} is a correction derived in bins of N_{PV}, $\langle\mu\rangle$, η and $p_{\text{T}}^{\text{true}}$. The last term in Equation 5.21 contains the term Δp_{T} which initially has been used to move the jets back to the detector scale after correction for pile-up effects. However, it is observed that this Δp_{T}-shift produces a large amount of negative p_{T} jets, which cannot be correctly calibrated due to the multiplicative character of the MC JES method. So, the term is set to zero for now and will be re-evaluated in the future. This in turn has the implication that the pile-up calibration also partially corrects for the energy scale, thus the pile-up calibration and the MC JES calibration are no longer kept separate. In terms of the GSC, the sequential approach from the consolidated recommendations is aimed to be replaced with a neural network based GSC. As identified as calibration improvements in Section 5.2.4 and Section 5.2.3, the MC JES correction is performed using a p-spline to fit the jet energy response as a function of energy using the "NoPtCut" jet container and including jets with $p_{\text{T}} < 0\,\text{GeV}$. The calibration factors at high energies are set constant as a function of η at energies between 3 and 4 TeV. The η correction is performed with a polynomial function. The three basic calibration steps as described in Section 5.1.3 for a central η bin are shown in Figure 5.19. Calibration summary plots are shown Figure 5.18. The left plot in Figure 5.18 shows that, depending on the energy and η value, the response after the 3D pile-up residual calibration is already relatively close to one, in contrast to Figure 5.6, implying the new 3D residual pile-up calibration shifts the reco jet energy close to the truth jet energy. A good closure within 1 % for most of the energy and η bins is achieved after calibration with a non-closure in the forward region which is for the low energies a very extreme phase space. The closure and the closure quality plot indicate that, especially in the central detector region, a jet calibration down to p_{T} values of at least 15 GeV is possible.

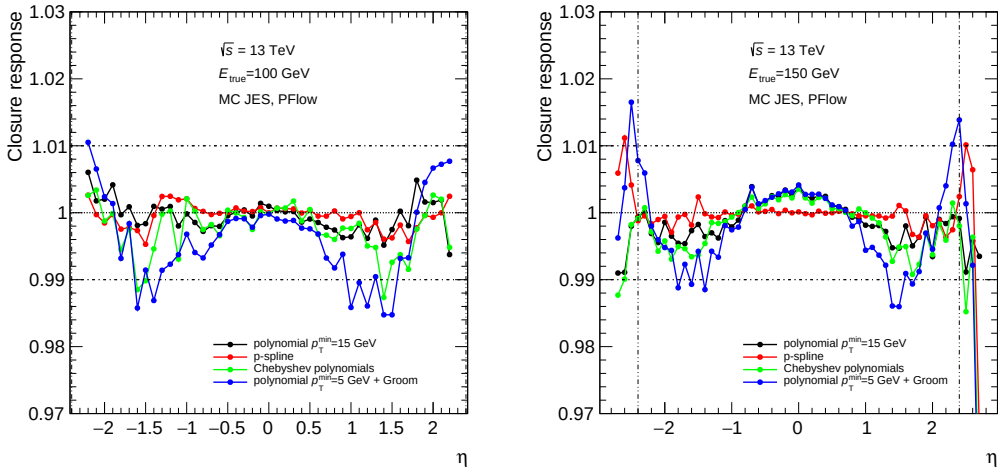

Figure 5.16: Comparison of different fitting techniques for the absolute MC JES calibration with 3D-pile-up calibrated small-R PFlow jets of the "NoPtCut" jet container at fixed energies values $E_{\text{true}} = 100\,\text{GeV}$ and $150\,\text{GeV}$. Shown are calibrations with polynomial fits fitted down to $p_{\text{T}} = 15\,\text{GeV}$ (black), the p-spline calibration (red), Chebyshev polynomial fits (green) and polynomial fit function fitted down to $p_{\text{T}} = 5\,\text{GeV}$ and combined with Groom's function in the forward region (blue). Horizontal dashed lines indicate the 1 % closure range, while the vertical dashed lines show the central detector region.

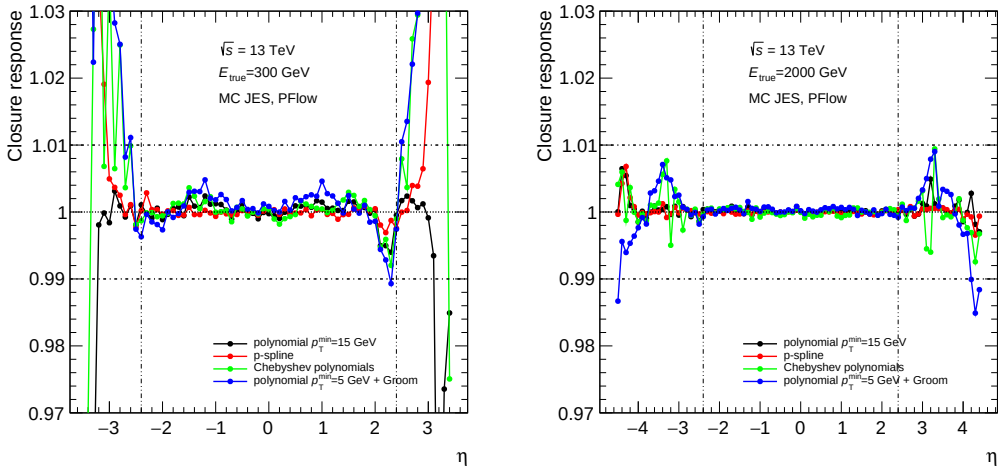

Figure 5.17: Comparison of different fitting techniques for the absolute MC JES calibration with 3D-pile-up calibrated small-R PFlow jets of the "NoPtCut" jet container at fixed energies values $E_{\text{true}} = 300\,\text{GeV}$ and $2000\,\text{GeV}$. Shown are calibrations with polynomial fits fitted down to $p_{\text{T}} = 15\,\text{GeV}$ (black), the p-spline calibration (red), Chebyshev polynomial fits (green) and polynomial fit function fitted down to $p_{\text{T}} = 5\,\text{GeV}$ and combined with Groom's function in the forward region (blue). Horizontal dashed lines indicate the 1 % closure range, while the vertical dashed lines show the central detector region.

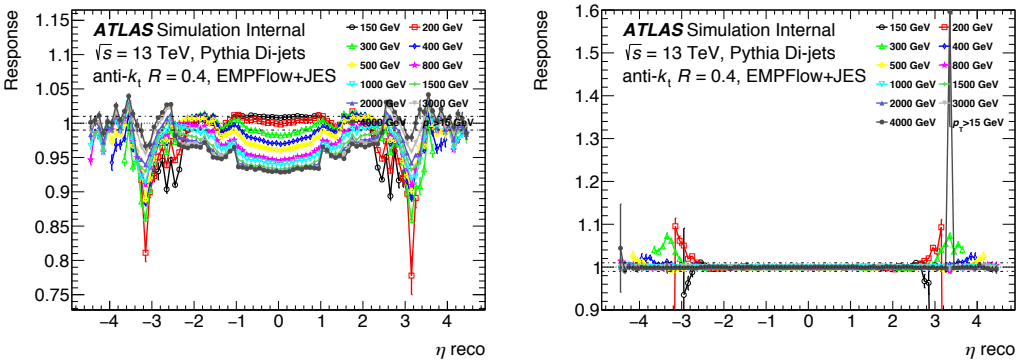

Figure 5.18: Jet response at fixed energies as a function of η before (left) and after (right) the MC JES calibration step. A very good closure within 1 % for most of the energy and η values is reached. The non-closure at $\eta \sim 3.1$ for $E = 4$ TeV is caused by statistical limitations in that phase space but corrected for with a calibration fractor freezing between 3 and 4 TeV.

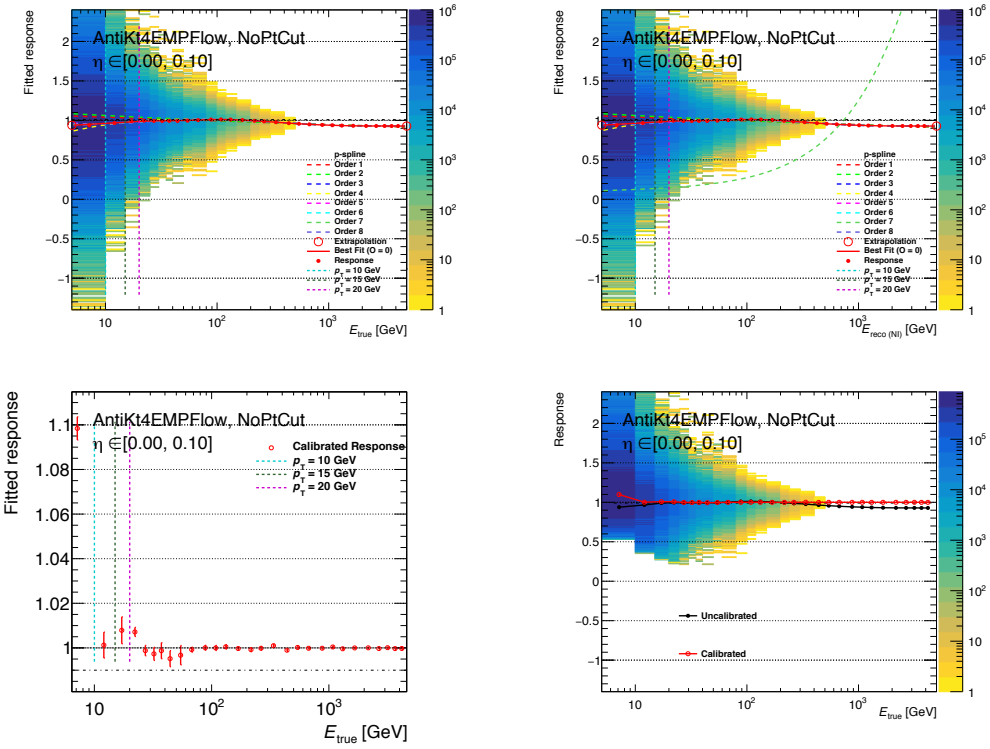

Figure 5.19: MC JES calibration for a central η bin. The top left figure shows the jet response against the true energy E_{true} for reconstructed jets. The top right plot shows the jet calibration as function of the numerical inversed energy. The two lower plots show the closure check with calibrated reconstructed jets. For the two plots on top, polynomial fits for the orders 1 to 8, corresponding to the old calibration strategy, are shown in addition to the used p-spline in red. While the filled red circles represent the response points in each energy bin, the empty red circles at the left and right edge of the p-spline represent the used extrapolation points. Since the x-axis is binned in energy, three vertical lines represent the p_{T} values of 10, 15 and 20 GeV to guide to eye.

CHAPTER 6

Analysis Strategy and Event Selection

6.1 Strategy

Although all Higgs boson measurements are compatible with SM expectations so far, it is still possible that uncertainties of measurements accommodate BSM physics. Many observations show that the SM describes only a small fraction of the total energy density of the Universe. Possible extensions of the SM predict the existence of new particles, with some of them matching the properties of dark matter. Higgs portal models further describe a coupling of the Higgs boson to dark matter candidates, see Section 2.2.3. If dark matter particle candidates have a sufficiently small mass m_χ, these particles may be produced in decays of the Higgs boson. The target of the analysis is the direct search for invisible Higgs boson decays or in absence of an observed signal excess over the background-only prediction to set an upper limit on the branching ratio of the Higgs boson's invisible decay modes $\mathcal{B}_{\text{inv}}$, defined by

$$\mathcal{B}_{\text{inv}} = \frac{\Gamma_{\text{inv}}}{\sum_j \Gamma_j}, \tag{6.1}$$

with the partial decay widths Γ_j and j runs over all possible partial decay widths. The SM predicts an invisible Higgs boson branching fraction of 0.12 % via the process

$$H \to ZZ \to 4\nu. \tag{6.2}$$

It is challenging to constrain the invisible decay modes of the Higgs boson experimentally using the total visible decay width measurements $\Gamma_{\text{H,tot}}$ of the Higgs boson since the SM prediction is $\Gamma_{\text{H,tot}} \sim 4.07\,\text{MeV}$, which is below the resolution of both the ATLAS and CMS detector. It should be noted that direct searches for invisible Higgs boson decays and indirect constraints on $\mathcal{B}_{\text{inv}}$ from global fits of measurements of visible Higgs boson decay channels are complementary. Global fits place indirect constraints on $\mathcal{B}_{\text{BSM}}$ which includes both invisible $\mathcal{B}_{\text{inv}}$ and undetected decays $\mathcal{B}_{\text{undet}}$. An excess in both direct and indirect searches would confirm a signal, while a non-zero branching fraction in indirect constraints without an signal excess in direct searches would indicate undetected decay channels $\mathcal{B}_{\text{undet}}$. The combined upper limit on $\mathcal{B}_{\text{inv}}$ from global fits to all Higgs boson couplings from ATLAS and CMS is 0.34 at 95 % confidence level [178, 179]. The strategy for a direct search for invisible Higgs boson decays as a search for new physics, such as dark matter candidates χ, is motivated by Higgs portal models with a proposed Higgs boson decay of

$$H \to \chi\chi, \tag{6.3}$$

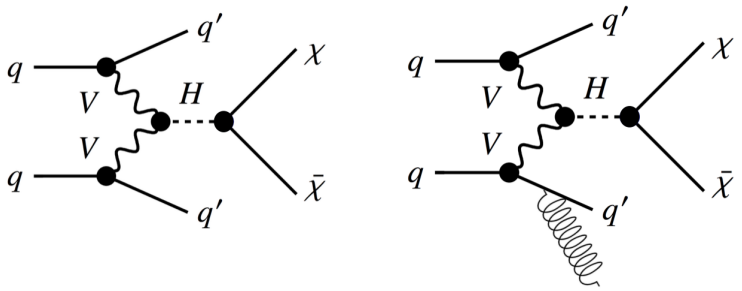

Figure 6.1: Representative Feynman diagrams of VBF Higgs boson production in the t-channel, where the Higgs boson subsequently decays to invisible dark matter candidates χ. Two outgoing partons q' form jets with a VBF signature. The vector bosons V can be Z or W bosons. The diagram on the right shows the emission of an additional jet (final state radiation). Similar diagrams are possible in the s- and u-channel, whereby s-channel diagrams and interferences are suppressed in the VBF phase space [180]. The figure on the left shows the additional emission of final state radiation.

with an invisible final state signature. To have objects to trigger on and to detect recoiling particles as $E_{\mathrm{T}}^{\mathrm{miss}}$, visible objects in addition to WIMP candidates χ need to be present in the channel sketched in Equation 6.3 such as initial state radiation (mono-jet search) or tagging jets from a VBF Higgs boson production (VBF+$E_{\mathrm{T}}^{\mathrm{miss}}$ search) resulting in a process

$$\underbrace{q\bar{q} \rightarrow H}_{\text{VBF}} \rightarrow \chi\bar{\chi} + 2 \text{ jets}. \tag{6.4}$$

Also a search for potential heavier or lighter mediators ξ than the Higgs boson for this process is performed, i.e.

$$\underbrace{q\bar{q} \rightarrow \xi}_{\text{VBF}} \rightarrow \chi\bar{\chi} + 2 \text{ jets}. \tag{6.5}$$

The ggF Higgs boson production cross section is much larger than that of VBF Higgs boson production in proton-proton collisions at the TeV scale. Nevertheless, the dark matter search presented in this analysis targets the VBF Higgs boson production channel for two reasons. First, the ggF process would need a boost by an additional gluon in the event, originating from initial state radiation, while VBF has a natural boost due to two recoiling jets. Second, searches for dark matter are more promising if the focus is on channels where the cross section of signal and background processes is in comparable order. In addition, the VBF signature allows for an efficient background suppression. Therefore, the VBF Higgs boson production is expected to be the most sensitive individual channel for a direct search for dark matter in invisible Higgs boson decays and is the primary signal process for the presented analysis. A Feynman diagram of the signal is shown in Figure 6.1. A second contribution to the proposed signal originates from gluon fusion Higgs boson production (ggF + 2 jets):

$$\underbrace{q\bar{q} \rightarrow H}_{\text{ggF}} \rightarrow \chi\bar{\chi} + 2 \text{ jets}. \tag{6.6}$$

This non-negligible contribution from ggF Higgs boson production is also treated as signal, where no interference between VBF and ggF Higgs boson production is considered. Further, VH and ttH Higgs boson production are treated as signal though the contribution is negligible. The main background processes are decays of weak gauge bosons $V = Z, W$ with final state neutrinos or unidentified leptons, multijet processes and with smaller contribution also diboson, single top and $t\bar{t}$ processes. The V+jets background is estimated with MC and constrained in CRs with identified leptons, the multijet background is estimated with a couple of independent data-driven techniques and the minor backgrounds are taken from simulation. The background modelling is described in more detail in Section 8.

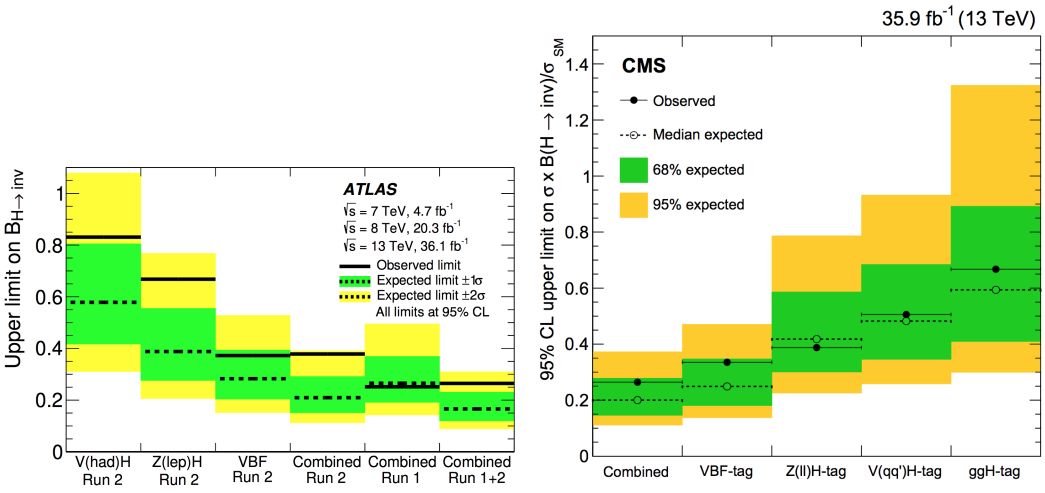

Figure 6.2: Limits on invisible Higgs boson branching fraction from ATLAS [183] and CMS [194].

Similar searches for dark matter have been performed in ATLAS, CMS and other experiments such as LEP [181] before. The ATLAS Run I analysis for an invisibly decaying Higgs boson produced in VBF used 20.3 fb^{-1} of $\sqrt{s} = 8\,\text{TeV}$ data and observed (expected) an upper limit of 0.28 (0.31) on $\mathcal{B}_{\text{inv}}$ of SM Higgs boson to invisible decays at 95 % confidence level [182]. The corresponding first Run II analysis [1] is based on 36 fb^{-1} data measured at $\sqrt{s} = 13\,\text{TeV}$ and thus benefited from higher luminosity and was affected by higher cross sections for both background and signal processes. The observed (expected) limit is 0.37 (0.28) at 95 % confidence level. The discrepancy between the observed and expected limit is still within the observed 1σ band of 0.20 and 0.39. However, the limit was not improved with respect to the Run I analysis. The overall sensitivity can be improved by a combination of the limits from multiple channels, such as the VBF, ggF and associated Higgs boson production with a Z boson or top quarks. As mentioned above, the VBF Higgs boson to invisible channel is the most sensitive one and is central part of the Higgs boson to invisible combination [183], as shown in Figure 6.2. A selection of limits on invisible Higgs boson decays in different production channels from CMS and ATLAS is presented in Table 6.1. Other recent dark matter searches are performed in the monophoton [184], single top [185], monojet [186] and diphoton final states [187]. Orthogonality of the individual searches is ensured for an easier statistical combination of the individual channels.

Table 6.1: Observed (expected) 95 % confidence level limits in % from a selection of earlier CMS and ATLAS invisible Higgs boson decay searches and corresponding combinations. Some of the presented limits only used a subset of the full data set from the corresponding run. Also the various channels and combinations from CMS and ATLAS include different decay modes of particles and thus cannot be directly compared.

Experiment	LHC Run	VH	ZH	$t\bar{t}H$	VBF	Combination
ATLAS	I	78 (86) [188]	75 (62) [189]		28 (31) [182]	25 (27) [178]
CMS	I		81 (83) [190]		65 (49) [190]	
ATLAS	early II	83 (58) [191]	67 (39) [191]		37 (28) [1]	26 (17) [183]
CMS	early II		40 (42) [192]	46 (48) [193]	33 (25) [194]	19 (15) [194]

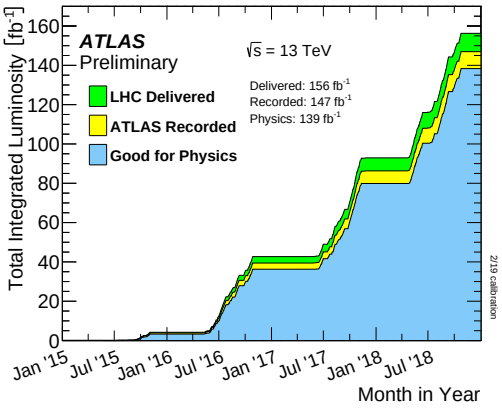

Figure 6.3: Luminosity of recorded data in ATLAS for the Run II period from 2015 to 2018.

6.2 Data and Simulation

6.2.1 Data sets and Triggers

The full Run II data set collected at $\sqrt{s} = 13$ TeV at the LHC is used. Data from Run I collected at $\sqrt{s} = 7$ and 8 TeV is not included. The ATLAS detector recorded 139 fb^{-1} of data between 2015 and 2018 with a data-taking efficiency of 94 % of which 95 % are good for physics analyses as illustrated in Figure 6.3 and Table 6.2. The total luminosity $\mathcal{L}$ is known with a precision of 1.7 % [124]. Events used in the analysis need to be in the good runs list (GRL), i.e. events in luminosity blocks with poor detector quality and events where different detector parts had operational problems are rejected.

The signal region data has been recorded with $E_{\mathrm{T}}^{\mathrm{miss}}$ triggers [195], listed in Table 6.3. The ATLAS $E_{\mathrm{T}}^{\mathrm{miss}}$ triggers are based on p_{T} imbalance determined from energy deposited in the calorimeter system only. The HLT thresholds were raised several times in the data-taking periods 2015 to 2018 to reduce the trigger rate since this rate increases typically exponentially with the number of pile-up collisions at fixed thresholds. The most stringent HLT threshold, used in the years 2017 and 2018 is $E_{\mathrm{T}}^{\mathrm{miss}} = 110$ GeV, while 2015 and 2016 operated at thresholds of $E_{\mathrm{T}}^{\mathrm{miss}} = 70$ GeV and $E_{\mathrm{T}}^{\mathrm{miss}} = 90$ GeV, respectively. In 2015 and 2016, also a HLT single jet trigger with a threshold of 400 GeV was used to include events that should have passed the L1 $E_{\mathrm{T}}^{\mathrm{miss}}$ trigger but failed due to a firmware bug. The $E_{\mathrm{T}}^{\mathrm{miss}}$ triggers are only fully efficient for $E_{\mathrm{T}}^{\mathrm{miss}} > 200$ GeV as shown in Figure 6.4. $E_{\mathrm{T}}^{\mathrm{miss}}$ trigger scale factors t_s as function of the offline $E_{\mathrm{T}}^{\mathrm{miss}}$ are applied when the turn-on curves in simulation and data do not match and are derived for each data-taking period separately. The scale factors are defined as the ratio of the data and the MC efficiency and are fitted with a functional form of

$$t_s = \frac{1}{2}\left(1 + \mathrm{erf}\left(\frac{x - p_0}{\sqrt{2}p_1}\right)\right), \tag{6.7}$$

with fit parameters p_i, x is the $E_{\mathrm{T}}^{\mathrm{miss}}$ value and erf is the error function. The scale factors t_s are measured with a tag and probe technique in control regions with a looser selection as applied in the signal region. For this, $Z \to \mu\mu$ and $W \to \mu\nu$ events are used and the difference in scale factors of those events is used as a systematic uncertainty.

In control regions for V+jets backgrounds, the lowest unprescaled single and dilepton triggers are used as summarised in Table 6.4 [197, 198]. For single leptons, the triggers thresholds range from 20 to 26 GeV for the tightest lepton identification operating point. For dilepton triggers, the thresholds are lower with a looser lepton

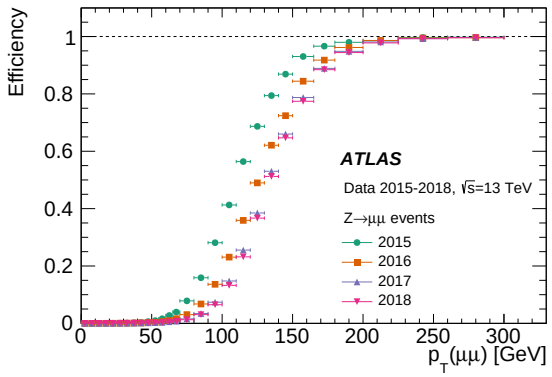

Figure 6.4: Combined L1 and HLT efficiency for the lowest unprescaled $E_{\mathrm{T}}^{\mathrm{miss}}$ triggers for the data-taking periods 2015 to 2018 measured in a $Z \rightarrow \mu\mu$ selection, in which muons are treated as invisible objects and thus represents $E_{\mathrm{T}}^{\mathrm{miss}}$, as function of Z boson p_{T} [196].

identification requirement. The single lepton triggers are "or"-ed with the dilepton triggers. The offline leptons are required to match the online trigger items, and trigger scale factors and their uncertainties are applied. In the muon control regions, also the $E_{\mathrm{T}}^{\mathrm{miss}}$ triggers have been used to recover additional muon efficiency since muons are mostly invisible in the calorimeter and are treated in the $E_{\mathrm{T}}^{\mathrm{miss}}$ trigger calculations of the p_{T} imbalance similar to neutrinos. Using the same $E_{\mathrm{T}}^{\mathrm{miss}}$ triggers for the muon control region and the signal region reduces the impact of systematic uncertainties in the trigger turn-on curve. For events fulfilling only the lepton triggers, the muon trigger scale factors are used, while for events passing the $E_{\mathrm{T}}^{\mathrm{miss}}$ trigger the SR $E_{\mathrm{T}}^{\mathrm{miss}}$ trigger scaling factors are applied.

The multijet background from RnS relies on inclusive data recorded with a set of single jet HLT triggers with p_{T} thresholds ranging from 15 to 400 GeV. This data is unprescaled to obtain a smooth p_{T} spectrum following the description in Section 7.2.2.

To avoid a bias of the analysers, the majority of the recorded data was blinded in signal enriched regions during the analysis phase. No region with a signal to background ratio larger than 20 % other than the SR already used for the 36 fb^{-1} analysis [1] was unblinded until the analysis strategy was freezed and the unblinding approved by the ATLAS collaboration.

Table 6.2: Run II data-taking year, corresponding MC simulation campaign, delivered luminosity $\mathcal{L}$ in ATLAS and average as well as peak number of bunch average crossings $\langle\mu\rangle$.

Period	MC campaign	$\mathcal{L}$ [fb^{-1}]	Average $\langle\mu\rangle$	Peak $\langle\mu\rangle$
2015	mc16a	3.2	13.4	15
2016	mc16a	32.9	25.1	45
2017	mc16d	43.9	37.8	80
2018	mc16e	60.1	36.1	60
2015-2018	mc16ade	139.1	33.8	80

6.2.2 Monte Carlo Simulation

The analysis relies on the comparison of observational data with SM or BSM expectations, which allows for testing different signal hypotheses. The generation of physics events at the LHC can be carried out using MC simulation techniques in which the interactions between the partons within a proton-proton collision are

Table 6.3: $E_{\mathrm{T}}^{\mathrm{miss}}$ triggers used for the Run II data-taking in 2015 to 2018. The years and run numbers in which HLT thresholds changed are listed.

Period	$E_{\mathrm{T}}^{\mathrm{miss}}$ trigger
all 2015	HLT_xe70_mht
2016, runs ≤ 302872	HLT_xe90_mht_L1XE50
2016, runs > 302872	HLT_xe110_mht_L1XE50
2015–2016	HLT_noalg_J400
2017 runs	HLT_xe110_pufit_L1XE55
2018 runs	HLT_xe110_xe70_L1XE50

Table 6.4: List of single lepton (top) and dilepton triggers (bottom) used to select events for the lepton CRs.

Period	e trigger	μ trigger
all 2015	HLT_e24_lhmedium_L1EM20VH HLT_e60_lhmedium HLT_e120_lhloose	HLT_mu20_iloose_L1MU15 HLT_mu50
2016 runs ≤ 304008	HLT_e24_lhtight_nod0_ivarloose HLT_e60_lhmedium_nod0 HLT_e140_lhloose_nod0	HLT_mu50 HLT_mu26_ivarmedium
2016 runs > 304008	HLT_e26_lhtight_nod0_ivarloose HLT_e60_lhmedium_nod0 HLT_e140_lhloose_nod0	HLT_mu50 HLT_mu26_ivarmedium
2017 runs	HLT_e26_lhtight_nod0_ivarloose HLT_e60_lhmedium_nod0 HLT_e140_lhloose_nod0 HLT_e300_etcut	HLT_mu26_ivarmedium HLT_mu50 HLT_mu60_0eta105_msonly
2018 runs	HLT_e26_lhtight_nod0_ivarloose HLT_e26_lhtight_nod0 HLT_e60_lhmedium_nod0 HLT_e140_lhloose_nod0 HLT_e300_etcut	HLT_mu26_ivarmedium HLT_mu50 HLT_mu60_0eta105_msonly
2015	HLT_2e12_lhloose_L12EM10VH	HLT_mu18_mu8noL1
2016	HLT_2e17_lhvloose_nod0	HLT_mu22_mu8noL1
2017	HLT_2e24_lhvloose_nod0	HLT_mu22_mu8noL1
2018	HLT_2e17_lhvloose_nod0_L12EM15VHI	HLT_mu22_mu8noL1

simulated, i.e. the matrix elements (MEs) $\mathcal{M}$ of the hard-scatter process are computed under consideration of the proton substructure described by PDFs usually implemented via the "Les Houches Accord PDF Interface" (LHAPDF) library [199]. In addition, the QCD or QED parton showering, underlying event, hadronisation and hadron decays are simulated as sketched in Figure 6.5.

The detector simulation GEANT4 [201] calculates the interaction of the particles with the detector. General purpose event generators can be used to combine the simulation of the hard process, the parton shower and other effects. Also effects of close-by bunch crossings, cavern background or pile-up are considered in simulation via the injection of additional events within the same bunch-crossing. The pile-up contribution is overlaid using minimum bias events onto the hard-scatter event based on a Poisson distribution around a fixed mean number of additional proton-proton interactions per bunch crossing $\langle\mu\rangle$. Since this in general differs from the data distribution, a pile-up reweighting is performed for all MC samples to account for that difference by deriving correction factors from data and simulation parametrised in $\langle\mu\rangle$. MC simulations including experimental effects are termed to be at reconstruction (reco) level. Event generation excluding experimental effects and the detector simulation are referred to be at truth-level, which for example also include parton-information. The size of the generated MC sample of a process with cross section σ is weighted corresponding to the integrated luminosity

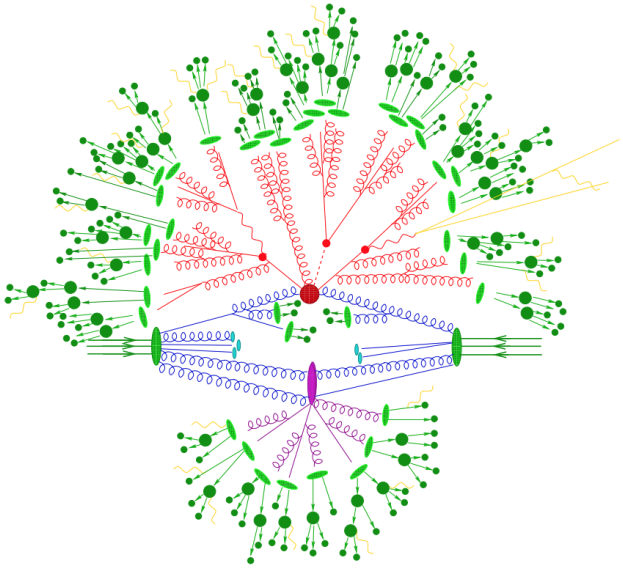

Figure 6.5: Sketch of a typical simulation of a hard proton-proton collision (red blob), secondary hard-scatter event (purple blob), parton shower (red and purple tree structure around blobs), hadronisation process (green blob) and hadron decays (dark green blobs and arrows) [200].

$\mathcal{L}$ of the recorded data using Equation 3.11 and thus the event weights w are calculated according to

$$w = \frac{\sigma \cdot w_{\text{MC}} \cdot \epsilon \cdot k \cdot w_{\text{event}} \cdot \mathcal{L}}{N}, \tag{6.8}$$

where σ is the cross section calculated by the MC generator, w_{MC} is an internal event weight of the generator (e.g. if events are generated in p_{T}-slices), ϵ is the filter efficiency of the generator, k is a factor considering higher-order corrections which are not considered in the event generation, w_{event} includes experimental effects such as pile-up reweighting factors or trigger efficiencies, $\mathcal{L}$ is the integrated luminosity and N the number of generated events (sum of weights w_{MC}).

Important systematic uncertainties originate from the limited precision of MC simulation caused by fixed scale choices in the event generation, such as the renormalisation or factorisation scales, limited order of perturbative calculations (higher-order corrections) or the modelling of the initial-state PDF and the parton shower following the hard-scatter process.

The signal and background processes for the presented analysis are simulated with various MC event generators and with different precision as summarised in Table 6.5 and described in the following:

- The Higgs boson signal is simulated with SM $H \rightarrow 4\nu$ processes, where a 100 % branching ratio into this final state is assumed. VBF Higgs boson production is generated at next-to-leading order (NLO) with Powheg [202], interfaced with Pythia8 [172] for parton shower with the PDF4LHC15 PDF set [203] and the AZNLO tune. The MC prediction is normalised to an approximate-NNLO QCD cross section with NLO EWK corrections. Additional VBF samples with modified Higgs boson masses m_H are generated. NLO EWK corrections $\alpha^{\text{HAWK}}_{\text{NLO EWK}}$ to SM VBF Higgs boson production are derived separately with Hawk [204] and are parametrised as $\alpha^{\text{HAWK}}_{\text{NLO EWK}} = -3.5 \cdot 10^{-4}\,\text{GeV}^{-1}\, p_{\text{T}}^{\text{Higgs}} - 0.043$ with the Higgs boson transverse momentum $p_{\text{T}}^{\text{Higgs}}$. Higgs boson production via gluon fusion is simulated at NNLO in QCD using Powheg NNLOPS and the PDF4LHC15 next-to-NLO (NNLO) PDF set as well as the AZNLO tune of Pythia8 is used. The ggF prediction from MC is normalized to the next-to-NNLO

(NNNLO) cross section in QCD plus EWK corrections at NLO. VH production is simulated at NLO in QCD using the PowHegBox v2 generator with the PDF4LHC15 PDF set Some CRs are affected by VBF $H \rightarrow WW$ production, which is modeled with the same set of generators.

- Important backgrounds are V/VV+jets processes. The processes are split into QCD and EWK components, based on the order in the EWK coupling constant α_{EWK}, which is α^2_{EWK} in the former and α^4_{EWK} in the latter case. The EWK component is further divided into semileptonic diboson diagrams where the final-state jets originate from the decay of one of the two V bosons and VBF events, which contain only one V and the jets originate from the incoming quarks. Interference terms in the order α^3_{EWK} are negligible. These configurations are used for both the QCD and EWK production of single boson V+jets [205] and diboson VV+jets [206], which are produced with Sherpa [207] with the `NNPDF3.0nnlo` PDF set [208]. The QCD production of V+jets is performed at NLO for up to two jets and at LO for up to four jets calculated with the Comix [209] and OpenLoops libraries [210, 211] and the MEPS@NLO prescription for parton shower matching. The samples are normalised to an inclusive NNLO cross section calculation. The QCD V+jets samples are filtered in m_{jj} at ME level using the k_t algorithm [212] as jet criterion for the ME to the parton shower matching to enhance the statistics in the SR at high m_{jj}. EWK VBF production of V+jets is performed at LO in Sherpa and for technical reasons reweighted to NLO according to Herwig samples [213]. The Z+jets events are weighted as function of m_{jj}, such that the ratio of the QCD W+jets and Z+jets cross sections matches a dedicated NLO QCD and NLO EWK calculation in a VBF phase space as detailed in Section 8.1.3. VV processes are simulated at NLO in QCD for zero or one additional partons and at LO and at most three extra partons. Loop-induced diboson production is generated at LO for up to one additional parton. Compared to previous analysis iterations, the V+jets sample size was significantly increased and the impact of MC statistical uncertainties reduced by factor of ~ 2.
- Events from multijet processes are generated with Pythia 8.230 at LO for dijet production interfaced to a p_{T} ordered parton shower. The `NNPDF2.3lo` PDF set is used for the hard-scattering, the shower and the multiparton interaction simulation. The Atlas 2014 set of parameters (A14 tune) is used [173]. Since QCD dijet production has a steeply falling cross section, the generation is filtered in leading jet p_{T}.
- Other backgrounds, namely $t\bar{t}$, tW and single-top production, are generated with PowHegBox at NLO with the `NNPDF3.0nlo` PDF set, interfaced to Pythia 8.230 for the parton shower, hadronisation and underlying event using the A14 tune [214].

6.3 Object and Event Selection

Three types of regions are used in the analysis, defined as:

- signal regions (SRs), which are regions enriched by signal events, while background processes are heavily suppressed
- control regions (CRs), regions which are dominated by background processes with minor contribution of signal events. CR are usually used to optimise or normalise the background processes
- roughly signal-free validation regions (VRs) used to validate the background estimation and the extrapolation from CRs to SRs.

The definition of the SRs, based on an optimised cut-based event selection [215–219], and the binning scheme is presented in this section.

First, the object definition and preselection is presented, followed by the SR event selection and categorisation. The definition of CRs and VRs is described in context of the background estimation strategy in Chapter 8. A selection requirement is in the following termed as a “cut”.

Table 6.5: Summary of MC event generators used for the simulation of different background and signal processes.

Process	Generator	ME Order	PDF	Parton Shower	Tune
ggF	Powheg NNLOPS	NNLO	PDF4LHC15 NNLO	Pythia8	AZNLO
VBF	Powheg	NLO	PDF4LHC15	Pythia8	AZNLO
VH	PowhegBox v2	NLO	PDF4LHC15	Pythia8	AZNLO
QCD V+jets	Sherpa v2.2.1, Sherpa v2.2.7 (m_{jj}-filtered)	NLO (up to 2-jets), LO (up to 4-jets)	NNPDF3.0nnlo	Sherpa MEPS@NLO	Sherpa
EWK V+jets	Herwig 7.2.1	NLO	MMHT2014NLO	Herwig angular-order	Herwig 7.2
VV+jets (including $gg \to VV$+jets)	Sherpa v2.2.1 or Sherpa v2.2.2	NLO (up to 1-jet), LO (up to 3-jets)	NNPDF3.0nnlo	Sherpa MEPS@NLO	Sherpa
EWK VV+jets	Sherpa v2.2.1 or Sherpa v2.2.2	LO	NNPDF3.0nnlo	Sherpa MEPS@LO	Sherpa
V+jets α^3_{EWK} interference	MadGraph5_aMC@NLO	LO	PDF4LHC15	Pythia8	
$t\bar{t}$	PowhegBox v2	NLO	NNPDF3.0nlo	Pythia8	A14
multijet	Pythia 8.230	LO	NNPDF2.3lo	Pythia8	A14

6.3.1 Object Definition and Preselection

The jets are PFlow objects reconstructed with the anti-k_t algorithm with a radius parameter of $R = 0.4$ (small-R), calibrated with the Atlas calibration chain correcting for pile-up and detector effects as well as data and simulation differences. Jets are reconstructed for $p_{\text{T}} > 20\,\text{GeV}$ as well as $|\eta| < 4.5$, while jets used in the SR and CRs need to fulfil $p_{\text{T}} > 25\,\text{GeV}$. For jets with $|\eta| < 2.5$ and $p_{\text{T}} < 60\,\text{GeV}$ a pile-up jet removal based on tracking and vertexing is performed using the JVT likelihood discriminator [162], which is described in more detail in Section 7.6. A medium JVT working point of 0.2 corresponding to hard-scatter jet efficiency of $\sim 98\,\%$ is used. The loose $E_{\text{T}}^{\text{miss}}$ working point as described in Section 4.8 is used. A jet cleaning is performed to remove jets from non-collision backgrounds (e.g. via noisy calorimeter cells, cosmic muons or beam-halo proton interactions) based on calorimeter signal quality, shape observables of the energy deposits and track properties based on the charged energy faction [220, 221]. Events with a jet failing these requirements are removed. Since the sensitivity of the analysis is based on at least two jets in the final state, a tight jet cleaning working point is used with a high beam-induced background rejection. The lepton and photon definitions are given in Table 6.6, following the description in Chapter 4.

No baseline leptons l or photons γ are expected in the final state in the SR. The lepton veto effectively suppresses the V+jets backgrounds. Since no isolation requirements are applied to the leptons fulfiling the loose identification working point, the lepton veto is also sensitive to non-prompt leptons from heavy-flavour decays which are eventually a sign of EWK processes with neutrinos. No explicit veto on τ leptons is used since a central third jet veto (TJV) removes most central hadronically-decaying τ leptons and leptonically decaying τ leptons are rejected with lepton vetoes. The photon veto is placed to ensure orthogonality of this search with the separate VBF Higgs boson to invisible + γ search [222]. Also events with more than four hard-scatter jets and more than one reconstructed b-jet with $p_{\text{T}} > 25\,\text{GeV}$ are removed to reject $t\bar{t}$ processes and to ensure orthogonality to the $t\bar{t} + E_{\text{T}}^{\text{miss}}$ analysis [223] for future combinations. Further, a primary vertex with at least two associated tracks needs to be present in the event.

The identification and reconstruction of particles and jets are independent of one another. Therefore, a

Table 6.6: Lepton and photon definitions used in the analysis. Shown are the object identification working points (ID WP), the transverse momentum p_T, pseudorapidity range $|\eta|$, the isolation requirements and longitudinal as well as transverse impact parameters. For the leptons also barrel-endcap ECal transition regions are considered, which are excluded for photons. The baseline objects are used to veto against them in signal regions, while signal leptons are used for dedicated control regions with identified leptons from a leptonic Z or W boson decay. Electron and muons fakes, predominantly from jets, are also used in the Z and W control selections.

Object		ID WP	p_T [GeV]	$\|\eta\|$	Isolation	$\|z_0 \sin(\theta)\|$ [mm]	$\|d_0\|/\sigma(d_0)$
baseline e		loose	> 4.5	< 2.47	-	-	-
signal e	W	tight	> 30				
	Z	loose	> 4.5	< 2.47	FCTightTrackOnly	< 0.5	< 5
fake e	W	loose but not tight	> 30				
baseline μ		very loose	> 4	< 2.7	-	-	-
signal μ	W	medium	> 30	< 2.7			
	Z	medium	> 7	< 2.5	FCHighPtCaloOnly	< 0.5	< 3
fake μ	W	loose but not medium	> 30	< 2.7			
γ		loose	> 15	< 2.37	FixedCutTight	-	-

geometrical overlap removal is performed to avoid double-counting of energy measured in the detector but associated to different objects. The overlap removal is based on the angular separation of objects in y-ϕ-space $\Delta R_{y,\phi}$. For the lepton-jet overlap removal, the $\Delta R_{y,\phi}$ threshold depends on the lepton p_T since boosted objects tend to be collimated. The overlap removal is summarised in Table 6.7.

Table 6.7: Summary of the overlap removal between two objects with the corresponding matching criteria. The objects are (baseline) electrons e, muons μ, photons γ and jets.

Removed	Kept	Matching condition
e	e	shared ID track, e with lower p_T removed
μ	e	μ with calorimeter deposits and shared ID track
e	μ	shared ID track
γ	e	$\Delta R_{y,\phi} < 0.4$
γ	μ	$\Delta R_{y,\phi} < 0.4$
jet	e	$\Delta R_{y,\phi} < 0.2$
e	jet	$\Delta R_{y,\phi} < \min(0.4, 0.04 + 10\,\text{GeV}/p_T^e)$
jet	μ	number of tracks < 3 and $\Delta R_{y,\phi} < 0.2$
μ	jet	$\Delta R_{y,\phi} < \min(0.4, 0.04 + 10\,\text{GeV}/p_T^\mu)$
jet	γ	$\Delta R_{y,\phi} < 0.4$

6.3.2 Event Selection

The event selection is optimised with multivariate techniques to maximise the signal sensitivity, which is a trade-off between maximising the signal efficiency and effectively rejecting background processes. The target signal process for this search is an invisibly decaying Higgs boson which is produced in proton-proton collisions in VBF. Based on this, the core of the SR event selection are two jets originating from a VBF Higgs boson production plus a large amount of E_T^{miss}. A typical candidate for a SR event is shown in Figure 6.6.

Main ingredients of the SR selection are E_T^{miss}, $\Delta\phi_{jj}$, m_{jj} and the jet multiplicity n_{jet}. The lower E_T^{miss} threshold is 160 GeV to select events at the E_T^{miss} trigger efficiency turn-on plateau as well as to suppress contributions from multijet processes which accumulate at lower E_T^{miss} values. In fact, the majority of the SR is defined for $E_T^{miss} > 200$ GeV. In addition, to select Higgs boson events produced in VBF and to suppress multijet contamination, selection criteria on the invariant mass of the leading dijet system, $m_{jj} > 800$ GeV, and the jet separation of the two leading jets in η, $\Delta\eta_{jj} > 3.8$, are applied. Selection cuts on $\Delta\eta_{jj}$ and m_{jj} are further

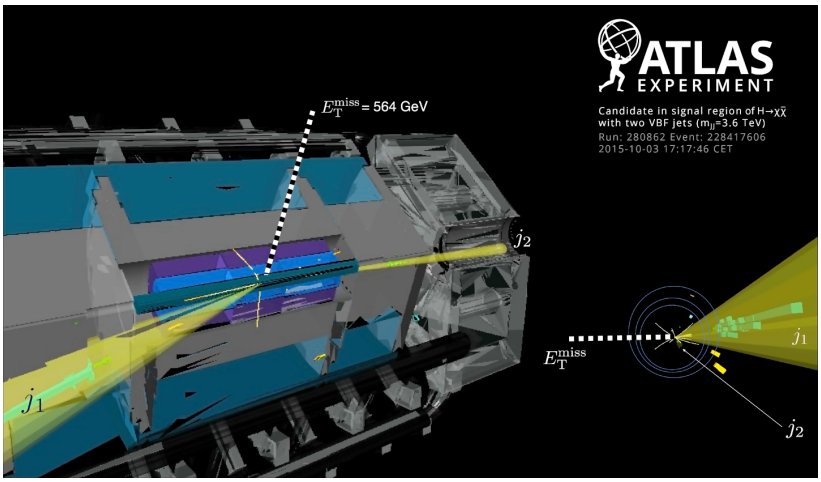

Figure 6.6: Candidate event recorded in 2015 in ATLAS for a Higgs boson produced via VBF and decaying into invisible dark matter candidates giving an experimental signature of two jets (yellow cones) with $m_{jj} = 3.6\,\text{TeV}$ and $E_T^{miss} = 564\,\text{GeV}$ (dashed line). [224].

separating between V+jets backgrounds and signal processes. Multijet events with a typical back-to-back topology in the transverse plane can be further suppressed by cutting on the dijet separation in the azimuthal direction with $\Delta\phi_{jj} < 2$. One of the most efficient discriminants between signal processes and the multijet background is a veto on additional hard-scatter jet activity. An optimisation procedure showed that the lowest possible p_T threshold of 25 GeV is most efficient in rejecting background events with a small loss in signal efficiency. The jets are expected in different hemispheres of the detector and to be high-energetic. The jet momentum selection requirements for the leading and subleading jet are $p_{T,1} > 80\,\text{GeV}$ and $p_{T,2} > 50\,\text{GeV}$, respectively. The requirement $\eta_1 \cdot \eta_2 < 0$ achieves that the two leading jets are in different detector hemispheres as expected for VBF topologies. A cut on the soft E_T^{miss} term is applied. The soft E_T^{miss} term consists of all tracks associated to the PV_0 which are not associated to any hard object. Therefore, it is sensitive to extra leptons or central charged activity. While EWK signal processes do not have any color flow and thus small QCD radiation between the two leading jets, strong processes have large QCD radiation. A E_T^{soft} requirement ensures that central charged activity is small. A cut $E_T^{soft} < 20\,\text{GeV}$ rejects roughly 10 % background for 1 % signal. It also rejects $W \to \mu\nu$ events in which the muon μ is not identified but a track was found. Further, it removes events from QCD V+jets production, where a jet is low in p_T so that it is associated with the soft E_T^{miss} term. To remove highly mis-measured multijet events where fake E_T^{miss} is produced by a failed pile-up tagging, a E_T^{miss} dependent cut on the missing hadronic activity H_T^{miss} is applied, defined by

$$H_T^{miss} > \begin{cases} 180\,\text{GeV}, & \text{if } E_T^{miss} > 200\,\text{GeV} \\ 140\,\text{GeV}, & \text{if } E_T^{miss} \in [160, 200]\,\text{GeV} \end{cases}. \tag{6.9}$$

The two leading forward jets are tagged as pile-up if fJVT < 0.5 (loose working point) if $E_T^{miss} > 200\,\text{GeV}$ and fJVT < 0.2 (very tight working point) if $E_T^{miss} \in [160, 200]\,\text{GeV}$. i.e.:

$$\text{fJVT} < \begin{cases} 0.5, & \text{if } E_T^{miss} > 200\,\text{GeV} \\ 0.2, & \text{if } E_T^{miss} \in [160, 200]\,\text{GeV} \end{cases}. \tag{6.10}$$

The fJVT cut is applied for $20 < p_T < 120\,\text{GeV}$ and $|\eta| > 2.4$. The hard-scatter efficiency of forward jet vertex tagging is 93 % for jets with $p_T > 50\,\text{GeV}$, while rejecting 58 % of the pile-up jets. Applying the fJVT cut to all jets would result in the production of fake E_T^{miss} due to the wrong removal of hard-scatter jets. Although

PFlow jets are used, the fJVT score is copied from the corresponding EMTopo jet (since there was no ATLAS recommendation for PFlow fJVT at time of analysis fixing). Also a cut on the jet timing t_{jet} with $|t_{\text{jet}}| < 11$ ns is applied, where the jet timing is defined as the energy-weighted average of the timing of the constituent clusters. The jet timing threshold allows for suppressing stochastic pile-up jets, which have significantly wider jet timing distribution due to their mostly out-of-time pile-up origin.

In principle, only dijet events are expected in the SR, where the two tagging jets originate from the VBF Higgs boson production. A third jet veto rejects events where any additional central hard-scatter jet or any additional forward jet with $p_{\text{T},3} > 25\,\text{GeV}$ is present, which effectively suppresses multijet, V+jets and $t\bar{t}$ backgrounds. Nevertheless, to account for initial state radiation (ISR) or final state radiation (FSR), which is mostly soft bremsstrahlung in form of gluons, SR bins with exactly three and four hard-scatter jets in the final state are added to improve the overall signal sensitivity by help of the additional statistics. The identification of events with additional jets from ISR or FSR relies on centrality C_j and the comparison of the relative invariant mass of different jet subsystems. QCD gives a description of the colour flow from the initial state particles towards the final state particles. Colour charge is a conserved quantity in QCD and thus the final state radiation structure depends on the colour flow between the involved particles. In EWK VBF Higgs boson production, no colour flow between the two leading jets is expected, i.e. no additional radiation in the central pseudorapidity range. A variable quantifying how central an additional third or fourth jet j is relative to the two leading jets is centrality C_j, defined by

$$C_j = \exp\left(-\frac{4}{(\eta_1 - \eta_2)^2} \cdot \left(\eta_j - \frac{\eta_1 + \eta_2}{2}\right)^2\right). \tag{6.11}$$

If the additional jet is exactly between the tagging jets, i.e. $\eta_j = (\eta_1 + \eta_2)/2$, then $C_j = 1$. If the additional jet is aligned with one of the jets in η, then $C_j \to 1/e$. If the additional jet is more forward than the tagging jets ($\eta_j \to \infty$), then $C_j \to 0$. An upper threshold on centrality of 0.6 is chosen to reject strong V+jets backgrounds, i.e. $C_{j=\{3,4\}} < 0.6$. To further select events with additional jets stemming from FSR of the tagging jets, the invariant mass of the jet system consisting of the additional jet $i = 3, 4$ and either the leading or the subleading jet should be small compared to the dijet invariant mass m_{jj}. This is expressed in the variable

$$m_{\text{rel},i} = \frac{\min\{m_{1i}, m_{2i}\}}{m_{\text{jj}}} \tag{6.12}$$

where m_{1i} and m_{2i} are the invariant mass of the dijet system of the leading jet and the additional jet and the subleading jet and the additional jet, respectively. Low invariant masses indicate that the additional jet is roughly aligned with one of the leading jets and thus more likely from FSR. It is required that the relative invariant masses fulfil $m_{\text{rel},i=\{3,4\}} < 0.05$.

The minimal SR selection criteria are summarised in Table 6.8. To improve the signal sensitivity, the SR selection is split into 16 orthogonal subregions with an optimised binning scheme, described in Section 6.3.3. Based on these SR selection requirements, the VBF (ggF) SM Higgs boson signal selection efficiency is $\sim 1\,\%$ ($\sim 0.01\,\%$). The ggF Higgs boson production contributes $\sim 14\,\%$ of the total signal. Compared to the previous analysis iteration $\sim 50\,\%$ more signal events on the same data set are selected.

6.3.3 Binning Scheme

The SR is categorised into several sub-regions (bins) to account for the dependence of the signal strength on certain observables. To maximise the signal sensitivity, the SR is binned in four observables: n_{jet}, $\Delta\phi_{\text{jj}}$, m_{jj} and $E_{\text{T}}^{\text{miss}}$, leading to 16 SR bins in total:

- For $E_{\text{T}}^{\text{miss}} > 200\,\text{GeV}$, the SR is sliced in five bins in m_{jj}, defined by $[0.8, 1.0, 1.5, 2.0, 3.5, \infty)\,\text{TeV}$. On top, a splitting in $\Delta\phi_{\text{jj}}$ is done in two bins: $\Delta\phi_{\text{jj}} < 1$ and $1 \leq \Delta\phi_{\text{jj}} < 2$, giving 10 bins in total for $n_{\text{jet}} = 2$

Table 6.8: Minimal SR selection. Additional tighter selection requirements are applied in different SR bins.

Quantity	Cut	Description
jets	PFlow + anti-k_t ($R = 0.4$)	jet definition
JVT	> 0.2	hard-scatter jet identification, tight WP
$E_{\mathrm{T}}^{\mathrm{miss}}$	$> 160\,\mathrm{GeV}$	missing transverse momentum (loose)
$E_{\mathrm{T}}^{\mathrm{soft}}$	$< 20\,\mathrm{GeV}$	soft track $E_{\mathrm{T}}^{\mathrm{miss}}$ term
m_{jj}	$> 0.8\,\mathrm{TeV}$	invariant mass of leading dijet system
$\Delta\phi_{\mathrm{jj}}$	< 2	dijet separation in ϕ
$\Delta\eta_{\mathrm{jj}}$	> 3.8	dijet separation in η
$H_{\mathrm{T}}^{\mathrm{miss}}$	$> 140\,\mathrm{GeV}$	missing hadronic momentum (no JVT)
$p_{\mathrm{T},1}$	$> 80\,\mathrm{GeV}$	leading jet p_{T}
$p_{\mathrm{T},2}$	$> 50\,\mathrm{GeV}$	subleading jet p_{T}
$\mathrm{fJVT}_{1,2}$	< 0.5	forward JVT score of leading two jets
$\lvert t_{\mathrm{jet}}\rvert$	$< 11\,\mathrm{ns}$	jet timing
n_{jet}	$\in \{2, 3, 4\}$	number of hard-scatter jets with $p_{\mathrm{T}} > 25\,\mathrm{GeV}$ in final state
n_{l}	$= 0$	lepton veto (baseline)
n_{γ}	$= 0$	photon veto (baseline)
$n_{b-\mathrm{jet}}$	< 2	number of b-jets with $p_{\mathrm{T}} > 25\,\mathrm{GeV}$ (MV2C10 77 % WP)
C_{j}	< 0.6	centrality for $n_{\mathrm{jet}} \in \{3, 4\}$
$m_{\mathrm{rel},j}$	< 0.05	maximum of relative m_{jj} ratios for $n_{\mathrm{jet}} \in \{3, 4\}$

and $E_{\mathrm{T}}^{\mathrm{miss}} > 200\,\mathrm{GeV}$.

- Three additional SR bins in the lower $E_{\mathrm{T}}^{\mathrm{miss}}$ range of $160 < E_{\mathrm{T}}^{\mathrm{miss}} < 200\,\mathrm{GeV}$ divided in three bins of m_{jj} defined by $[1.5, 2, 3.5, \infty)\,\mathrm{TeV}$ are added (note that in these bins the $H_{\mathrm{T}}^{\mathrm{miss}}$ and fJVT cuts are modified, while $\Delta\phi_{\mathrm{jj}}$ is used inclusively, i.e. $\Delta\phi_{\mathrm{jj}} \in [0, 2]$). Summed with the 10 bins described above, this gives 13 bins in total for $n_{\mathrm{jet}} = 2$.
- Three additional SR bins, allowing $n_{\mathrm{jet}} = 3, 4$ and thus accounting for for ISR and FSR if additional requirements on jet centrality C_j and m_{rel} are fulfilled, are added for $E_{\mathrm{T}}^{\mathrm{miss}} > 200\,\mathrm{GeV}$ in three bins of m_{jj} defined by $[1.5, 2, 3.5, \infty)\,\mathrm{TeV}$.

The multi-dimensional binning scheme is summarised in Table 6.9 and sketched in Figure 6.7. A detailed overview of the bin-by-bin SR selection is given in Table 6.10. As described in Section 6.3, in addition to the VBF Higgs boson production also the ggF Higgs boson production is treated as signal. While the Higgs boson produced in VBF tends have a large values of m_{jj} and $\Delta\eta_{\mathrm{jj}}$ (like the EWK V+jets background), the ggF Higgs boson production accumulates at low m_{jj} and low $\Delta\eta_{\mathrm{jj}}$ values (like the strong V+jets background).

Table 6.9: Binning scheme in the SR. In total 16 SR bins are defined by splitting in n_{jet}, $E_{\mathrm{T}}^{\mathrm{miss}}$, $\Delta\phi_{\mathrm{jj}}$ and m_{jj}.

Bin number	n_{jet}	$E_{\mathrm{T}}^{\mathrm{miss}}$ [GeV]	$\Delta\phi_{\mathrm{jj}}$	m_{jj} [TeV]	Naming
1				$\in [0.8, 1]$	
2				$\in [1, 1.5]$	
3	2	> 200	< 1	$\in [1.5, 2]$	low $\Delta\phi_{\mathrm{jj}}$
4				$\in [2, 3.5]$	
5				> 3.5	
6				$\in [0.8, 1]$	
7				$\in [1, 1.5]$	
8	2	> 200	$[1, 2]$	$\in [1.5, 2]$	high $\Delta\phi_{\mathrm{jj}}$
9				$\in [2, 3.5]$	
10				> 3.5	
11				$\in [1.5, 2]$	
12	$\in \{3, 4\}$	> 200	$[0, 2]$	$\in [2, 3.5]$	high n_{jet}
13				> 3.5	
14				$\in [1.5, 2]$	
15	2	$\in [160, 200]$	$[0, 2]$	$\in [2, 3.5]$	low $E_{\mathrm{T}}^{\mathrm{miss}}$
16				> 3.5	

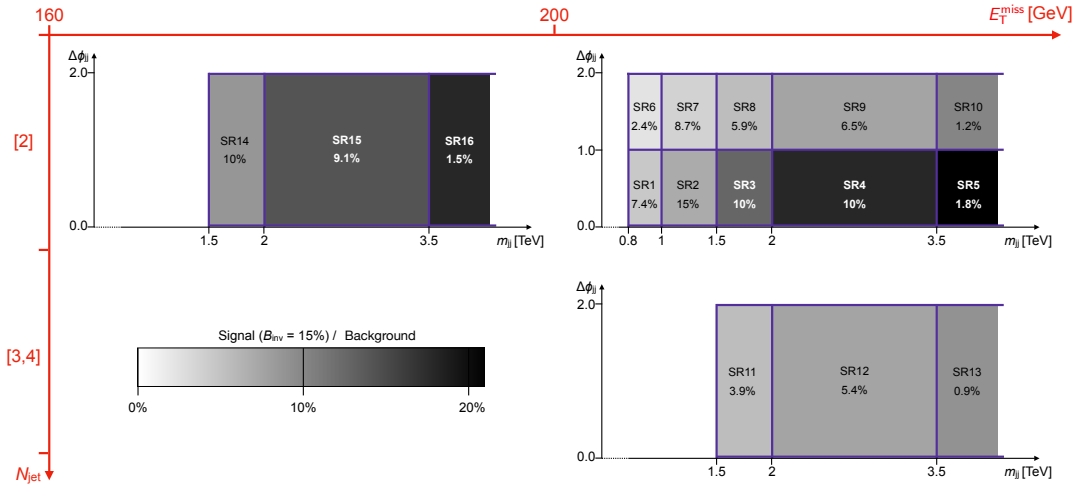

Figure 6.7: Sketch of the SR binning scheme. The ratio of signal and background events as well as the signal fraction is shown in each bin.

Table 6.10: Bin-by-bin SR selection requirements.

Quantity \ SR bin	1/6	2/7	3/8	4/9	5/10	11/12/13	14/15/16
n_{jet}	2	2	2	2	2	$\in \{3, 4\}$	2
E_T^{miss} [GeV]	> 200	> 200	> 200	> 200	> 200	> 200	$\in [160, 200]$
m_{jj} [TeV]	$\in [0.8, 1]$	$\in [1, 1.5]$	$\in [1.5, 2]$	$\in [2, 3.5]$	> 3.5	$\in [1.5, 2; 2, 3.5; > 3.5]$	$\in [1.5, 2; 2, 3.5; > 3.5]$
$\Delta\phi_{jj}$	$\in [0, 1]/[1, 2]$	$\in [0, 1]/[1, 2]$	$\in [0, 1]/[1, 2]$	$\in [0, 1]/[1, 2]$	$\in [0, 1]/[1, 2]$	$\in [0, 2]$	$\in [0, 2]$
$\Delta\eta_{jj}$	> 3.8	> 3.8	> 3.8	> 3.8	> 3.8	> 3.8	> 3.8
$p_{T,1}$ [GeV]	> 80	> 80	> 80	> 80	> 80	> 80	> 80
$p_{T,2}$ [GeV]	> 50	> 50	> 50	> 50	> 50	> 50	> 50
$p_{T,3}$ [GeV]	< 25	< 25	< 25	< 25	< 25	-	< 25
$fJVT_{1,2}$	< 0.5	< 0.5	< 0.5	< 0.5	< 0.5	< 0.5	< 0.2
$\lvert t_{jet} \rvert$ [ns]	< 11	< 11	< 11	< 11	< 11	< 11	< 11
JVT	> 0.2	> 0.2	> 0.2	> 0.2	> 0.2	> 0.2	> 0.2
$\eta_1 \cdot \eta_2$	< 0	< 0	< 0	< 0	< 0	< 0	< 0
H_T^{miss} [GeV]	> 180	> 180	> 180	> 180	> 180	> 180	> 140
E_T^{soft} [GeV]	< 20	< 20	< 20	< 20	< 20	< 20	< 20
n_γ	$= 0$	$= 0$	$= 0$	$= 0$	$= 0$	$= 0$	$= 0$
n_l	0	$= 0$	$= 0$	$= 0$	$= 0$	$= 0$	$= 0$
n_{b-jet}	< 2	< 2	< 2	< 2	< 2	< 2	< 2
$C_{j=3,4}$	-	-	-	-	-	< 0.6	-
$m_{rel,j=3,4}$	-	-	-	-	-	< 0.05	-

CHAPTER 7

Rebalance and Smear

The proper determination of the multijet background is usually one of the biggest background estimation challenges in searches for new physics. Due to the large cross section of multijet processes at the TeV-scale in proton-proton collisions, the effective luminosity for multijet samples generated with MC generators such as Pythia is much smaller than the corresponding amount of multijet events in data. Since the multijet background is expected to be small in the VBF Higgs boson to invisible search due to its low acceptance, using MC simulation solely to estimate the contribution of multijet events in the SR would lead to a small statistical precision corresponding to large event weights and large uncertainties. Also, multijet events with fake $E_{\mathrm{T}}^{\mathrm{miss}}$ due to mis-measurements are expected to be inaccurately modelled in the current Atlas detector simulation Geant4. In addition, both theoretical and experimental uncertainties further increase the uncertainties of MC estimates. Therefore a more advanced approach to estimate the multijet background must be used. Rebalance and Smear (RnS) is a sophisticated data-driven technique to estimate the multijet background for signal topologies consisting of jets and $E_{\mathrm{T}}^{\mathrm{miss}}$ and has already been used in different analyses in Atlas [225–227] and Cms [228–234]. The main principles of RnS are shown in Figure 7.1. It is closely related to the well established jet smearing [235]. Both the jet smearing and RnS are essentially sampling techniques. The main difference of the jet smearing to RnS is that the latter uses a rebalancing of the hard-scatter (and pile-up) jets to obtain an unbiased seed sample, while the jet smearing uses a tight cut on the $E_{\mathrm{T}}^{\mathrm{miss}}$ significance to select well measured seed events. In addition, especially for a VBF topology, the consideration of pile-up jets is crucial, which are included in RnS, while in jet smearing techniques typically only hard-scatter jets are smeared. So, RnS aims to be more inclusive than the widely used jet smearing and to describe various important effects related to pile-up jets.

The RnS method can be used with both data or MC simulation as input. A data-driven as well as a MC-based RnS version are implemented and utilised for the multijet background estimation, whereby the difference in the prediction of the data-driven and the MC-based RnS technique is considered as a systematic uncertainty in the final multijet background estimation. It should be noted that also the MC-based RnS technique is a data-driven background estimation strategy since the normalisation is done in suited CRs with data.

RnS is substantially modified and improved for the pile-up enriched data-taking periods in Run II compared to earlier versions of RnS. For the first time, the multijet background is splitted into two parts - the hard-scatter-only topology and the combinatorial background. Different multijet interactions leading to SR-like topologies are presented in Section 7.1. The input samples for RnS are described in Section 7.2. As a first step, hard-scatter and pile-up jets need to be identified. Subsequently, Section 7.3 describes the definition of two different multijet topologies, the selection of seed events as well as the rebalancing procedure of reco-level events. Both the jet smearing as well as the rebalancing are fundamentally based on jet resolution maps, whose measurement is described in Section 7.4. Since the jet smearing changes the jet and event kinematics, the pile-up tagging is re-evaluated after the smearing step, see Section 7.6. Rebalanced jets are smeared multiple times to increase the

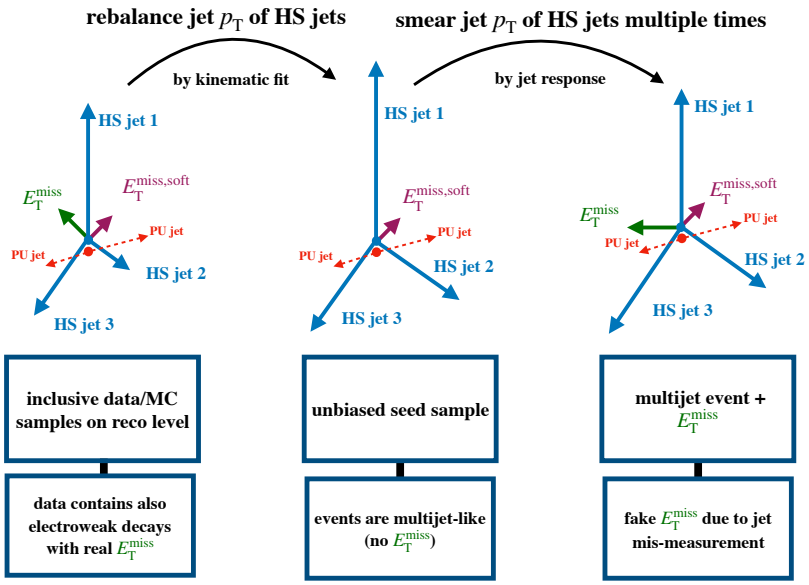

Figure 7.1: Sketch of the RnS technique. Hard-scatter jets (blue arrows) are rebalanced and subsequently smeared multiple times, while (soft) pile-up jets (red arrows) and the E_T^{soft} term (purple arrow) stay constant. While the E_T^{miss} term (green arrow) is minimised in the rebalancing of the reco events, it is re-introduced in the jet smearing. The key improvement with respect to earlier RnS version is the independent handling of hard-scatter and pile-up jets. In the MC-based RnS, all pile-up jets are constant, while in the data-driven RnS, the pile-up jets with $p_T > 25$ GeV are commonly rebalanced and those with $p_T < 25$ GeV are constant.

statistics of the prediction, see Section 7.5, whereby various techniques are implemented to further increase the sample size. In order to determine the fractions of the HS-only and HS+PU topologies and to account for data and simulation differences, a normalisation of the RnS prediction is performed in single jet triggered data. The Higgs boson to invisible search is performed in E_T^{miss} triggered data, therefore the trigger efficiency turn-on must be considered in the RnS multijet prediction, described in Section 7.8. RnS is a complex technique and thus various systematic uncertainties need to be discussed and evaluated, which is discussed in Section 7.9.

The data-driven as well as the MC-based RnS techniques are described simultaneously in the following and their differences are highlighted at the respective places.

7.1 Multijet Background in VBF Topologies

The multijet background in the presented VBF Higgs boson to invisible search is caused by two different classes of multijet events:

- multijet events from single multijet processes due to jet mis-measurements, jet loss due to the detector acceptance or initial and final state radiation (HS-only)
- multijet events with an interplay of multiple multijet processes, i.e. the mixing of hard-scatter and pile-up processes mainly caused by pile-up tagging in-efficiencies and vertex mis-measurements (HS+PU). This effect is also called the combinatorial background, sketched in Figure 7.2.

Jet mis-measurements are caused by different detector effects producing fake E_T^{miss}, which affect in different

ways the structure of the jet response distribution:

- The ATLAS detector has a limited energy resolution and thus cannot measure the energy of jets or particles with infinite precision. Especially high-energetic jets can punch through the calorimeter system and produce a p_{T} imbalance. Also dead or inactive detector material can cause jet loss.
- Jets are reconstructed with the anti-k_t jet clustering algorithm and thus it may happen that particles are not contained in a small-R jet radius (out-of-cone effect) or below reconstruction thresholds. On the other side, it may happen that the jet clustering algorithm may include background particles in the jet cone from a different source.
- Issues in the overlap removal of leptons and jets or photons and jets.
- Pile-up noise, mistagging and inaccurate pile-up calibrations.

An additional source of $E_{\mathrm{T}}^{\mathrm{miss}}$ in multijet events, which in this thesis is also included in the term jet mis-measurement, is caused by neutrinos both at reconstruction and particle level:

- Non-prompt neutrinos producing real $E_{\mathrm{T}}^{\mathrm{miss}}$ can be produced in heavy quark decays, especially b-quarks. In 24 % of the cases, b-quarks decay leptonically to (non-isolated) electrons e or muons μ and the corresponding neutrinos which are invisible for the detector and thus cause a p_{T} imbalance.

The interplay of jet mis-measurements and hard-scatter jet loss combined with the production of jets via initial and final state radiation is an important contribution to the multijet background in final states with jets and $E_{\mathrm{T}}^{\mathrm{miss}}$. In the following, a multijet event from simulation is presented, which is sketched in Figure 7.3, which is close to enter the SR of invisibly decaying Higgs bosons produced in VBF due to the combinatorial mixing of hard-scatter and pile-up jets:

- event
  - event number: 18807482, data set ID: 361022, event weight: 124020
- truth jets
  - jet 1: $p_{\mathrm{T}} = 76.4\,\mathrm{GeV},\ \eta = 0.45,\ \phi = 2.22$
  - jet 2: $p_{\mathrm{T}} = 46.8\,\mathrm{GeV},\ \eta = 0.33,\ \phi = -1.24$
  - jet 3: $p_{\mathrm{T}} = 18.3\,\mathrm{GeV},\ \eta = 2.99,\ \phi = -0.92$
  - jet 4: $p_{\mathrm{T}} = 15.7\,\mathrm{GeV},\ \eta = 4.12,\ \phi = 2.79$
- reco event
  - $E_{\mathrm{T}}^{\mathrm{miss}} = 139.2\,\mathrm{GeV}$, $H_{\mathrm{T}}^{\mathrm{miss}} = 79.8\,\mathrm{GeV}$, $m_{\mathrm{jj}} = 409.08\,\mathrm{GeV}$, $\Delta\eta_{\mathrm{jj}} = 3.50$, $\Delta\phi_{\mathrm{jj}} = 0.84$
- reco jets
  - jet 1: $p_{\mathrm{T}} = 85.1\,\mathrm{GeV},\ \eta = 0.46,\ \phi = 2.19$, no pile-up tag, truth matched (HS)
  - jet 2: $p_{\mathrm{T}} = 61.5\,\mathrm{GeV},\ \eta = -3.04,\ \phi = 1.35$, no pile-up tag, not truth matched (PU)
  - jet 3: $p_{\mathrm{T}} = 41.7\,\mathrm{GeV},\ \eta = 0.32,\ \phi = -1.28$, pile-up tagged, truth matched (HS)
  - jet 4: $p_{\mathrm{T}} = 26.6\,\mathrm{GeV},\ \eta = -0.85,\ \phi = -1.08$, pile-up tagged, not truth matched (PU)
  - jet 5: $p_{\mathrm{T}} = 22.6\,\mathrm{GeV},\ \eta = 4.16,\ \phi = 2.87$, no pile-up tag, truth matched (HS)
  - jet 6: $p_{\mathrm{T}} = 21.6\,\mathrm{GeV},\ \eta = 1.46,\ \phi = 0.32$, pile-up tagged, not truth matched (PU)

In this example, the two leading reco jets originate from different vertices since only the leading jet is a hard-scatter jet. The second leading jet cannot be matched to a truth jet within $\Delta R < 0.1$, thus it is a pile-up jet that is wrongly identified as a hard-scatter jet. Since the two leading jets are unrelated, the event has a small $\Delta\phi_{\mathrm{jj}}$-value corresponding to a relatively large value of $E_{\mathrm{T}}^{\mathrm{miss}}$. The two remaining jets with $p_{\mathrm{T}} > 25\,\mathrm{GeV}$ are both tagged by JVT as central pile-up jets. The remaining two jets are below $p_{\mathrm{T}} = 25\,\mathrm{GeV}$. Thus, a third jet veto with $p_{\mathrm{T}}^{j3} < 25\,\mathrm{GeV}$ would not reject this event. Given the large MC event weight of $O(10^5)$, it is important to evaluate the multijet background carefully and to consider these hard-scatter and pile-up jet mixing effects forming the combinatorial background. The hard-scatter and pile-up mixing can occur in particular if forward jets without tracks are present and the background is dependent on the number of pile-up interactions.

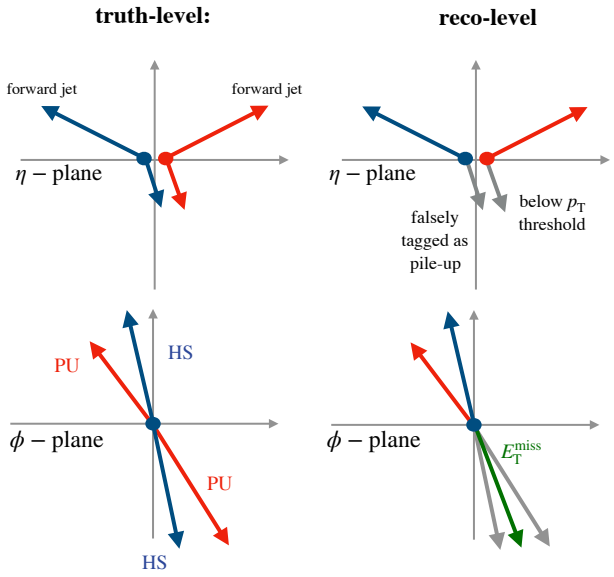

Figure 7.2: Mixing of hard-scatter and pile-up jets due to a pile-up mis-tagging in a multijet event. If for example both central jets, one HS and one pile-up jet, are removed and the two forward jets remain, the situation in the ϕ-plane shows that the E_T^{miss} caused by a failed pile-up tagging can correspond to small $\Delta\phi_{jj}$-values between the two leading jets.

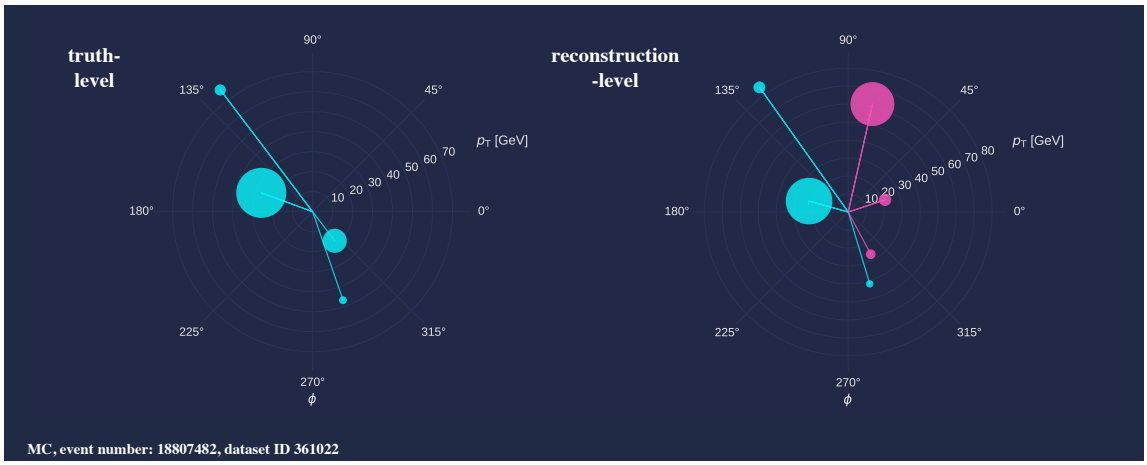

Figure 7.3: Event display in the transverse plane of a multijet event which is close to enter the SR from simulation on truth-level and reco-level. The size of the arrows scales with p_T, while the size of the bubbles scales with $|\eta|$. Jets from the hard-scatter process are drawn in light blue, pile-up jets in pink. Note that jets with $p_T < 20$ GeV are not reconstructed.

7.2 Input

7.2.1 MC-based RnS

The input for the MC-based RnS approach are Pythia dijet samples as described in Section 6.2.2. These samples are composed of events with at least two reconstructed final state jets. Two statistical independent sets of simulation generated with Pythia8 are used, matching the individual data-taking conditions, trigger menus and known, or in case of mc16e expected, $\langle\mu\rangle$ profiles as summarised in Table 6.2. Jets used as input for RnS are clustered with the anti-k_t algorithm ($R = 0.4$) using topo clusters only (EMTopo) since the PFlow algorithm intrinsically suppresses and removes central pile-up activity based on charged track measurements. However, the pile-up information is essential for a correct calculation of $H_{\mathrm{T}}^{\mathrm{miss}}$ and therefore for the trigger efficiency emulation. Also, the fJVT and JVT re-calculation is much more challenging for PFlow jets due to missing central pile-up jet information and a potential correlation of the track response and the jet response. Although missing pile-up information could be restored at AOD level, due to time constraints for the analysis it was favoured to use EMTopo jets where the needed pile-up information is available. For a better emulation of the PFlow nature with the used EMTopo jet collections, the jet smearing in RnS is performed using the PFlow jet resolutions as detailed in Section 7.4.

7.2.2 Data-driven RnS

The input for the data-driven RnS technique is data collected at $\sqrt{s} = 13\,\mathrm{TeV}$ in the data-taking periods 2015 to 2018 triggered by a suite of mostly prescaled single jet HLT triggers. This data is also used for the normalisation of the RnS multijet background prediction. As in the MC-based RnS technique small-R EMTopo jets clustered with the anti-k_t algorithm are used.

In order to reduce the rate at which data is recorded and thus to save storage space and computing time, a prescaling for single jet triggers below leading jet p_{T} of 400 GeV is used to record only every n$^{\mathrm{th}}$ triggered event [236]. The thresholds of the utilised single jet triggers range from 15 GeV to 460 GeV. To account for the prescaling statistics loss, weights for the collected data to account for trigger prescales have to be determined in order to maximise the seed sample statistics and thus to avoid a bias of the RnS prediction due to large event weights. The unprescaling procedure is not affected by any HLT trigger turn-on. A HLT prescale PS_i on a single jet trigger i can be seen as trigger with efficiency $1/PS_i$. The logical "and"-combination of two prescaled single jet triggers $i = 1, 2$ is then given by $1/(PS_1 PS_2)$, while the "or"-combination is given by $1 - (1 - 1/PS_1)(1 - 1/PS_2)$. The probability that an event is triggered by any of the HLT triggers with a p_{T} threshold below $p_{\mathrm{T}}^{\mathrm{online}}$ is given by

$$p(\text{triggered and selected} \mid p_{\mathrm{T}}^{\mathrm{online}}) = 1 - \prod_{i=1}^{N_{\mathrm{fired}}} \left(1 - \frac{1}{PS_i}\right), \tag{7.1}$$

where the triggeres which could have fired are denoted by N_{fired}. This determines the prescale weights w_{PS} via

$$w_{\mathrm{PS}} = \frac{1}{p(\text{triggered and selected} \mid p_{\mathrm{T}}^{\mathrm{online}})}. \tag{7.2}$$

The unprescaling procedure allows to keep every seed event and therefore maximises the seed sample statistics. Figure 7.4 shows the online jet p_{T} distribution before and after un-prescaling and shows a smooth p_{T}-distribution after applying the weights from the un-prescaling. The online HLT jets are limited to $|\eta| < 3.2$, i.e. events with no central jet activity are missed. However, for multijet events it is expected to have also central jet activity considering pile-up jets down to 15 GeV. Due to the nature of the single jet triggeres, the prescale weight has a p_{T} dependence, especially regarding the leading jet $p_{\mathrm{T}}^{\mathrm{lead}}$. Events with a low-$p_{\mathrm{T}}$ leading jet get usually a higher

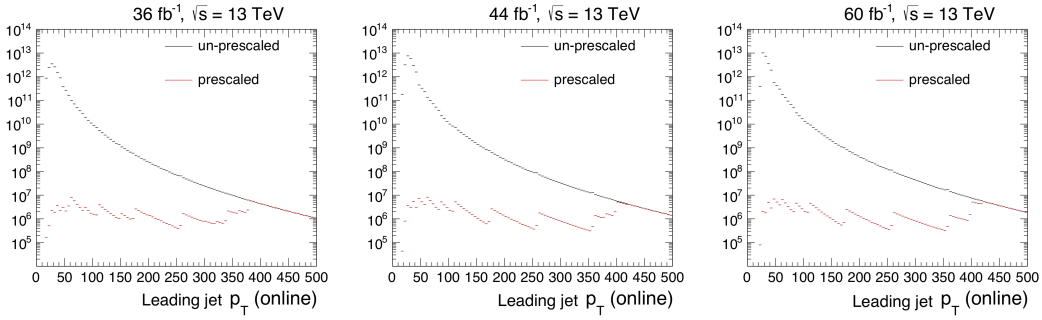

Figure 7.4: Prescaled and un-prescaled distribution of leading online jet p_{T} for 2015+2016 (left), 2017 (middle) and 2018 data (right). In the prescaled case, sharp HLT trigger turn-ons are visible, which vanish after un-prescaling. No significant deviation from the expected smooth shape is observed.

prescale weight w_{PS}. To enter the SR with a dijet VBF topology, a low-p_{T} jet at seed level must undergo a huge pull in the jet smearing, which is less likely than a pull in the order of 1. On the other side, events with high-p_{T} jets at seed level, which more likely will enter the SR, usually have a smaller pre-scale weights w_{PS}. In the following the prescale weight is termed as a data event weight w.

7.3 Seed Selection and Rebalancing

Two different multijet event topologies are selected in which the two important effects, the hard-scatter jet mis-measurement and the mixing of hard-scatter and pile-up jets (combinatorial background), are estimated individually. The former effect is in the following called HS-only topology, while the latter is termed as HS+PU topology. Different physics effects contribute to the HS-only and the HS+PU topologies as described in Section 7.1. For the MC-based approach, the HS-only and HS+PU topologies are defined based on the number of pile-up jets with $p_{\mathrm{T}} > 50\,\mathrm{GeV}$ at seed level, i.e. prior to rebalancing, denoted as n_{PU50}. For this, the identification of hard-scatter and pile-up reco jets on seed event level is performed via a geometrical truth-reco jet-matching based on ΔR in η-ϕ-space, defined as

$$\Delta R \begin{cases} < 0.1, & \text{jet is treated as hard-scatter jet} \\ \geq 0.1, & \text{jet is treated as pile-up jet} \end{cases} . \tag{7.3}$$

The combinatorial multijet background is determined by checking if one of the leading jets, which is identified as a hard-scatter jet, is a pile-up jet on truth-level, from which the MC-based definition of the multijet topologies follows:

- HS-only topology: $n_{\mathrm{PU50}} = 0$
- HS+PU topology: $n_{\mathrm{PU50}} \geq 1$

The HS+PU topology is defined by the presence of any seed level pile-up jet with $p_{\mathrm{T}} > 50\,\mathrm{GeV}$, where the 50 GeV momentum threshold exactly corresponds to the p_{T} cut for the subleading jet used in all SRs and CRs. To allow the definition of the HS-only and HS+PU topology in that straight way, the pile-up jets in each event must be freezed, i.e. the transverse momenta of pile-up jets are constant in both the rebalancing and smearing, described below. If a seed-level pile-up jet is present after the jet smearing as well as the subsequent pile-up jet removal and the event enters the dijet SR or CRs, one of the true hard-scatter jets must have been lost (otherwise a third jet veto would discard the event) and it occured a mixing of hard-scatter and pile-up jets caused by a jet mis-measurement, failed pile-up tagging and hard-scatter jet loss.

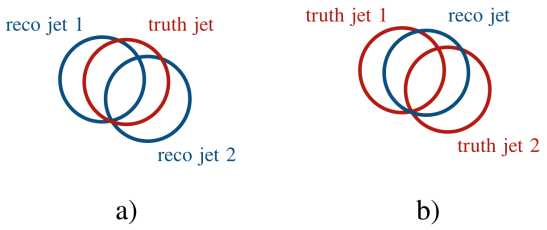

Figure 7.5: Sketch of truth jet splitting (a) and merging (b).

For the data-driven RnS approach, which uses single jet triggered data as seed events, also two kind of multijet event topologies are selected. However, the template definition is more challenging due to missing truth-level information in data. The identification of hard-scatter and pile-up jets relies on the tagging via JVT in the central region and fJVT in the forward region. Central jets for $|\eta| < 2.4$ with $20 < p_{\mathrm{T}} < 120\,\mathrm{GeV}$ are tagged depending on the p_{T} with different JVT working points, while forward jets with $35 < p_{\mathrm{T}} < 120\,\mathrm{GeV}$ are tagged with the loose working point, see Table 7.1.

Table 7.1: Pile-up jet identification as used in the data-driven RnS technique according to the $E_{\mathrm{T}}^{\mathrm{miss}}$ tenacious jet definition. Forward jets with $p_{\mathrm{T}} < 35\,\mathrm{GeV}$ are treated as pile-up.

$\lvert\eta\rvert$	p_{T} [GeV]	JVT	fJVT
< 2.5	$\in [20, 40]$	> 0.91	-
< 2.5	$\in [40, 60]$	> 0.59	-
< 2.5	$\in [60, 120]$	> 0.11	-
$[2.5, 4.5]$	$\in [35, 120]$	-	< 0.5

The first multijet topology consists of events with at least two hard-scatter jets and only soft pile-up jets with $p_{\mathrm{T}} < 25\,\mathrm{GeV}$ (HS-only). These events represent the contribution where the pile-up tagging worked well without a large contribution from hard-scatter and pile-up mixing (due to mis-tagging at seed selection level). The second multijet topology describing the combinatorial background consists of events with at least two hard-scatter jets and a number of pile-up jets with significant p_{T}, with at least two pile-up jets with $p_{\mathrm{T}} > 25\,\mathrm{GeV}$ and potentially more soft underlying pile-up jets with $p_{\mathrm{T}} < 25\,\mathrm{GeV}$ (HS+PU-topology). To ensure that these pile-up jets are indeed two related jets from a single multijet process, the jets are required to be roughly back-to-back in ϕ, i.e. $\Delta\phi_{\mathrm{jj}}(\mathrm{PU}) > 2.7$. No events with not exactly two seed-level pile-up jets are considered. Further, events defining the HS+PU topology must fulfil a requirement that the average transverse momentum $\langle p_{\mathrm{T}} \rangle^{\mathrm{PU}}$ of the two leading pile-up jets with $p_{\mathrm{T}} > 25\,\mathrm{GeV}$ in the event is $\langle p_{\mathrm{T}} \rangle^{\mathrm{PU}} > 40\,\mathrm{GeV}$. The correct definition and identification of the HS-only and HS+PU topologies is crucial for the performance of the RnS method. If the topologies are chosen badly or defined too close to the signal region, a normalisation in a multijet-dominated CR leads to an overestimation of the normalisation of the topologies, potentially leading to an overprediction of the multijet background in the signal regions. The data-driven RnS topology definition can be summarised as follows:

- HS-only topology: $\langle p_{\mathrm{T}} \rangle^{\mathrm{PU}} < 25\,\mathrm{GeV}$, $n_{\mathrm{HS}} > 2$
- HS+PU topology: $\langle p_{\mathrm{T}} \rangle^{\mathrm{PU}} > 40\,\mathrm{GeV}$, $\Delta\phi_{\mathrm{jj}}(\mathrm{PU}) > 2.7$, $n_{\mathrm{HS}} > 1$, $n_{\mathrm{PU}} = 2$,

where $n_{\mathrm{HS(PU)}}$ is the number of seed-level hard-scatter (pile-up) jets. It should be noted that the separation efficiency of the HS-only and the HS+PU topologies is lower than in a MC-based RnS technique, which benefits from truth-level information.

The seed selection identifies events which are used as input for RnS. Two aspects are relevant for the seed event selection:

- selecting events which may be relevant for the SRs and CRs after passing them through RnS
- selecting events which can be rebalanced with a kinematic fit

A large amount of unnecessary computing time and disk space can be saved by applying some seed event selection requirements, described in the following. In the MC-based approach, the presence of at least two hard-scatter jets at seed level is required for both topologies, $n_{\mathrm{HS}} \geq 2$, in order to allow for a SR topology with at least two jets and that a rebalancing of the reco-level hard-scatter event is possible. Further, at least one jet with $p_{\mathrm{T}} > 30\,\mathrm{GeV}$ is required. Very loose selection requirements are applied on three variables: $m_{\mathrm{jj}} > 0.15\,\mathrm{TeV}$, $\Delta\phi_{\mathrm{jj}} < 2.6$ and $\Delta\eta_{\mathrm{jj}} > 2.4$. Events with unphysical pile-up jets are rejected to ensure a smoothly falling p_{T} distribution after properly weighting the MC samples according to the delivered luminosity per data-taking period. The following requirement is used:

$$0.6 < \langle p_{\mathrm{T}} \rangle / p^{\mathrm{true}}_{\mathrm{T,j_1}} < 1.4, \tag{7.4}$$

where $\langle p_{\mathrm{T}} \rangle = \frac{1}{2}(p_{\mathrm{T,j_1}} + p_{\mathrm{T,j_2}})$ is the average transverse momentum of the two leading reconstructed jets and $p^{\mathrm{true}}_{\mathrm{T,j_1}}$ is transverse momentum of the leading truth jet. This filter is important to ensure that simulated p_{T} distributions of multijet events are smooth since the generation of MC events is done in different slices in p_{T}, see also Figure 5.9, and the event weights are calculated according to this slicing and the corresponding cross sections. If the randomly overlayed pile-up event has a more energetic jet than the simulated hard-scatter event (in this case the pile-up event becomes effectively the hard-scatter event), the event weights are not correctly assigned to the event, which might result in spikes in the p_{T} distribution. As described above, a truth-matching is performed to identify hard-scatter and pile-up jets. However, a truth-matching is not a fully efficient identification of hard-scatter and pile-up jets and suffers under truth jet splitting (one truth jet is reconstructed as multiple reco jets) and truth jet merging (multiple truth jets are reconstructed as one reco jet), sketched in Figure 7.5. In terms of a jet response $E_{\mathrm{reco}}/E_{\mathrm{truth}}$, the truth jet splitting leads to an artificially small response since the matched reco jets only carries a fraction of the truth energy, while the truth jet merging leads to an artificially large response since the energy of the reco jet is overestimated. To reject events with a unreliable truth-matching, a cut on $H_{\mathrm{T}}^{\mathrm{miss}}$(matched) is introduced which serves as a quality measure of the truth-matching. $H_{\mathrm{T}}^{\mathrm{miss}}$(matched) is calculated from truth jets and defined as

$$H_{\mathrm{T}}^{\mathrm{miss}}(\mathrm{matched}) = -\Big|\sum_i \vec{p}_{\mathrm{T},j_i}\Big|, \tag{7.5}$$

where i runs over the reco-matched truth jets. Large values of $H_{\mathrm{T}}^{\mathrm{miss}}$(matched) indicate problems on reco-level, e.g. mis-reconstructed, mis-measured or missing reco jets. Typical examples for badly matched events are cases where a jet is reconstructed as two jets by the reconstruction algorithm, the reco jet fluctuated below $p_{\mathrm{T}} < 20\,\mathrm{GeV}$ while the corresponding truth jet has $p_{\mathrm{T}} > 20\,\mathrm{GeV}$. When determining the upper threshold for $H_{\mathrm{T}}^{\mathrm{miss}}$(matched), it must be ensured that no bias on kinematic distributions, especially for the variables the SR is binned, $E_{\mathrm{T}}^{\mathrm{miss}}$, m_{jj} and $\Delta\phi_{\mathrm{jj}}$, is introduced. In addition, a trade-off between statistics and matching-quality must be found. The cut is well motivated since only well-measured reco events shall be used in RnS, otherwise the rebalancing cannot reliable "unfold" this event to the corresponding truth-level, potentially resulting in unphysical event topologies. A cut of $H_{\mathrm{T}}^{\mathrm{miss}}$(matched) = 35 GeV is used to ensure that all significant hard-scatter jets in an event have been correctly identified. This is visualised for an inclusive selection (in the MJ CR defined in Table 7.5 without $H_{\mathrm{T}}^{\mathrm{miss}}$(matched) selection) for the MC campaign mc16e in Figure 7.6. In addition, events where the leading jet is a pile-up jet are rejected. However, the latter selection requirement is merely obsolete after cutting on the truth-matching quality condition. A summary of the seed event selection of the MC-based RnS is given in Table 7.2. Only events fulfiling these requirement are used in the rebalancing procedure.

In case of the data-driven RnS, modified selection criteria are used. A veto on baseline leptons l and photons γ, standard event and tight jet cleaning cuts are applied. Events must be contained in the ATLAS GRL. The seed event selection is summarised in Table 7.3. Since the seed event selection is relatively tight and the HS-only and HS+PU topology definition is not covering all events (events with $25 < \langle p_{\mathrm{T}} \rangle^{\mathrm{PU}} < 40\,\mathrm{GeV}$ are not

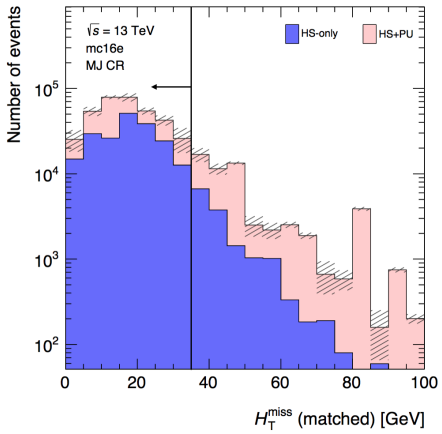

Figure 7.6: Distribution of $H_{\mathrm{T}}^{\mathrm{miss}}$(matched) for an inclusive selection in mc16e. The chosen upper threshold of 35 GeV is displayed by a black line with arrow.

Table 7.2: Seed event selection of the MC-based RnS technique.

Quantity	Cut	Description
n_{l}	$= 0$	baseline lepton veto
n_{γ}	$= 0$	baseline photon veto
n_{HS}	≥ 2	number of hard-scatter jets with $p_{\mathrm{T}} > 20\,\mathrm{GeV}$
m_{jj}	$> 150\,\mathrm{GeV}$	invariant mass of the leading dijet system
$\Delta\eta_{\mathrm{jj}}$	> 2.4	$\lvert\eta_1 - \eta_2\rvert$ of the leading dijet system
$\Delta\phi_{\mathrm{jj}}$	< 2.6	azimuthal separation of the leading dijet system
p_{T}	$> 30\,\mathrm{GeV}$	leading jet p_{T}
$\langle p_{\mathrm{T}}\rangle / p_{\mathrm{T,j_1}}^{\mathrm{true}}$	$\in [0.6, 1.4]$	reject unphysical pile-up from simulation
$H_{\mathrm{T}}^{\mathrm{miss}}$(matched)	$< 35\,\mathrm{GeV}$	truth-matching quality

Table 7.3: Seed event selection of the data-driven RnS technique.

Quantity	Cut	Description
n_{l}	$= 0$	baseline lepton veto
n_{γ}	$= 0$	photon veto
n_{jet}	≥ 3	jet multiplicity
m_{jj}	$> 150\,\mathrm{GeV}$	invariant mass of the leading dijet system
$\Delta\eta_{\mathrm{jj}}$	> 2.4	$\lvert\eta_1 - \eta_2\rvert$ of the leading dijet system
$\Delta\phi_{\mathrm{jj}}$	≤ 3	azimuthal separation of the leading dijet system
p_{T}	$> 30\,\mathrm{GeV}$	leading jet p_{T}

included), the majority of events are rejected and the multijet background normalisation has to be derived in a multijet-enriched CR.

Rebalancing is referring to the adjustment of the jet's four-momenta p^{μ}, in particular the transverse momenta p_{T} and azimuthal direction ϕ, for jets with $p_{\mathrm{T}} > 20\,\mathrm{GeV}$ within their corresponding experimental uncertainties by a least-square fit [237]. The aim of the rebalancing is to produce proxies of truth-level events and thus producing an unbiased QCD-like seed sample (on top of which the jet smearing is performed). The kinematic fit in the rebalancing is performed using a kinematic event fit with potential external kinematic constraints implemented via Lagrangian multipliers, where the solution is obtained by minimising a likelihood function L, which can be

formally written as

$$L(\vec{y}, \vec{a}, \vec{\lambda}) = S(\vec{y}) + 2 \sum_{k=1}^{m} \lambda_k f_k(\vec{y}, \vec{a}), \tag{7.6}$$

with the χ^2 term

$$S(\vec{y}) = \Delta\vec{y}^T C^{-1} \Delta\vec{y}, \tag{7.7}$$

where $\lambda_k f_k(\vec{y}, \vec{a})$ are the Lagrangian multiplieres depending on the observables $\vec{y}$ and un-measured parameters $\vec{a}$, which are obtained from linear or non-linear kinematic constraints. C is the covariance matrix defined by the jet energy or angular resolution and $\Delta\vec{y}$ can be interpreted as the difference of the true and observed value of $\vec{y}$. The entries of y are the jet values of p_T and ϕ for all jets in the event. In case of non-linear constraints, the solution must be found iteratively in a linearisation process, while a linear constraint can be solved directly. The minimization procedure aims for finding the optimal solution with minimising $S(\vec{y})$ and $\lambda_k f_k(\vec{y}, \vec{a}) = 0$. Solving numerically the maximum likelihood estimation, one obtains unbiased estimators or proxies of truth jet configuration. Thus, the kinematic fit is used to obtain p_T balance by adjusting all jets above a threshold (typically $p_\mathrm{T} > 20\,\mathrm{GeV}$) in p_T and ϕ within their experimental uncertainties to fulfill transverse momentum balance with respect to $H_\mathrm{T}^\mathrm{miss}$. More specifically, in the utilised data-driven and MC-based RnS techniques, hard-scatter and pile-up event topologies are handled independently. The hard-scatter jets are first rebalanced with respect to $E_\mathrm{T}^\mathrm{soft}$:

$$H_\mathrm{T}^\mathrm{miss}(\mathrm{HS}) = \Big| \sum_{i \in \mathrm{HS-jets}} \vec{p}_\mathrm{T}^{\,i} \Big| \equiv E_\mathrm{T}^\mathrm{soft}. \tag{7.8}$$

In case of the MC-based RnS all un-matched reco jets with $p_\mathrm{T} > 20\,\mathrm{GeV}$, i.e. the seed-level pile-up jets, are freezed in the rebalancing. In case of the data-driven RnS, the pile-up jets with $p_\mathrm{T} > 25\,\mathrm{GeV}$ are rebalanced independently to the hard-scatter event to fulfil perfect p_T balance, i.e.

$$H_\mathrm{T}^\mathrm{miss}(\mathrm{PU}) = \Big| \sum_{i \in \mathrm{PU-jets}} \vec{p}_\mathrm{T}^{\,i} \Big| \equiv 0, \tag{7.9}$$

where the sum runs over all pile-up jets i with $p_\mathrm{T} > 25\,\mathrm{GeV}$. Pile-up jets with $p_\mathrm{T} < 25\,\mathrm{GeV}$ are freezed in the rebalancing for the data-driven RnS. The rebalancing strategy of both the data-driven and MC-based RnS approach is summarised in Table 7.4.

Table 7.4: Rebalancing strategy of the data-driven and MC-based RnS technique. In the MC-based RnS technique the hard-scatter jets are rebalanced and all pile-up jets are constant. In the data-driven case, the hard-scatter jets and the pile-up jets with $p_\mathrm{T} > 25\,\mathrm{GeV}$ are rebalanced separately and the pile-up-tagged jets with $p_\mathrm{T} < 25\,\mathrm{GeV}$ remain constant.

	Hard-scatter jets	Pile-up jets
MC-based RnS	rebalanced	constant
data-driven RnS	rebalanced	rebalanced for $p_\mathrm{T} > 25\,\mathrm{GeV}$ constant for $p_\mathrm{T} < 25\,\mathrm{GeV}$

However, single jet triggered data also contains events with real $E_\mathrm{T}^\mathrm{miss}$, e.g. from electroweak decays producing invisible neutrinos or non-isolated leptons which are out of p_T or η acceptance. The rebalancing adjusts the kinematics of jets in the event to get rid of both the fake $E_\mathrm{T}^\mathrm{miss}$ and the real $E_\mathrm{T}^\mathrm{miss}$ in the event, except of the soft $E_\mathrm{T}^\mathrm{miss}$ term denoted as $E_\mathrm{T}^\mathrm{soft}$. This tiny contribution from events with real $E_\mathrm{T}^\mathrm{miss}$ and not fake $E_\mathrm{T}^\mathrm{miss}$ due to jet mis-measurements are made QCD-like in the rebalancing by absorbing the real $E_\mathrm{T}^\mathrm{miss}$ into the visible jets. In very rare cases this can lead to extraordinarily p_T pulls for visible jets but given the cross section for multijet and other processes this contribution is negligible. Thus RnS is safe against this contamination as sketched in Figure 7.7.

In the rebalancing, the kinematic variables ϕ and p_T of jets are modified within their experimental resolution, σ_ϕ and σ_{p_T}, respectively, while η is constant since it is not relevant for transverse momentum balance in the

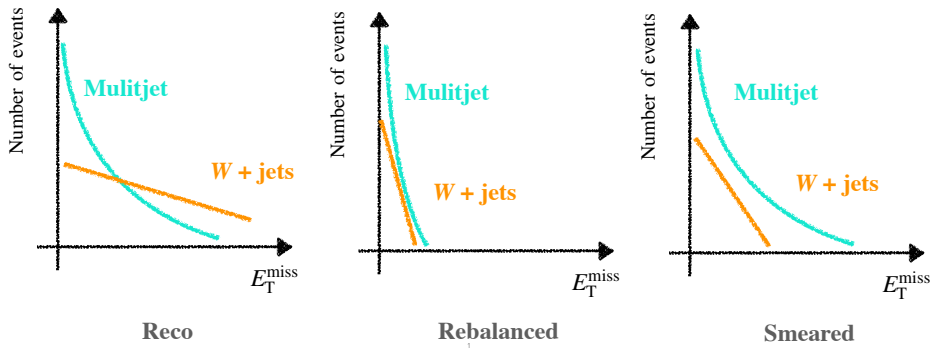

Figure 7.7: Events with real E_T^{miss}, e.g. caused by W+jets events, are made multijet-like in RnS and are negligible compared to the huge multijet cross section.

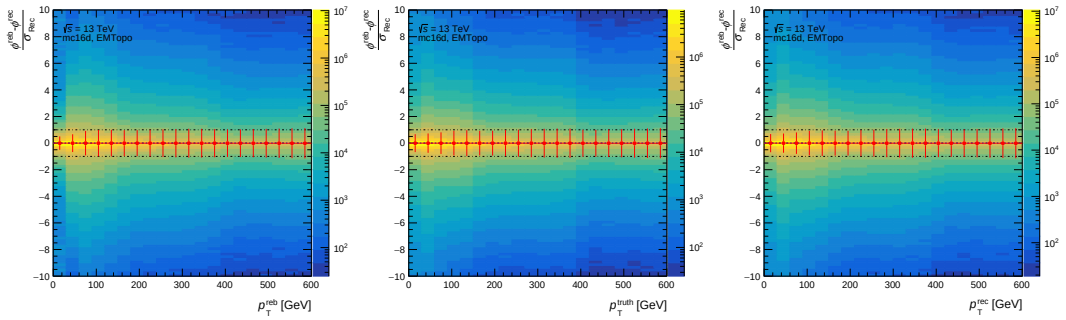

Figure 7.8: Pulls of jet ϕ as function the rebalanced p_T, the truth jet p_T and the reco p_T (seed jet).

x-y-plane. Since the ϕ-resolution is better than that of p_T, the latter usually undergoes the most substantial modification. The best fitting configuration is determined by a χ^2-test. If the fit does not converge, which is very rarely the case, the event is rejected (for example mono-jet events cannot be rebalanced but they are not selected anyway). Pull distributions of the rebalancing process are used to validate the rebalancing step in RnS. In general, a pull of a quantity $x = \{p_T, \phi\}$ with experimental uncertainty σ_x is defined as

$$\xi_x = \frac{x^{fit} - x}{\sigma_x}, \tag{7.10}$$

where x^{fit} is the resulting value of x after fitting. The pull ξ_x is normalised with respect to its uncertainty σ_x, hence the expected mean of the pull is zero with variance one. Pull plots are shown for Pythia dijet samples of the campaign mc16d. Figure 7.8 and 7.9 show the pulls of the reco jet with respect to the rebalanced jet of ϕ and p_T for all jets as a function of the relabanced p_T, the truth p_T and the reco p_T, respectively. The pulls of ϕ and p_T show overall the expected behaviour. However, especially the low p_T range suffers from experimental threshold effects: Reco jets are only stored for $p_T \geq 20\,\text{GeV}$. Truth-level jets are available until $p_T \geq 7\,\text{GeV}$. Rebalanced jets are based on reco jets but can be rebalanced with a negative pull to $p_T < 20\,\text{GeV}$.

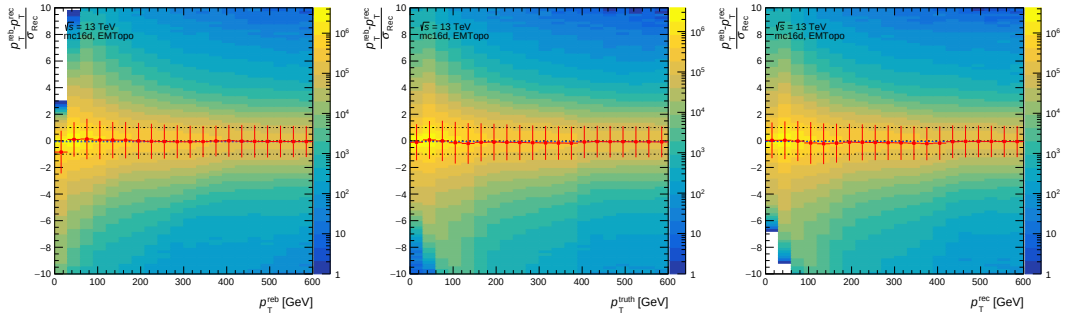

Figure 7.9: Pulls of jet p_T as function the rebalanced p_T, the truth jet p_T and the reco p_T (seed jet).

7.4 Jet Resolution

The jet response is a basic ingredient of RnS, affecting both the rebalancing and the jet smearing, and is measured specifically for the usage of RnS since a tight matching of reco and truth jets is needed as well as a proper treatment of non-Gaussian jet resolution effects. There are three contributions to the Gaussian part of the jet response, as written in Equation 3.8, including a p_T-dependent effect of electronic and pile-up noise, stochastic contributions from the sampling of calorimeters and other stochastic characters of the measurement and constant contributions caused by inactive detector material or leakage. While the value of N can be measured directly, S and C are determined in balanced dijet events. While the rebalancing only considers the Gaussian core $\mathcal{R}_{\text{core}}$ of the jet response due to technical reasons of the kinematic fit, the smearing is based on the full jet response distribution including the non-Gaussian tails $\mathcal{R}_{\text{tail}}$. The non-Gaussian contributions are predominantly caused by semi-leptonic heavy flavour quark decays, pile-up effects and instrumental limitations of the detector and are important for the description of jet mis-measurements and the production of large values of H_T^{miss} in multijet events. The jet response distributions are derived in simulation and binned in truth-values of energy E_{true}, η and b-tag. A fine binning of the jet response distributions also in $|\eta|$ is crucial to also consider detector transition regions with worse energy resolution especially for low energetic jets. A binning in b-tagged and light flavour jets is performed to consider the very low response values and larger non-Gaussian response tails from heavy flavour quark decays, whereby a b-jet tagging is only applied in the central detector region. The binning schemes for the true energy E_{true} and $|\eta|$ are

- E_{true} [GeV]: [0, 10, 20, 30, 40, 50, 70, 100, 140, 190, 250, 320, 400, 490, 590, 700, 820, 950, 1090 ,1240, 1400, 1570, 1750, 1940, 2140, 2350, 2600, 3000]
- $|\eta|$: [0.0, 0.5, 0.7, 0.9, 1.1, 1.3, 1.5, 1.8, 2.1, 2.5, 2.8, 3.0, 3.2, 3.4, 3.6, 5.0]

The truth-matching of a reco jet j^{reco} and a truth jet j^{true} is performed using

$$\Delta R(\text{j}^{\text{reco}}, \text{j}^{\text{true}}) = \sqrt{(\Delta\eta(\text{j}^{\text{reco}}, \text{j}^{\text{true}}))^2 + (\Delta\phi(\text{j}^{\text{reco}}, \text{j}^{\text{true}}))^2} < 0.1. \tag{7.11}$$

In addition, jet isolation-criteria are applied, i.e. no additional truth or reco jet activity p_T^{add} with $p_T^{\text{add}}/p_T^{\text{truth}} > 5\,\%$ in the vicinity of $\Delta R < 1.2$ of the truth-matched jet pair is allowed. If soft additional reco jets ($p_T^{\text{add}} < 2\,\%$ with respect to the truth jet) are present within $\Delta R < 0.8$, they are added to the nominator of the jet energy response $\mathcal{R}$ defined above. Representative distributions of the jet responses $\mathcal{R}$ are shown in Figure 7.11. In the low-energy range, the lower jet response tails suffer from a reconstruction jet p_T threshold. Further, a summary of the relative JER for various energies E_{true} as function of $|\eta|$ is shown in Figure 7.10.

Since the non-Gaussian tails of the jet response are very challenging to model in MC, they are validated in data using a dijet p_T-asymmetry technique as described in Section A.2, whereby the validation results are used

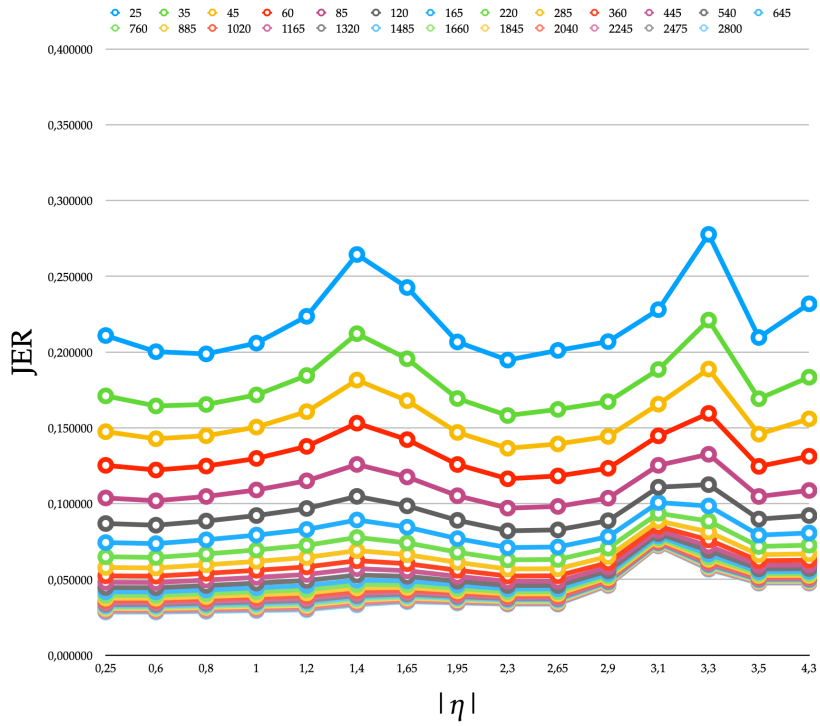

Figure 7.10: Relative JER as function of $|\eta|$ for various energies for the Gaussian core of the used jet energy response distributions.

to assign systematic uncertainties of the jet response distributions used in RnS, which is described in Section 7.9.

7.5 Jet Smearing

In order to emulate the production of $E_{\mathrm{T}}^{\mathrm{miss}}$ in multijet processes caused by jet mis-measurements, a jet smearing is performed with the rebalanced jet collection, i.e. the p_{T} of the jets is scaled with random scaling factors sampled according to PFlow jet resolutions as described in Section 7.4. In addition to p_{T} smearing, also the azimuthal direction ϕ of jets is randomly smeared within its resolution. An η-smearing is not used since the jet η values do not contribute to the p_{T} balance in the transverse plane. The validity of a jet smearing technique relies on two assumptions: Any source of jet fluctuation can be described by one jet response function and the jet smearing can be applied on a jet-by-jet basis, i.e. that any dependence of the jet response on event properties can be neglected. Based on the jet p_{T} scaling factor $r > 0$ and ϕ smearing terms $\delta\phi$, randomly obtained according the corresponding jet p_{T} (ϕ) resolution of the jet, the jet four-vector kinematics are modified according to

$$m \mapsto m' = r \cdot m \tag{7.12}$$
$$E \mapsto E' = r \cdot E \tag{7.13}$$
$$\phi \mapsto \phi' = \phi + \delta\phi \tag{7.14}$$
$$\eta \mapsto \eta' = \eta \text{ (unchanged)} \tag{7.15}$$
$$p_{\mathrm{T}} \mapsto p'_{\mathrm{T}} = \sqrt{(E')^2 - (m')^2}/\cosh(\eta'). \tag{7.16}$$

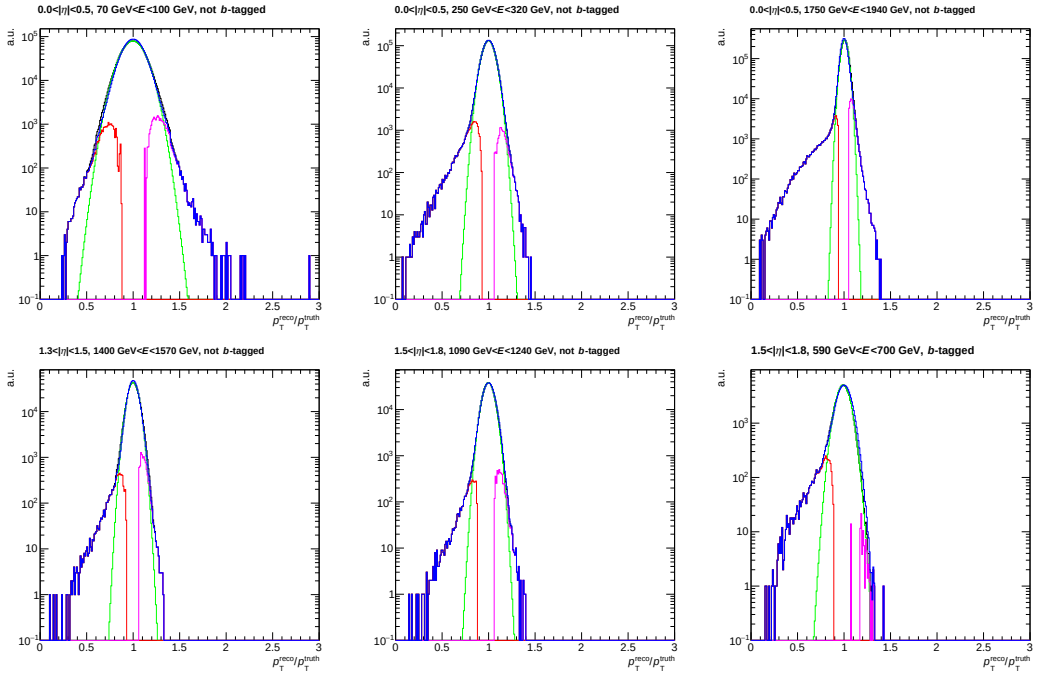

Figure 7.11: Examples of the jet response distributions for different energy ranges, η ranges and b-tags. The full distribution, obtained from PFlow jets in simulation, is shown in blue. The fit to the Gaussian core is shown in green. The lower non-Gaussian tail is plotted in red, while the upper tail is shown in pink.

In case of the MC-based RnS, only the hard-scatter jets (i.e. the truth-matched reco jets), are smeared, while the pile-up jets (un-matched reco jets) remain fixed. In the data-driven RnS, all hard-scatter jets and pile-up jets with $p_{\mathrm{T}} > 25\,\mathrm{GeV}$ are smeared, while pile-up jets with $p_{\mathrm{T}} < 25\,\mathrm{GeV}$ are freezed. The jet p_{T} smearing factors r as a function of the rebalanced jet p_{T} (inclusive in $|\eta|$) and as a function of $|\eta|$ (inclusive in p_{T}) are shown in Figure 7.12. The handling of tracks in the jet smearing approach is discussed in Section 7.6.1. In order to emulate the fake $E_{\mathrm{T}}^{\mathrm{miss}}$ production via hard-scatter and pile-up mixing, the pile-up tagging variables JVT and fJVT of a jet are re-calculated after the smearing procedure, discussed in detail in Chapter 7.6. Although the pile-up jets are constant in p_{T} and ϕ in the MC-based jet smearing, the pile-up tagging needs to be re-evaluated after the jet smearing for both hard-scatter and pile-up jets since changes in the pile-up-tagging in the hard-scatter event might also affect the pile-up tagging of pile-up jets, especially in case of fJVT. In addition, the tracks and therefore also the primary vertex ordering remain unchanged in RnS, as further described in Section 7.6. Finally, after the pile-up jet tagging, event observables such as $E_{\mathrm{T}}^{\mathrm{miss}}$, $\Delta\phi_{\mathrm{jj}}$, m_{jj}, $\Delta\eta_{\mathrm{jj}}$, $H_{\mathrm{T}}^{\mathrm{miss}}$ or H_{T} are calculated. Different strategies are possible to handle $E_{\mathrm{T}}^{\mathrm{soft}}$ during RnS, e.g. set it to zero prior to rebalancing, use it unmodified from the seed-level or to smear $E_{\mathrm{T}}^{\mathrm{soft}}$ similar to jets. However, the handling of $E_{\mathrm{T}}^{\mathrm{soft}}$ has no significant impact on the multijet prediction and thus in both MC-based and data-driven RnS the term $E_{\mathrm{T}}^{\mathrm{soft}}$ remains constant in RnS.

In context of the jet smearing, a variety of complementary techniques is developed to increase the effective statistics of the RnS multijet prediction ranging from multiple event smearing, azimuthal event rotation to artificially enhancing the tails of the jet response, described in more detail in the following.

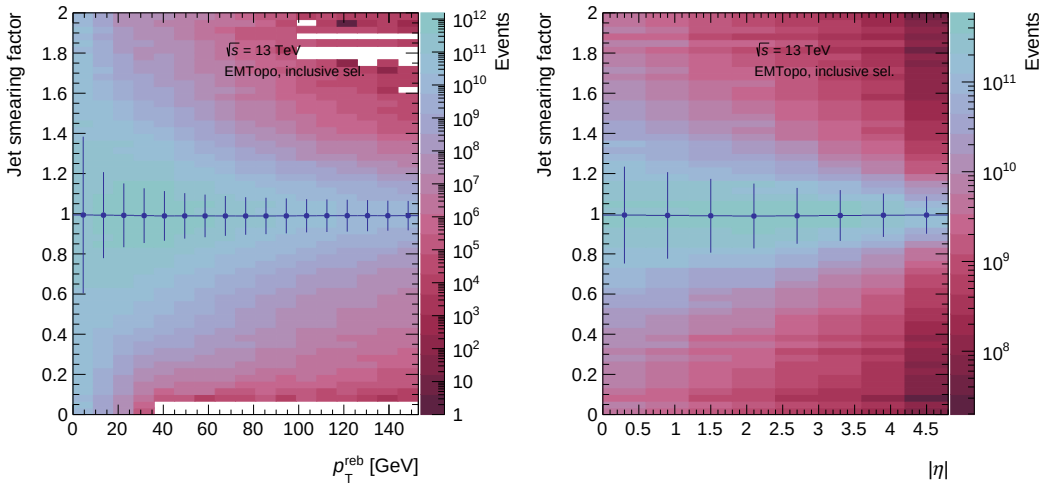

Figure 7.12: Jet smearing factors as a function of rebalanced jet p_T and η.

7.5.1 Weight-dependent Jet Smearing

The number of independent smearings of an event depends on its event weight, which is either the MC event weight or the data weight from the unprescaling procedure. Events with large seed-level event weights are smeared more often to avoid large event weights in the multijet prediction in SRs and CRs. Based on the weight w the events are smeared in the RnS procedure w-times if $1 \leq w \leq N_{\text{PSmax}}$ and N_{PSmax}-times if $w \geq N_{\text{PSmax}}$, where N_{PSmax} is the maximal value of the number of independent jet smearings of a seed event. The larger N_{PSmax}, the better, since the impact of events with a huge event weight w is reduced. However, the number of N_{PSmax} is bounded by the limited computational resources, i.e. to avoid an excessive amount of smearings for highly weighted events. The value of N_{PSmax} is typically chosen in the range $[100, 400]$. The number of smearings is considered in the resulting event weight w by reducing it accordingly. For example, a seed event with a weight $w = 100 < N_{\text{PSmax}}$ is smeared 100 times with resulting individual event weights of $w = 1$ assuming $N_{\text{PSmax}} = 200$. In contrast, an event with a weight $w = 600 > N_{\text{PSmax}}$ would be smeared $N_{\text{PSmax}} = 200$ times with resulting individual event weights of $w = 3$.

7.5.2 Azimuthal Hard-scatter Jet Rotation

To increase the effective statistics of the combinatorial background (HS+PU topology), a random rotation in the transverse plane of the hard-scatter jets with respect to the pile-up jets is performed. The number of ϕ-rotations is typically set in the range $N_{\delta\phi} \in [10, 100]$, while accordingly reducing the individual event weights by the inverse factor. The rotating angles $\delta\phi$ are randomly derived in the interval $[0, 2\pi)$. In addition to the hard-scatter jets, which point to the PV_0, also the soft missing transverse momentum term E_T^{soft}, consisting of all tracks pointing to the PV_0 but are not associated to any hard object, is rotated with the same angle $\delta\phi$. Pile-up jets and the track E_T^{miss} term pointing to the pile-up vertices are not modified in ϕ. The azimuthal rotation changes the kinematics of the event, e.g. E_T^{miss} produced by HS+PU-mixing might vary for different values of $\delta\phi$ between the hard-scatter and pile-up jets, reducing potential spikes due to large event weights in the distributions of observables. However, an azimuthal rotation in the HS-only topology will not increase the effective statistics since there is no overlayed significant pile-up activity which may change the event kinematics of a potential SR topology.

7.5.3 Enhancing of Non-Gaussian Tails

To further increase the statistics of the multijet prediction, especially of the hard-scatter-only topology (which does not gain statistics due to the azimuthal rotation), the non-Gaussian tails are artificially enhanced with modifying the event weights w accordingly. By this, larger mis-measurements of jets are enhanced, producing more often signal region topologies since for example a jet loss due to the 25 GeV threshold is more likely. While the measured non-Gaussian tails are roughly at the 1 % level in the jet response distribution (depending on E_{true} and η), the tails used for jet smearing are increased to a fraction of 30 % (enhanced fraction), i.e. jets are smeared 30 % of the time in the tails and 70 % of the time in the Gaussian core. For this approach, the tails are practically defined as the 1 % percentile (tail fraction) at the lower and upper tail of the jet response. With the chosen configuration the statistics in the tails is enhanced with a factor sixteen. The tail-enhancing is utilised for the three leading jets only, which are the relevant ones for producing a signal region topology, while for all other jets the original jet energy response is used. If a jet is smeared within the core, the event weight w must be increased since such a process is in reality more likely than parametrised by the jet response distribution with enhanced tails. Accordingly, the event weight must be reduced if an event is smeared in the tails. The correction factors of the event weight per jet are for the core

$$w_{\text{core}} = (1 - 2 \cdot \underbrace{0.01}_{\text{tail fraction}})/(1 - \underbrace{0.3}_{\text{enhanced fraction}}) \tag{7.17}$$

and for the tail

$$w_{\text{tail}} = (2 \cdot \underbrace{0.01}_{\text{tail fraction}})/(\underbrace{0.3}_{\text{enhanced fraction}}). \tag{7.18}$$

The factor 2 is included in both equations since there is a lower and an upper tail in the response distribution. For example, if the leading three jets are smeared within the tails, the event weight w must be multiplied with w_{tail}^3. If two jets are smeared within the core and one jet within the tails, the correction factor is $w_{\text{core}}^2 \cdot w_{\text{tail}}$ (recall that the tails are only enhanced for the leading three jets). The weight correction factor from enhancing the tails is denoted as w_{enhanced}. The modelling and enhancing of the tails of the jet response are only affecting the jet smearing step since the rebalancing is based only on the Gaussian core of the jet resolution. Closure checks of the tail enhancing procedure are shown in Figure 7.13.

7.6 Re-Evaluation of Pile-up Tagging

In order to estimate the multijet background for a VBF topology with a large amount of $E_{\text{T}}^{\text{miss}}$, it is important to consider the mixing of hard-scatter and pile-up jets potentially caused by pile-up tagging inefficiencies for hard-scatter jet identification which requires a evaluation of the pile-up tagging after the jet smearing. The general aim of pile-up tagging is to identify hard-scatter and pile-up jets and rejecting the latter. The re-evaluation of the pile-up tagging follows closely the original ATLAS JVT [162] and fJVT [128, 163] algorithms. However, some significant changes and assumptions are made which are discussed, evaluated and validated in the following. A first discussion in Section 7.6.1 refers to the treatment of the track and jet terms within RnS, which is relevant for the RnS technique in general but also has direct implications for the pile-up tagging re-evaluation. The re-calculation of JVT is discussed in Section 7.6.2, while the re-evaluation of fJVT is discussed in Section 7.6.3.

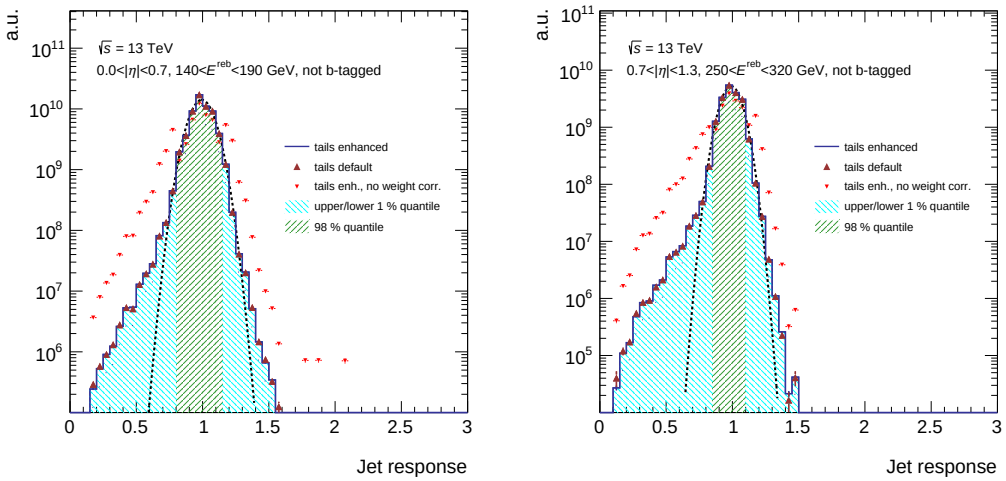

Figure 7.13: Validation of the enhancing of the non-Gaussian tails of the jet response distributions for two exemplary rebalanced energy and η range for light flavour jets. The dark red triangles represent the initial jet response distribution. The light red triangles is the response distribution after enhancing the tails (where the core is reduced accordingly). The dark blue histogram is the enhanced tail response distribution after correcting the jet weights with w_{core} or w_{tail}. The closure check is successful since the blue histogram and the dark red triangles match. Further the central 98 % percentile and the lower and upper 1 % percentile are drawn, corresponding to the definitions of the core and tail, respectively, as used in the tail enhancing. For completeness, a Gaussian fit, shown with a hashed line, is performed to the center of the distribution.

7.6.1 Track and Jet Response

In context of the evaluation of pile-up tagging, namely calculating the JVT and fJVT scores of jets based on track, vertex, jet and event kinematics, a potential correlation of the track and jet response has to be investigated. The discussion focuses on EMTopo jets, which are built from calorimeter energy deposits, while tracks are trajectories of charged particles measured in the ID. Therefore jet energy measurements and track measurements are expected to be mostly independent for EMTopo jets. For central PFlow jets, the situation is more complex due to the internal combination of topo-clusters and tracks within the PFlow algorithm. If the track response and the jet response can be shown to be independent for EMTopo jets, then the track measurement is not affect by a jet measurement in the calorimeter. This in turn implies that

- the tracks should not be modified during RnS (neither rebalanced, nor smeared)
- the vertex ordering based on the track momenta pointing to individual vertices remains unchanged in RnS
- track- and vertex-based variables, especially input variables for the JVT algorithm such as corrJVF, see Equation 7.21, are constant in RnS

The jet momentum response $\mathcal{R}_{\text{jet}}$ is defined in terms of transverse momentum p_{T}, i.e.

$$\mathcal{R}_{\text{jet}} = \frac{p_{\text{T,reco}}}{p_{\text{T,true}}}, \tag{7.19}$$

where $p_{\text{T,reco}}$ is the reconstructed jet momentum and $p_{\text{T,true}}$ the true jet momentum of the truth-matched jet, where the same matching criteria as described in Section 7.4 are used. The track response is defined as

$$\mathcal{R}_{\text{track}} = \frac{p_{\text{T,track}}}{p_{\text{T,true}}}, \tag{7.20}$$

where $p_{\text{T,track}}$ is the momentum of the tracks associated with the jet and pointing to the jet vertex. The binning in

η and E_{true} of the jet response is described in Section 7.4 and also used for the track response studies. The used MC samples are obtained from PYTHIA dijet simulation of the MC campaign mc16d weighted to a luminosity of 44 fb^{-1} using a EMTopo jet collection. The correlation check of the jet response and the track response is shown in the following selection of representative plots for different p_{T} and η ranges. The Figure 7.14-7.15 show that

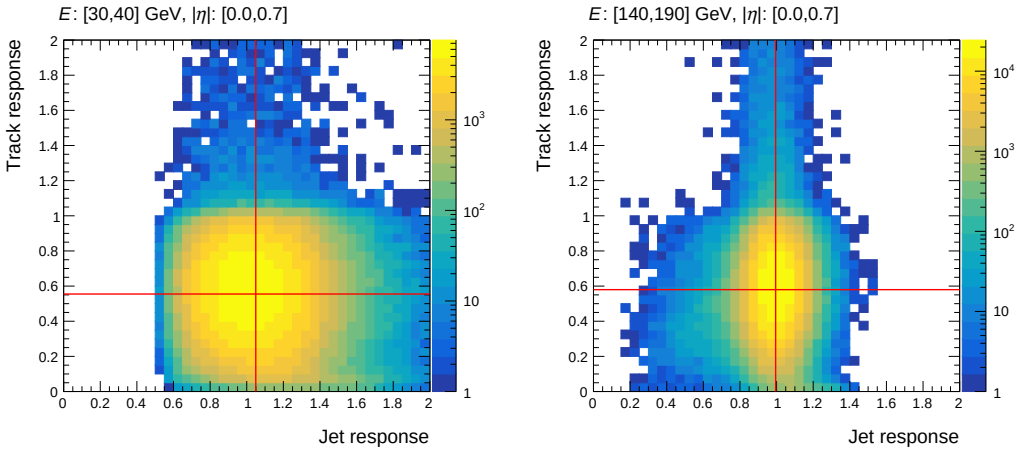

Figure 7.14: Scatter plots of the jet and the track response of jets for $E_{\text{true}} \in [30, 40]$ GeV ($E_{\text{true}} \in [140, 190]$ GeV) and $|\eta| \in [0.0, 0.7]$. The red lines indicate the mean values of the histograms with respect to $\mathcal{R}_{\text{jet/track}}$.

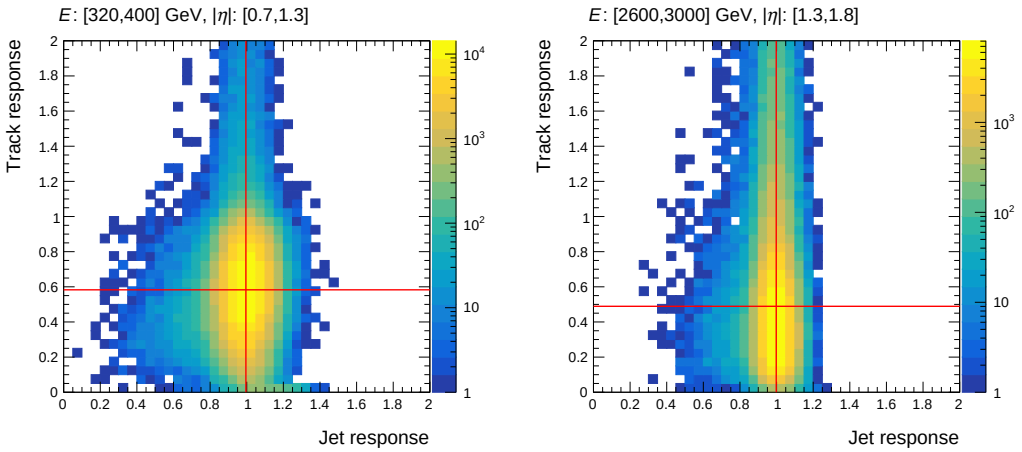

Figure 7.15: Scatter plots of the jet and the track response of jets for $E_{\text{true}} \in [320, 400]$ GeV and $|\eta| \in [0.7, 1.3]$ ($E_{\text{true}} \in [2.6, 3]$ TeV and $|\eta| \in [1.3, 1.8]$). The red lines indicate the mean values of the histograms with respect to $\mathcal{R}_{\text{jet/track}}$.

the track response $\mathcal{R}_{\text{track}}$ usually peaks around ~ 0.6 which corresponds to the charged fraction of the energy of central jets E_{CF}, which is measured in the ID, and is independent of the jet response $\mathcal{R}$ which is sensitive to both the charged fraction E_{CF} and the neutral fraction E_{NF} of the total energy $E = E_{\text{CF}} + E_{\text{NF}}$. The jet response $\mathcal{R}$ peaks around 1 and shows no strong correlation with the track response for various η and energy ranges.

7.6.2 Recalculation of JVT

The jet vertex tagger (JVT), used in the central detector region for the tagging of pile-up jets, is based on track, jet kinematics and vertex information. The JVT discriminator [162] is computed using the pile-up-insensitive variables corrJVF and $R_{p_{\mathrm{T}}}$, shown in Figure 7.16, which are defined as:

$$\mathrm{corrJVF} = \frac{\sum_k p_{\mathrm{T}}^{\mathrm{trk}_k}(PV_0)}{\sum_l p_{\mathrm{T}}^{\mathrm{trk}_l}(PV_0) + \frac{\sum_{n\geq 1}\sum_l p_{\mathrm{T}}^{\mathrm{trk}_l}(PV_n))}{k \cdot n_{\mathrm{trk}}^{\mathrm{PU}}}} \tag{7.21}$$

$$R_{p_{\mathrm{T}}} = \frac{\sum_k p_{\mathrm{T}}^{\mathrm{trk}_k}(PV_0)}{p_{\mathrm{T}}^{\mathrm{jet}}}. \tag{7.22}$$

The variable corrJVF is primarily defined by the tracks associated to a jet and the reconstructed vertices. In the following, the label "seed" is used for jets and properties prior to the RnS procedure, the seed jets, while the label "RnS" is used for jets and quantities after passing through RnS. A key assumption for EMTopo jets is that

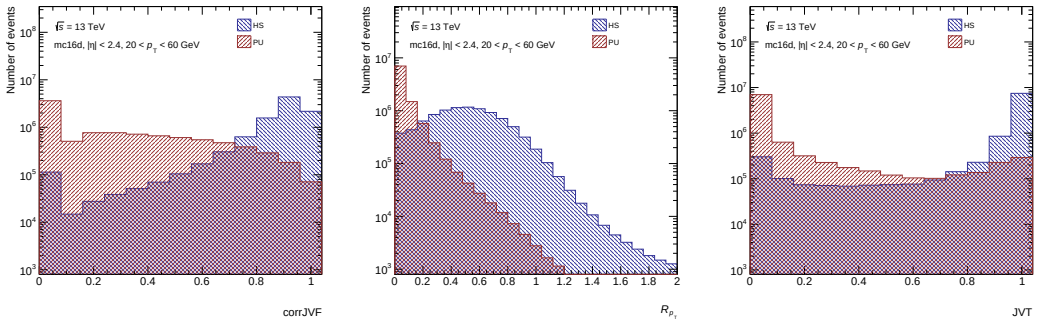

Figure 7.16: Representative distributions of the corrJVF, $R_{p_{\mathrm{T}}}$ and JVT discriminator for hard-scatter (blue) and pile-up (red) jets.

the track response is independent on the jet response, i.e. track measurements are independent on calorimeter measurements as validated in Section 7.6.1. Based on this, the ordering of primary vertices PV_i and track-based variables such as corrJVF are unchanged in the RnS procedure, i.e.

$$\mathrm{corrJVF}^{\mathrm{RnS}} = \mathrm{corrJVF}^{\mathrm{seed}} \tag{7.23}$$

$$PV_i^{\mathrm{seed}} = PV_i^{\mathrm{RnS}}. \tag{7.24}$$

However, the jet momentum p_{T} is modified in RnS, requiring a calculation of $R_{p_{\mathrm{T}}}$ via

$$R_{p_{\mathrm{T}}}^{\mathrm{RnS}} = \frac{\sum_i p_{\mathrm{T}}^{\mathrm{seed,trk}_i}(PV_0)}{p_{\mathrm{T}}^{\mathrm{RnS}}}. \tag{7.25}$$

The JVT score of a jet after passing through RnS, denoted by JVT $^{\mathrm{RnS}}$, is finally obtained by using the JVT likelihood as function of corrJVF$^{\mathrm{seed}}$ and $R_{p_{\mathrm{T}}}^{\mathrm{RnS}}$, shown in Figure 7.17. As a check of the performance of the JVT evaluation, Figure 7.17 also shows the correlation between the original and calculated JVT score (using reconstructed jets, i.e. no RnS is applied), and a very good agreement is observed.

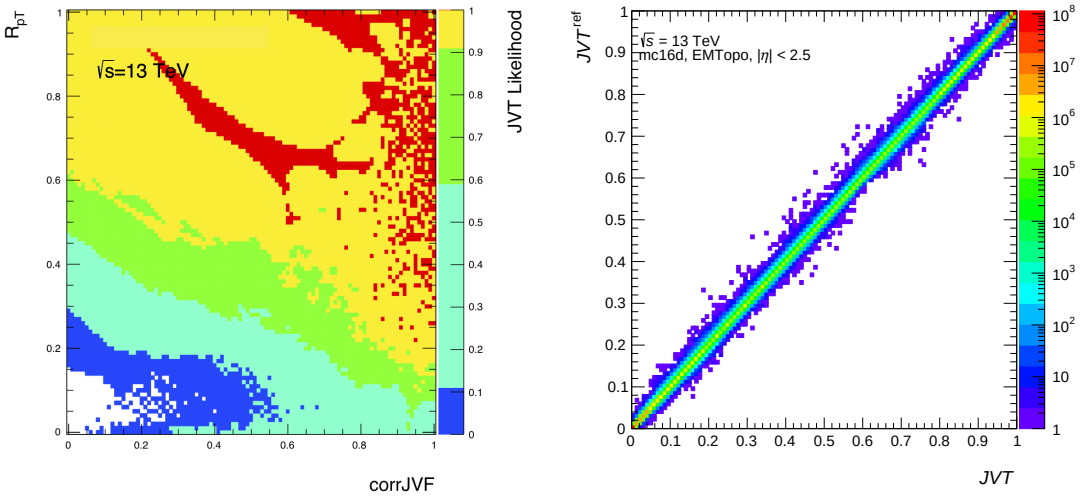

Figure 7.17: Left: Distribution of the JVT discriminator (z-axis) as function of corrJVF and R_{p_T}. Right: Cross-check of the JVT calculation using reco EMTopo jets using Pythia samples of the MC campaign mc16d.

7.6.3 Recalculation of fJVT

The discrimination of hard-scatter and pile-up jets is more challenging in the forward detector region where no tracking information is available. For $|\eta| \geq 2.4$, the forward jet vertex tagging (fJVT) algorithm [128, 163] is used. The calculation of fJVT is based on determining the weighted vectorial sum of $E_\mathrm{T}^\mathrm{miss}$ caused by central pile-up tracks and QCD pile-up jets for each primary vertex PV_i defined as:

$$\begin{aligned}\langle \vec{p}_\mathrm{T}^{\,\mathrm{miss}}\,(PV_i)\rangle &= -\frac{1}{2}(k \cdot \sum_{\mathrm{trk}\,\in\,PV_i} \vec{p}_\mathrm{T}^{\,\mathrm{trk}} + \sum_{\text{PU-jet}\,\in\,PV_i} \vec{p}_\mathrm{T}^{\,\mathrm{jet}}) \\ &= -\frac{1}{2}\left(k \cdot E_\mathrm{T}^{\mathrm{miss,trk}} + E_\mathrm{T}^{\mathrm{miss,jet}}\right),\end{aligned} \tag{7.26}$$

where the empiric factor $k = 2.5$ accounts for differences in the track and jet momenta measurements and the sum over the jets only considers central QCD pile-up jets, selected via the following set of requirements:

- central (covered by tracker): $|\eta| \leq 2.5$
- momentum threshold: $p_\mathrm{T} > 20\,\mathrm{GeV}$
- select pile-up jets: JVT < 0.11
- remove as stochastic pile-up if $p_\mathrm{T} < 35\,\mathrm{GeV}$ and $\Delta R_{p_\mathrm{T}}(PV_k) < 0.2$,

where $\Delta R_{p_\mathrm{T}}(PV_k)$ is the difference of mean and median of the values of $R_{p_\mathrm{T}}(PV_k)$ calculated for each vertex k. $\Delta R_{p_\mathrm{T}}(PV_k)$ tends to be large if the tracks of a jet originate from different vertices, as it is the case for stochastic pile-up jets. For each vertex i, the normalised projection of the $E_\mathrm{T}^\mathrm{miss}$ term $\langle \vec{p}_\mathrm{T}^{\,\mathrm{miss}}(PV_i)\rangle$ and the forward jet (fjet) under consideration is calculated via

$$\mathrm{fJVT}(PV_i) = \frac{\langle \vec{p}_\mathrm{T}^{\,\mathrm{miss}}(PV_i)\rangle \cdot \vec{p}_T^{\,\mathrm{fjet}}}{\vec{p}_\mathrm{T}^{\,\mathrm{fjet}} \cdot \vec{p}_\mathrm{T}^{\,\mathrm{f\,jet}}}, \tag{7.27}$$

where a forward jet is considered for $|\eta| \geq 2.5$ and $20 < p_\mathrm{T} < 120\,\mathrm{GeV}$. Forward jets with $p_\mathrm{T} > 120\,\mathrm{GeV}$ are tagged as hard-scatter. The proposition of this approach is that if at least one pile-up vertex PV_i ($i > 0$) is

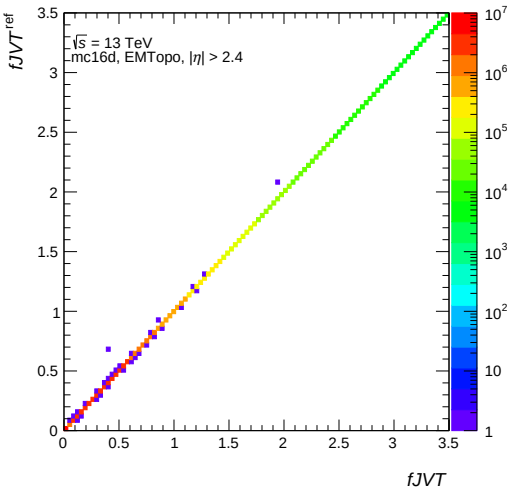

Figure 7.18: Check of the fJVT recalculation algorithm with reco EMTopo jets using Pythia samples of the MC campaign mc16d.

present in the event in which the averaged $E_{\mathrm{T}}^{\mathrm{miss}}$ of tracks and jets is back-to-back in the transverse plane with respect to a forward jet, then the forward jet likely also originates from that vertex PV_i since pile-up dijet events tend to be back-to-back in ϕ. Therefore the fJVT score of a forward jet is given by

$$\mathrm{fJVT} = \max_i \{\mathrm{fJVT}(PV_i)\}. \tag{7.28}$$

A forward jet is tagged as hard-scatter jet if its fJVT score is below a threshold, which is in the range $[0.2, 0.5]$ depending on the used operating point. In terms of RnS, as for the JVT calculation, the track term contributing to the total $E_{\mathrm{T}}^{\mathrm{miss}}$ per primary vertex PV_i is copied from the seed event, i.e.

$$E_{\mathrm{T}}^{\mathrm{miss,trk,RnS}} = E_{\mathrm{T}}^{\mathrm{miss,trk,seed}}, \tag{7.29}$$

since the jet and track responses are independent and the tracks therefore are unchanged in RnS. On the other side, the jet term $\mathrm{MET}_i^{\mathrm{jet}}$ changes within RnS since the transverse momentum p_{T} and the ϕ angle of both central and forward jets are modified in RnS. Thus the probability that a central jet is pile-up tagged changes. This in turn needs to be considered for the fJVT calculation since only central QCD pile-up jets are considered in the $\mathrm{MET}_i^{\mathrm{jet}}$-term. The calculation of the forward jet's fJVT score is done using Equation 7.26-7.28 by inserting $\mathrm{MET}_i^{\mathrm{trk,seed}}$, $\mathrm{MET}_i^{\mathrm{jet,RnS}}$ and $\vec{p}_{\mathrm{T}}^{\,\mathrm{fjet,RnS}}$ as defined above. The re-implementation of the Atlas fJVT algorithm under the given assumptions performs very well as visualized in Figure 7.18.

7.7 Fraction Fit

The RnS technique provides predictions for two topologies corresponding to two different multijet processes, a HS-only and a HS+PU topology. A fraction likelihood fit [238] to un-prescaled single jet triggered data (based on PFlow jet definition) in a suited MJ CR is performed to individually normalise the HS-only and the HS+PU-topologies and to determine the fractions of the multijet topologies. This is needed since the seed event selection has different efficiencies for both the HS-only and the HS+PU topology and, in case of the MC-based RnS, to account for data-simulation differences. Using Poisson statistics, the topologies are varied to match the

data in the MJ CR which in general impacts both the normalisation and shape, i.e. the event yield composition across bins, of the prediction.

Table 7.5: Selection requirements of the MJ CR in single jet triggered data.

Quantity	Cut
$E_{\mathrm{T}}^{\mathrm{miss}}$	$\in [100, 200]$ GeV
$\Delta\phi_{\mathrm{jj}}$	< 2
$\Delta\eta_{\mathrm{jj}}$	> 2.5
m_{jj}	> 400 GeV
leading jet p_{T}	> 80 GeV
leading jet fJVT	< 0.2
subleading jet p_{T}	> 50 GeV
subleading jet fJVT	< 0.2
third-leading jet p_{T}	< 25 GeV
$H_{\mathrm{T}}^{\mathrm{miss}}$	≥ 0 GeV
$E_{\mathrm{T}}^{\mathrm{miss,soft}}$	< 20 GeV

The MJ CR is defined as a loose multijet-enriched preselection, summarised in Table 7.5, and chosen to be inclusive for both the HS-only and the HS+PU topologies, dominated by multijet events and orthogonal to the SR. In order to get a valid normalisation of both topologies, the distribution in the MJ CR which is used for normalisation is required to discriminate between the HS-only and the HS+PU topology, providing sufficient statistics and the event yields of the HS-only and HS+PU topology should be of the same order of magnitude. A possible choice is the separation in the transverse plane between the two leading jets, $\Delta\phi_{\mathrm{jj}}$, which is separating between the HS-only and the HS+PU-topology since both topologies have a different underlying ϕ-structure: hard-scatter jets tend to be roughly back-to-back in ϕ due to the typical dijet structure of multijet processes. In contrast, events with hard-scatter and pile-up jet contributions have an uncorrelated structure in ϕ. However, in order to match the $E_{\mathrm{T}}^{\mathrm{miss}}$ selection in multijet CRs and SRs, smaller values of $\Delta\phi$ between the leading jets are more likely to be selected if a the pile-up tagging in the event failed, as illustrated in Figure 7.2. Since pile-up jets tend to be softer than hard-scatter jets, a certain amount of $E_{\mathrm{T}}^{\mathrm{miss}}$ can only be produced if the two leading jets point roughly into the same direction in ϕ.

The fraction fit is performed in each data-taking year separately to account for different pile-up and trigger conditions. The resulting fractions α_i of the HS-only and the HS+PU contributions are shown in Table 7.6. Smaller fluctuations between the data-taking periods are expected and observed due to fluctuations in both un-prescaled data and simulation and different detector as well as pile-up conditions. Since the highest value of $\langle\mu\rangle$ is observed in 2017 it is expected that the pile-up fraction is the largest in 2017. Further, the pile-up contribution in 2015/16 is expected to be the smallest due to lower pile-up in general. The resulting normalisation factor is given by $\alpha_i' = \alpha_i \cdot (N_{\mathrm{data}} - B_{\text{non-MJ}})/N_i$, where i refers to the HS-only or HS+PU component, N_{data} is the data yield, $B_{\text{non-MJ}}$ the event yield of non-multijet backgrounds and N_i the yield of topology i. In order to normalise the RnS prediction in data, the dominant background processes (Z and W+jets processes, obtained from simulation) are subtracted from the observed single jet triggered data in the multijet-dominated CR. Resulting post-fit distributions for the MC-based RnS technique are shown in Figure 7.19 for the individual data-taking periods. The difference between data-driven and MC-based fractions are caused by different topology definitions, topology purities and highly weighted events especially in case of the data-driven prediction in 2017. The valid extrapolation from the MJ CR to the SR is ensured by an additional normalisation in $E_{\mathrm{T}}^{\mathrm{miss}}$ triggered data close to the SR, see Section 8.2.1.

Table 7.6: Fractions α of the HS-only and the HS+PU topologies obtained in a fraction fit in the MJ CR in single jet triggered PFlow data.

	Data-taking period	HS-only fraction [%]	HS+PU fraction [%]
MC-based	2015/16	32	68
	2017	26	74
	2018	35	65
data-driven	2015/16	45	55
	2017	80	20
	2018	48	52

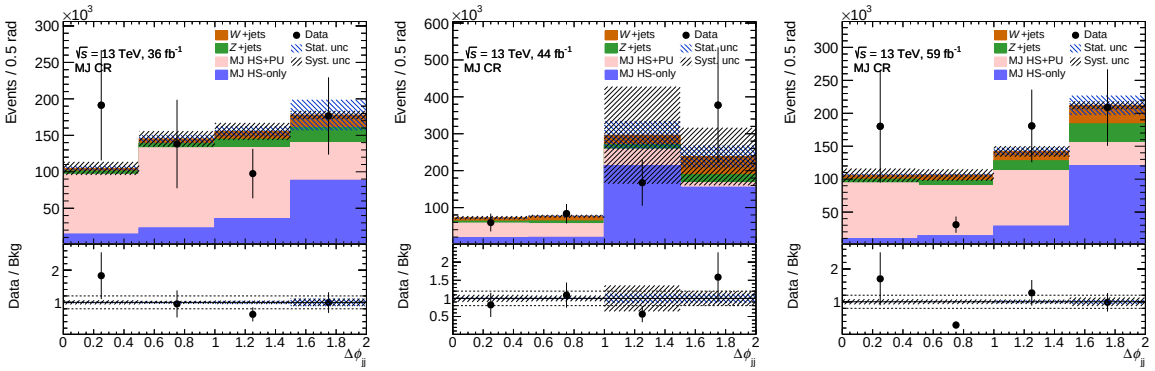

Figure 7.19: Fraction fit for the MC-basesd RnS for data 2015/16 ($\mathcal{L} = 36\,\text{fb}^{-1}$), 2017 ($\mathcal{L} = 44\,\text{fb}^{-1}$) and 2018 ($\mathcal{L} = 59\,\text{fb}^{-1}$) of the HS-only and HS+PU topology in $\Delta\phi_{\text{jj}}$ the MJ CR. While the HS+PU topology is dominant at low $\Delta\phi_{\text{jj}}$ values, the HS-only multijet events accumulate at large $\Delta\phi_{\text{jj}}$ values.

7.8 Trigger Efficiency

In this section a measurement of the $E_{\text{T}}^{\text{miss}}$ trigger efficiency turn-on curve measured in prescaled single jet triggered data is presented. Both the MC-based and the data-driven RnS techniques are normalised in single jet triggered data. Un-prescaled single jet triggered data is not affected by any relevant HLT trigger in-efficiency. Also any L1 trigger efficieny turn-on is negligible. In contrast, as described in Section 6.2.1, the $E_{\text{T}}^{\text{miss}}$ trigger efficiency for $E_{\text{T}}^{\text{miss}} \sim 150\,\text{GeV}$ can be significantly below 100 %, which is relevant for parts of the SR and CRs defined at low $E_{\text{T}}^{\text{miss}}$. Therefore every individual smeared multijet event from RnS must be associated with a trigger efficiency scale factor which is obtained from measurements of the trigger efficiency turn-on curves. The parametrised trigger efficiencies are mainly used to compare the multijet prediction from RnS in low $E_{\text{T}}^{\text{miss}}$ CRs in $E_{\text{T}}^{\text{miss}}$ triggered events but the trigger efficiencies are also applied in the SRs though these are mainly defined in the $E_{\text{T}}^{\text{miss}}$ trigger efficiency plateau, see Figure 6.4. Section 7.8 describes a two-dimensional parmetrisation, which is used for the RnS multijet estimate in the full Run II VBF+$E_{\text{T}}^{\text{miss}}$ analysis. Appendix A.4 presents alternative $E_{\text{T}}^{\text{miss}}$ trigger efficiency parametrisations using more sophisticated MVA techniques for future usages. In RnS, after the jet smearing step, only a limited fraction of the information compared to the trigger level are available, making it challenging to emulate the real efficiency of the $E_{\text{T}}^{\text{miss}}$ trigger. The inputs for the $E_{\text{T}}^{\text{miss}}$ trigger decision are mainly online quantities, meaning amongst others prior to calibration or pile-up removal. Therefore, a two-dimensional parametrisation based on two variables, the hadronic activity H_{T} and the missing hadronic activity $H_{\text{T}}^{\text{miss}}$ prior to pile-up removal, quantities which are close to the trigger-relevant online quantities, is introduced. The $E_{\text{T}}^{\text{miss}}$ trigger efficiency $\epsilon_{\text{Trigger}}$ is derived for each data-taking period separately in data in order to consider the different detector, trigger and pile-up conditions in the years 2015 to 2018. Small-R EMTopo jets are used which are reconstructed with the anti-k_t algorithm. The trigger efficiency $\epsilon_{\text{Trigger}}$

is defined in bins of H_{T} and $H_{\mathrm{T}}^{\mathrm{miss}}$ for a given selection as

$$\epsilon_{\mathrm{Trigger}} = \frac{N_{E_{\mathrm{T}}^{\mathrm{miss}}\text{ + single jet}}}{N_{\text{single jet}}}, \tag{7.30}$$

i.e. it is the ratio of the number of $E_{\mathrm{T}}^{\mathrm{miss}}$-triggered and single jet triggered events $N_{E_{\mathrm{T}}^{\mathrm{miss}}\text{ + single jet}}$ and single jet triggered events $N_{\text{single jet}}$. The calculation of $\epsilon_{\mathrm{Trigger}}$ relies on prescaled single jet triggered data for which it is known if the $E_{\mathrm{T}}^{\mathrm{miss}}$ trigger was activated or not. A loose event selection is used for the determination of $\epsilon_{\mathrm{trigger}}$ including good run list, standard jet, event and detector cleaning cuts, a photon and baseline lepton veto, $E_{\mathrm{T}}^{\mathrm{soft}} < 20\,\mathrm{GeV}$, leading jet $p_{\mathrm{T}} > 80\,\mathrm{GeV}$ and subleading jet $p_{\mathrm{T}} > 50\,\mathrm{GeV}$ and $\Delta\phi_{\mathrm{jj}} < 2.5$ if $n_{\mathrm{jet}} > 1$. In the first place no veto on a third jet is placed. It was also studied how the trigger efficiency looks like with a third jet veto of the form third-jet $p_{\mathrm{T}} < 25\,\mathrm{GeV}$ applied but this reduces sample statistics significantly. A photon and baseline lepton veto is used to suppress non-multijet processes. However, the effect of non-multijet backgrounds in single jet triggered data such as V+jets is negligible for the mainly topology dependent trigger efficiency emulation (the trigger should not distinguish between a V+jets event or a multijet event with same kinematics). The relative uncertainty $\delta\epsilon_{\mathrm{trigger}}$ from the two-dimensional parametrisations (maps) is obtained as a function of $E_{\mathrm{T}}^{\mathrm{miss}}$. For each $E_{\mathrm{T}}^{\mathrm{miss}}$-bin the quantity

$$\delta\epsilon_{\mathrm{Trigger}} = \frac{|\epsilon_{\mathrm{real}} - \epsilon_{\mathrm{map}}|}{\epsilon_{\mathrm{map}}} \tag{7.31}$$

is calculated, where ϵ_{real} is the "real" trigger efficiency defined as the ratio of the number of $E_{\mathrm{T}}^{\mathrm{miss}}$-triggered events $N_{\mathrm{triggered}}$ and all collected events N_{all}, i.e.

$$\epsilon_{\mathrm{real}} = \frac{N_{E_{\mathrm{T}}^{\mathrm{miss}}\text{ + single jet}}(E_{\mathrm{T}}^{\mathrm{miss}})}{N_{\text{single jet}}(E_{\mathrm{T}}^{\mathrm{miss}})} \tag{7.32}$$

and ϵ_{map} is defined as

$$\epsilon_{\mathrm{map}} = \frac{(N_{\text{single jet}} \cdot \epsilon_{\mathrm{Trigger}})(E_{\mathrm{T}}^{\mathrm{miss}})}{N_{\text{single jet}}(E_{\mathrm{T}}^{\mathrm{miss}})}. \tag{7.33}$$

The uncertainty $\delta\epsilon_{\mathrm{trigger}}$ is treated as symmetric around $\epsilon_{\mathrm{trigger}}$. For the relevant $E_{\mathrm{T}}^{\mathrm{miss}}$ bins the relative uncertainties are given in Table 7.7. The trigger efficiency uncertainties are found to be $< 3\,\%$ for $E_{\mathrm{T}}^{\mathrm{miss}} > 200\,\mathrm{GeV}$, which makes up the majority and most sensitive part of the SR. In the range 160 to 200 GeV the uncertainty increases, especially for the data-taking periods 2017 and 2018, while the uncertainty for 2015/16 further increases for $E_{\mathrm{T}}^{\mathrm{miss}} < 160\,\mathrm{GeV}$. The $E_{\mathrm{T}}^{\mathrm{miss}}$ trigger efficiencies obtained from single jet triggered multijet events in inclusive data for the data-taking periods 2015 to 2018 are shown in Figure 7.20-7.22. The corresponding $E_{\mathrm{T}}^{\mathrm{miss}}$ trigger efficiency uncertainties as a function of the offline $E_{\mathrm{T}}^{\mathrm{miss}}$ are shown as well. The efficiency $\epsilon_{\mathrm{Trigger}}$ of the trigger increases with increasing values of $H_{\mathrm{T}}^{\mathrm{miss}}$, which closely correlates with $E_{\mathrm{T}}^{\mathrm{miss}}$ and H_{T}. Especially it is $H_{\mathrm{T}}^{\mathrm{miss}} \leq H_{\mathrm{T}}$ - by definition there cannot be more missing hadronic activity in the event than hadronic activity. Since the parametrisation of the trigger efficiency uncertainty is done with variables which are not used in the parametrisation, it is avoided to obtain artificially small uncertainties, for which $E_{\mathrm{T}}^{\mathrm{miss}}$ is a suited candidate which in general differs from $H_{\mathrm{T}}^{\mathrm{miss}}$.

7.9 Statistical and Systematic Uncertainties

Systematic uncertainties are uncertainties which occur due to the experimental setup or theoretical assumptions. They have to be distinguished from statistical uncertainties which are caused by the limited size of the data

Table 7.7: Relative uncertainties of the $E_{\mathrm{T}}^{\mathrm{miss}}$ trigger efficiencies of the two dimensional H_{T}-$H_{\mathrm{T}}^{\mathrm{miss}}$-parametrisation for the $E_{\mathrm{T}}^{\mathrm{miss}}$ bins relevant for the SR.

Period	$E_{\mathrm{T}}^{\mathrm{miss}}$ [GeV]	Rel. unc. [%]
15/16	[160, 200]	3.7
	> 200	1.4
17	[160, 200]	16.6
	> 200	2.8
18	[160, 200]	16.1
	> 200	2.6

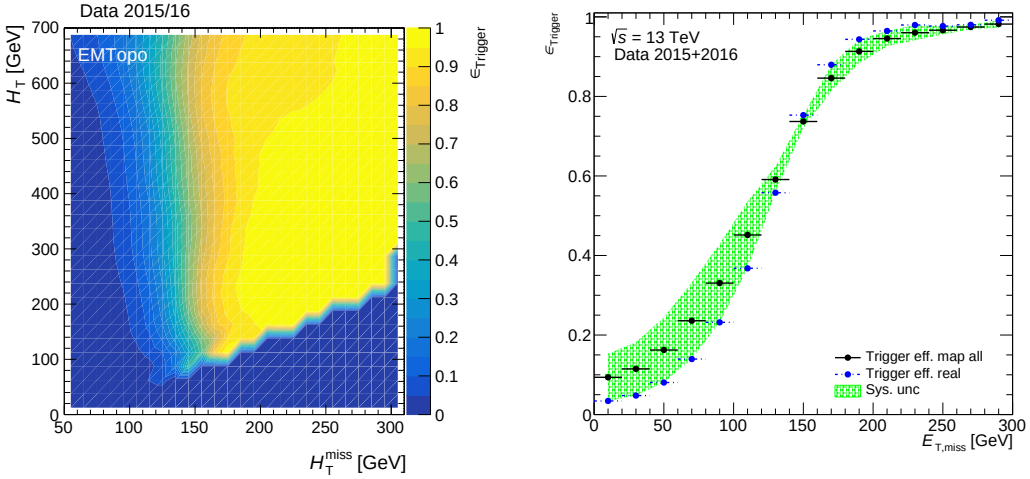

Figure 7.20: Efficiency of the $E_{\mathrm{T}}^{\mathrm{miss}}$ trigger binned in H_{T} and $H_{\mathrm{T}}^{\mathrm{miss}}$ derived in multijet events in 2015 and 2016 data and $E_{\mathrm{T}}^{\mathrm{miss}}$ trigger efficiency uncertainty as function of offline $E_{\mathrm{T}}^{\mathrm{miss}}$.

sample. Usually, the evaluation of systematic uncertainties and their handling in the analysis fit model, eventually due to complex correlations, is one of the biggest challenges in searches for new physics. This section presents statistical and systematic uncertainties of the RnS sampling technique and discusses if they are negligible or need to be propagated to the SR abd CR prediction.

7.9.1 Bootstrapping

A seed event boostrapping is used to determine the most realistic statistical uncertainty of the RnS prediction including the effect of limited statistics of the RnS seed sample. Due to multiple seed event smearing, the RnS prediction with n events in SR bin i can be caused by m seed events with weights $w > 0$, whereby $m < n$, so that some seed events enter the SR bin i multiple times. This can be a coincidence or it can be a feature of the seed level event (e.g. where a jet loss by a JVT mis-tag is very likely if a jet fluctuates slightly in p_{T} below 60 GeV, faking a VBF topology). A proper bootstrapping is in particular also needed for the MC-based RnS technique since the pile-up events are unchanged and thus identicial copies of pile-up events with different overlayed hard-scatter processes may enter the SR multiple times. Therefore it is in general important to consider the seed sample statistics in the statistical uncertainty which would not be considered if just $\delta w = \sqrt{\sum_i w_i^2}$ is used as statistical uncertainty, where w is the event weight, but can be achieved with a bootstrapping procedure [239, 240]. However, if events in the SR have small weights w and the prediction in some SR bins is not caused by

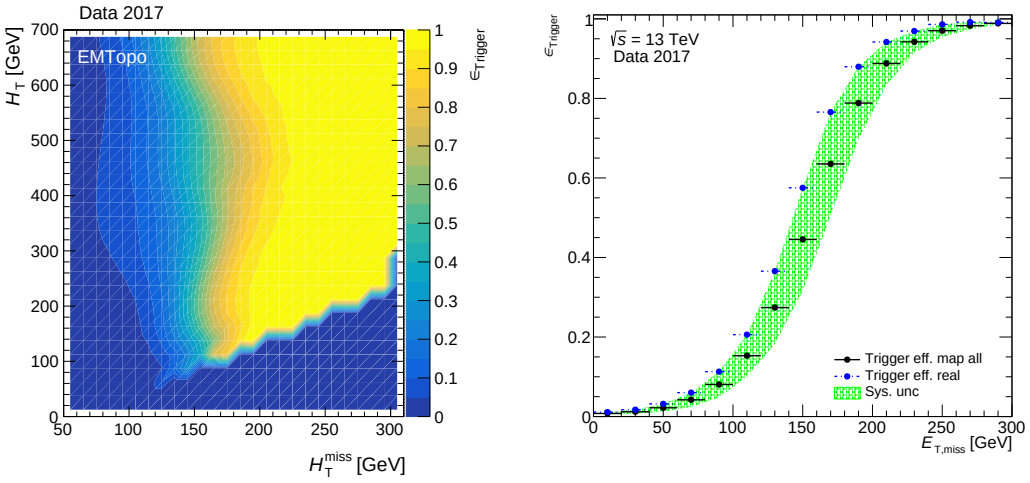

Figure 7.21: Efficiency of the $E_{\mathrm{T}}^{\mathrm{miss}}$ trigger binned in H_{T} and $H_{\mathrm{T}}^{\mathrm{miss}}$ derived in multijet events in 2017 data and $E_{\mathrm{T}}^{\mathrm{miss}}$ trigger efficiency uncertainty as function of offline $E_{\mathrm{T}}^{\mathrm{miss}}$.

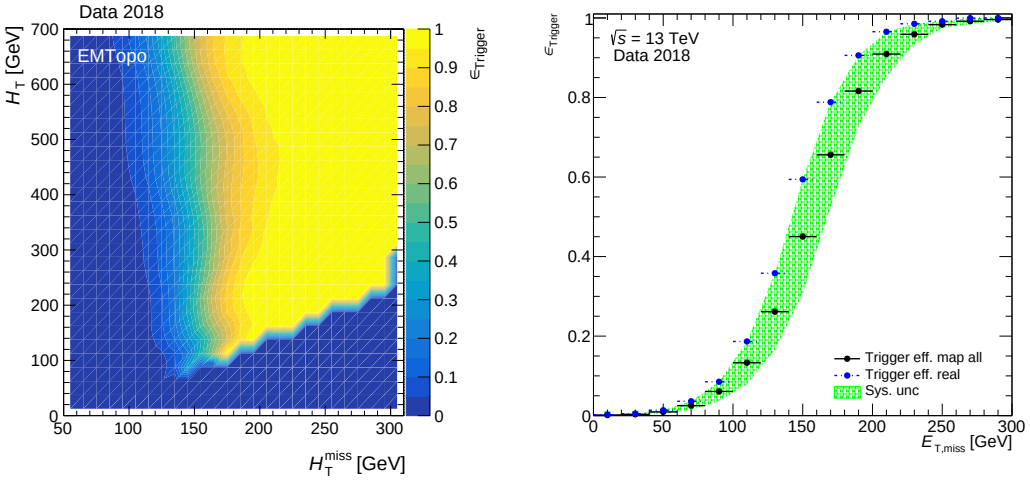

Figure 7.22: Efficiency of the $E_{\mathrm{T}}^{\mathrm{miss}}$ trigger binned in H_{T} and $H_{\mathrm{T}}^{\mathrm{miss}}$ derived in multijet events in 2018 data and $E_{\mathrm{T}}^{\mathrm{miss}}$ trigger efficiency uncertainty as function of offline $E_{\mathrm{T}}^{\mathrm{miss}}$.

single (highly-weighted) seed events, the difference between δw and a proper bootstrapping uncertainty should be small. In the chosen bootstrapping technique, seed events which enter the SR bins after the smearing are combined to single contributions with a weight equal to the sum of the individual weights from each SR bin to which the particular seed event is contributing. From the ensemble of seed events contributing to the SR, 1000 pseudo-data sets with the same number of events are randomly drawn, allowing for seed events to be selected multiple times and thus the event yield in each SR bin can fluctuate. The standard deviation of the pseudo-data set ensemble is used as the estimator for the statistical uncertainty which is mostly $< 10\,\%$ in the different SR bins (more details can be found in Table 8.7).

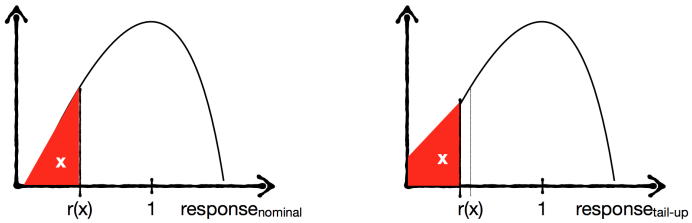

Figure 7.23: Sketch of the simultaneous smearing of the nominal prediction and its systematic variations (here tail-up) using the same random percentile of a jet response distribution.

7.9.2 Jet Energy Resolution Uncertainties

Two individual systematics related to the modelling of the jet energy response are currently considered in RnS:

- Gaussian core-up variation by 15 % (core-up)
- non-Gaussian tail-up variation by 50 % (tail-up)

As described in Section 7.4, the jet response distributions are derived in simulation and validated with a data-driven approach. The RnS prediction without systematic variation is termed in the following as nominal. The core-up variation widens the core of the fitted Gaussian curve of the jet response distribution by 15 %, while the integral of the Gaussian distribution remains constant. Similar, the tail-up variation enlarges the non-Gaussian tails by 50 %, making more extreme jet mis-measurements more likely. It should be noted that the upper and lower non-Gaussian tails of the jet response are not symmetric and thus affects jet down- and up-fluctuations in different ways. In particular the third jet veto at $p_{\mathrm{T}} = 25\,\mathrm{GeV}$ used in most of the analysis bins (1-10 and 14-16) is sensitive to these variations. Further, it is assumed that the corresponding tail-down and core-down variations are equal to tail-up and core-up, respectively, i.e. the core and tail variations are assumed to be symmetric. A measurement of the tail-up and core-up scale factors for the systematic variations is presented in Section A.2. While the non-Gaussian core is relatively good modelled and thus a 15 % uncertainty is really conservative, a proper modelling of the non-Gaussian tails is very challenging due to different physics effects causing the tails and biases such as p_{T} thresholds. An uncertainty of 50 % is assigned. The statistical uncertainties are correlated along the nominal prediction and the variations. Without correlated statistics, the independent statistical fluctuations based on the random smearing in RnS could not be separated from the impact of the systematic variation, thus the systematic variations would contain to a large amount a statistical component and based on this may be overestimated. Therefore, the simultaneous smearing, which was used the first time for the full Run II 140 fb^{-1} analysis, helps to reduce the multijet uncertainties. This is achieved by drawing a random number $x \in [0, 1]$ for each smeared jet and taking the jet response $\mathcal{R}(x)$ belonging to the percentile of the corresponding jet response distribution, as shown in Figure 7.23. Distribution percentiles describe the percentage of values that fall below a given score in a distribution: If a value r lies at the n^{th} percentile of a distribution, then the value r is greater than n % of the other values. The resulting symmetrised, systematic variations are treated as fully correlated across all SR bins. The evaluation of the RnS jet response systematic uncertainties in the MJ CR are shown in Figure 7.24. The total uncertainty band is obtained by adding the uncertainties in quadrature:

$$\delta_{\mathrm{response,rel}} = \sqrt{\left(\frac{n_{\text{core-up}} - n_{\text{nominal}}}{n_{\text{core-up}} + n_{\text{nominal}}}\right)^2 + \left(\frac{n_{\text{tail-up}} - n_{\text{nominal}}}{n_{\text{tail-up}} + n_{\text{nominal}}}\right)^2}, \tag{7.34}$$

where n_i represents the event yield of the respective component for $i \in \{\text{nominal}, \text{core-up}, \text{tail-up}\}$. The same procedure is used in all relevant analysis regions (before applying the trigger efficiency scale factors).

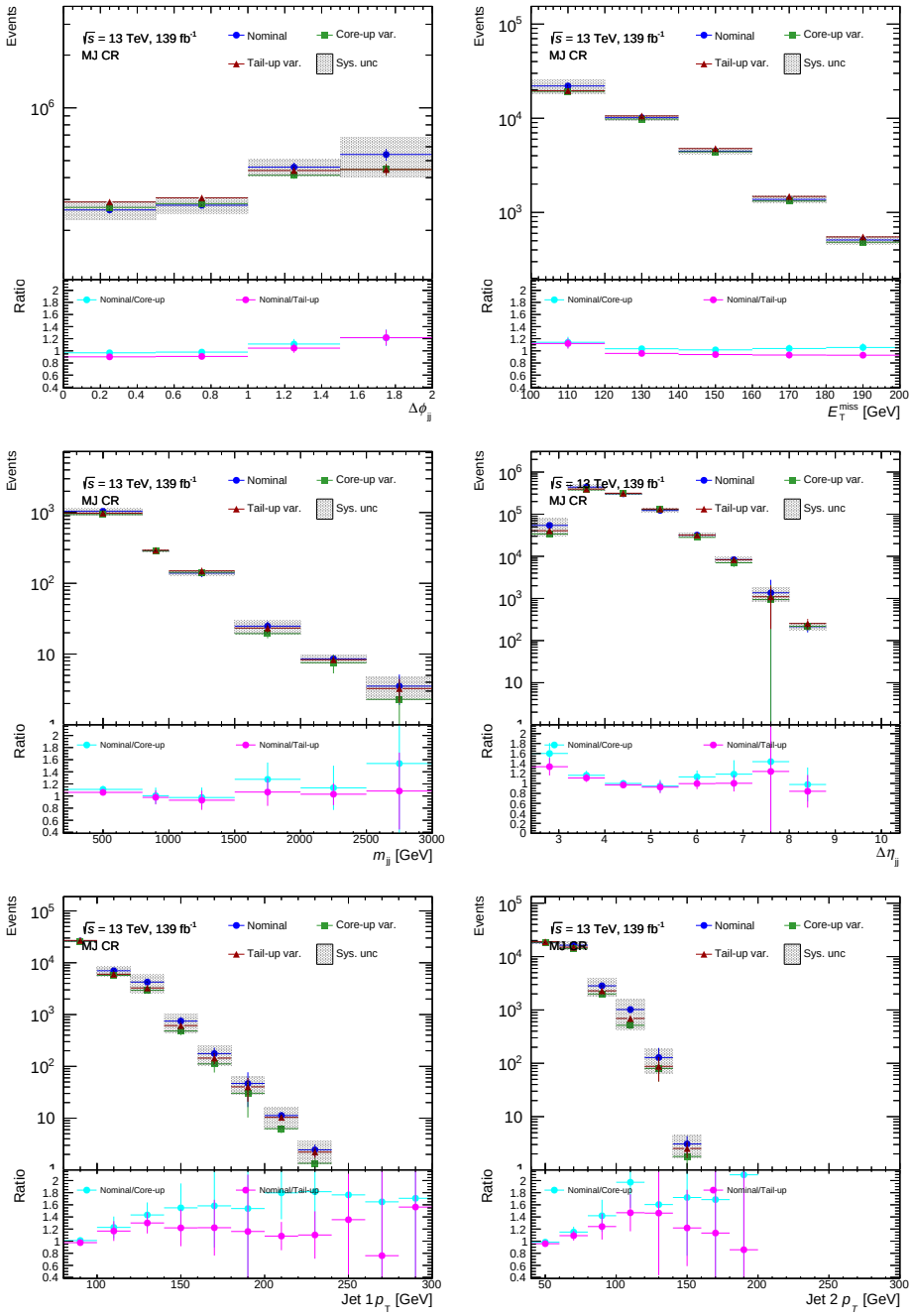

Figure 7.24: Evaluation of the jet response core-up (50 %) and jet response tail-up (15 %) systematic uncertainties of RnS in the MJ CR for Pythia samples from the MC simulation campaign mc16d.

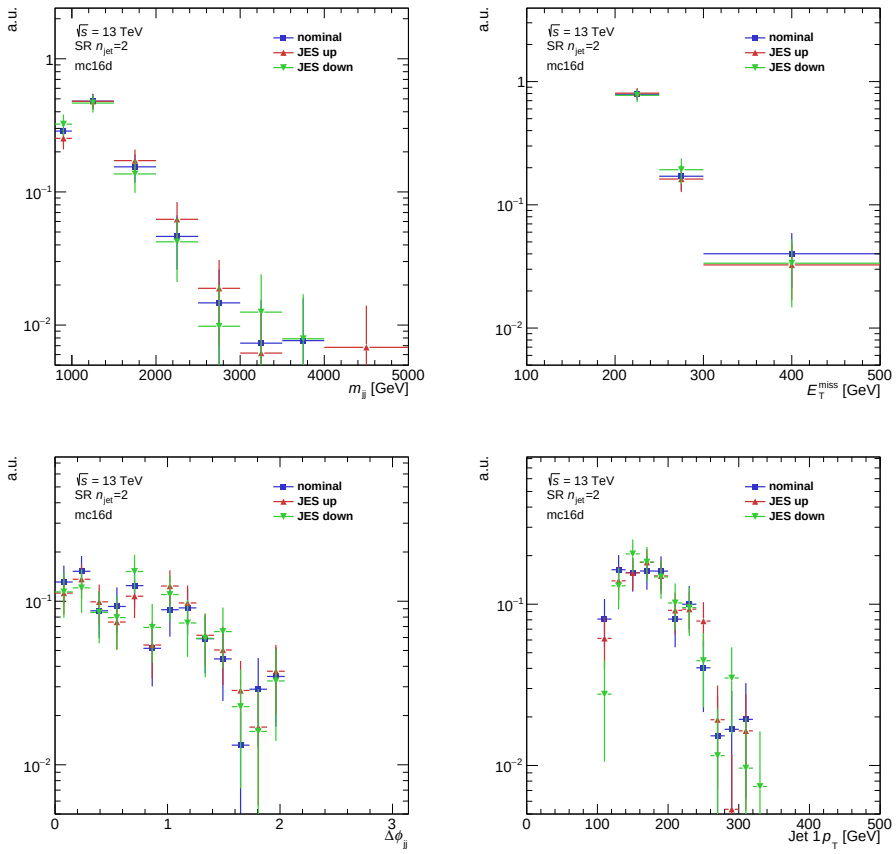

Figure 7.25: Impact of a flat 4 % up and down JES systematic variation on the kinematic shapes of m_{jj}, E_T^{miss}, $\Delta\phi_{jj}$ and leading jet p_T in the inclusive dijet SR with respect to the nominal prediction.

7.9.3 Jet Energy Scale Uncertainty

A potential impact of the JES uncertainty on the SR RnS prediction is studied to consider potential data and MC differences. For this test, the JES uncertainty is set to ±4 % flat in jet p_T and η. This is not a proper parametrisation of the true JES uncertainty but it is rather conservative. As for the jet response uncertainty, the statistics of the JES up and down variations are fully correlated with the nominal prediction, i.e. there is no statistical component due to different seeds. The impact of up and down systematic variations on the m_{jj}, E_T^{miss}, $\Delta\phi_{jj}$ and leading jet p_T shape in the inclusive dijet SR (bin $1-10$) is shown in Figure 7.25. No significant impact is observed. Thus, no extra RnS shape uncertainty is used to account for the JES uncertainty.

7.9.4 Jet Response Tail Threshold

The non-Gaussian tails of the jet response distribution are only considered if the jet has a sufficiently high p_T in order to ensure that in particular the lower tail is representative and free of a bias due to a threshold effect of the reco jet p_T threshold. This lower momentum border is denoted as $p_{T,min}$. For $p_T < p_{T,min}$, only the core obtained via a Gaussian fit to the jet response distribution is considered. It was studied if the choice of $p_{T,min}$ needs to be included as an additional systematic uncertainty for the RnS multijet prediction. No significant difference which

exceeds statistical uncertainties between $p_{\mathrm{T,min}} = 30\,\mathrm{GeV}$ and $p_{\mathrm{T,min}} = 60\,\mathrm{GeV}$ could be observed, neither in the loose MJ CR nor in the SR. Therefore the choice of $p_{\mathrm{T,min}}$ is not considered as an individual RnS multijet systematic. A choice of $p_{\mathrm{T,min}} = 30\,\mathrm{GeV}$ is chosen as the most conservative approach. Threshold effects which bias the lower tail mainly affect pile-up jets and therefore has, with exception of a third jet veto, no impact on SR topologies.

7.9.5 Fraction Fit Uncertainties

The result of the fraction fit, see Section 7.7, may depend on the binning, the region or the variable used to normalise the HS-only and HS+PU topology. In addition, the fit itself setting the fractions of the HS-only and the HS+PU topologies has an uncertainty. However, the fit errors are not meaningful since un-prescaled data is used to fit the fractions of the HS-only and HS+PU predictions [241]. The uncertainty of the data is given by the prescale weight and thus is mostly larger than the corresponding Poisson uncertainty of the event yield. However, the technical implementation of the fraction fit assumes Poisson statistics for both data and MC and thus underestimates the statistical data uncertainty. No uncertainty from the fraction fit is directly considered in the RnS multijet background SR prediction. No significant shape influence on the SR is expected from fraction fit uncertainties since the SR is dominated by the HS-only component. Potential event yield influences are absorbed in the normalisation process in the multijet CRs in $E_{\mathrm{T}}^{\mathrm{miss}}$ triggered data and the associated non-closure uncertainty, see Section 8.2.1.

7.10 Closure Checks

The performance check of the multijet prediction obtained with the RnS technique is performed via closure plots in which a comparison of the RnS prediction to data in suited CRs is shown for the individual data-taking periods and the full data set. The data used for closure plots is triggered with single jet triggers, see Section 7.8, and un-prescaled following the procedure described in Section 7.2.2. To compare the RnS multijet prediction to data, also the other relevant backgrounds are considered. The V+jets background is used pre-fit, i.e. before constraining them in their individual CRs as implemented in the analysis fit model, which is valid due to the small contribution of these non-multijet backgrounds in the multijet CR. Other minor backgrounds such as top quark events or multiboson processes can be neglected. Since the RnS prediction is compared to single jet triggered data or simulation, the trigger efficiency as described in Section 7.8 is not applied in these closure plots. The HS+PU topology is drawn in red, while the HS-only topology is shown in blue.

Performance plots for the MC-based RnS technique in the multijet CR as defined in Section 7.7 in single jet triggered data are shown in Figure 7.26-7.26. In addition, closure plots in MC are shown in Appendix A.5. The same is shown with statistical uncertainties only for the data-driven RnS technique in Figure 7.30-7.33.

7.11 Signal Region Prediction

In this section the characteristics of multijet events entering the SR is analysed. Trigger efficiency weights and scale factors from a normalisation in $E_{\mathrm{T}}^{\mathrm{miss}}$-triggered data, see Section 8.2.1, are not applied, i.e. changes in event count and small changes in the observable's shapes are expected for the final RnS multijet prediction. While these effects are evaluated year-by-year, the plots in this section show the summed RnS predictions from the individual years. The SR distributions for the dijet SR (bin 1–10 and 14–16) and the $n_{\mathrm{jet}} = \{3, 4\}$ SR (bin 11–13) are shown in Figure 7.34 and Figure 7.35.

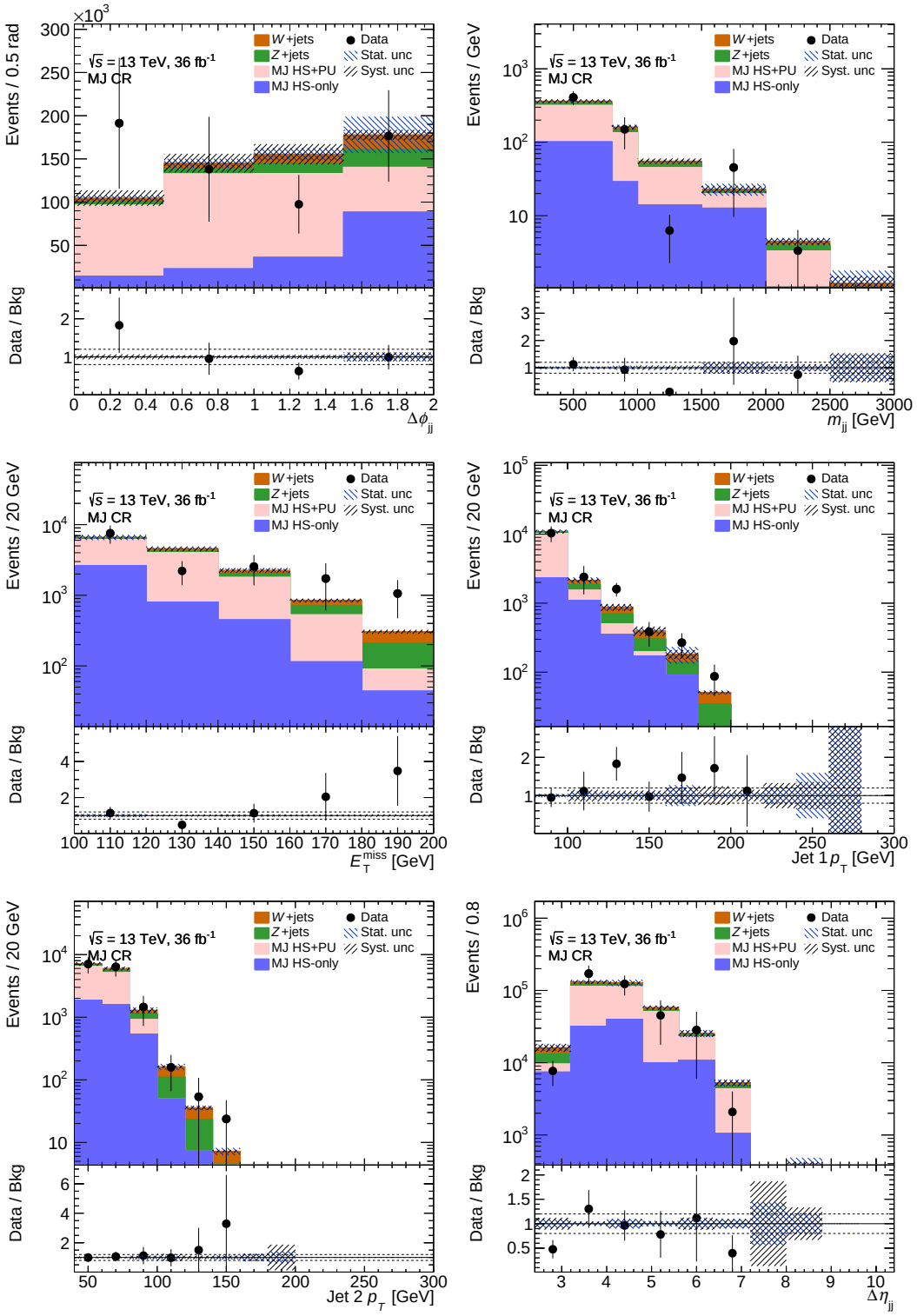

Figure 7.26: Closure checks of the MC-based RnS prediction in the MJ CR for the 2015/16 data set corresponding to $\mathcal{L} = 36\,\text{fb}^{-1}$.

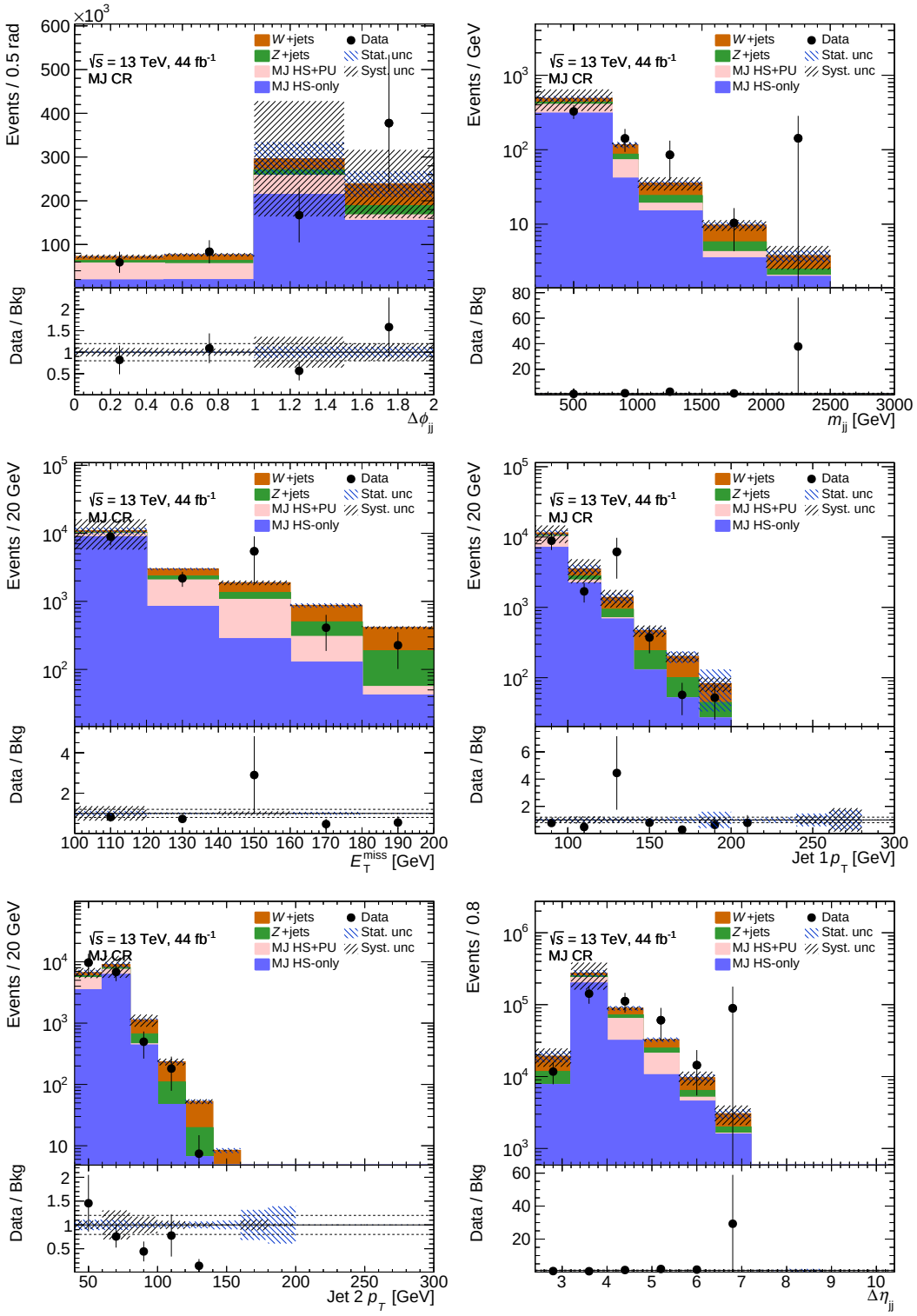

Figure 7.27: Closure checks of the MC-based RnS prediction in the MJ CR for the 2017 data set corresponding to $\mathcal{L} = 44\,\text{fb}^{-1}$.

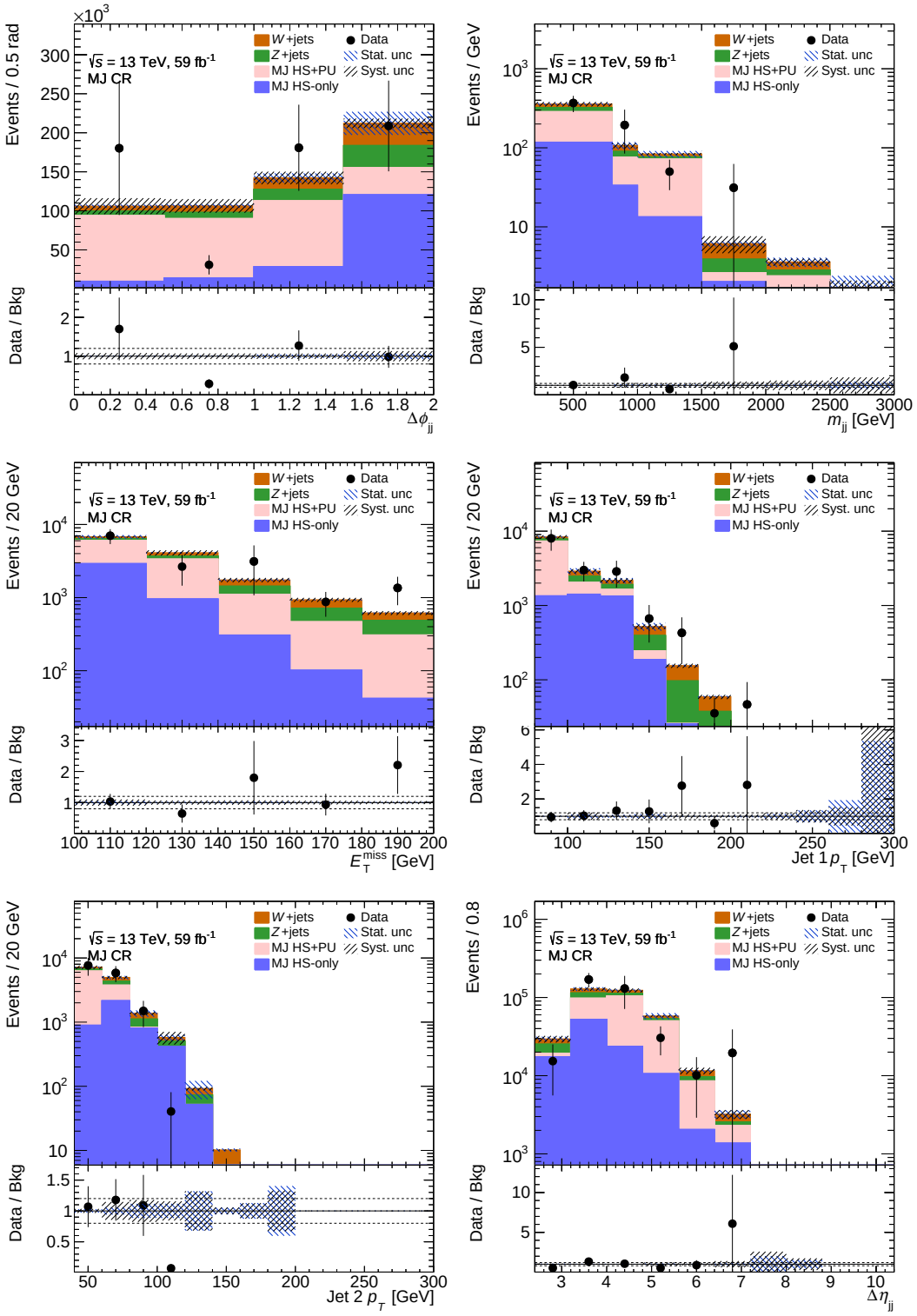

Figure 7.28: Closure checks of the MC-based RnS prediction in the MJ CR for the 2018 data set corresponding to $\mathcal{L} = 59\,\text{fb}^{-1}$.

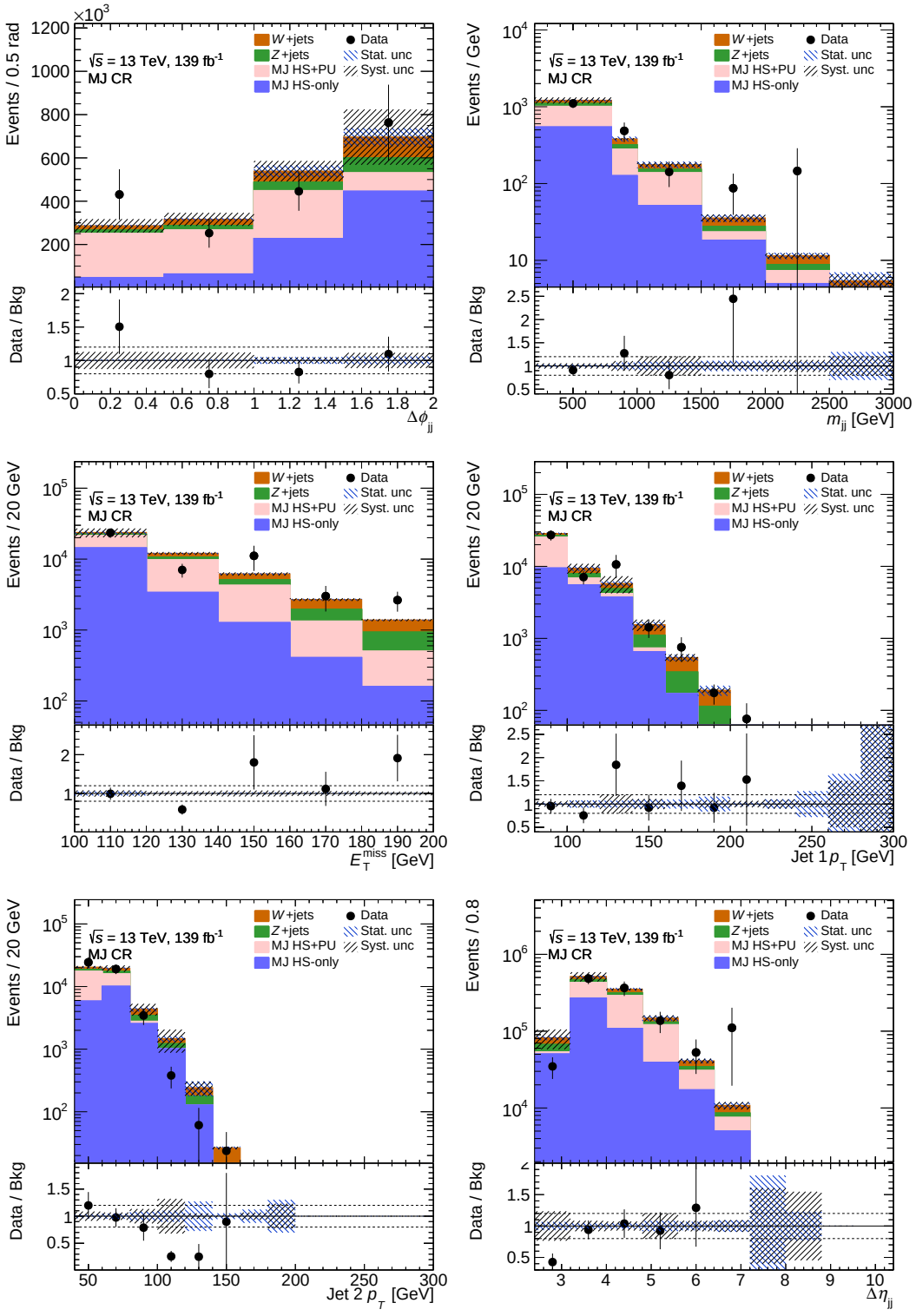

Figure 7.29: Closure checks of the MC-based RnS prediction in the MJ CR for the full data set corresponding to $\mathcal{L} = 139\,\text{fb}^{-1}$, which is the sum of the prediction for the individual data-taking periods between 2015 and 2018.

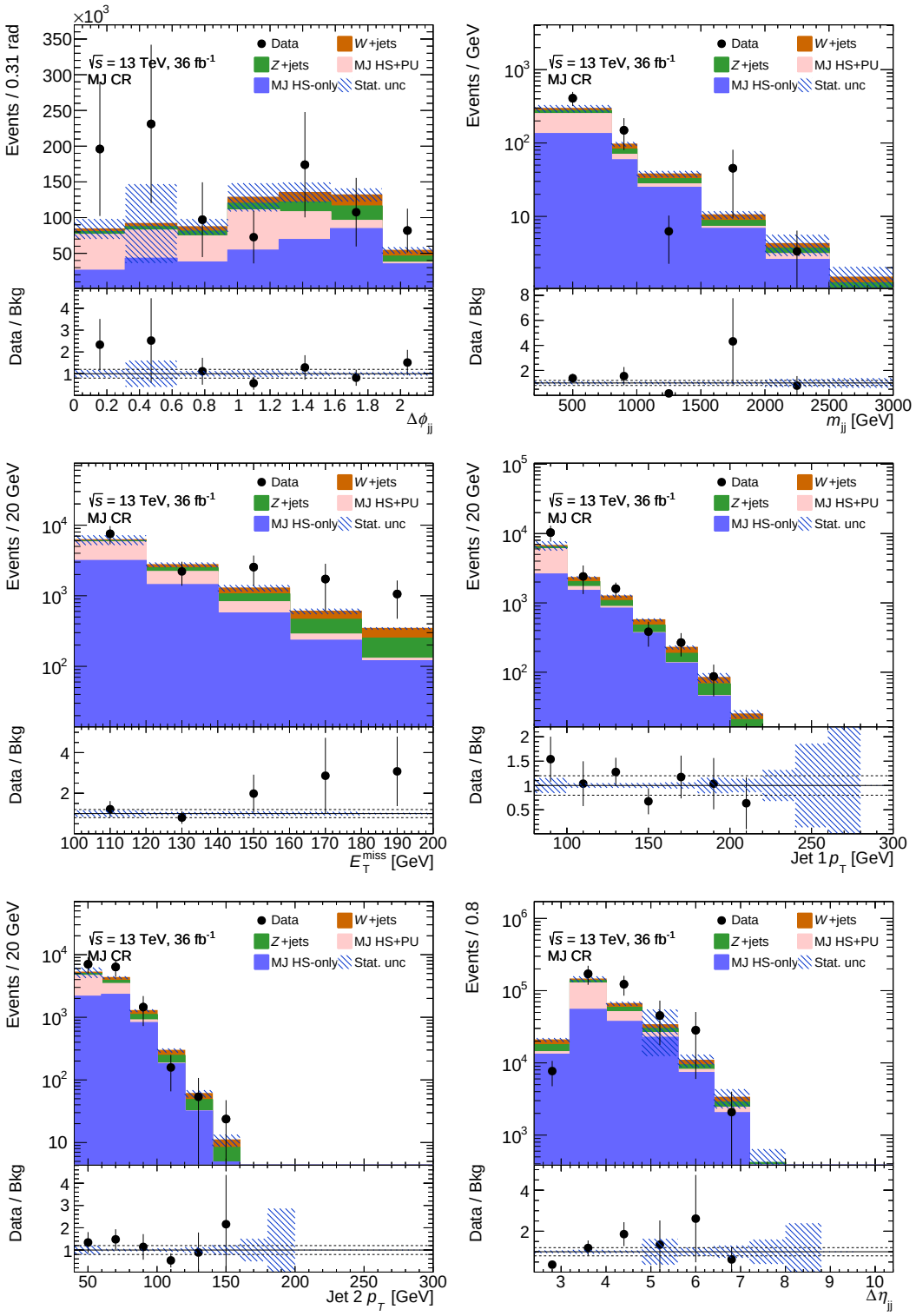

Figure 7.30: Closure checks of the data-driven RnS prediction in the MJ CR for the 2015/16 data set corresponding to $\mathcal{L} = 36\,\text{fb}^{-1}$.

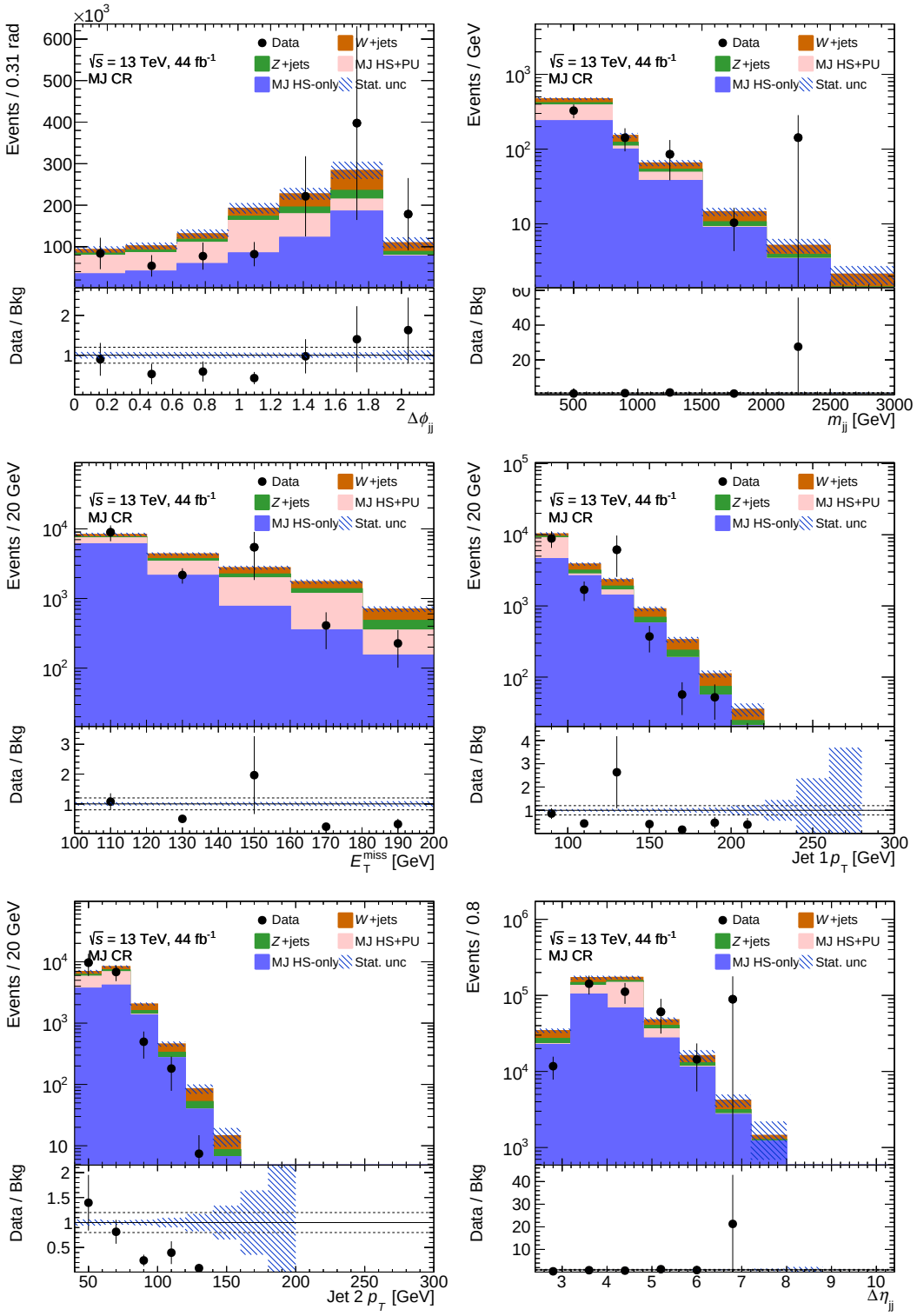

Figure 7.31: Closure checks of the data-driven RnS prediction in the MJ CR for the 2017 data set corresponding to $\mathcal{L} = 44\,\text{fb}^{-1}$.

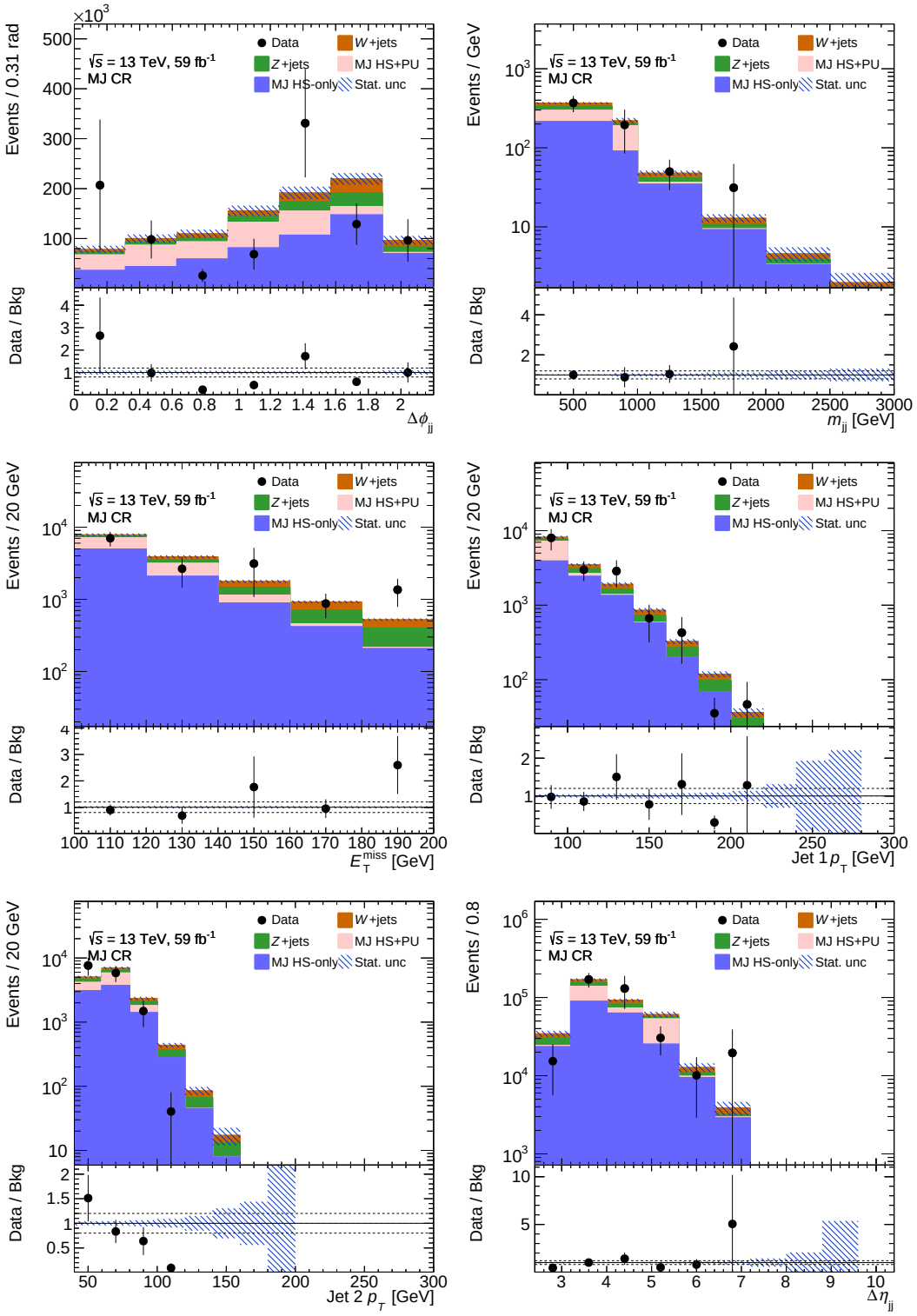

Figure 7.32: Closure checks of the data-driven RnS prediction in the MJ CR for the 2018 data set corresponding to $\mathcal{L} = 59\,\text{fb}^{-1}$.

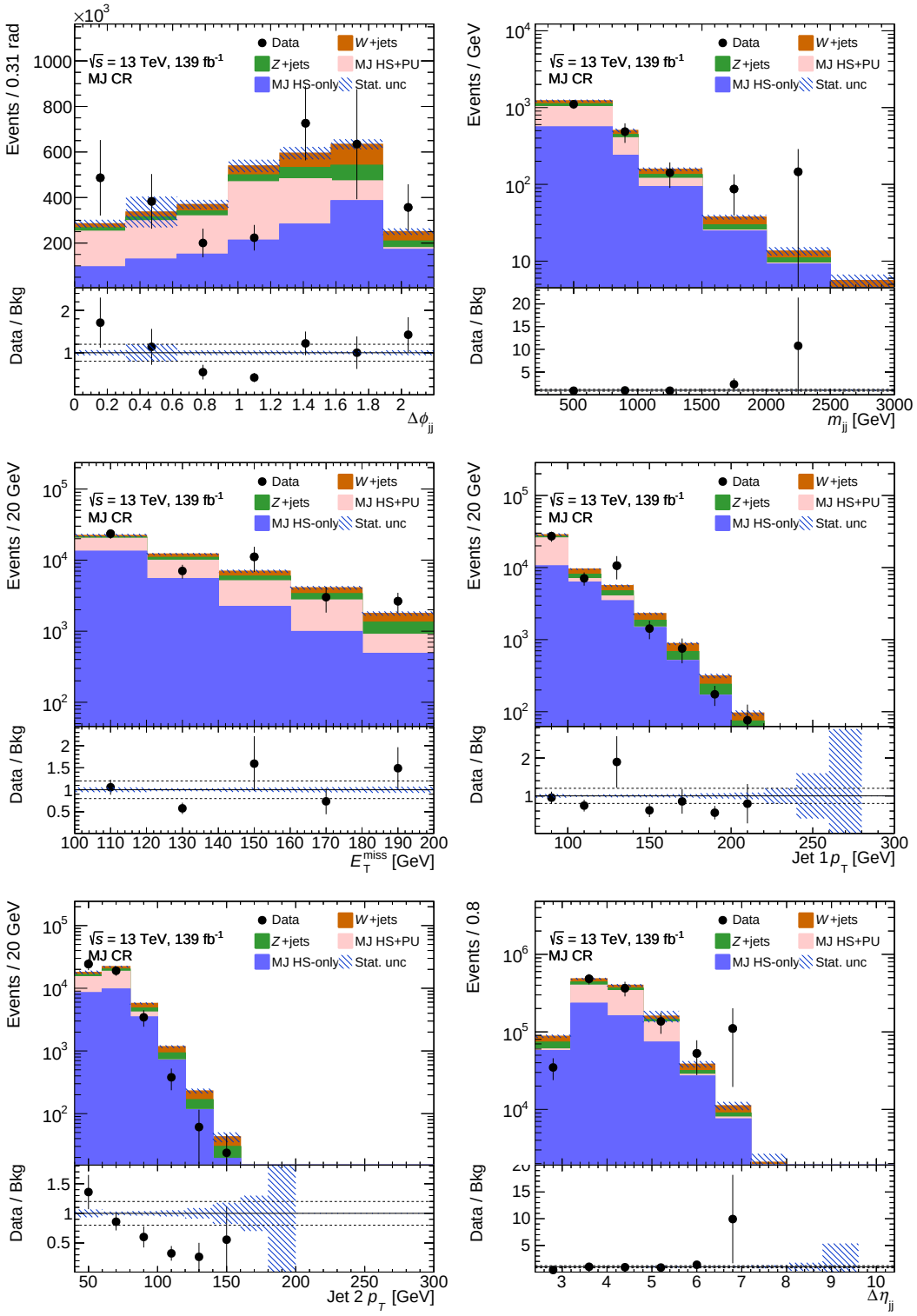

Figure 7.33: Closure checks of the data-driven RnS prediction in the MJ CR for the full data set corresponding to $\mathcal{L} = 139\,\text{fb}^{-1}$, which is the sum of the prediction for the individual data-taking periods between 2015 and 2018.

All events in the MC-based RnS prediction entering the SR have event weights $w < 10$, thus the effective statistics is significantly improved compared to the direct usage of Pythia MC samples in the VBF+$E_{\mathrm{T}}^{\mathrm{miss}}$ phase space.

The HS-only template is highly dominant in the SR for both the MC-based and data-driven RnS technique. In the former case, the inclusive SR prediction consists of > 95 % of events associated to the HS-only template, whereby the fraction of events associated with the HS+PU topology is larger in the SR bins 11–13, which allow for $n_{\mathrm{jet}} = \{3, 4\}$. The HS+PU topology is suppressed in the SR phase space mainly due to its low m_{jj} and low $H_{\mathrm{T}}^{\mathrm{miss}}$ values. Despite the dominance of the HS-only topology, pile-up effects leading to the combinatorial background are not negligible since the relative RnS multijet prediction correlates with the pile-up conditions in the data-taking periods, strongly implying a pile-up influence. It is worth noting that for the MC-based RnS technique, the definition of the topologies via a truth-matching in RnS cannot guarantee that the HS-only topology is pure in true hard-scatter jets. Effects such as the overlay of hard-scatter and pile-up jets and other jet clustering problems are not resolved in a truth-matching. Further, differences in the pile-up physics between data and simulation need to be considered. In case of the data-driven RnS, the template definition is less pure due to pile-up tagging inefficiencies. Therefore, the HS-only topology also includes events with significant pile-up jets.

The number of b-jets in the SR is of special interest since the non-Gaussian jet response tails of b-jets are significantly larger than that of light flavour jets which corresponds to larger probability of producing large $E_{\mathrm{T}}^{\mathrm{miss}}$ values or $H_{\mathrm{T}}^{\mathrm{miss}}$ values in the jet smearing procedure due to a jet loss via pile-up tagging or p_{T}-thresholds. For the MC-based RnS prediction, the fraction of events with one central b-jet in the SR is ∼ 20 % and with two b-jets 0 % due to the second b-jet veto in the SR selection as described in Section 6.3.2.

7.12 Summary and Discussion

RnS is sampling technique providing full event kinematics for multijet process in final states with $E_{\mathrm{T}}^{\mathrm{miss}}$ and jets and is closely related to the widely used jet smearing method. Different novel versions of RnS are developed which rely on the invention of an independent handling of hard-scatter and pile-up jets in RnS. In total, three different RnS approaches were implemented, evaluated and tested:

- MC-based RnS
- data-driven RnS
- classical RnS (see Appendix A.6)

The MC-based RnS approach is the primary method used for the RnS multijet prediction in the full Run II analysis, while the difference to the data-driven prediction is used as a methodical systematic uncertainty to ensure that any data-simulation differences are covered by uncertainties. The methodology of the data-driven and the MC-based RnS techniques are summarised in Table 7.8. For completeness, also the classic RnS version as described in Appendix A.6 is presented, which has been used for the early Run II analysis with $\mathcal{L} = 36\,\mathrm{fb}^{-1}$ [1] and is currently not utilised any longer. A comparison of the different techniques is shown in Appendix A.8 for different kinematic observables and two control selections.

Overall, the RnS method provides a good modelling of the multijet background which is evaluated in form of closure checks and comparisons to other independent multijet background estimation methods such as the pile-up CR method described in Section 8.2.2 . RnS significantly increases the effective statistics of the multijet prediction compared to pure MC samples.

The data-driven RnS technique has significant advantages compared to the classical RnS version as used in the corresponding $36\,\mathrm{fb}^{-1}$ analysis since the hard-scatter and pile-up events are handled independently. An imbalance in the pile-up event is not affecting the hard-scatter rebalancing process in the kinematic fit. However, there are rare cases where the pile-up tagging went wrong and thus the rebalancing is not able to provide

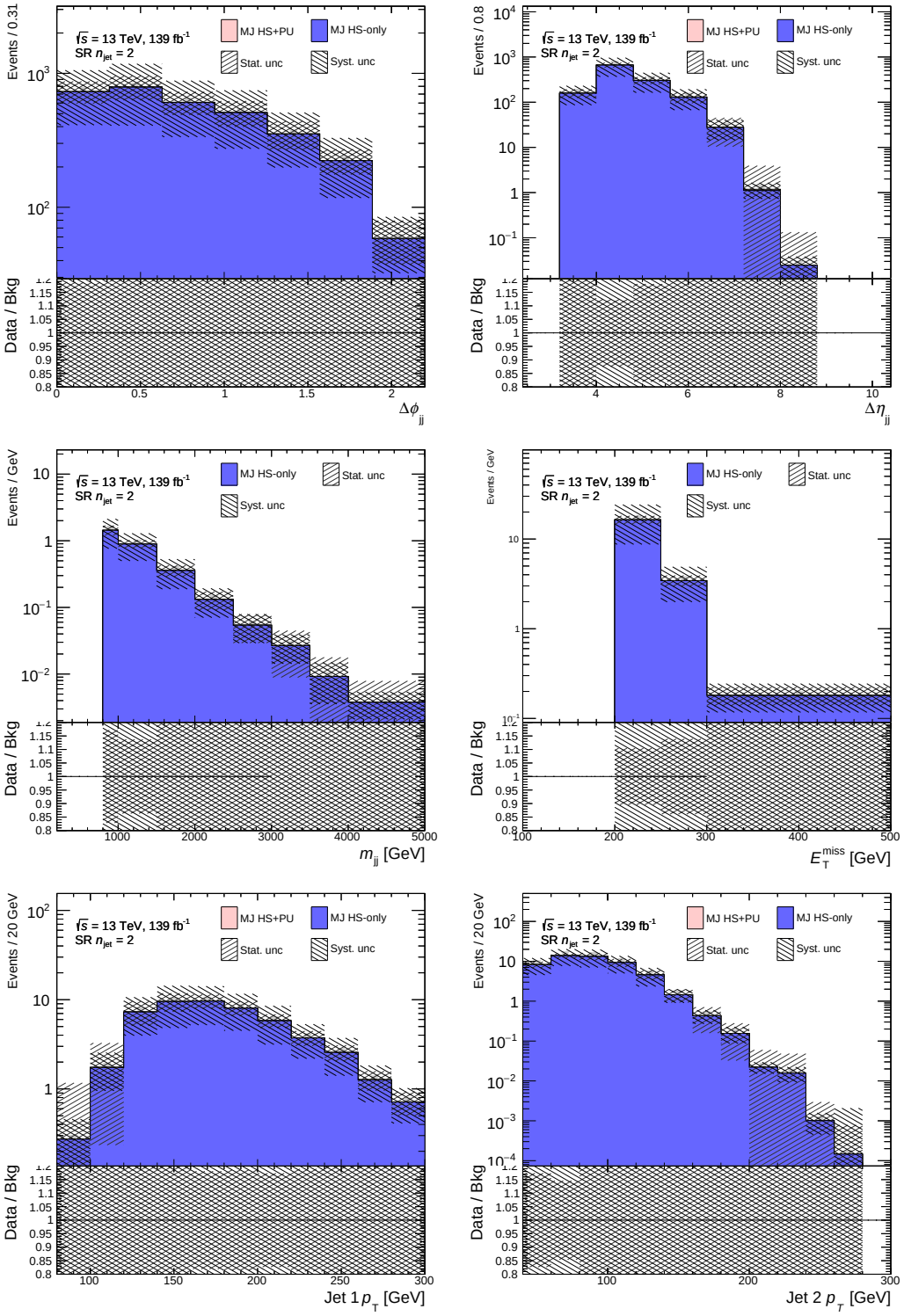

Figure 7.34: Signal region predictions of the MC-based RnS prediction in the dijet SR for the full data set corresponding to $\mathcal{L} = 139\,\text{fb}^{-1}$, which is the sum of the prediction for the individual data-taking periods between 2015 and 2018 prior to applying any year-by-year normalisation in $E_{\text{T}}^{\text{miss}}$-triggered data or $E_{\text{T}}^{\text{miss}}$-trigger efficiency emulation. Shown are statistical and systematic uncertainties from the jet energy response.

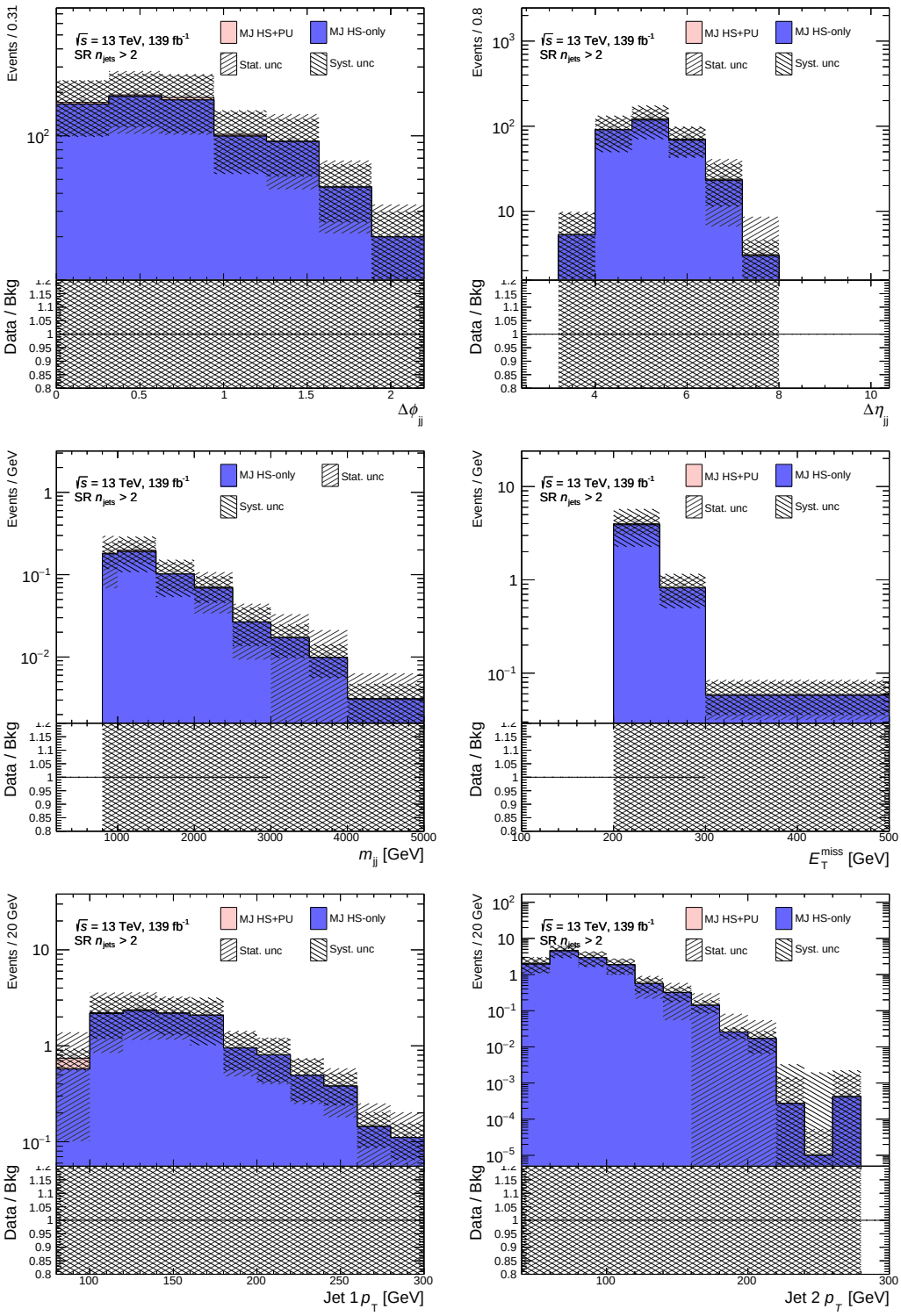

Figure 7.35: Signal region predictions of the MC-based RnS prediction in the $n_{\text{jet}} = \{3,4\}$ SR for the full data set corresponding to $\mathcal{L} = 139\,\text{fb}^{-1}$, which is the sum of the prediction for the individual data-taking periods between 2015 and 2018 prior to applying any year-by-year normalisation in $E_{\text{T}}^{\text{miss}}$-triggered data or $E_{\text{T}}^{\text{miss}}$-trigger efficiency emulation. Shown are statistical and systematic uncertainties from the jet energy resolution.

Table 7.8: Summary of the basic features of the data-driven, MC-based and classic RnS techniques. The first section describes the data and jet collections used as input for RnS and for prediction normalisation. The second section contains information on the rebalancing and smearing configurations. The following sections include details on systematic uncertainties, the trigger efficiency emulation strategy and the role of the method in the full Run II VBF+$E_{\mathrm{T}}^{\mathrm{miss}}$ analysis. Detailed explanations of the listed features are given in the text.

Feature	Data-driven RnS	MC-based RnS	Classic RnS
RnS input events	jet triggered data	Pythia MC	jet triggered data
RnS input jets	EMTopo	EMTopo	EMTopo
fraction fit events	jet triggered data	jet triggered data	-
fraction fit jets	PFlow	PFlow	-
seed pile-up tagging	JVT and fJVT, see Table 7.1	ΔR truth-matching	-
seed selection	see Table 7.3	see Table 7.2	see Table A.2
HS-PU splitting	yes	yes	no
PU-freezing	$p_{\mathrm{T}} < 25\,\mathrm{GeV}$	$p_{\mathrm{T}} \geq 0\,\mathrm{GeV}$	-
rebalancing	all hard-scatter, pile-up $p_{\mathrm{T}} > 25\,\mathrm{GeV}$ sep.	only hard-scatter	all inclusively
N_{PSmax}	400	200	100
azimuthal rotations	20	20	20
enhancing tails	yes	yes	yes
stat. unc.	bootstrapping	bootstrapping	bootstrapping
jet response core-up	15 %	15 %	-
jet response tail-up	50 %	50 %	-
non-closure unc.	yes	yes	-
trigger eff.	H_{T}-$H_{\mathrm{T}}^{\mathrm{miss}}$-maps	H_{T}-$H_{\mathrm{T}}^{\mathrm{miss}}$-maps	H_{T}-$H_{\mathrm{T}}^{\mathrm{miss}}$-maps
analysis role	methodical uncertainty	prediction	not used
prior usages	[3]	-	[1]

a proxy of the underlying truth-level event. These events may lead to a bias. To avoid these, a tight seed selection is used, where only dijet pile-up events are selected. This reduced the probability that the pile-up tagging in the event failed due to the typical dijet pile-up structure. However, a tight seed selection also comes with the risk of introducing a kinematic bias. Unfortunately this is observed. Due to the selection of roughly back-to-back dijet pile-up events, the fJVT distribution is biased and cannot be appropriately modelled. A multijet underprediction around $p_{\mathrm{T}} \sim 120\,\mathrm{GeV}$ in the leading jet p_{T} distribution is observed. The origin of the non-closure is not fully understood yet but it is likely related to the fJVT pile-up tagging which is only applied for momenta of $p_{\mathrm{T}} < 120\,\mathrm{GeV}$. However, this is not criticial since the prediction is normalised in suited CRs as further described in Section 8.2.1.

In the MC-based RnS approach, the HS-only and HS+PU topologies are obtained from MC simulation but normalised in un-prescaled single jet triggered data thus it is still a data-driven technique. This alternative aims for improving the RnS technique by providing a better identification of hard-scatter and pile-up jets via a truth-matching. The efficient pile-up identification makes it possible to define the topologies more robust and thus allows to drop tight seed selection criteria of the purely data-driven method. In addition, the pile-up jets can be frozen within RnS and only the usually high-energetic hard-scatter jets are modified, making the MC-based RnS method more robust than the data-driven RnS approach, where both hard-scatter and pile-up jets are rebalanced separately. As in the data-driven RnS, the MC-based RnS technique struggles with a proper description of the jet fJVT distributions due to significant data-simulation fJVT efficiency differences.

It is difficult to study the impact of pile-up jets for the multijet background in detail since truth pile-up jet information is typically not stored in simulated samples. This can in principle be improved in the future with the production of dedicated samples including the truth pile-up information. This would allow for a better identification of hard-scatter and pile-up jets and would lead to a fundamental understanding of the nature of multijet events in the SR.

Other issues of the presented MC-based and data-driven RnS refer to the jet momentum thresold corresponding

to a jet loss/gain-asymmetry at the 20 GeV p_{T} border. Jets with $p_{\mathrm{T}} > 20\,\mathrm{GeV}$ at seed level can be rebalanced or smeared to momenta of $p_{\mathrm{T}} < 20\,\mathrm{GeV}$ and thus can be lost after applying selection requirements. However, no jets with $p_{\mathrm{T}} < 20\,\mathrm{GeV}$ can be gained in the smearing or rebalancing since these jets are not included in the jet collections. In particular, due to the steeply falling p_{T} distribution of multijet events and the p_{T}-dependent energy resolution, a jet gain would be more likely than a jet loss.

The rebalancing step in RnS has a couple of conceptional problems that may prevent that certain events can be correctly rebalanced to the underlying truth-level events. The following effects are relevant:

- The reco p_{T} threshold at 20 GeV causes that no jet activity below this p_{T}-threshold is available. A potential p_{T} imbalance at reco level would be corrected with modifying the jets with $p_{\mathrm{T}} > 20\,\mathrm{GeV}$ which can result in differences to the truth-level event.
- Events at reco-level are rebalanced using the resolution of the corresponding reco jet in the event. However, for the rebalancing step it is not known if the corresponding truth jet fluctuated down or up in p_{T}. For example, a reco jet with $p_{\mathrm{T}} = 30\,\mathrm{GeV}$ could be observed but the corresponding truth jet could have $p_{\mathrm{T}} = 60\,\mathrm{GeV}$ (with a very good resolution, so the reco jet corresponds to a very extreme mis-measurement) or $p_{\mathrm{T}} = 10\,\mathrm{GeV}$ (with a worse resolution). Nevertheless, the resolution used for the rebalancing fit would correspond to a 30 GeV jet. The corresponding effect is small both in size and frequency.
- Certain $|\eta|$ ranges, e.g. transition regions of the detector, have a worse resolution than other parts of the detector. This resolution effect, mainly affecting the low p_{T}-regime, corresponds to a migration in p_{T} from low p_{T} to high p_{T} (due to the falling p_{T} spectrum), i.e. certain η regions have an excess in high-p_{T} jets. This detector effect is not corrected with a kinematic fit in the transeverse plane.
- The asymmytric non-Gaussian tails, which are more relevant for downwards p_{T} mis-measurements, are not explicitly considered in the rebalancing, which is based on the Gaussian part of the resolution.
- Within an independent rebalancing of the hard-scatter and pile-up sub-events, a wrong pile-up tagging can lead to a different topologies for both the hard-scatter and pile-up event as compared to the corresponding truth-level event.

Though the rebalancing might not correctly restore the original truth-level event, the starting point for the jet smearing is nevertheless an unbiased multijet event without prompt $E_{\mathrm{T}}^{\mathrm{miss}}$ and minimum $H_{\mathrm{T}}^{\mathrm{miss}}$ (events which cannot be rebalanced are discarded).

The jet smearing is arguably the core of RnS and is based on jet resolution maps measured in MC simulation and validated in data. However, the measured resolution maps are not perfect and do not include all relevant effects such as a jet reconstruction efficiency (for both EMTopo and PFlow jets the reconstruction efficiency for $p_{\mathrm{T}} > 40\,\mathrm{GeV}$ is $> 98\,\%$). The measurement of the jet response in MC is biased by a p_{T} threshold effect in MC since reco jets are only stored down to $p_{\mathrm{T}} = 20\,\mathrm{GeV}$ which introduces a cut-off in the lower tail of the jet response in the low E_{true} bins. However, potential modelling issues of the jet response are covered with conservative systematic uncertainties on the core and the tail of the parametrised jet response. The jet smearing technique is implemented with complementary techniques increasing the effective statistics of the RnS multijet prediction. The artificial enhancing of non-Gaussian tails is arguably the most efficient way to increase the statistical precision of RnS since it does not increase the computing time but it sets the focus on interesting events with significant jet mis-measurements. In contrast, the azimuthal rotation increases the computing time since more independent smearings are performed but the rotation effectively increases the seed level statistics. Finally, the weight-dependent jet smearing is the basis for avoiding highly-weighted events in the multijet prediction. These improvements regarding the effective statistics of the multijet prediction are fundamental for the usage of RnS in the challenging VBF phase space at high $E_{\mathrm{T}}^{\mathrm{miss}}$-values.

Both the p_{T} threshold effects as well as the problems of the rebalancing (except of the pile-up jet identification) can be tackled with a truth jet smearing approach using MC simulation since truth jets are avaiable down to $p_{\mathrm{T}} < 10\,\mathrm{GeV}$. In addition, a rebalancing would not be needed. Further, benefiting from truth-level information in MC, a binning of the jet response in quark-induced and gluon-induced jets could potentially improve the

parametrisation of the jet response. A first version of this modified truth jet smearing method is presented in Section A.7.

For a variety of reasons, related to the trigger efficiency emulation as well as the JVT and $H_{\mathrm{T}}^{\mathrm{miss}}$ re-calculations, RnS uses EMTopo jets as input jet collection, while the analysis relies on PFlow jets. To cope with the difference between PFlow and EMTopo jets, the RnS prediction is normalised in data in a CR relying on PFlow jets and, in addition, RnS uses PFlow jet resolutions for the smearing of the EMTopo jets. As an improvement for the future, new samples combining PFlow and EMTopo jet information could resolve the issue of missing pile-up information.

The MC-based RnS technique identifies well-matched events via the quantity $H_{\mathrm{T}}^{\mathrm{miss}}$(matched). However, this quantity might be biased in very rare cases if two back-to-back truth jets, which are not matched to any reco jet, cancel in the $H_{\mathrm{T}}^{\mathrm{miss}}$(matched) calculation. As a potential improvement, the so-called H_{T}-imbalance, ΔH_{T}, can be introduced. Given the total hadronic activity of the matched truth jets

$$H_{\mathrm{T}}(\mathrm{matched}) = \sum_i p_{\mathrm{T},i}, \tag{7.35}$$

where i runs over the reco-matched truth jets, the H_{T}-imbalance ΔH_{T} can be defined as

$$\Delta H_{\mathrm{T}} = H_{\mathrm{T}}(\mathrm{matched}) - H_{\mathrm{T}}(\mathrm{truth}), \tag{7.36}$$

where in H_{T}(truth) all truth jets are considered. ΔH_{T} should be small if the significant truth jets are matched to a corresponding reco jet. It has to be studied how the quantities ΔH_{T} and $H_{\mathrm{T}}^{\mathrm{miss}}$(matched) correlate and which selection requirement, maybe even a selection in a two dimensional plane spanned by ΔH_{T} and $H_{\mathrm{T}}^{\mathrm{miss}}$(matched), is the most effective method for rejecting badly matched events without loosing much seed-level statistics.

CHAPTER 8

Background Estimation

In this chapter the background estimation strategy is presented. The dominant backgrounds arise from V+jets processes, while smaller backgrounds circumference multijet processes, top quark and multiboson production. The pre-fit background contributions in the SR are displayed in Figure 8.1. The modelling of the background processes is a challenging and important aspect of the analysis. Depending on the background process and its contribution in the SR, MC simulation only cannot be used to model all the relevant physics for different reasons, e.g. limited statistics in case of multijet or limited precision with large associated theoretical uncertainties and kinematic mis-modellings in case of V+jets, so data-driven methods are additionally used to constrain the background predictions. A summary of the background estimation strategy is given in Table 8.1.

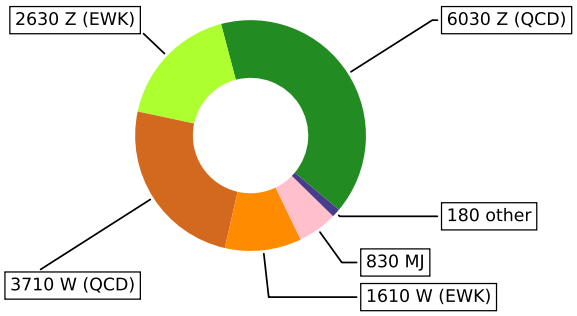

Figure 8.1: Pre-fit contributions from different background processes in the inclusive SR.

The estimation strategy for the V+jets, the fake-leptons and the multijet background is described in this chapter in more detail. Representative Feynman diagrams for EWK and strong Z+jets production and diboson processes are shown in Figure 8.2. Minor background processes, contributing at a far smaller level than the dominant V+jets and the subdominant multijet background in the SR and CRs, are $t\bar{t}$, single top quark t, multiboson processes VV and VVV with mis-reconstructed or unidentified final state leptons, and VBF Higgs boson production with $H \to WW$ and $H \to \tau^+\tau^-$ decays. These processes are evaluated directly using MC simulation with nominal cross section values and are commonly termed as "other" background events.

The MC generators used for simulation of background processes are listed in Section 6.2.2 and the incorporation of the background estimates and the associated uncertainties in the analysis fit model are described in Chapter 9.

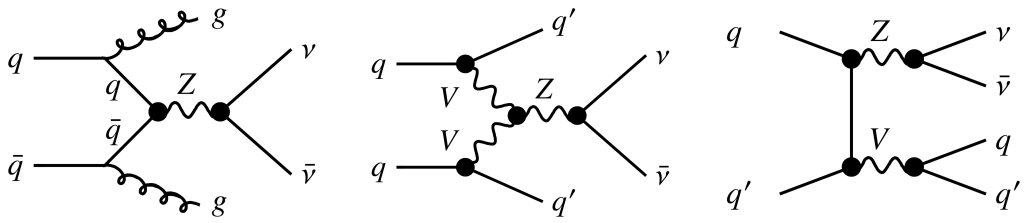

Figure 8.2: Representative Feynman diagrams of strong (left) and EWK (middle) Z+jets and EWK diboson (right) processes.

Table 8.1: Summary of the estimation methods for important background processes in SRs and CRs, used control samples and references to detailed descriptions.

Background process	Method	Control Sample	Reference
$Z \to \nu\nu$+jets	MC and CR in data	$Z \to \ell\ell$+jets	Section 8.1.2
		$W \to \ell\nu$+jets	Section 8.1.3
$W \to \ell_{\text{lost}}\nu$+jets	MC and CR in data	$W \to \ell\nu$+jets	Section 8.1.1
μ fakes	CR in data	$W \to \mu\nu$+jets (anti-ID)	Section 8.1.1
e fakes	CR in data	$W \to e\nu$+jets (anti-ID)	Section 8.1.1
Multijet	RnS and CR in data	multijet CR	Chapter 7, Section 8.2.1
	CR in data	pile-up CR	Section 8.2.2
$t\bar{t}$	MC-only		
Multiboson (VV, VVV)	MC-only		
$H \to WW, H \to \tau\tau$	MC-only		

8.1 V+jets

The dominant background process for the VBF Higgs boson to invisible search is the production of gauge bosons $V = W, Z$ in association with final state jets. The relevant vector boson decay modes are

$$Z \to \nu\nu$$
$$W \to \ell_{\text{lost}}\nu,$$

with $\ell = e, \mu$. In the following, the term EWK V+jets production refers to production modes which are at $O(\alpha_{\text{EWK}}^4)$ at LO, while the term strong V+jets production describes processes $O(\alpha_{\text{EWK}}^2)$ at LO. Due to interferences of these production modes, the separation into QCD and EWK V+jets is essentially meaningless at NLO. In order to enter the SRs two jets must be present in the final state in addition to some large amount of $E_{\text{T}}^{\text{miss}}$, which may be caused by neutrinos ν or lost leptons ℓ_{lost}. A lepton ℓ is termed as lost if it is undetected due to the limited p_{T} and pseudorapidity detector acceptance or lepton identification requirements.

Since it is very challenging to model V+jets processes with the needed precision and to reduce both experimental and theoretical uncertainties, the V+jets background prediction obtained from MC simulation is normalised using several CRs with a data-driven transfer factor method, described in more detail in Section 9.2. The CRs are are based on selected $Z \to \ell\ell$ and $W \to \ell\nu$ processes which have similar kinematics than the corresponding SR processes. The lepton multiplicity n_ℓ and the relevant processes for the SR and V+jets CRs are visualised in Figure 8.3.

8.1.1 W Boson Background

The W CR is used to constrain the $W \to \ell_{\text{lost}}\nu$ background in the SR via a normalisation factor in the fit model. The CR consists of events with leptonic W decays in which the lepton is reconstructed and identified, in

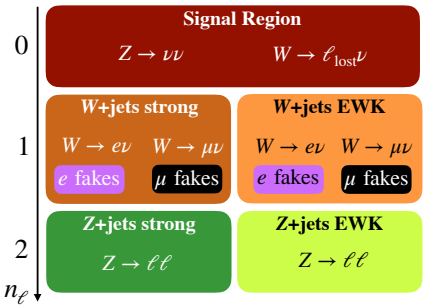

Figure 8.3: Lepton multiplicity n_ℓ for the SR and the V+jets CRs.

contrast to the SR where the lepton is lost. The leptonic W boson decay mode is $W \to \ell\nu$ with $\ell = e, \mu$ and the corresponding neutrinos ν. In order to account for different fakes in the electron and muon channel, the W CRs is divided into lepton flavour. The production cross sections of single produced W+jets in proton-proton collisions are different for W^+ and W^- bosons. W^+ bosons are dominantly produced by $u\bar{d}$ partons, while W^- are mostly produced by $d\bar{u}$. Since protons are states of uud valence quarks, this leads to an electric charge asymmetry for the W+jets background in favour of W^+ production. Nevertheless, no splitting of the W boson CRs in electric charge is done in this analysis.

Several selection requirements are applied to reach a high W boson purity in the CR. Events in the $W \to e\nu$ CR are triggered with single electron triggers and in the $W \to \mu\nu$ CR with muon or $E_{\text{T}}^{\text{miss}}$ triggers. As described in Table 6.6, tight p_{T} requirements are used for the leptons to ensure the triggers operate at the efficiency plateau and to reduce the contribution from lepton fakes. Electrons in the W CR need to fulfil $p_{\text{T}} > 30\,\text{GeV}$ and have to pass the tight identification operating point and p_{T}-dependent isolation criteria. Muons must have $p_{\text{T}} > 30\,\text{GeV}$, $|\eta| < 2.47$ and must filfil the medium identification working point. An overlap removal of muons with respect to electrons, jets and photons is performed to avoid any double-counting of energy. Loose isolation and medium track quality criteria are applied. Requirements on the longitudinal impact parameter $|z_0 \sin(\theta)| < 0.5\,\text{mm}$ and the transverse impact parameters $|d_0|/\sigma(d_0) < 3$ are applied so that the track is associated with PV_0. A veto on events with not exactly one reconstructed signal lepton but additional baseline lepton activity as defined in Section 6.3 is applied.

A challenge in the W boson CRs is the presence of electron and muon fakes, contributing at a percent level to the total background, which are estimated in the electron and muon channel with similar techniques based on scale factors associated with fake lepton CRs.

Fake electrons originate predominantly from multijet processes where a jet is mis-identified as an electron which fulfils the required isolation criteria. Although such a mis-identification is very rare, the large multijet cross section at the LHC makes it necessary to assess the fake background carefully following an estimation strategy as sketched in Figure 8.4. Particles can escape the acceptance of the detector, are inaccurately reconstructed or fail to be reconstructed altogether, typically resulting in $E_{\text{T}}^{\text{miss}}$. To quantify the consistency of the reconstructed $E_{\text{T}}^{\text{miss}}$ with these resolution and identification efficiencies, the $E_{\text{T}}^{\text{miss}}$ significance S can be used, which is defined as

$$S = \frac{E_{\text{T}}^{\text{miss}}}{\sqrt{E_{\text{T}}}}. \tag{8.1}$$

S is used as a proxy of the $E_{\text{T}}^{\text{miss}}$ resolution. Since in the SR no visible lepton is expected, the $E_{\text{T}}^{\text{miss}}$ definition in the CR is modified such that it excludes leptons, i.e. treats leptons as invisible particles, so that the $E_{\text{T}}^{\text{miss}}$

significance is given by

$$S_{\text{MET}} = \frac{E_{\text{T}}^{\text{miss}}}{\sqrt{p_{\text{T}}^{j_1} + p_{\text{T}}^{j_2} + p_{\text{T}}^{e}}}, \tag{8.2}$$

with the (sub-)leading jet momentum $p_{\text{T}}^{j_{1,2}}$ and the electron momentum p_{T}^{e}. The $E_{\text{T}}^{\text{miss}}$ significance S_{MET} is separating between fake and real electrons since multijet events do not contain a prompt neutrino corresponding to lower values of $E_{\text{T}}^{\text{miss}}$ and S_{MET}. Therefore the single electron W CR is defined at $E_{\text{T}}^{\text{miss}}$ significance values of $S_{\text{MET}} > 4\sqrt{\text{GeV}}$. Events failing this requirement are used to define a fake electron CR which is enriched in mis-identified jets. A $W \rightarrow e\nu$ anti-ID CR, with fake electrons defined as electrons passing the loose identification working point but not the tight identification requirement of signal electrons is used to determine a transfer factor from the fake-e CR to the W CR. A template of the fake electrons in the anti-ID CR is determined by subtracting the MC predictions (V, multiboson, Higgs boson and $t\bar{t}$ processes) from data in that region. Following this selection requirements, the ratio R_{S} of the number of data events with $S_{\text{MET}} > 4\sqrt{\text{GeV}}$ and with $S_{\text{MET}} < 4\sqrt{\text{GeV}}$ is calculated in bins of m_{jj}. No binning in other variables like $\Delta\phi_{\text{jj}}$ is needed since no dependence is observed. For statistical reasons, the calculation of R_{S} is averaged over the three data-taking periods, whereby all three data-taking periods give statistically compatible values of R_{S} in the range between 0.5 and 0.25, despite varying pile-up conditions in different years. This is shown in the right figure in Figure 8.5. The resulting ratio R_{S} is used as scale factor in the fit model for the fake electron contribution n_{fake} in the fake-e CR as visualised in Figure 8.5. The scale factor R_{S} multiplied with $n_{\text{fake},e}$, which is a free fit parameter, provides an estimate of the expected background from fake electrons in the $W \rightarrow e\nu$ CR at a level of ~ 3 %.

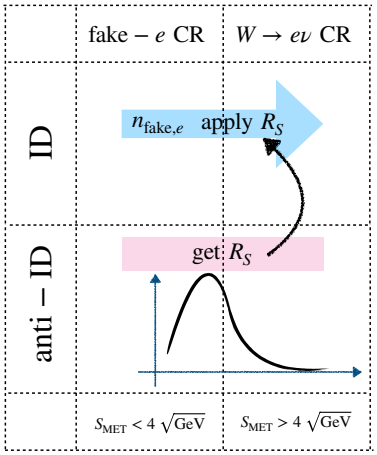

Figure 8.4: Estimation strategy of the number of fake-e due to multijet events in the $W \rightarrow e\nu$ CR. $n_{\text{fake},e}$ is the number of fake electrons, mostly from multijet processes, in the fake-e CR and used as free fit parameter. A similar technique is used for the muon fakes in $n_{\text{fake},\mu}$ the $W \rightarrow \mu\nu$ CR. The scale factor R_S is calculated as the ratio of the number of events with $S_{\text{MET}} > 4\sqrt{\text{GeV}}$ and $S_{\text{MET}} < 4\sqrt{\text{GeV}}$ in the anti-ID CR and multiplied with $n_{\text{fake},e}$ in the ID region.

Similar to electron fakes, muon fakes originating from a jet mis-identification contribute to the $W \rightarrow \mu\nu$ CR. Although muon fakes are less important than electron fakes, a careful treatment of muon fakes with a similar technique as used for the electron fakes is done. Unlike for electrons, a muon anti-ID CR is not fake-enriched at low S_{MET} values. Therefore, the transverse mass m_{T} is used to select a fake-μ CR, where m_{T} is defined as

$$m_{\text{T}} = \sqrt{2E_{\text{T}}^{\mu} E_{\text{T}}^{\text{miss}} (1 - \cos(\Delta\phi(\mu, E_{\text{T}}^{\text{miss}})))}, \tag{8.3}$$

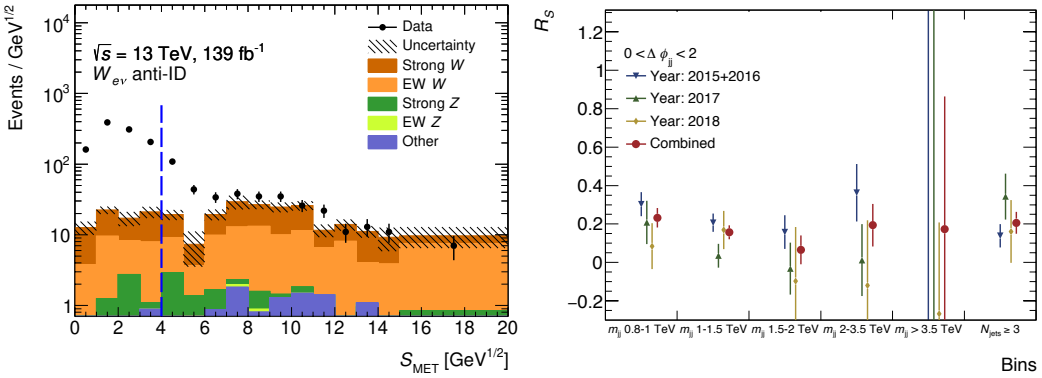

Figure 8.5: Left: Comparison of S_{MET} in data and simulation for the $W \to e\nu$ anti-ID CR, for which the electron passes a loose identification but not the tight one. The excess in data, accumulating at low S_{MET}, is caused by multijet events containing an electron fake. Right: ratio R_S of number of events with high S_{MET} to those with low values as a function of m_{jj} for three years of data-taking separately. The rightmost bin displays R_S for the event selection with three and four jets.

where $\Delta\phi(l, E_{\text{T}}^{\text{miss}})$ is the transverse angle between the muon μ and the missing transverse momentum $E_{\text{T}}^{\text{miss}}$ caused by neutrinos ν and $E_{\text{T}}^{\text{miss}} = |\vec{E}_{\text{T}}^{\text{miss}}|$ is defined as

$$\vec{E}_{\text{T}}^{\text{miss}} = -\left(\vec{E}_{\text{T}}^{l} + \vec{u}_{\text{T}}\right), \tag{8.4}$$

with the recoil in the transverse plane $\vec{u}_{\text{T}}$, which is the vectorial sum of E_{T} of all reconstructed calorimeter clusters except of the ones associated with the leptons l [242]. Note that the $E_{\text{T}}^{\text{miss}}$-term includes the visible lepton. A m_{T} cut of $> 20\,\text{GeV}$ significantly suppresses jets which mimic muons in the $W \to \mu\nu$ CR since these are usually aligned with $\vec{E}_{\text{T}}^{\text{miss}}$. In order to determine a transfer factor R_M, another CR, the $W \to \mu\nu$ anti-ID CR, is enriched by fake muons by selecting muons which do not fulfil the signal muon identification requirement. The V, VV, H and $t\bar{t}$ background events in that region are subtracted from the event yield in the $W \to \mu\nu$ anti-ID CR. The remaining excess of data minus background events corresponds to multijet events faking muons. The calculation of R_M, which is the pass to fail ratio of $m_{\text{T}} > 20\,\text{GeV}$, is averaged over the three data-taking periods for statistical reasons. The values of R_M range from 0 to 0.5 in the different m_{jj}-bins but are statistically compatible, so that R_M is averaged over the m_{jj} bins resulting in an value of $R_M = 0.29 \pm 0.15$.

The W CR selection is summarised in Table 8.2. Other event selection criteria and the event categorisation into sixteen bins remain as in the SR. The strong W+jets contribution is dominant compared to the EWK W+jets contribution in both the electron and muon W+jets CR. The fraction of Z+jets contamination is $\sim 1\,(2)\,\%$ in the electron (muon) W+jets CR. Signal and multijet processes are negligible and the contribution from other background processes is $< 5\,\%$. Distributions of the observed event yield and the MC expectation in the W CR prior to the likelihood fit are shown in Figure 8.6. A reasonable pre-fit modelling in the W CR is observed. Statistical uncertainties on the fake scale factors $R_{\text{S,M}}$ are propagated as uncertainties to the analysis fit model.

8.1.2 Z Boson Background

The $Z \to \ell\ell$ CR is used to constrain the irreducible $Z \to \nu\nu$ background in the SR. This background in the SR is estimated with simulation, see Section 6.2.2, and constraint with free floating normalisation factors derived in the $Z \to \ell\ell$ CR, in which the data is triggered with electron, muon or $E_{\text{T}}^{\text{miss}}$ triggers. The final state leptons $\ell = e, \mu$ in the Z boson decay must be of opposite electric charge and same lepton flavour. The Z boson is

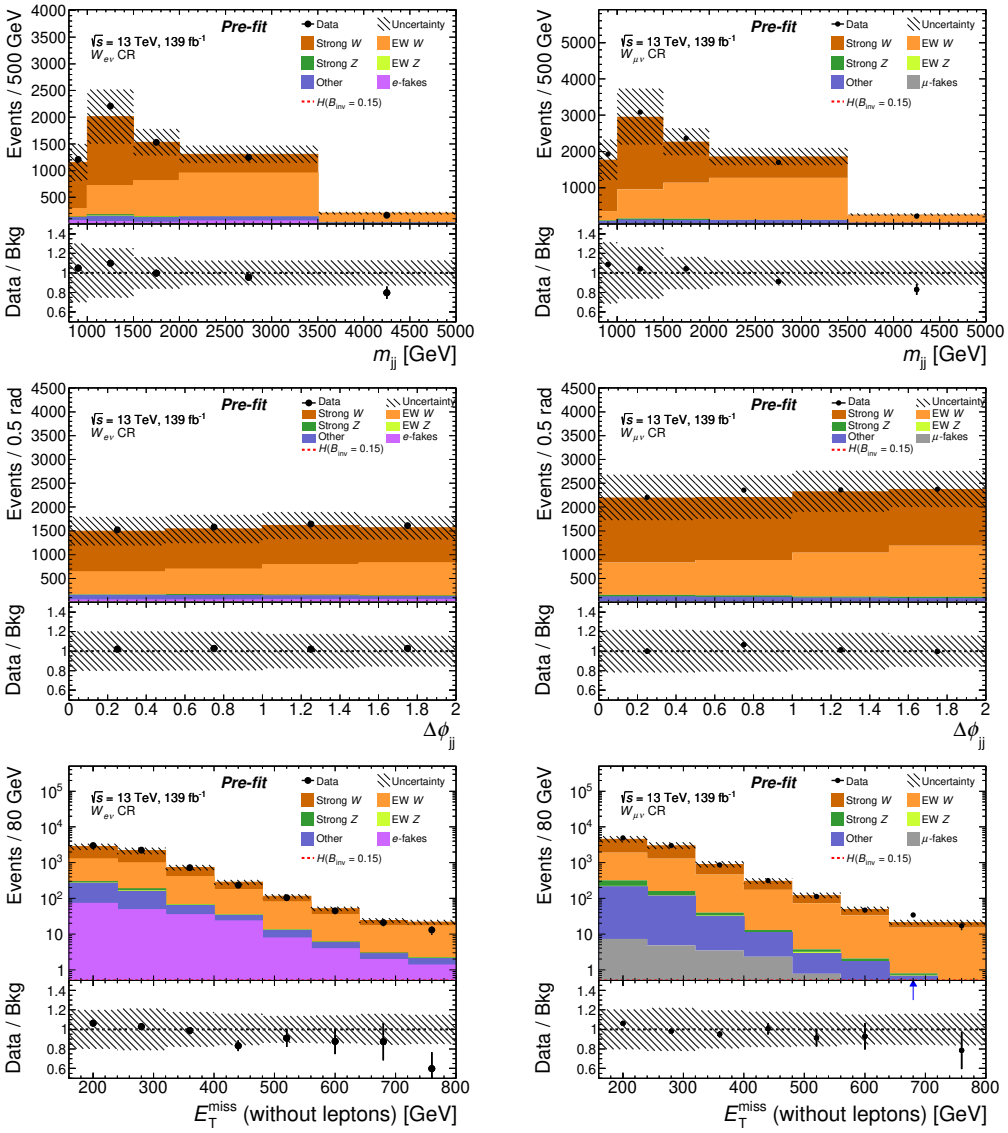

Figure 8.6: Distributions of m_{jj}, $\Delta\phi_{jj}$, and E_T^{miss} (without leptons) in the W CR for $W \to e\nu$ (left) and $W \to \mu\nu$ (right). The simulation is normalised to cross section times luminosity and is shown before the likelihood fit. The hatched band indicates statistical and reconstruction systematic uncertainties.

Table 8.2: Selection of the W CR. Cuts which are not mentioned are treated as in the SR.

Quantity	Cut	Description
n_ℓ	= 1	number of signal leptons, veto on additional (baseline) leptons
n_γ	= 0	photon veto
p_{T}^{ℓ}	> 30 GeV	leading lepton momentum (trigger plateau)
S_{MET}	$> 4\sqrt{\mathrm{GeV}}$	$E_{\mathrm{T}}^{\mathrm{miss}}$ significance, only for $W \to e\nu$
trigger	single electron	trigger requirement for $W \to e^{\pm}\nu$
m_{T}	> 20 GeV	transverse mass, only for $W \to \mu\nu$
trigger	$E_{\mathrm{T}}^{\mathrm{miss}}$ or single and dimuon	trigger requirement for $W \to \mu\nu$

produced in EWK processes and the two tagging jets can be produced in EWK or strong interactions. While the strong Z+jets production is a dominant background at low m_{jj} values ($\sim$ 50 % of the total SR background), the EWK Z+jets production is dominant at high m_{jj} ($\sim$ 45 % of the total SR background).

A thoughtful event selection is performed for a high purity of Z+jets events in the $Z \to \ell\ell$ CR with a high selection acceptance. As shown in Table 6.6, for electrons the loose likelihood-based electron identification working point is used to increase the selection acceptance in that phase space. Further, p_{T}-dependent isolation criteria are applied since the electron should not be located close to a jet, which would indicate a heavy-flavour quark decay with secondary leptons. Further, requirements on the longitudinal impact parameter $|z_0 \sin(\theta)| < 0.5$ mm and the transverse impact parameter $|d_0|/\sigma(d_0) < 5$ are applied so that the electron track is associated with the primary vertex PV_0. For muons, loose track quality, loose isolation conditions and the medium isolation working point are utilised. To ensure that a muon track is associated with PV_0, selection requirements on the longitudinal impact parameter $|z_0 \sin(\theta)| < 0.5$ mm and the transverse impact parameters $|d_0|/\sigma(d_0) < 3$ are appied. A veto on events with not exactly two reconstructed signal leptons and events with any additional baseline lepton activity is applied. The leading lepton has $p_{\mathrm{T}}^{\ell} > 30$ GeV to ensure that the single lepton trigger is operating at the efficiency plateau, while the subleading lepton has $p_{\mathrm{T}}^{\ell} > 7$ GeV. The signal leptons are identified for $|\eta| < 2.47$ excluding the crack region of $|\eta| \in [1.37, 1.52]$. In addition, the invariant mass of the dilepton system $m_{\ell\ell}$ must be consistent with the mass of the Z boson m_Z, i.e. $|m_{\ell\ell} - m_Z| < 25$ GeV. Further $E_{\mathrm{T}}^{\mathrm{miss,no\ lepton}} < 70$ GeV is required, where the lepton momenta are added in the $E_{\mathrm{T}}^{\mathrm{miss}}$ calculation to mimic the corresponding SR kinematics, to suppress multiboson (VV and VVV) and $H \to WW$ and $H \to \tau\tau$ events. For the Z+jets background, a large $E_{\mathrm{T}}^{\mathrm{miss}}$ contribution in the event is produced by jet mis-measurements, while for the mentioned multiboson and Higgs boson processes large parts of $E_{\mathrm{T}}^{\mathrm{miss}}$ are caused by leptonically decaying W bosons or τ leptons, where prompt neutrinos ν are produced.

The Z CR selection is summarised in Table 8.3 and other selection criteria and the event categorisation into sixteen bins follows the SR strategy. The $Z \to ee$ and $Z \to \mu\mu$ CRs are merged to simplify the fit model. As detailed in Section 8.1.3, a correlation with the W+jets processes is implemented in the analysis fit model. The event selection leads to a purity of the $Z \to \ell^+\ell^-$ CR of > 90 % in all analysis bins, where 95 % of the contamination originates from multiboson (VV, VVV) and Higgs boson $\to WW$ or $H \to \tau\tau$ decays, while 5 % originate from top quark processes. No relevant fraction of signal, W+jets or multijet processes is observed. Roughly 65 % of the Z events in the CR arise from strong Z+jets processes, while the remaining 35 % arise from EWK Z+jets processes. Distributions of the observed event yield and the MC expectation in the Z CR prior to the likelihood fit are shown in Figure 8.7 in which the reweighting procedure described in Section 8.1.3 is applied. A reasonable pre-fit modelling in the $Z \to \ell\ell$ CR is observed.

8.1.3 V+jets Reweighting

Instead constraining the irreducible $Z \to \nu\nu$+jets background only with $Z \to \ell\ell$+jets events, which are limited in statistics in the $Z \to \ell\ell$ CR due to the low $Z \to \ell\ell$ branching fraction and acceptance, one can benefit

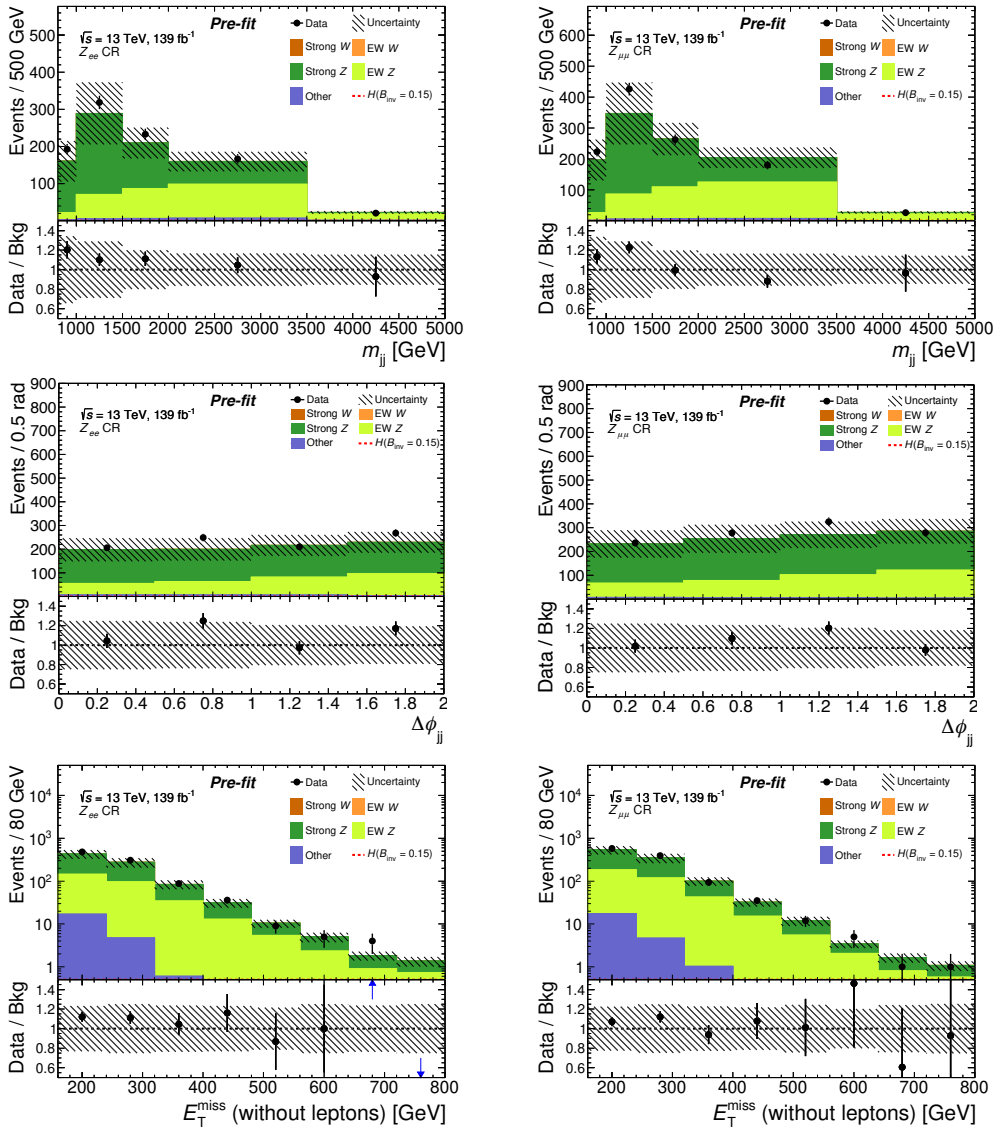

Figure 8.7: Distributions of m_{jj}, $\Delta\phi_{jj}$, and E_T^{miss} (without leptons) in the Z CR for $Z \to ee$ (left) and $Z \to \mu\mu$ (right) after reweighting with the Z/W ratio. The simulation is normalised to cross section times luminosity and is shown before the likelihood fit. The hatched band indicates statistical and reconstruction systematic uncertainties.

Table 8.3: Selection of the Z CR. Cuts which are not mentioned are treated as in the SR.

Quantity	Cut	Description
n_ℓ	$= 2$	number of signal leptons (no other baseline lepton)
n_γ	$= 0$	photon veto
$\lvert m_{\ell\ell} - m_Z \rvert$	$< 25\,\text{GeV}$	Z boson mass window
$p_\text{T}^{\ell_1}$	$> 30\,\text{GeV}$	leading signal lepton momentum (trigger plateau)
$p_\text{T}^{\ell_2}$	$> 7\,\text{GeV}$	subleading signal lepton momentum
$E_\text{T}^{\text{miss,no lepton}}$	$< 70\,\text{GeV}$	suppress multiboson and Higgs boson processes, visible lepton added to E_T^miss
trigger	electron, muon, E_T^miss	trigger requirement
$q_{\ell_1} \cdot q_{\ell_2}$	< 0	oppositely charged leptons

from the larger statistics of the $W \to \ell\nu$+jets control selection to constrain the $Z \to \nu\nu$+jets background more accurately. This approach relies on the strong correlation of Z and W+jets processes in the VBF phase space and requires the development of a dedicated kinematic correlation scheme based on radiative corrections with associated uncertainties of Z+jets and W+jets processes. A similar approach has been applied in the monojet dark matter search [186, 243] but the reweighting scheme used for V+1jet processes is not applicable in the VBF phase space. Instead, a one-dimensional reweighting of the Atlas MC to full NLO in QCD×EWK, see Figure 8.8, as function of m_{jj} is used [244]. The following formula describes a one-dimensional reweighting of Atlas MC samples for Z+jets production in the variable $x = m_{jj}$ with remaining variables $\mathbf{y}$:

$$\frac{\mathrm{d}}{\mathrm{d}x}\frac{\mathrm{d}}{\mathrm{d}\mathbf{y}}\sigma^{Z,m}(\epsilon^V_\text{MC}, \epsilon_\text{TH}) = \frac{\mathrm{d}}{\mathrm{d}x}\frac{d}{d\mathbf{y}}\sigma^{Z,m}_\text{MC}(\epsilon^Z_\text{MC})\left[\frac{R^{Z/W,m}_\text{TH}(x, \epsilon_\text{TH})}{R^{Z/W,m}_\text{MC}(x, \epsilon_\text{MC})}\right] = \frac{\mathrm{d}}{\mathrm{d}x}\frac{d}{d\mathbf{y}}\sigma^{Z,m}_\text{MC}(\epsilon^Z_\text{MC}) \cdot R^{Z/W,m}, \tag{8.5}$$

where

$$R^{Z/W,m}_\text{TH}(x, \epsilon_\text{TH}) = \frac{\frac{\mathrm{d}}{\mathrm{d}x}\sigma^{Z,m}_\text{TH}(\epsilon^Z_\text{TH})}{\frac{\mathrm{d}}{\mathrm{d}x}\sigma^{W,m}_\text{TH}(\epsilon^W_\text{TH})} \tag{8.6}$$

is the ratio of Z to W in a selection close to the SR for m = QCD or EWK and $R^{Z/W}$ denotes the double-ratio of the NLO Z/W calculation and the MC prediction. The label MC and TH correspond to cross sections from MC and high-order theory predictions, respectively, and ϵ_i describes nuisance parameters of related uncertainties described in Section 9.3.2. The left-hand side in Equation 8.5 represents the resulting analysis-level distribution, while the right-hand side consists of the full analysis selection term multiplied with a double-ratio of the theory correction $R^{Z/W}_\text{TH}$ and the Atlas MC V+jets ratio $R^{Z/W}_\text{MC}$ from a Rivet routine [245] where some higher order corrections ($\sim \alpha_s^2\alpha^3_\text{EWK}$ and $\sim \alpha_s\alpha^4_\text{EWK}$) are missing. Interference terms between EWK and QCD V+jets production are negligible at LO ($\sim 1\,\%$ level) as well as at NLO, so strong and EWK modes can be handled separately. The correction factors are derived with the following key selection criteria: leading jet $p_\text{T} > 100\,\text{GeV}$, subleading jet $p_\text{T} > 50\,\text{GeV}$, $m_{jj} > 0.5\,\text{TeV}$, $\Delta\eta_{jj} > 2.5$ and weak boson $p_\text{T} > 150\,\text{GeV}$. All object and variable definitions are synchronised between the theorists and the simulation. The resulting NLO Z/W corrections for QCD and EWK V+jets production of the Atlas (N)LO Sherpa MC simulation are displayed in Figure 8.9, whereby associated uncertainties are described in more detail in Section 9.3.2. The size of the corrections is explained by the difference of the full NLO theory correction and the VBF approximation used for the Atlas MC (neglecting interference terms and s-channel diagrams) and the intereference with the EWK diboson processes for the EWK V+jets events. While corrections from strong V+jets are small (1–10 %) in the relevant m_{jj}-range, the EWK V+jets corrections are larger at low m_{jj} values ($\sim 20\,\%$) and decrease with increasing m_{jj}. A validation of the theory corrections and background estimates is performed in a likelihood fit in a high-$\Delta\phi_{jj}$ VR, see Chapter 10. The high-$\Delta\phi_{jj}$ VR is defined for $2 < \Delta\phi_{jj} < 2.5$, $E_\text{T}^\text{miss} > 200\,\text{GeV}$ (due to increased multijet background for $\Delta\phi_{jj} > 2$) and $n_\text{jet} = 2$ in five bins in m_{jj} as binned in the SR, while all other selection criteria remain as in the SR. The background estimates follow the estimation strategy for $\Delta\phi_{jj} < 2$ with dedicated CRs for V+jets and fake background events, while the multijet background is estimated with RnS as described in

Section 8.2.

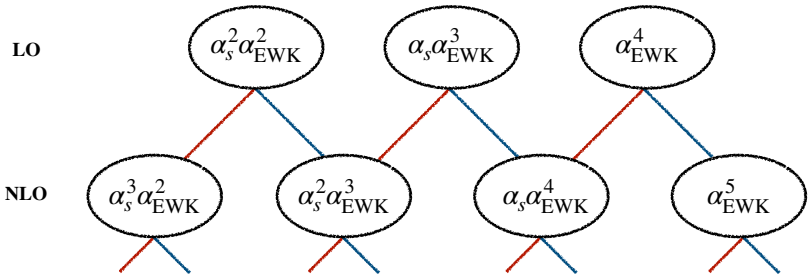

Figure 8.8: All orders of α_{EWK} and α_s for different EWK and strong V+jets processes at full NLO.

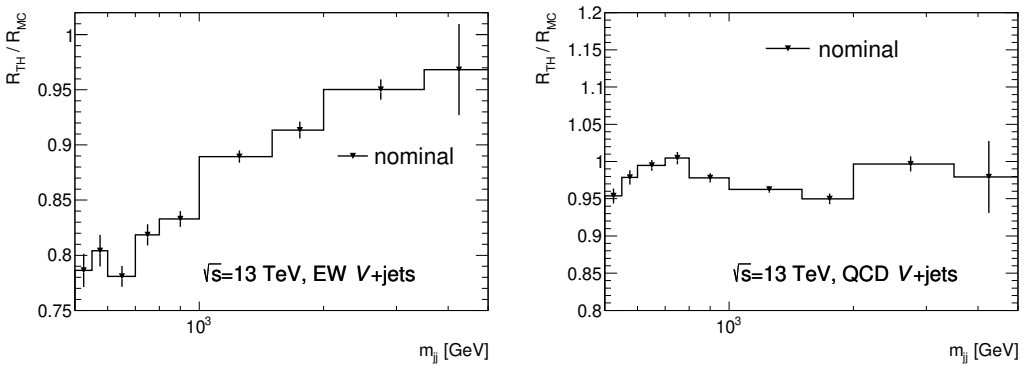

Figure 8.9: Z/W EWK (left) and QCD (right) theory corrections. The error bars correspond to the MC statistical uncertainty. The corrections are larger for EWK Z+jets and the correction factors are < 1.

8.2 Multijet Background

Multijet events can enter the SR due to the production of fake $E_{\mathrm{T}}^{\mathrm{miss}}$ caused by inadequate detector measurements and incorrect pile-up tagging. Although extreme jet mis-measurements are seldom, the multijet cross section is very large. Thus, for statistical reasons, it is not possible to estimate the multijet background in a high-$E_{\mathrm{T}}^{\mathrm{miss}}$ plus VBF phase space using for instance Pythia MC samples directly as further explained in Section 7.

The multijet background is heavily suppressed by the SR requirements of $E_{\mathrm{T}}^{\mathrm{miss}} > 160\,\mathrm{GeV}$, $\Delta\phi_{\mathrm{jj}} < 2$, $m_{\mathrm{jj}} > 0.8\,\mathrm{TeV}$ and a third jet veto. A cut on $H_{\mathrm{T}}^{\mathrm{miss}} > 140\,\mathrm{GeV}$ effectively rejects the combinatorial multijet background. Nevertheless, the multijet background is still important and must be estimated with care to avoid large uncertainties.

In the Run I analysis [182], the multijet background has been estimated with a data-driven jet smearing technique based on a multijet-enriched CR defined with a SR-inverted $|\Delta\phi(\mathrm{j}, E_{\mathrm{T}}^{\mathrm{miss}})|$ requirement between the jets j and $E_{\mathrm{T}}^{\mathrm{miss}}$. For the first Run II analysis [1] with $36\,\mathrm{fb}^{-1}$ data, the multijet background estimation has been done with data-driven RnS techniques. For the full Run II paper, to further decrease statistical as well as systematic uncertainties, an additional independent estimate, a leading jet fJVT-inverted CR approach ("pile-up CR"), is developed, in addition to more sophisticated versions of RnS. The final background prediction in the individual SR bins is evaluated with a combination of normalisations and shapes from RnS and the pile-up CR technique.

The determination of the RnS multijet prediction is discussed in Section 8.2.1. The pile-up CR strategy is detailed in Section 8.2.2 and the combination with the RnS method in Section 8.2.3.

8.2.1 Rebalance And Smear Prediction

The RnS technique can be seen as a sampling technique providing multijet prediction with full event kinematics and large statistics even in phase spaces where widely used MC generators do not provide sufficient events. The development and implementation of the RnS method is presented in detail in Chapter 7. In this section it is described how the RnS multijet prediction, i.e. the outcome of the RnS method, is controlled, normalised and validated in $E_{\mathrm{T}}^{\mathrm{miss}}$ triggered data in regions close to the SR. The MC-based RnS technique is used for the benchmark prediction and the difference to the data-driven RnS prediction is used as systematic uncertainty. While the HS-only multijet background and the combinatorial background are estimated separately in RnS, this is not done in $E_{\mathrm{T}}^{\mathrm{miss}}$ triggered data and both components are commonly referred to as the multijet background.

Two orthogonal CRs are used to normalise the RnS multijet prediction in a plane spanned by $E_{\mathrm{T}}^{\mathrm{miss}}$ and m_{jj} in $E_{\mathrm{T}}^{\mathrm{miss}}$ triggered data, sketched in Figure 8.10. The CRs are defined orthogonal to the SR, named as "low m_{jj}" and "mid m_{jj}". The corresponding selections are summarised in Table 8.4. Several cuts are relaxed compared to the SR selection to enhance the multijet background fraction. The low m_{jj} region is defined at small m_{jj} values between 0.2 and 0.8 TeV, while the $E_{\mathrm{T}}^{\mathrm{miss}}$ selection is relaxed to $E_{\mathrm{T}}^{\mathrm{miss}} > 150\,\mathrm{GeV}$ and the SR $H_{\mathrm{T}}^{\mathrm{miss}}$ requirement is dropped completely. To further increase the multijet contribution in that region, the $\Delta\eta_{\mathrm{jj}}$ requirement is reduced to $|\eta| > 2.5$ but with a simultaneous need for one of the two leading jets detected in the forward region. In the mid m_{jj} region m_{jj} values between 0.8 and 1.5 TeV are allowed. Orthogonality to the SR is ensured with an upper $E_{\mathrm{T}}^{\mathrm{miss}}$ threshold of $E_{\mathrm{T}}^{\mathrm{miss}} < 200\,\mathrm{GeV}$. As in the low m_{jj} region, the $H_{\mathrm{T}}^{\mathrm{miss}}$ requirement is dropped to increase the multijet contribution.

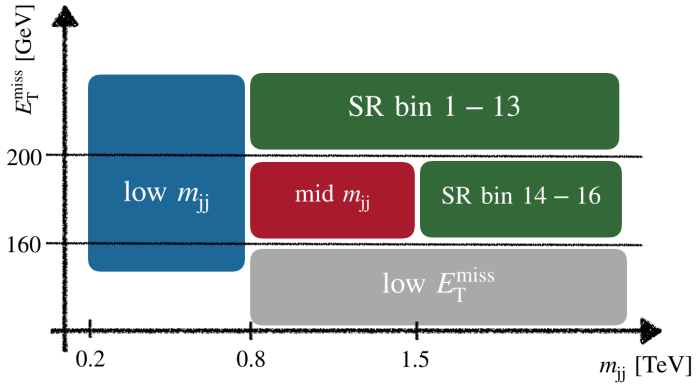

Figure 8.10: Definition of multijet CRs, VR and SR in the $E_{\mathrm{T}}^{\mathrm{miss}}$-$m_{\mathrm{jj}}$-plane.

The normalisation factors for the RnS multijet background prediction are determined via

$$\gamma = \frac{N_{\mathrm{data}} - B_{\text{non-MJ}}}{N_{\mathrm{MJ}}}, \tag{8.7}$$

where N_{data} is the data yield, $B_{\text{non-MJ}}$ is the non-multijet background mostly consisting of V+jets, which are obtained from simulation but normalised in the respective single- and dilepton CRs in data, and N_{MJ} is the observed multijet event yield predicted by RnS. The additional normalisation (after a first normalisation is performed in single jet triggered data in RnS) is motivated to account for potential in-efficiencies of the HLT jet

triggers, issues in the $E_{\mathrm{T}}^{\mathrm{miss}}$ trigger turn-on parametrisations and potential kinematic mis-modellings such as fJVT.

However, since the multijet CRs are not dominated by multijet but by V+jets processes, the normalisation as given in Equation 8.7 is only derived for $\Delta\phi_{\mathrm{jj}} < 1$, where the multijet contribution is larger as compared to $\Delta\phi_{\mathrm{jj}} > 1$.The multijet normalisation is given by the average $\gamma = (\gamma_1 + \gamma_2)/2$ from the scale factors $\gamma_{1/2}$ in the low m_{jj} and mid m_{jj} CRs. A non-closure uncertainty is assigned to the RnS multijet prediction given by half of the difference of the normalisation factors, i.e. $|\gamma_1 - \gamma_2|/2$. The multijet scale factors and the non-closure uncertainty are derived individually per data-taking period and are treated fully correlated along the analysis bins. The normalisation factors γ and the uncertainty are summarised in Table 8.5. In addition, a low $E_{\mathrm{T}}^{\mathrm{miss}}$ VR is defined. Since in this region the RnS prediction suffers from large trigger efficiency uncertainties, the region is only used for RnS shape validations. Closure plots of the MC-based RnS prediction in the low m_{jj} and mid m_{jj} CRs are shown in Figure 8.11-8.16. A good agreement of the background predictions in $E_{\mathrm{T}}^{\mathrm{miss}}$-triggered data is observed.

Table 8.4: Multijet CR definition of the low m_{jj} and mid m_{jj} CRs used for normalisation and the low $E_{\mathrm{T}}^{\mathrm{miss}}$ VR. Cuts which are not listed are used as in the SRs.

Quantity	Low m_{jj}	Mid m_{jj}	Low $E_{\mathrm{T}}^{\mathrm{miss}}$
m_{jj} [TeV]	[0.2, 0.8]	[0.8, 1.5]	> 0.8
$E_{\mathrm{T}}^{\mathrm{miss}}$ [GeV]	> 150	[160, 200]	[150, 200]
$H_{\mathrm{T}}^{\mathrm{miss}}$ [GeV]	≥ 0	≥ 0	≥ 0
$\Delta\eta_{\mathrm{jj}}$	> 2.5	> 3.8	> 3.8
other	$\lvert\eta_1\rvert > 2.5$ or $\lvert\eta_2\rvert > 2.5$	-	-

Table 8.5: Normalisation factor γ with relative uncertainty obtained as the arithmetic average from γ_1 and γ_2 derived in the low m_{jj} and mid m_{jj} Multijet CRs for each data-taking period separately.

Year	γ_1 (low m_{jj})	γ_2 (mid m_{jj})	γ (average)	Rel. non-closure unc. [%]
2015/16	0.17	0.38	0.27	40.74
2017	0.55	1.54	1.04	47.12
2018	0.48	0.97	0.73	34.25

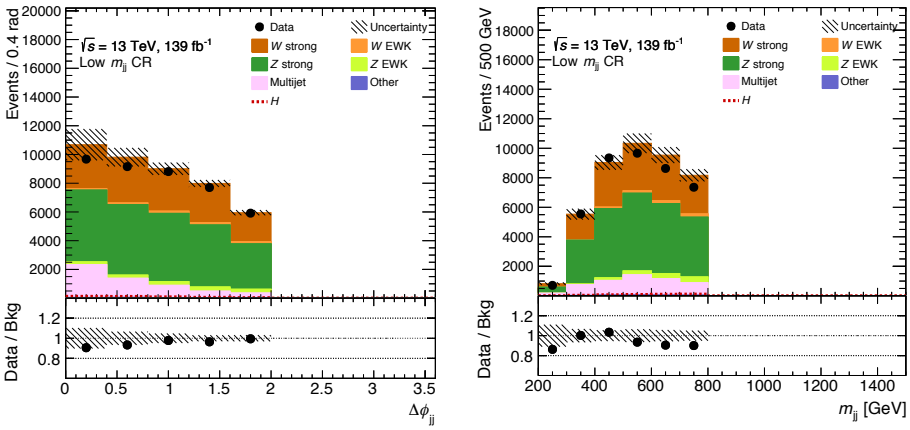

Figure 8.11: Closure plots of the MC-based RnS prediction in the low m_{jj} CR for 139 fb^{-1} and $E_{\mathrm{T}}^{\mathrm{miss}}$-triggered data for $\Delta\phi_{\mathrm{jj}}$ and m_{jj}. The V+jets are taken from simulation but normalised in the respective lepton CR.

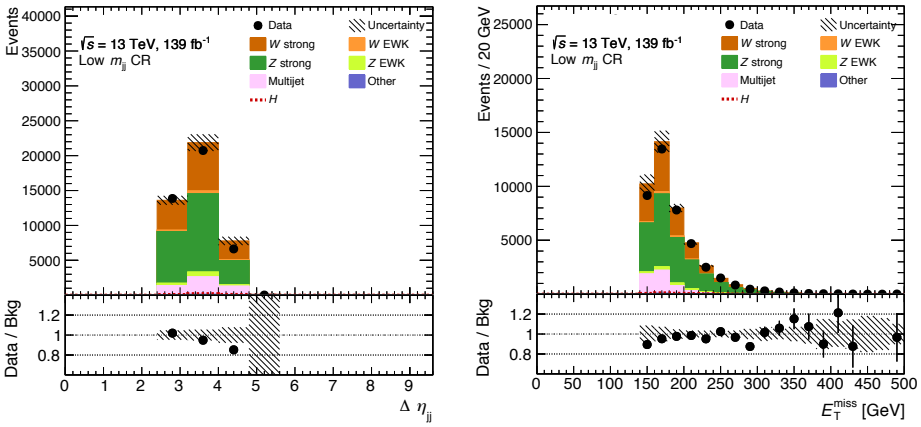

Figure 8.12: Closure plots of the MC-based RnS prediction in the low m_{jj} CR for 139 fb^{-1} and E_T^{miss}-triggered data for $\Delta\eta_{jj}$ and E_T^{miss}. The V+jets are taken from simulation but normalised in the respective lepton CR.

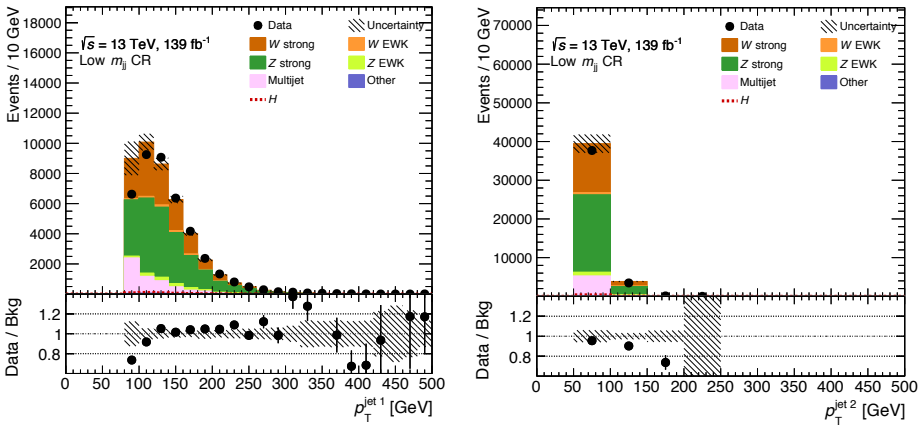

Figure 8.13: Closure plots of the MC-based RnS prediction in the low m_{jj} CR for 139 fb^{-1} and E_T^{miss}-triggered data for leading and subleading p_T. The V+jets are taken from simulation but normalised in the respective lepton CR.

A suite of uncertainties is related to the RnS multijet background estimate. Since RnS is a jet smearing sampling technique relying on the jet response obtained in MC and constrained in data, two uncertainties are assigned to the modelling of the core and tails of the jet response. Symmetrised core-up and tail-up variations of 15 % and 50 % are used, respectively. A systematic non-closure uncertainty is associated with the RnS prediction which is obtained from the difference of the normalisation factors in the two multijet CRs in E_T^{miss}-triggered data. Further, the MC-based and the data-driven RnS approach are compared in each SR bin. The difference of both predictions is taken as a methodical uncertainty to account for differences in simulation and data, e.g. the pile-up or p_T modelling, and differences in the methodology, e.g. the HS-only and HS+PU templates are defined in different ways as described in Section 7.3. A summary of the RnS multijet prediction with the individual systematic uncertainties is given in Table 8.6. The RnS multijet prediction in the SR is at the order of 6 % of the total background and roughly scales with increasing pile-up conditions. The largest contribution from multijet is in the lower m_{jj} bins and decreases as expected with increasing m_{jj} and E_T^{miss}. The bin by bin RnS multijet prediction with uncertainties for the full data set is summarised in Table 8.7.

Apart from the SR multijet estimate, another estimate is needed for the high $\Delta\phi_{jj}$ VR as introduced in Section

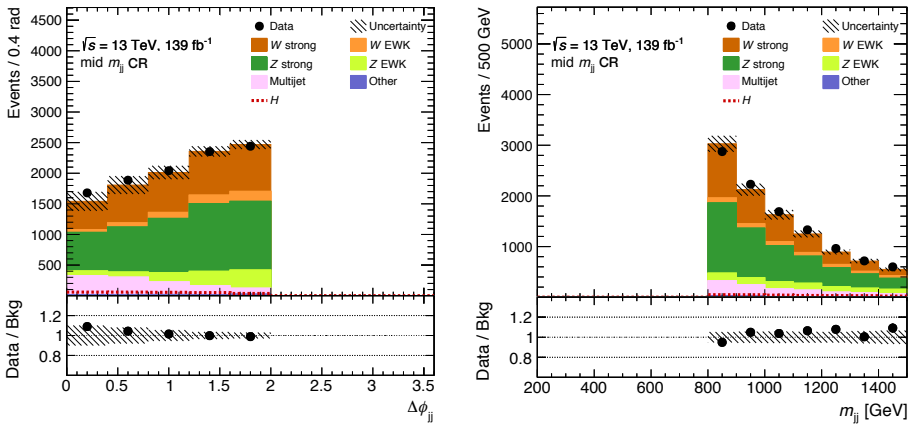

Figure 8.14: Closure plots of the MC-based RnS prediction in the mid m_{jj} CR for 139 fb^{-1} and E_T^{miss}-triggered data for $\Delta\phi_{jj}$ and m_{jj}. The V+jets are taken from simulation but normalised in the respective lepton CR.

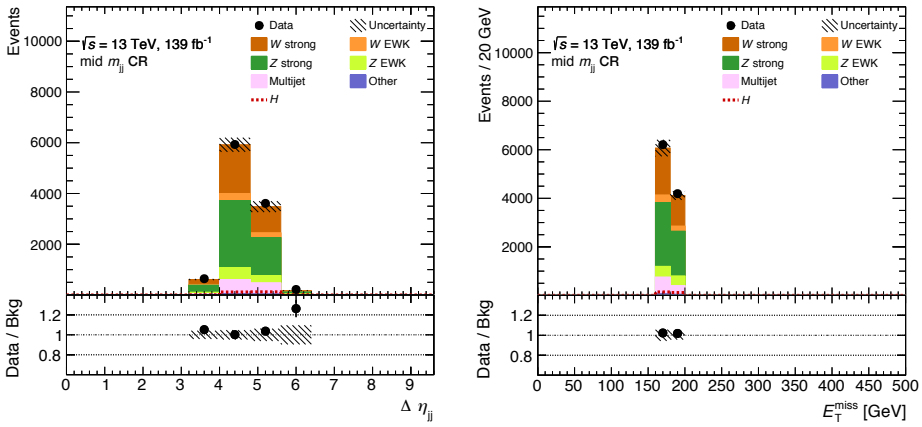

Figure 8.15: Closure plots of the MC-based RnS prediction in the mid m_{jj} CR for 139 fb^{-1} and E_T^{miss}-triggered data for $\Delta\eta_{jj}$ and E_T^{miss}. The V+jets are taken from simulation but normalised in the respective lepton CR.

8.1.3. For statistical reasons, the RnS multijet estimate for the VR is normalised in different CRs than the estimate for the SR. The normalisation is done for each data-taking period separately in two CRs from which the resulting normalisation factor is averaged, the first defined for $2.8 < \Delta\eta_{jj} < 3.8$ (low-$\Delta\eta_{jj}$ CR) and the second for $\Delta\eta_{jj} > 3.8$ (high-$\Delta\eta_{jj}$ CR), in a multijet-enriched low E_T^{miss}-range between 100 GeV and 160 GeV. As in the SR, the systematic core-up and tail-up variations are normalised following the same procedure and the V+jets background are taken from simulation and normalised in the corresponding lepton CRs. The average multijet scale factors in the high-$\Delta\phi_{jj}$ VR are 0.72 ± 0.32 (2015/16), 1.27 ± 0.51 (2017) and 2.24 ± 0.60 (2018), where the uncertainty is defined as the half of the spread of the scale factors from the low-$\Delta\eta_{jj}$ and high-$\Delta\eta_{jj}$ multijet CRs.

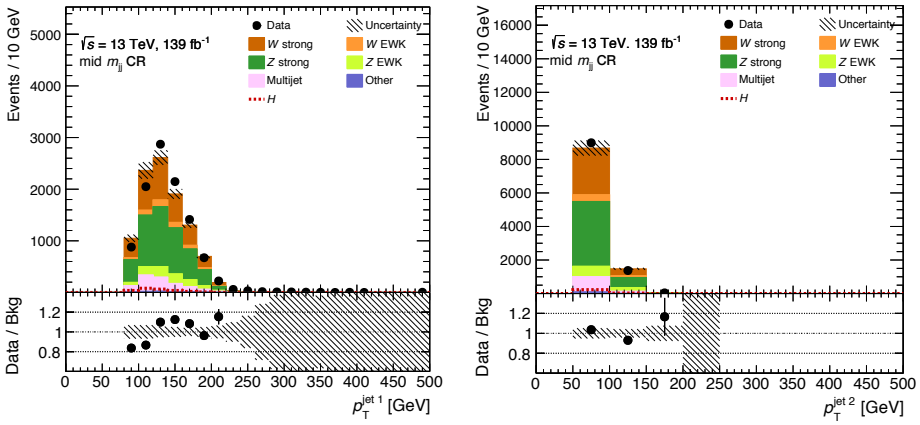

Figure 8.16: Closure plots of the MC-based RnS prediction in the mid m_{jj} CR for 139 fb^{-1} and E_T^{miss}-triggered data for leading and subleading p_T. The V+jets are taken from simulation but normalised in the respective lepton CR.

Table 8.6: RnS multijet prediction with relative uncertainties. Shown is the multijet event yield per data-taking year, the pre-fit fraction of multijet events in the total background, the statistical uncertainties, the jet response shape uncertainties (Gaussian core and non-Gaussian tail), the non-closure uncertainty and the uncertainty from difference of the MC-based and data-driven RnS technique.

Year(s)	Event yield	Fraction [%]	Stat. [%]	Core-up [%]	Tail-up [%]	Non-closure [%]	Data vs. sim [%]
2015/16	112.8	2.8	3.7	3.9	2.5	2.4	40
2017	385.9	8.8	4.9	4.5	5.8	7.0	47
2018	414.6	7.0	3.2	8.7	5.9	-0.4	34

8.2.2 Pile-up Control Region Prediction

The pile-up CR technique is a fully independent data-driven transfer factor method inspired by widely used fake factor methods to estimate the multijet background in the SR [219]. The method uses selected E_T^{miss}-triggered events where the leading jet is fJVT-tagged as pile-up as a multijet CR and thus is highly enriched in pile-up jets. The extrapolation from the CR to the SR is performed with a transfer factor R_{MJ} measured in situ in multijet enriched low E_T^{miss} regions. More specifically, the pile-up CR is defined by reversing the SR fJVT requirement of the leading jet by

$$\text{fJVT} > \begin{cases} 0.5, & \text{if } E_T^{miss} > 200\,\text{GeV} \\ 0.2, & \text{if } E_T^{miss} \in [160, 200]\,\text{GeV} \end{cases}. \tag{8.8}$$

Inverting the fJVT cut for the leading jet leads to a CR which is very pure in multijet while other background processes are highly suppressed. In contrast, inverting also or alternatively the fJVT score of the subleading jet would highly increase the contribution of V+jets background events and is thus not considered. In fact, to increase the statistics in the pile-up CR, the SR fJVT requirement of the subleading jet is dropped completely which means that in most cases both of the leading jets are tagged as pile-up by the fJVT algorithm in the pile-up CR.

The selection of the pile-up CR is summarised in Table 8.8. The fJVT requirement corresponds to an implicit cut on the leading jet p_T and η. The fJVT score is only evaluated for jets between $20 < p_T < 120$ GeV and $|\eta| > 2.5$, while jets with $p_T > 120$ GeV or $|\eta| < 2.5$ are treated as hard-scatter jets (fJVT = 0). Therefore, by definition, a jet with $p_T > 120$ GeV or a central jet cannot fail the fJVT SR condition. This also affects the

Table 8.7: MC-based RnS multijet prediction for 139 fb^{-1} in all sixteen SR bins with absolute uncertainties. Shown are the multijet event yield, the statistical uncertainty according to the bootstrapping, the non-closure uncertainty, the core-up and tail-up uncertainties of the jet response and the difference of the MC-based and data-driven RnS method (Data vs. sim).

SR bin	Event yield	Stat.	Non-closure	Core-up	Tail-up	Data vs. sim
1	107.944	7.815	43.425	0.064	-0.019	-0.102
2	152.075	9.001	61.281	-0.013	0.025	-0.050
3	59.318	6.896	24.370	-0.039	-0.063	0.198
4	36.243	6.135	15.019	-0.063	0.049	0.197
5	3.433	1.583	1.457	-0.109	0.042	0.156
6	36.638	4.476	14.913	0.021	0.009	-0.219
7	80.691	7.956	32.882	-0.018	0.016	0.015
8	29.879	3.351	12.059	0.090	-0.078	0.025
9	23.011	4.232	9.573	-0.073	0.032	0.252
10	1.640	0.568	0.683	-0.172	0.006	0.105
11	35.907	6.703	15.347	0.411	0.223	-0.215
12	32.532	5.103	13.712	0.209	0.122	0.215
13	3.527	1.514	1.478	0.303	0.526	0.161
14	139.043	16.931	56.451	-0.076	-0.079	-0.333
15	164.741	78.066	61.460	0.057	0.065	0.298
16	5.987	1.830	2.323	0.180	0.030	0.089

subleading p_{T} and $\Delta\phi_{\text{jj}}$ due to the fixed $E_{\text{T}}^{\text{miss}}$ requirement and the m_{jj} distribution due to its correlation with jet p_{T}. The jet multiplicity selection in the pile-up CR is relaxed from dijet events to $n_{\text{jet}} \in \{2, 3, 4\}$ to allow for a pile-up tagging of the leading jet: the fJVT algorithm looks for central pile-up activity which is back-to-back in ϕ to a forward jet. Without central pile-up activity, the forward jet cannot be be tagged as pile-up by fJVT and thus staying with a dijet selection as defined in the SR would reduce the statistics in the pile-up CR dramatically and in addition it would spoil the stability of the transfer factor $R_{\text{MJ},i}$ as a function of $E_{\text{T}}^{\text{miss}}$. The latter effect can be explained kinematically: The SR is defined by dijet events with $E_{\text{T}}^{\text{miss}} > 200\,\text{GeV}$ and leading jet $p_{\text{T}} > 80\,\text{GeV}$, while in contrast the pile-up CR is by construction limited to leading jet $p_{\text{T}} \leq 120\,\text{GeV}$. Thus it is unlikely to produce $E_{\text{T}}^{\text{miss}} > 200\,\text{GeV}$ with dijet events limited in p_{T}, in particular for high $\Delta\phi_{\text{jj}}$ values. Increasing the allowed jet multiplicity n_{jet} supports the production of large $E_{\text{T}}^{\text{miss}}$ values, especially if the additional jets are aligned with the leading jets. The m_{rel} and centrality C requirements are used in the SR bins 11–13 to select events with final state radiation from one or both of the two tagging jets, i.e. targeting jet multiplicities of 3 or 4 similar to the pile-up CR. The m_{rel} is dropped for the pile-up CR bins 6–10 to avoid a bias of the jet selection and to increase the statistics. In these analysis bins, the two leading jets tend to be back-to-back. Cutting on m_{rel} in this event topology would bias the kinematics of the selected events. Except of the jet multiplicity n_{jet} and m_{rel}, all selection criteria and data-taking requirements remain the same as in the SR and thus the pile-up CR provides a region which is relatively close to the SR. Any kinematic difference between the pile-up CR and the SR is either negligible (e.g. the SR is not binned in jet p_{T}) or corrected with a binned transfer factor $R_{\text{MJ},i}$.

The distributions of m_{jj} and $\Delta\phi_{\text{jj}}$ in the pile-up CR are shown in Figure 8.17 for $E_{\text{T}}^{\text{miss}} \in [160, 200]\,\text{GeV}$. The V+jets contamination is at the level of 5 % for $E_{\text{T}}^{\text{miss}} > 200\,\text{GeV}$ and 8 % for $E_{\text{T}}^{\text{miss}} \in [160, 200]\,\text{GeV}$, i.e. the pile-up CR region has a very high purity.

Table 8.8: Selection criteria for the pile-up CR. Other selection requirements remain as in the SR.

	SR bin 1 – 5	SR bin 6 – 10	SR bin 14 – 16
Jet 1 fJVT	> 0.5	> 0.5	> 0.2
Jet 2 fJVT	≥ 0.0	≥ 0.0	≥ 0.0
n_{jet}	$= \{2, 3, 4\}$	$= \{2, 3, 4\}$	$= \{2, 3, 4\}$
m_{rel}	< 0.05	≥ 0.00	< 0.05

The pile-up CR and the determination of the transfer factor $R_{\text{MJ},i}$ is derived separately for each SR bin i. More

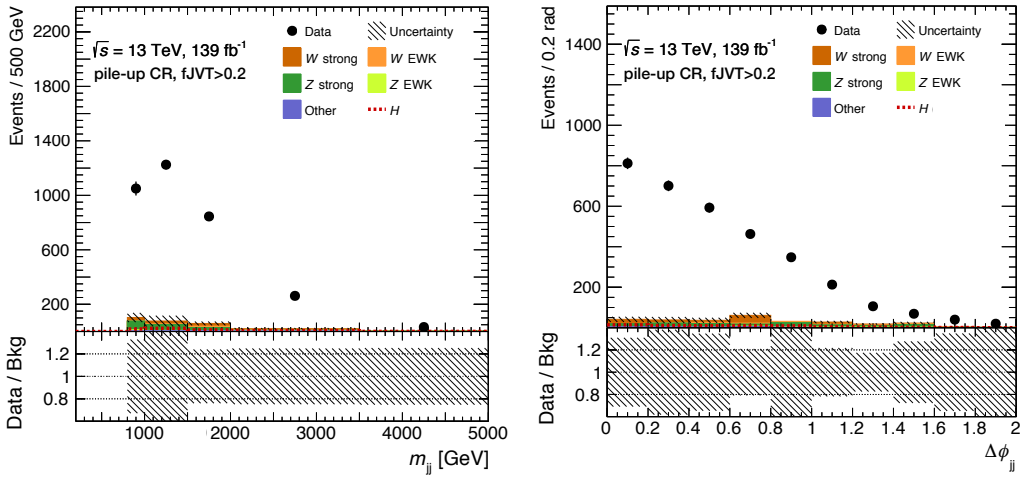

Figure 8.17: The sum of CRs with leading jet fJVT larger than 0.2 is shown for m_{jj} and $\Delta\phi_{jj}$ for $160 < E_T^{miss} < 200$ GeV. The multijet background in that region corresponds to the difference of data and the small non-multijet contribution [219].

explicitly, the multijet prediction $N_{MJ,i}$ in SR bin i is defined via the transfer factor $R_{MJ,i}$ by

$$N_{MJ,i} = R_{MJ,i} \cdot N_{MJ,i}^{\text{rev. fJVT}}, \tag{8.9}$$

where $N_{MJ,i}^{\text{rev. fJVT}}$ is the number of multijet events in the corresponding pile-up CR, given by the excess of data with respect to the non-multijet background events $B_{\text{non-MJ},i}^{\text{rev. fJVT}}$ from simulation:

$$N_{MJ,i}^{\text{rev. fJVT}} = N_{\text{data},i}^{\text{rev. fJVT}} - B_{\text{non-MJ},i}^{\text{rev. fJVT}}. \tag{8.10}$$

Following the definition of the pile-up CR, the transfer factor $R_{MJ,i}$ from the pile-up CR to the SR used in Equation 8.9 is given by the ratio of the number of multijet events passing the fJVT requirement (pass fJVT) and those failing (rev. fJVT). The selection in the nominator thus requires $n_{jet} = 2$, while the selection in the denominator requires $n_{jet} \in [2, 4]$. The transfer factor $R_{MJ,i}$ is measured directly for each analysis bin i, where a multijet-enriched E_T^{miss} selection with $110 < E_T^{miss} < 200\,(160)$ GeV and $m_{jj} > 0.8$ TeV for fJVT $> 0.5\,(0.2)$ is used. According to Equation 8.8, the required fJVT value of the jets depends on the target SR bin, i.e. the fJVT threshold is 0.5 if the target SR bin has $E_T^{miss} > 200$ GeV and 0.2 for the SR bins with $160 < E_T^{miss} < 200$ GeV, even if the transfer factor is measured at lower E_T^{miss} values. Formally, the transfer factor $R_{MJ,i}$ is defined by

$$R_{MJ,i} = \frac{N_{MJ,i}^{\text{pass fJVT}}}{N_{MJ,i}^{\text{rev. fJVT}}} = \frac{N_{\text{data},i}^{\text{pass fJVT}} - B_{\text{non-MJ},i}^{\text{pass fJVT}}}{N_{\text{data},i}^{\text{rev. fJVT}} - B_{\text{non-MJ},i}^{\text{rev. fJVT}}}, \tag{8.11}$$

where the superscript pass fJVT refers to events fulfiling the SR fJVT and selection requirements. The non-multijet contribution in the measurement of $R_{MJ,i}$ is significantly larger for passing fJVT compared to failing fJVT and is normalised in the corresponding one and two lepton CRs. The methodology of the pile-up CR transfer factor method is sketched in Figure 8.18. The dependence of the transfer factor $R_{MJ,i}$ on kinematic variable such as $\Delta\phi_{jj}$, m_{jj} or leading jet p_T are checked for different E_T^{miss} ranges. The transfer factor $R_{MJ,i}$ is binned in m_{jj} and $\Delta\phi_{jj}$ and shown to be independent of E_T^{miss} within a flat 20 % uncertainty. The transfer factor decreases with increasing m_{jj} from 2.29 to 1.82 at low $\Delta\phi_{jj}$ (SR bin 1-5) and increases with increasing m_{jj} from 1.75 to 3.38 at high $\Delta\phi_{jj}$ (SR in 6-10), where for statistical reasons an inclusive transfer factor of

$R_{\mathrm{MJ},i\in\{6,10\}} = 1.80$ is determined. For $160 < E_{\mathrm{T}}^{\mathrm{miss}} < 200\,\mathrm{GeV}$ (SR bin 14-16), $R_{\mathrm{MJ},i}$ ranges between 0.32 and 0.37.

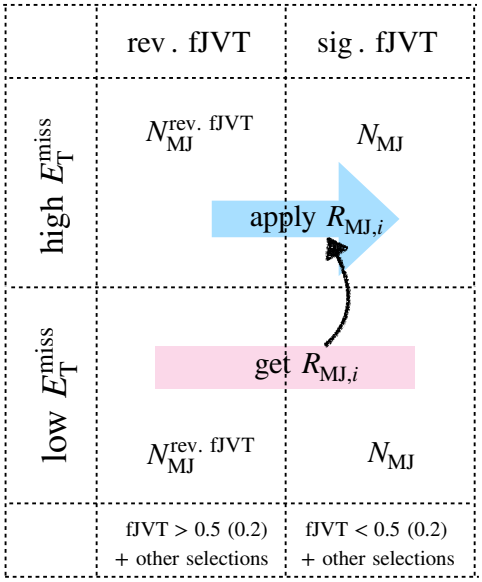

Figure 8.18: Visualisation of the pile-up CR transfer factor method. The transfer factor $R_{\mathrm{MJ},i}$ in region i is measured in a low $E_{\mathrm{T}}^{\mathrm{miss}}$ selection and used to extrapolate from the pile-up CR with reversed fJVT values for the leading jet to the SR for the analysis bins $i \in [1-10] \cup [14-16]$.

A validation of the pile-up CR method is performed in a low $E_{\mathrm{T}}^{\mathrm{miss}}$ CR with $110 < E_{\mathrm{T}}^{\mathrm{miss}} < 150\,\mathrm{GeV}$, $0.5 < m_{\mathrm{jj}} < 1.5\,\mathrm{TeV}$ and fJVT < 0.5 for the two leading jets as shown in Figure 8.19. The fJVT requirement is loosened from 0.2 to 0.5 in that low $E_{\mathrm{T}}^{\mathrm{miss}}$ region to further increase the multijet contribution. A very good agreement is observed.

8.2.3 Combination of RnS and pile-up CR

A combination of the MC-based RnS technique and the pile-up CR approach for the multijet background estimation is used to provide a multijet estimate with uncertainties as small as possible. Prior to combining both techniques, it is validated that both the RnS and the pile-up CR approach give a consistent multijet prediction. First, the MC-based RnS prediction, the data-driven RnS prediction and the pile-up CR method are compared in a loose m_{jj} CR defined by $150 < E_{\mathrm{T}}^{\mathrm{miss}} < 200\,\mathrm{GeV}$, $m_{\mathrm{jj}} < 1.5\,\mathrm{TeV}$, $\Delta\phi_{\mathrm{jj}} < 1$ as well as fJVT < 0.5 for the two leading jets and is shown in Figure 8.20. A reasonable agreement of all methods is shown, while the largest deviations occur at $m_{\mathrm{jj}} < 0.8\,\mathrm{TeV}$. The inclusive SR prediction from both methods are compatible as well, while RnS predicts 912 ± 383 events, the pile-up CR methods predicts 892 ± 194.

A comparison of the m_{jj} shapes in the SR bins 1–10 is shown in Figure 8.21. The statistical significance s of the deviation is approximately calculated via

$$s = \frac{|N_{\mathrm{RnS}} - N_{\text{pile-up CR}}|}{\sqrt{\delta N_{\mathrm{RnS}}^2 + \delta N_{\text{pile-up CR}}^2}}, \tag{8.12}$$

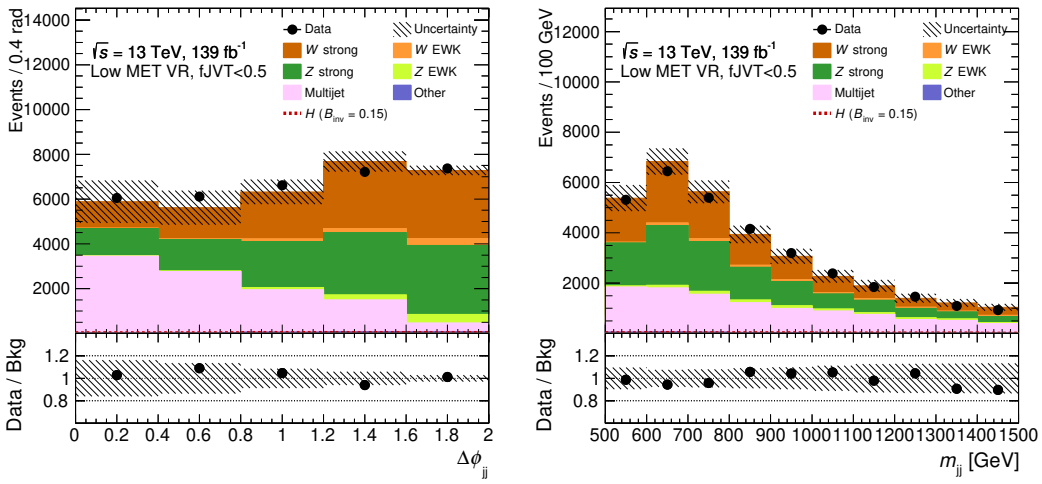

Figure 8.19: Validation of the pile-up CR multijet background prediction in a low $E_{\mathrm{T}}^{\mathrm{miss}}$ region with $110 < E_{\mathrm{T}}^{\mathrm{miss}} < 150\,\mathrm{GeV}$ for $\Delta\phi_{\mathrm{jj}}$ (left) and m_{jj} (right). The uncertainties include statistical and systematic uncertainties.

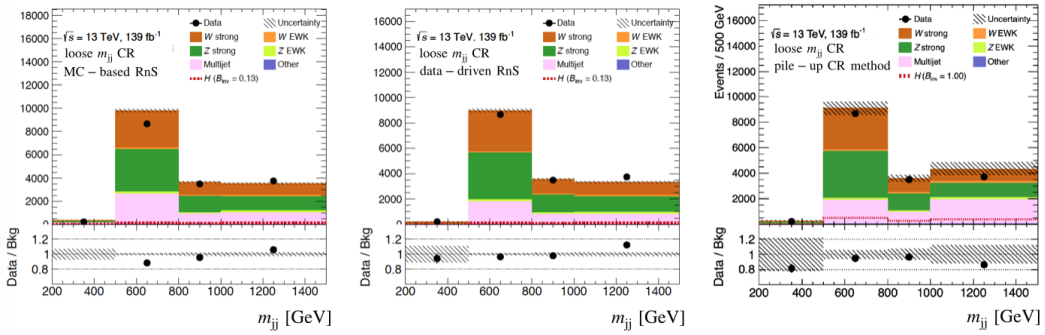

Figure 8.20: Comparison of the MC-based (left) and data-driven (middle) RnS multijet prediction and the pile-up CR method (right). The RnS prediction shows statistical uncertainties only while the pile-up CR method prediction shows statistical and systematic uncertainties.

with the relative event yields N_i (normalised to unity) and uncertainty δN_i. The predicted m_{jj} shapes of both methods agree reasonably in these bins except of SR bin 1 where a difference of about $4.6\,\sigma$ is observed. Since both methods are fully independent, it is not expected that the predictions agree within statistical uncertainties only. In SR bin 1 the predictions are averaged and half of the spread of the difference of both methods is taken as an additional systematic uncertainty. Since SR bin 1 is not very sensitive to the expected signal, the impact of this additional uncertainty on the result is negligible.

The combination of shapes and event counts from RnS and the pile-up CR method works as follows. The SR bins 11–13 are not estimated with the pile-up CR approach due to the jet multiplicity selection since events with jet multiplicities of 3 and 4 are already used to determine the multijet contribution in the SR bins 1–10 and 14–16. An extrapolation from the pile-up CR into the SR with $n_{\mathrm{jet}} \in \{3, 4\}$ is therefore not implemented to keep the fit model simple and to avoid complex correlations between the pile-up CR estimates for the multijet background in the dijet and high n_{jet} SR bins. Thus, the SR bins 11–13 are estimated with RnS only. Since the RnS prediction suffers from $E_{\mathrm{T}}^{\mathrm{miss}}$ trigger efficiency uncertainties in the low $E_{\mathrm{T}}^{\mathrm{miss}}$ range corresponding to the SR bins 14–16, these SR bins are estimated with the pile-up CR. To minimise uncertainties, the SR bins 1–5 are estimated with the pile-up CR method, whereby the event yield in bin 1 is averaged with the RnS prediction.

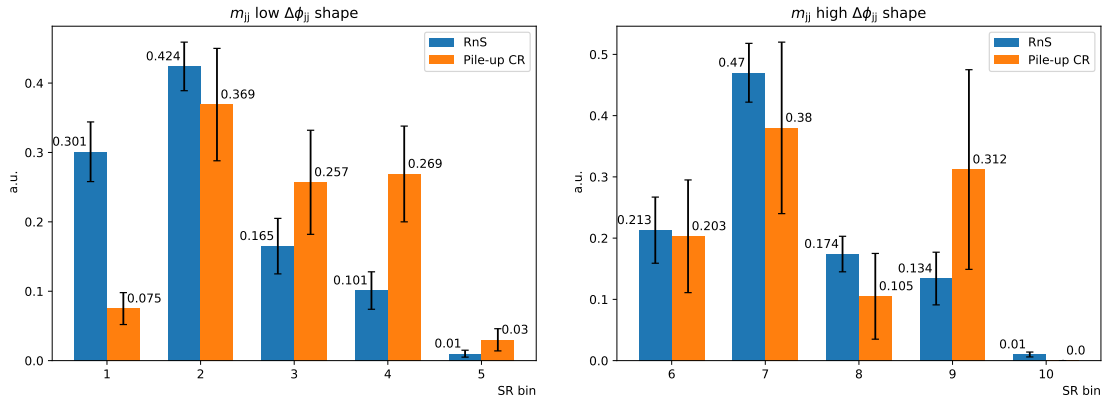

Figure 8.21: Comparison of the m_{jj} shapes predicted by RnS and pile-up CR technique at low $\Delta\phi_{jj}$ (SR bin 1–5) and at high $\Delta\phi_{jj}$ (SR bin 6–10). For the pile-up CR m_{jj} shape, only statistical uncertainties are included, while for the RnS m_{jj} shape statistical and the correlated jet response uncertainties are included.

Due to statistical limitations of the pile-up CR in the SR bins 6–10, the normalisation is determined inclusively in these bins while the m_{jj} shape is determined by RnS.

Given the combination of RnS and the pile-up CR method, a suite of uncertainties is associated with the multijet background modelling, summarised together with the SR event yields in Table 8.9. An uncertainty on the transfer factor $R_{MJ,i}$ (fully correlated between high $\Delta\phi_{jj}$ and low $\Delta\phi_{jj}$ for $E_T^{miss} > 200$ GeV but uncorrelated with $R_{MJ,i}$ for $160 < E_T^{miss} < 200$ GeV) plus a statistical uncertainty from the transfer factor $R_{MJ,i}$ (20–27 %) are included in the pile-up CR prediction. From the RnS side, statistical uncertainties, a non-closure uncertainty, the difference of the data-driven and MC-based RnS methods and jet response core and tail shape variations are included, summarised in Table 8.6. The difference in the m_{jj} shape between the RnS prediction and the pile-up CR method in SR bin 1, likely caused by statistical fluctuations combined with minor mismodellings in the low m_{jj} regime, is covered with a 60 % uncertainty.

Table 8.9: Pre-fit multijet background in the inclusive SR with associated uncertainties from RnS and the pile-up CR method. The inclusive uncertainty is estimated by adding all sources quadratically and a range of the uncertainties for the 16 SR bins is shown as well. Also shown are the SR bins where the methods are utilised.

	RnS		pile-up CR		
incl. SR multijet pred.	912 ± 383		892 ± 194		
utilised in SR bins	1, [6, 10], [11, 13]		[1, 5], {6 – 10}, [14, 16]		
	Uncertainties [%]				
source	inclusive	per bin	source	inclusive	per bin
stat.	9	6-46	stat.	8.6	16-49 (bin 1–5 only)
non-closure	40	37-43	syst. (transfer factor)	20	20-27
jet energy response (15 % core)	5.8	1-41			
jet energy response (50 % tail)	5.4	1-53			
data vs. simulation	4.9	2-30			

CHAPTER 9

Statistical Treatment and Uncertainties

In this chapter the fundamentals of the statistical treatment [246], the analysis likelihood fit model and the experimental as well as theory systematic uncertainties are described.

9.1 Statistical Concepts

The search for WIMP candidates in the VBF Higgs boson to invisible decay channel is performed with a profile likelihood fit using binned distributions of sensitive observables in form of histograms in various analysis regions based on background predictions, signal models and observed data. The event yield prediction N^{exp} can be written as

$$N^{\text{exp}}(\mu, \theta) = \mu \cdot S(\theta) + B(\theta), \tag{9.1}$$

where the parameter of interest (POI) is the signal strength μ, parametrising the rate of signal events S in the region of interest with background events $B = \sum_x B_x$ for background species x. The signal strength μ is chosen such that

$$\mu = \begin{cases} 0, & \text{background} - \text{only model} \\ 1, & \text{specific signal model} \end{cases} . \tag{9.2}$$

The best values of μ and of additional nuisance parameters (NPs) θ, used for the inclusion of systematic uncertainties, are obtained in a profile maximum likelihood fit. The likelihood function $\mathcal{L}(N^{\text{obs}} \mid N^{\text{exp}})$ of observing N^{obs} data events, when S signal events and B background events are expected, is given by the product of Poisson probabilities $\mathcal{P}(N^{\text{exp}} \mid N^{\text{obs}})$ by

$$\mathcal{L}(N_i^{\text{obs}} = N_i \mid \mu, \theta) = \prod_i \frac{1}{N_i!}(\mu S_i + B_i)^{N_i} \exp(-(\mu S_i + B_i)) \cdot \prod_j \mathcal{G}(0 \mid \theta_j), \tag{9.3}$$

where i runs over the bins of both SRs and CRs. Standard Gaussian distributions $\mathcal{L}^{\text{NP}} = \prod_j \mathcal{G}(0 \mid \theta_j)$ are used to model the NPs θ_j which can be constrained in additional auxiliary and calibration measurements. Additional NPs are used for statistical uncertainties in form of generalised Poisson distributions. The inclusion of uncertainties in the statistical model decreases the sensitivity of the analysis with respect to the POI μ by giving the fit more flexibility to match the prediction to the observed data. The maximisation procedure of the binned likelihood fit results in values of the signal strength μ and NPs θ that maximise the likelihood function, written as $\hat{\mu}$ and $\hat{\theta}$. These maximum likelihood estimators are the set of parameters giving overall the best agreement between the prediction and the data under consideration of systematic and statistical uncertainties. In the fit a profiling is performed, i.e. the NPs θ are expressed as a function of the signal strength μ and thus

approximately absorbed during the fitting. Following the Neyman-Pearson lemma [247], the most powerful test statistic q_μ in frequentist statistics for hypothesis testing at the LHC is given by the corresponding negative logarithmic profile likelihood ratio as

$$q_\mu = -2 \ln \left(\frac{\mathcal{L}\left(\mu, \hat{\hat{\theta}}(\mu)\right)}{\mathcal{L}\left(\hat{\mu}, \hat{\theta}\right)} \right) \tag{9.4}$$

where the nominator is maximised for all NPs θ for a given μ, while the denominator describes the global maximum of the total phase space in μ and θ. The notation with double-hats $\hat{\hat{\theta}}(\mu)$ represents the value of parameters that maximise the likelihood for a specific and fixed value of μ, i.e. the conditional maximum likelihood estimator of $\theta(\mu)$, while $\hat{\mu}$ and $\hat{\theta}$ are the unconditional maximum likelihood estimators. Following Wilk's and Wald's theorem [248], under certain conditions, the distribution of q_μ approaches a χ^2 distribution which is approximately independent on the NPs, i.e. the profile likelihood test only depends on μ. Using the test statistic q_μ defined in Equation 9.4, different signal hypothesis $\mu \geq 0$ can be tested. When searching for a signal of new physics one defines a null hypothesis H_0 as the background-only prediction ($\mu = 0$). H_0 is tested against the alternative H_1, defined as the signal plus background hypothesis for a specific nominal signal model μ, so by definition a discovery is an excess regarding the SM prediction. In the presented case, only models with $\mu \geq 0$ are considered (one-sided hypothesis tests), where a new signal corresponds on average to an increase in the event count in the SR. In a discovery measurement, the null hypothesis (background-only model) based on the test statistic according to $\mu = 0$ is rejected in favour of a signal hypothesis, resulting in

$$q_0 = \begin{cases} -2 \ln \left(\frac{\mathcal{L}(0, \hat{\hat{\theta}}(0))}{\mathcal{L}(\hat{\mu}, \hat{\theta})} \right) & , \text{ if } \hat{\mu} \geq 0, \\ 0 & , \text{ if } \hat{\mu} < 0. \end{cases} \tag{9.5}$$

Larger values of the test statistic q_0 corresponds to an increasing incompatibility in form of an under-prediction with the observed data. In absence of an observed signal, the roles of H_0 and H_1 are flipped to set an upper limit on the signal strength μ, thus H_0 is the signal plus background hypothesis tested against the background-only model H_1 and H_0 is rejected if it is not found to be significant. The test statistic q_μ results in

$$q_\mu = \begin{cases} -2 \ln \frac{\mathcal{L}\left(\mu, \hat{\hat{\theta}}(\mu)\right)}{\mathcal{L}\left(0, \hat{\hat{\theta}}(0)\right)}, & \text{if } \hat{\mu} \leq 0, \\ -2 \ln \frac{\mathcal{L}\left(\mu, \hat{\hat{\theta}}(\mu)\right)}{\mathcal{L}(\hat{\mu}, \hat{\theta})}, & \text{if } 0 \leq \hat{\mu} \leq \mu, \\ 0, & \text{if } \hat{\mu} > \mu \end{cases} . \tag{9.6}$$

In this case, a small value of q_μ implies that the observed data is in good agreement with the tested model. The first constraint $0 \leq \hat{\mu}$ corresponds to positive signal rate and the other contraint, $\hat{\mu} < \mu$, implies that an upward fluctuation in data of the form $\hat{\mu} > \mu$ is not interpreted as evidence against the signal hypothesis μ. The compatibility of an observation and the tested hypothesis H is calculated with a p-value, which is a measure of the statistical significance. The p-value is the frequentist probability value, assuming a hypothesis H is true, of observing data of equal or greater incompatibility with the expectation assumed by the hypothesis H. The p-values for the tested hypothesis are calculated from the probability density functions $f(q_\mu \mid \mu, \theta)$ of the corresponding test statistic q_μ. In case of the background-only hypothesis, the p-value is calculated via

$$p_B = \int_{-\infty}^{q_\mu^{\text{obs}}} f(q_0 \mid 0) \, \mathrm{d}q_0, \tag{9.7}$$

while for the signal plus background hypothesis it is

$$p_{S+B} = \int_{q_\mu^{\text{obs}}}^{\infty} f(q_\mu \mid \mu)\, \mathrm{d}q_\mu, \tag{9.8}$$

where q^{obs} is the observed value of the test statistic given the measured data and $f(q_\mu \mid \mu)$ is the probability density function of q_μ given a signal strength μ. For example, when performing a search for a new physics signal, the background-only hypothesis must be rejected. If the corresponding p-value is below a pre-defined level, then the hypothesis can be seen as excluded. The p-value can be translated to the Gaussian significance Z via

$$Z = \Phi^{-1}(1 - p), \tag{9.9}$$

where Φ^{-1} is the inverse of the quantile of a normalised Gaussian distribution. To avoid a claim of a false discovery, the significance of an observation needs to exceed $Z = 5$ corresponding to $p = 2.87 \cdot 10^{-7}$, amongst others to protect against the look-elsewhere effect which describes the phenomenon of a statistically significant observation caused just by chance due to the large size of the parameter space. In terms of limit settings, the statistical significance threshold is set to $Z = 1.64$ ($p = 0.05$). From the p-values of the hypothesis also the frequentist confidence level (CL) [249] can be calculated, which provides a more reasonable way to set upper limits by avoiding accidental exclusion of signals to which the measurement is not sensitive. Given the p-value of the signal plus background model $p_{\text{S+B}}$ and the background-only model p_{B}, the frequentist exclusion CL is given by

$$\text{CL}_s = \frac{p_{\text{S+B}}}{1 - p_{\text{B}}}, \tag{9.10}$$

where the p-value of the signal plus background model, $p_{\text{S+B}}$, is penalised with $1 - p_{\text{B}}$, which is small if the analysis has small sensitivity to the signal model. The upper limit is defined as the largest value of the POI which is not excluded given the pre-defined significance level $\alpha = 0.05$, which corresponds to a $1 - \alpha = 95\,\%$ CL upper limit.

9.2 Analysis Fit Model

A profile likelihood fit is performed in all statistical independent CRs and SRs to predict the expected background in the SR and to measure the signal strength μ following the description in Section 9.1. In absence of an observed signal excess, an upper limit on the branching fraction $\mathcal{B}_{\text{inv}}$ of invisibly decaying Higgs bosons is set at 95 % CL using the asymptotic formula for one-sided frequentist confidence level. The fit model is implemented via the widely used HistFactory and HistFitter frameworks [250, 251] using a likelihood function built from all SRs, described in Section 6.3.2, and CRs for V+jets, lepton fakes and multijet processes as described in Chapter 8.

The likelihood function for the observed yield in the SR is given as a product of Poisson probabilities from signal and background predictions by

$$\mathcal{L}^{\text{SR}} = \prod_i \mathcal{P}\left(N_i^{\text{SR}} \mid \mu \cdot S_i^{\text{SR}} + \beta_i \cdot R^{Z/W} \cdot B_{Z,i}^{\text{SR}} + \beta_i \cdot B_{W,i}^{\text{SR}} + B_{\text{MJ},i}^{\text{SR}} + B_{\text{other},i}^{\text{SR}}\right), \tag{9.11}$$

where N_i^{SR} is the observed SR yield. $B_{W,i}^{\text{SR}}$ and $B_{Z,i}^{\text{SR}}$ are the W+jets and Z+jets yields from simulation, $B_{\text{MJ},i}^{\text{SR}}$ is the multijet background estimate, $B_{\text{other},i}^{\text{SR}}$ is the yield of other backgrounds, S_i^{SR} is the expected yield for an invisible Higgs boson and β_i are a free floating fit parameters per SR bin i.

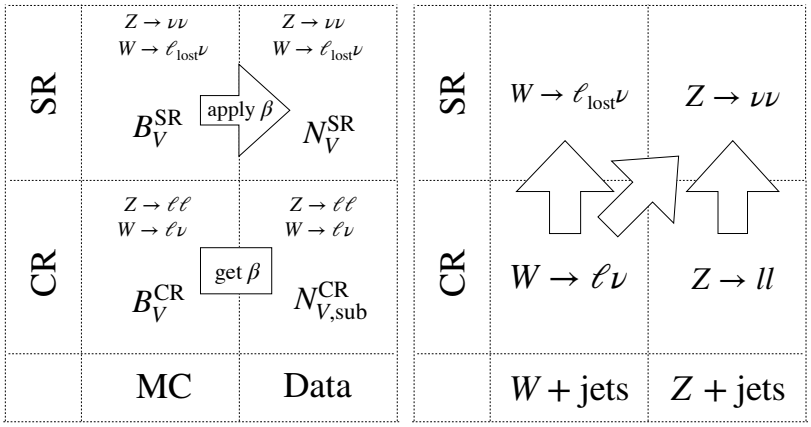

Figure 9.1: Sketch of the method used to extrapolate from V+jets CR selections to the SR. The figure on the left shows the scaling of the SR prediction from simulation with a normalisation factor β derived in the CR (in the fit β is also fitted simultaneously in the SR). The figure on the right shows the extrapolation from the V+jets CRs to the corresponding SRs with the possibility to constrain the $Z \to \nu\nu$ background with the $W \to \ell\nu$ control selection. The notation is described in the text and the analysis bin index i for each CR and SR is omitted in this sketch.

The likelihood function for the yields in V+jets CR is given by

$$\begin{aligned}\mathcal{L}^{V\text{+jets CR}} = \quad & \prod_i \mathcal{P}\left(N_i^{Z\text{CR}} \mid \beta_i \cdot \cdot R^{Z/W} \cdot B_{Z,i}^{Z\text{CR}} + B_{\text{non-}Z,i}^{Z\text{CR}}\right) \\ & \prod_i \mathcal{P}\left(N_i^{W\mu\nu\text{CR}} \mid \beta_i \cdot B_{W,i}^{W\mu\nu\text{CR}} + B_{\text{non-}W,i}^{W\mu\nu\text{CR}} + R_{M,i} \cdot n_{\text{fake-}\mu,i}\right) \\ & \prod_i \mathcal{P}\left(N_i^{We\nu\text{CR}} \mid \beta_i \cdot B_{W,i}^{We\nu\text{CR}} + B_{\text{non-}W,i}^{We\nu\text{CR}} + R_{S,i} \cdot n_{\text{fake-}e,i}\right)\end{aligned} \tag{9.12}$$

where β_i are the same free parameters as in Equation 9.11 and propagate the CR constraints to the expected W and Z background yields in the SR. $N_i^{Z\text{CR}}$, $N_i^{W\mu\nu\text{CR}}$ and $N_i^{We\nu\text{CR}}$ are the observed data yields in the $Z \to \ell\ell$, $W \to e\nu$ and $W \to \mu\nu$ CRs, respectively. $B_{W,i}^{W\mu\nu\text{CR}}$ and $B_{W,i}^{We\nu\text{CR}}$ are the predicted pre-fit W+jets yields from MC split by lepton flavour, and $B_{Z,i}^{Z\text{CR}}$ are the Z+jets events in simulation scaled by the ratio of Z/W as a function of m_{jj} as detailed in Section 8.1.3. The $B_{\text{non-}Z,i}^{Z\text{CR}}$, $B_{\text{non-}W,i}^{W\mu\nu\text{CR}}$, and $B_{\text{non-}W,i}^{We\nu\text{CR}}$ are the simulated yields due to non-Z, non-W and non-fake lepton contributions to these CRs. The "fake" leptons are described with free fit parameters, $n_{\text{fake-}e/\mu,i}$ for electron and muon fakes, respectively, multiplied by fake ratio factors $R_{S/M,i}$. Further, β_i are a free parameters per analysis bin translating the constraints from the W and Z CRs via a transfer factor, which allows for the cancellation of theoretical uncertainties between the CR and SR, into the SR. For this the Atlas Z MC is reweighted with $R^{Z/W}$ at full NLO, see Equation 8.5. Smaller differences between the SR and CR originate from acceptance effects due to the event selection and systematic uncertainties, e.g. related to leptons or triggers, affecting the SR and CR in a different manner. The same β_i are used for the W+jets and Z+jets processes. Also an inclusive scale factor for both the EWK and QCD V+jets production is used, so the ratio of QCD V+jets to EWK V+jets is taken from simulation.

The amount of electron and muons fakes in the W+jets CR, $n_{e-\text{fake}}$ and $n_{\mu-\text{fake}}$, respectively, are constraint in the two fake-lepton CRs as detailed in Section 8.1.1. Accordingly, the likelihood function for the fake-e and

fake-μ CRs is given by

$$\begin{aligned}\mathcal{L}^{\text{fake CR}} &= \prod_i \mathcal{P}\left(N_i^{\text{fake-}\mu\text{ CR}} \mid \beta_i \cdot B_{W,i}^{\text{fake-}\mu\text{ CR}} + B_{\text{non-}W,i}^{\text{fake-}\mu\text{ CR}} + n_{\text{fake-}\mu,i}\right) \\ &\quad \prod_i \mathcal{P}\left(N_i^{\text{fake-}e\text{ CR}} \mid \beta_i \cdot B_{W,i}^{\text{fake-}e\text{ CR}} + B_{\text{non-}W,i}^{\text{fake-}e\text{ CR}} + n_{\text{fake-}e,i}\right)\end{aligned} \tag{9.13}$$

with the W boson contribution $B_{W,i}^{\text{fake-}e/\mu\text{ CR}}$ scaled by the same β_i as in the SR and W CR, the non-W boson contribution $B_{\text{non-}W,i}^{\text{fake-}e/\mu\text{ CR}}$ and the fakes $n_{\text{fake-}e/\mu,i}$ of electrons and muons, respectively.

The multijet background estimation strategy is described Section 8.2 and is based on a combination of the predictions from RnS and the pile-up CR method. In most of the SR bins, the pile-up CR is used to constrain the free fit parameters $n_{\text{PU-MJ},i}$ which are then scaled with the transfer factor $R_{\text{MJ},i}$, see Equation 8.11. One individual multijet CR is used for the SR bins 1–5 and 14–16, respectively, while in the SR bins 6–10 the inclusive prediction is constraint by the pile-up CR for statistical reasons, but the distribution of events in the individual bins $f_{\text{RnS},i}$, i.e. the m_{jj}-shape for $\Delta\phi_{\text{jj}} > 1$, is predicted by the MC-based RnS method. For the SR bins 11–13 the prediction is obtained solely by the MC-based RnS method as normalised in the respective mid m_{jj} and low m_{jj} CR (pre-fit). The corresponding likelihood is given as the product of Poisson probabilities by

$$\mathcal{L}^{\text{MJ CR}} = \prod_{i\in[1,5]\cup\{6-10\}\cup[14,16]} \mathcal{P}\left(N_i^{\text{MJ CR}} \mid B_{\text{non-MJ},i}^{\text{MJ CR}} + n_{\text{PU-MJ},i}\right) \tag{9.14}$$

where $B_{\text{non-MJ},i}^{\text{MJ CR}}$ is the non-multijet contribution determined from simulation and $B_{\text{MJ},i}^{\text{SR}}$ is the multijet yield in bin i. The full multijet estimate that enters the SR likelihood given in Equation 9.11 is given by

$$B_{\text{MJ},i}^{\text{SR}} = \begin{cases} n_{\text{PU-MJ},i} \cdot R_{\text{MJ},i}, & \text{if } i \in [1,5] \cup [14,16] \\ n_{\text{PU-MJ},\{6-10\}} \cdot R_{\text{MJ},\{6-10\}} \cdot f_{\text{RnS},i}, & \text{if } i \in [6,10] \\ B_{\text{MJ-RnS},i}^{\text{SR}}, & \text{if } i \in [11,13] \end{cases}. \tag{9.15}$$

Overall, the full likelihood expression in all SRs and CRs is given by

$$\begin{aligned}\mathcal{L}(\mu,\vec{\beta},\vec{n},\vec{\theta} \mid \vec{N}) &= \mathcal{L}^{\text{SR}} \cdot \mathcal{L}^{\text{MJ CR}} \cdot \mathcal{L}^{V\text{+jets CR}} \cdot \mathcal{L}^{\text{fake CR}} \cdot \mathcal{L}^{\text{NP}} \\ &= \prod_i \mathcal{P}\left(N_i^{\text{SR}} \mid \mu \cdot S_i^{\text{SR}} + \beta_i \cdot R^{Z/W} \cdot B_{Z,i}^{\text{SR}} + \beta_i \cdot B_{W,i}^{\text{SR}} + B_{\text{MJ},i}^{\text{SR}} + B_{\text{other},i}^{\text{SR}}\right) \\ &\quad \prod_{i\in[1,5]\cup\{6-10\}\cup[14,16]} \mathcal{P}\left(N_i^{\text{MJ CR}} \mid B_{\text{non-MJ},i}^{\text{MJ CR}} + n_{\text{PU-MJ},i}\right) \\ &\quad \prod_i \mathcal{P}\left(N_i^{Z\text{CR}} \mid \beta_i \cdot R^{Z/W} \cdot B_{Z,i}^{Z\text{CR}} + B_{\text{non-}Z,i}^{Z\text{CR}}\right) \\ &\quad \prod_i \mathcal{P}\left(N_i^{W\mu\nu\text{CR}} \mid \beta_i \cdot B_{W,i}^{W\mu\nu\text{CR}} + B_{\text{non-}W,i}^{W\mu\nu\text{CR}} + R_M \cdot n_{\text{fake-}\mu,i}\right) \\ &\quad \prod_i \mathcal{P}\left(N_i^{\text{fake-}\mu\text{ CR}} \mid \beta_i \cdot B_{W,i}^{\text{fake-}\mu\text{ CR}} + B_{\text{non-}W,i}^{\text{fake-}\mu\text{ CR}} + n_{\text{fake-}\mu,i}\right) \\ &\quad \prod_i \mathcal{P}\left(N_i^{We\nu\text{CR}} \mid \beta_i \cdot B_{W,i}^{We\nu\text{CR}} + B_{\text{non-}W,i}^{We\nu\text{CR}} + R_{S,i} \cdot n_{\text{fake-}e,i}\right) \\ &\quad \prod_i \mathcal{P}\left(N_i^{\text{fake-}e\text{ CR}} \mid \beta_i \cdot B_{W,i}^{\text{fake-}e\text{ CR}} + B_{\text{non-}W,i}^{\text{fake-}e\text{ CR}} + n_{\text{fake-}e,i}\right) \\ &\quad \prod_j \mathcal{G}\left(0 \mid \theta_j\right).\end{aligned} \tag{9.16}$$

9.3 Systematic Uncertainties

When performing a measurement at the LHC, different sources of uncertainties must be considered. First, there are statistical uncertainties caused by the limited sample size of the data and simulation. Second, there

Table 9.1: Summary of experimental systematic uncertainties considered in the VBF+$E_{\mathrm{T}}^{\mathrm{miss}}$ analysis.

Event	
Luminosity	1.7 % uncertainty on the luminosity (normalisation)
PRW_DATASF	pile-up profile uncertainty data vs. sim
Electrons	
EL_EFF_Trigger_TOTAL_1NPCOR_PLUS_UNCOR	trigger efficiency
EL_EFF_Reco_TOTAL_1NPCOR_PLUS_UNCOR	reconstruction efficiency
EL_EFF_ID_TOTAL_1NPCOR_PLUS_UNCOR	ID efficiency
EL_EFF_ChargeIDSel_TOTAL_1NPCOR_PLUS_UNCOR	charge ID efficiency
EL_EFF_Iso_TOTAL_1NPCOR_PLUS_UNCOR	isolation efficiency
EG_SCALE_ALL	energy scale
EG_RESOLUTION_ALL	energy resolution
Lepton inefficiency	
eleANTISFEL_EFF_ID_TOTAL_1NPCOR_PLUS_UNCOR	ID inefficiency
Muons	
MUON_EFF_TrigSystUncertainty MUON_EFF_TrigStatUncertainty	trigger efficiency
MUON_EFF_RECO_STAT MUON_EFF_RECO_SYS	reconstruction and ID efficiency for $p_{\mathrm{T}} > 15$ GeV
MUON_EFF_RECO_STAT_LOWPT MUON_EFF_RECO_SYS_LOWPT	reconstruction and ID efficiency for $p_{\mathrm{T}} < 15$ GeV
MUON_EFF_ISO_STAT MUON_EFF_ISO_SYS	isolation efficiency
MUON_EFF_TTVA_STAT MUON_EFF_TTVA_SYS	track-to-vertex association efficiency
MUON_SCALE	energy scale
MUON_ID	energy resolution from inner detector
MUON_MS	energy resolution from muon system
MUON_SAGITTA_RESBIAS	muon sagitta-related
MUON_SAGITTA_RHO	muon sagitta-related
jets	
JET_EffectiveNP	energy scale uncertainty split into 15 components
JET_EtaIntercalibration_NonClosure_*	jet-intercalibration in situ uncertainty (6)
JET_BJES_Response	calorimeter response to b-jets
JET_Flavor_Composition	jet composition between quarks and gluons
JET_Flavor_Response	calorimeter response on gluon-initiated jets
JET_JER_DataVsMC_MC16	jet-related uncertainty
JET_JER_EffectiveNP	jet energy resolution uncertainty split into 12 parameters
JET_JvtEfficiency	JVT pile-up tagging
JET_fJvtEfficiency	fJVT pile-up tagging
JET_Pileup_OffsetMu	μ modelling in MC
JET_Pileup_OffsetNPV	N_{PV} modelling in MC
JET_Pileup_PtTerm	p_{T} dependence of pile-up correction
JET_Pileup_RhoTopology	modelling of event energy density in MC
JET_PunchThrough_MC16	GSC punch-through correction
JET_SingleParticle_HighPt	high p_{T} unc. from single hadrons and test-beam measurements
$E_{\mathrm{T}}^{\mathrm{miss}}$	
xeSFTrigWeight	trigger efficiency uncertainty
MET_SoftTrk_ResoPerp	track-based soft term related to transversal resolution uncertainty
MET_SoftTrk_ResoPara	track-based soft term related to longitudinal resolution uncertainty
MET_SoftTrk_ScaleUp	track-based soft term related to longitudinal scale uncertainty
MET_SoftTrk_ScaleDown	track-based soft term related to longitudinal scale uncertainty

are systematic uncertainties, which can be divided into experimental uncertainties, background modelling uncertainties and theory uncertainties. The different sources of systematic uncertainties are described in this chapter. Section 9.3.1 presents a description of the important experimental uncertainties, while Section 9.3.2 described the theoretical uncertainties. Uncertainties related to the background modelling are already described in Section 8. The handling of the uncertainties mostly follows the official ATLAS recommendations produced by the different working groups providing the calibrations and uncertainties.

9.3.1 Experimental Uncertainties

In this section the experimental systematic uncertainties are presented. A summary is given in Table 9.1 and the sources of uncertainties are described in the following.

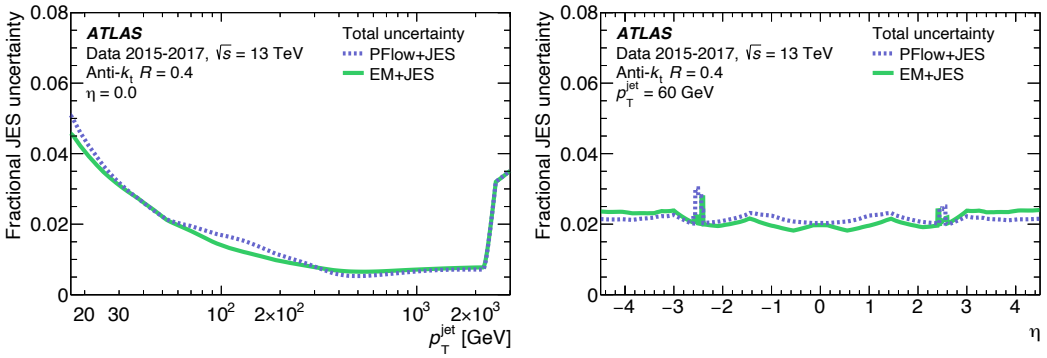

Figure 9.2: Fractional JES uncertainties for fixed $\eta = 0$ as a function of p_{T} (a) and for fixed $p_{\mathrm{T}} = 60\,\mathrm{GeV}$ as function of η (b). The hashed blue line represents PFlow jets, the green line EMTopo jets [184].

- **Luminosity**: An uncertainty on the measured integrated luminosity $\mathcal{L}$ must be included. For the full Run II data-taking period the relative uncertainty is 1.7 %, obtained with the LUCID-2 sub-detector [124], see Section 3.3.2.
- **Pile-up Modelling**: The pile-up profile in simulation and data is in general not the same since simulation is carried out with a fixed value of $\langle\mu\rangle$. To account for this difference a pile-up reweighting with an associated uncertainty is performed. The weights are derived in data as a function of $\langle\mu\rangle$ and applied to simulation.
- **Trigger**: Additional uncertainties arise from the usage of $E_{\mathrm{T}}^{\mathrm{miss}}$, jet, lepton and muon triggers and the corresponding trigger efficiency uncertainties arising from differences in data and simulation [131, 195, 197, 198].
- $\boldsymbol{E_{\mathrm{T}}^{\mathrm{miss}}}$: The $E_{\mathrm{T}}^{\mathrm{miss}}$ terms are quantities built from other objects such as jets or tracks. Associated uncertainties of the input object measurements are propagated to the $E_{\mathrm{T}}^{\mathrm{miss}}$ quantities. The track-based $E_{\mathrm{T}}^{\mathrm{soft}}$ term has uncertainties associated with its transversal and longitudinal (with respect to the hard $E_{\mathrm{T}}^{\mathrm{miss}}$ term) uncertainties on soft term scale and resolution, measured in data to simulation comparisons [164].
- **Leptons and Photons**: Different uncertainties are related to electron, photon and muon measurements, which are in particular relevant in the V+jets CRs. These uncertainties include amongst others reconstruction, identifications and isolation efficiencies as well as energy scale and resolution uncertainties [138, 145]. For muons, additional uncertainties are considered, such as track-to-vertex association, MS energy resolution and muon sagitta uncertainties. Further an uncertainty on the inefficiency scale factor for the lepton veto is assigned. The uncertainties are derived on the event yield by applying one σ variations.
- **Jets**: More than 70 NPs are related to PFlow jet measurements and the MC-based and in situ calibrations originating amongst others from the η-intercalibration, b-jet response, flavour composition and response, energy resolution and scale, pile-up tagging efficiencies (JVT and fJVT), pile-up calibration uncertainties (ρ topology, p_{T} correction and offset to N_{PV} and $\langle\mu\rangle$) and punch-through [184]. Usually only a reduced set of NPs is considered in the fit model based on eigenvalue decomposition. The systematic uncertainties for PFlow and EMTopo are in a similar range. For PFlow, higher pile-up uncertainties are balanced by smaller in situ uncertainties. The systematic uncertainties in JES for central jets with $|\eta| < 1.2$ show a p_{T}-dependence and range from 5 % at $p_{\mathrm{T}} \sim 20\,\mathrm{GeV}$, 1 % for $250\,\mathrm{GeV} < p_{\mathrm{T}} < 2\,\mathrm{TeV}$ to 3.5 % for $p_{\mathrm{T}} > 2.5\,\mathrm{TeV}$. Exemplary distributions of the JES uncertainty are shown in Figure 9.2. The absolute JER uncertainty ranges from 1.5 % at $p_{\mathrm{T}} \sim 2\,\mathrm{GeV}$ to 0.5 % at $p_{\mathrm{T}} \sim 300\,\mathrm{GeV}$, where an example is shown in Figure 9.3.

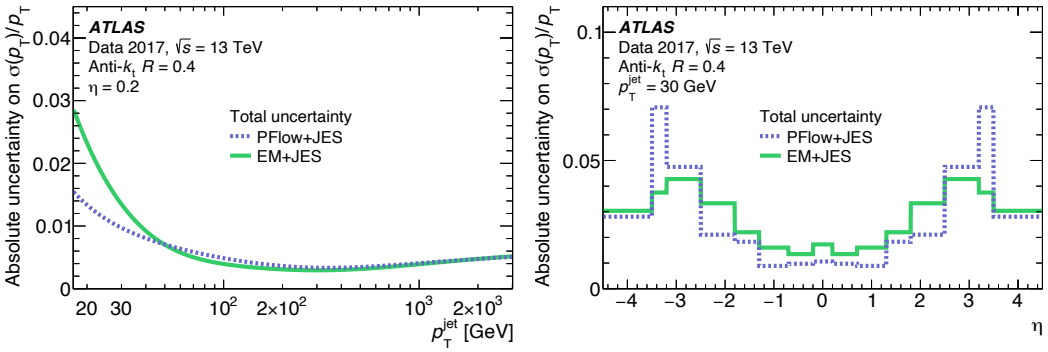

Figure 9.3: Fractional JER uncertainties at fixed $\eta = 0.2$ as a function of p_{T} (a) and for fixed $p_{\mathrm{T}} = 60\,\mathrm{GeV}$ as function of η (b). The hashed blue line represents PFlow jets, the green line EMTopo jets [184].

9.3.2 Theory Uncertainties

Theoretical systematic uncertainties arise from fixed scale choices and modellings of the event generation, parametrisation of the proton substructure or limited precision of perturbative calculations in partonic cross section calculations and thus are relevant for both background and signal processes. Section 9.3.2 summarises systematic uncertainties related to background estimates and Section 9.3.2 describes theory uncertainties related to the signal process.

Background Uncertainties

The QCD and EWK V+jets processes, which are the dominant backgrounds, are simulated at fixed orders with Sherpa and Herwig as described in Section 6.2.2. The generation of these events is based on fixed choices of important parameters and are related to higher-order MEs and parton shower matching uncertainties:

- **CKKW:** The ME matching (CKKW) scale is used for calculating the overlap between the parton shower and matrix element objects [252].
- **Resummation:** The resummation scale is the scale used for the resummation of gluon emission in parton shower calculations.
- **Factorisation and Renormalisation:** Factorisation scale μ_{F} and renormalisation scale μ_{R} are scale choices in fixed-order ME calculation. In the framework of perturbation theory these scales arise from the handling of infrared (IR) and ultraviolet (UV) divergences.

The uncertainties on μ_{R}, μ_{F} and the resummation scale are evaluated by varying them up and down with a factor two around the nominal value.The scales μ_{R} and μ_{F} are varied on an event basis by calculating alternative event weights for the different scale choices within Sherpa and thus the statistics is fully correlated between the nominal prediction and the variations. The uncertainties are determined by taking an envelope of the seven point scale variations by varying μ_{R} and μ_{F} (seven combinations of scale variations arise from the central value, both scales independently up and down and both scales coherently up or down). For strong (EWK) V+jets the uncertainties range from $^{+27}_{-18}$ % ($^{+11}_{-9}$ %) at low m_{jj} bins to $^{+43}_{-26}$ % ($^{+29}_{-20}$ %) at high m_{jj} bins.

For the resummation and CKKW scale, the systematic variations are determined with independent samples. While the CKKW matching scale is varied around the nominal value of 20 GeV down to 15 GeV and up to 30 GeV, the resummation scales is varied up and down by factor two with respect to its nominal value. Due to limited computing ressources, this is performed with a reweighting scheme as a function of p_{T}^{V} and n_{jet} on truth-level which is applied to the fully reconstructed sample of the nominal prediction from which the absolute symmetrised uncertainty is determined by half of the spread of the up- and down-variations in each analysis

bin using a relaxed SR selection. The resulting resummation (CKKW) scale uncertainties range from 4–8 % (4–6 %).

PDF uncertainties originate from experimental uncertainties of the datasets and the functional form used for PDF fits and uncertainties from the DGLAP evolution [125–127]. For V+jets, they are evaluated by calculating the standard deviation of the nominal parametrisation choice (NNPDF) and 100 PDF replicas of it, resulting in a 1–2 % uncertainty.

The correlation of Z and W boson processes is described in Section 8.1.3 in which the Z+jets background is reweighted to full NLO on the ratio of Z and W+jets processes whereby uncertainties of the W+jets and Z+jets are fully correlated and mostly cancel in the fit method. The reweighting is performed separetely for QCD and EWK V+jets processes and is affected by several sources of systematic uncertainties which are also derived as function of $x = m_{\mathrm{jj}}$ [244]. QCD as well as mixed QCD-EWK uncertainties are derived as the difference of LO and NLO theory calculations (2–5 %) via

$$\delta R^{Z/W,m}_{\mathrm{QCD}}(x) = \left| R^{Z/W,m}_{\mathrm{NLO\,QCD}}(x) - R^{Z/W,m}_{\mathrm{TH}}(x) \right| \tag{9.17}$$

and

$$\delta R^{Z/W,m}_{\mathrm{Mix}}(x) = \left| R^{Z/W,m}_{\mathrm{NLO\,QCD+EWK}}(x) - R^{Z/W,m}_{\mathrm{TH}}(x) \right|, \tag{9.18}$$

respectively, using the notation introduced in Section 8.1.3 and

$$R^{Z/W,m}_{\mathrm{TH}}(x) = R^{Z/W,m}_{\mathrm{(N)LO\,QCD\times EWK}}(x) \tag{9.19}$$

for production mode $m = \mathrm{QCD}, \mathrm{EWK}$. Parton shower uncertainties for the EWK samples are derived in Herwig7 by comparing the dipole recoil model and an angular ordered parton shower model (3–5 %) [253], i.e.

$$\delta R^{Z/W,m}_{\mathrm{PS}}(x) = \left| R^{Z/W,m}_{\mathrm{Herwig7,\,dipole\times EW}}(x) - R^{Z/W,m}_{\mathrm{Herwig7,AO}}(x) \right| \tag{9.20}$$

while for the strong V+jet samples this is evaluated by comparing the nominal correction $R^{Z/W,m}_{\mathrm{TH}}(x)$ with a correction plus parton shower $R^{Z/W,m}_{\mathrm{(N)LOPS\,QCD\times EWK}}(x)$ via

$$\delta R^{Z/W,m}_{\mathrm{PS}}(x) = \left| R^{Z/W,m}_{\mathrm{(N)LOPS\,QCD\times EWK}}(x) - R^{Z/W,m}_{\mathrm{TH}}(x) \right|, \tag{9.21}$$

For the QCD V+jet samples, reweighting uncertainties caused by a selection difference of the analysis and the theoretical NLO corrections are evaluated with Sherpa, which are derived with a looser selection, most prominantely with a missing third jet veto for the strong V+jets. The uncertainty is derived via

$$\delta R^{Z/W,m}_{\mathrm{Rew}}(x) = \left| R^{Z/W,m}_{\mathrm{Sherpa,TJV}}(x) - R^{Z/W,m}_{\mathrm{Sherpa}}(x) \right|. \tag{9.22}$$

and results in uncertainties ranging from 2–13 %. For the EWK V+jets, the theory corrections are derived in three bins in $\Delta\phi_{\mathrm{jj}}$ given by 0–1, 1–2, > 2, and inclusively. While the inclusive Z/W correction is used, the differences from the inclusive correction to the correction from the three binnings are assigned as conservative systematic uncertainties calculated via

$$\delta R^{Z/W,m}_{\mathrm{Rew}\,i}(x) = \left| R^{Z/W,m}_{\mathrm{TH,binned}\,i}(x) - R^{Z/W,m}_{\mathrm{TH}}(x) \right|, \tag{9.23}$$

where the index i refers to individual $\Delta\phi_{\mathrm{jj}}$ bins. The differences mainly originate from the interference with EWK diboson production and are small for small $\Delta\phi_{\mathrm{jj}}$ and increase with increasing $\Delta\phi_{\mathrm{jj}}$. The individual systematics uncertainties on the theory Z/W corrections are shown as function of m_{jj} in Figure 9.4.

For the other backgrounds no separate theoretical uncertainties are included since these backgrounds contribute ≤ 5 % in CRs or SRs.

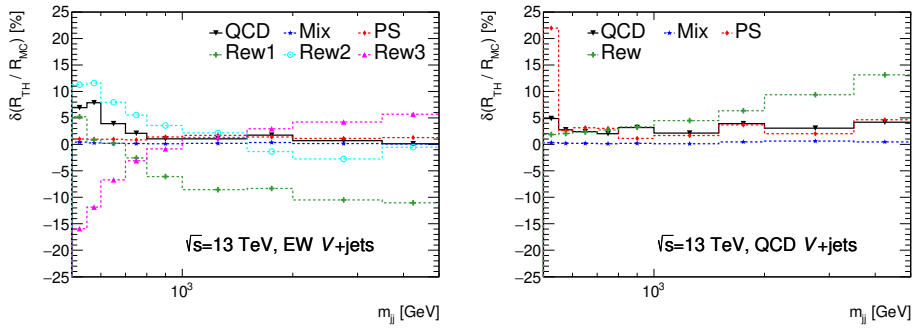

Figure 9.4: Theory systematic uncertainties for the Z/W correlation for EWK V+jets (left) and strong V+jets (right) production. The different sources of uncertainties are described in the text. Large uncertainties of the parton shower (PS) for the strong V+jets at low m_{jj} values are outside of the analysis selection.

Signal Uncertainties

Dominant sources of uncertainties on the VBF and ggF Higgs boson signal are parton shower, PDF, QCD and EWK scale uncertainties. The production cross sections and uncertainties are used according to the LHC Higgs boson working group prescriptions [254] for the POWHEG generator and the PYTHIA8 parton showering. For the VBF signal, the m_{jj}-dependent renormalisation and factorisation scales μ_R and μ_F, respectively, are varied independently and a Steward-Tackmann (ST) technique [255] is used for the third, fourth and fifth jet veto uncertainty resulting in uncertainties in the range of 1–3 %. The parton shower uncertainty is determined in bins of $\Delta\phi_{jj}$ and m_{jj} with a comparisons of the HERWIG7 PS and the PYTHIA8 samples resulting in uncertainties of 2–4 %. Furthermore, PDF uncertainties from the NNPDF set are included via variations of the nominal PDF set with a resulting uncertainties in the order of 1–2 %. Further, the VBF signal receives a p_T-dependent NLO EWK correction from HAWK with an uncertainty of 2 %.

Similar uncertainties are used for the ggF Higgs boson signal. In addition to the PDF and parton shower uncertainties, the ST scheme is used for the jet bin migration uncertainty resulting in 45 % (41 %) for the $n_{jet} = 2$ ($n_{jet} = 3, 4$) bin.

9.3.3 Uncertainty Correlation Scheme

The experimental uncertainties are fully correlated across all SRs and CRs and all analysis bins.

Also full correlation is assumed for the Z and W+jets theory uncertainties between SRs and CRs, allowing for large cancellation of these uncertainties in the fit, but the EWK and QCD contributions of each process are treated uncorrelated.

While the PDF uncertainties are fully correlated across all analysis bins, different correlation schemes across the analysis bins are possible for the V+jets theory uncertainties, which can be tested in Asimov fits and from which the most conservative one is chosen: The uncertainties are split into seventeen components from which 16 are fully uncorrelated in each of the sixteen analysis bins, and one compontent fully correlated along the analysis bins ensuring that the combined uncertainty is equal to the inclusive uncertainty, where the latter ensures that a splitting of the inclusive uncertainty in various analysis bins, e.g. in m_{jj}, should not reduce the overall uncertainty assigned with it.

CHAPTER 10

Results and Interpretation

10.1 Results

The fitting procedure is evaluated using the full 139 fb^{-1} Run II data set as described in Chapter 9. First, a fit in the high $\Delta\phi_{jj}$ VR is performed. Then, it is checked for a signal discovery by testing the compatibility of the data with the background-only hypothesis in the SR. If no signal excess is observed, upper limits on the invisibly Higgs boson branching fraction can be set, which is 0.12 % according to the SM but which could be much larger as predicted by several BSM scenarios [82, 84].

The high-$\Delta\phi_{jj}$ VR-only fit considers unblinded data and simulation in the $2 < \Delta\phi_{jj} < 2.5$ VR, but no actual SR data nor simulation for $\Delta\phi_{jj} < 2$ is included according to the blinding strategy. The region is binned in five m_{jj}-bins and the signal strength μ is floated in this fit but the signal contribution is < 13 %, from which ~ 80 % originates from VBF and 20 % from ggF, which is below the blinding threshold of ~ 20 %. As shown in Figure 10.1, a very good post-fit modelling is observed in the high-$\Delta\phi_{jj}$ VR, and the agreement is improved compared to the pre-fit modelling, which validates background estimates as well as the Z boson MC reweighting as function of m_{jj} and justifies the usage of the reweighting procedure, which is well motivated from the high correlation of the W and Z processes in the VBF phase space.

Then, fits are performed including observed data in the unblinded SR [4]. Under the assumption of SM production cross sections, the asymptotic formulae for the frequentist CL_s approach can be used to set a 95 % CL upper limit on the invisible Higgs boson branching fraction $\mathcal{B}_{\text{inv}}$. The post-likelihood fit yields are shown and compared to data in the Tables 10.1 as well as 10.2 and in Figure 10.2, where the background predictions are scaled according to the best fitting parameters. The dominant background contributions in the SR are the EWK and QCD V+jets processes followed by multijet events. At low m_{jj} values, the QCD Z+jets background is the largest background followed by QCD W+jets production. The EWK Z+jets and W+jets production is at the level of the multijet contribution. At high m_{jj} values, the EWK production of Z+jets and W+jets are dominant with roughly equal contributions while the multijet background, the QCD V+jets and other backgrounds, which include $t\bar{t}$, VV and VVV processes as well as VBF Higgs boson to $\tau\tau$ and WW, are far smaller. The m_{jj} and $\Delta\phi_{jj}$ post-fit distribution in the inclusive SR is shown in Figure 10.3 and Figure 10.4. The uncertainties on the background are derived in the fit using all nuisance parameters and correlation schemes as described in more detail in Section 9.3.

No significant signal excess over the background-only prediction is found. Thus the fit is used to extract an upper limit on the invisible Higgs boson branching fraction $\mathcal{B}_{\text{inv}}$ by finding the smallest signal which still allows for rejecting the signal plus background hypothesis. The measured and expected limits plus the expected $1\,\sigma$ and $2\,\sigma$ uncertainty ranges are summarised in Table 10.3. The expected limit is determined by replacing the observed data yields in the SR by yields and best fit parameters predicted by the background-only model,

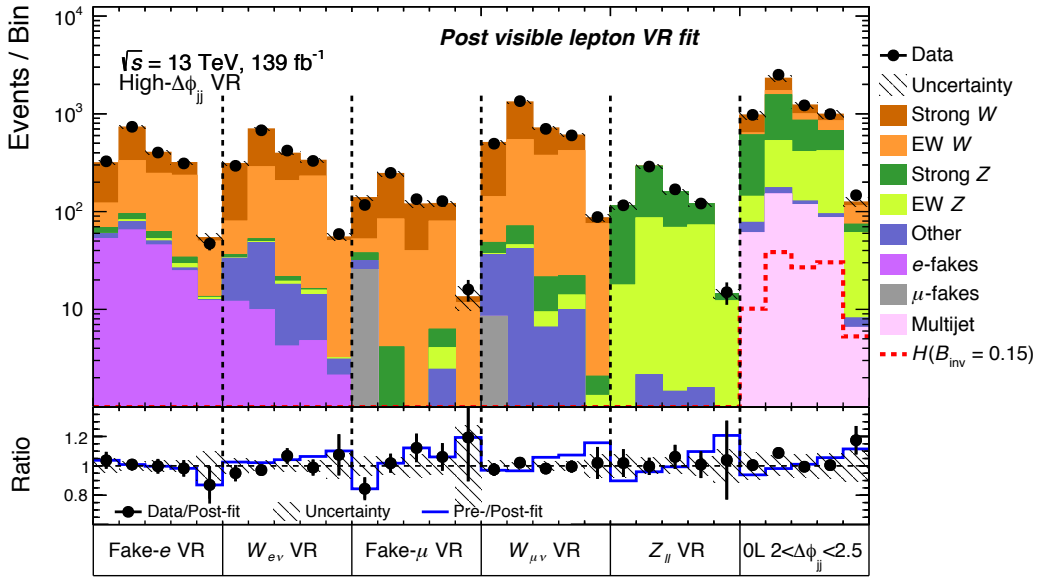

Figure 10.1: Likelihood fit distribution in the high $\Delta\phi_{jj}$ VR and the corresponding CRs in five bins of m_{jj}. Yields and uncertainties are shown post-fit.

whereby the signal strength is floating in the fit. The observed (expected) limit is

$$\mathcal{B}_{\text{inv}} < 0.145 \left(0.103^{+0.041}_{-0.028}\right) \text{ at } 95\,\% \text{ CL}.$$

A $1.02\,\sigma$ excess is observed as visible in the high m_{jj} bins in Figure 10.3, so the result is fully compatible within uncertainties with the expected result.

The impact of different groups of systematic uncertainties on the upper limit is shown in Table 10.4 and is evaluated by fixing the nuisance parameters of a group of systematic uncertainties to their best fit values. For this, independent fits are performed and the $1\,\sigma$-uncertainty on the limit $\sigma_{\text{no}\,\theta_j}$ is quadratically subtracted from the nominal uncertainty that includes all systematic uncertainties, i.e. the fractional uncertainty σ_{θ_j} of the group of uncertainties θ_j is obtained by

$$\sigma_{\theta_j} = \sqrt{\sigma^2_{\text{total}} - \sigma^2_{\text{no}\,\theta_j}}, \tag{10.1}$$

with the total uncertainty σ_{total}. Leading uncertainties are data and MC statistics, multijet and the lepton fake modelling whose impact is increased compared to previous the analyses since the W CR is also used to constrain the Z+jets background.

The measured upper limit on $\mathcal{B}_{\text{inv}}$ is a significant improvement compared to the result $\mathcal{B}_{\text{inv}} < 0.37\,(0.28)$ of the previous analysis iteration [1], mainly caused by the following modifications:

- increased data statistics due to $139\,\text{fb}^{-1}$ data collected in Run II
- improved multijet background modellings with a combination of the novel RnS and pile-up CR methods
- significant refinements of the V+jet modelling, amongst others with a m_{jj}-dependent Z/W boson reweighting using a new EWK and QCD NLO calculation in the VBF phase space
- data-driven estimate of muon fakes in the W CRs
- increased MC statistics with fast filtered simulations optimised for the VBF+$E_{\text{T}}^{\text{miss}}$ phase space especially for strong V+jets processes

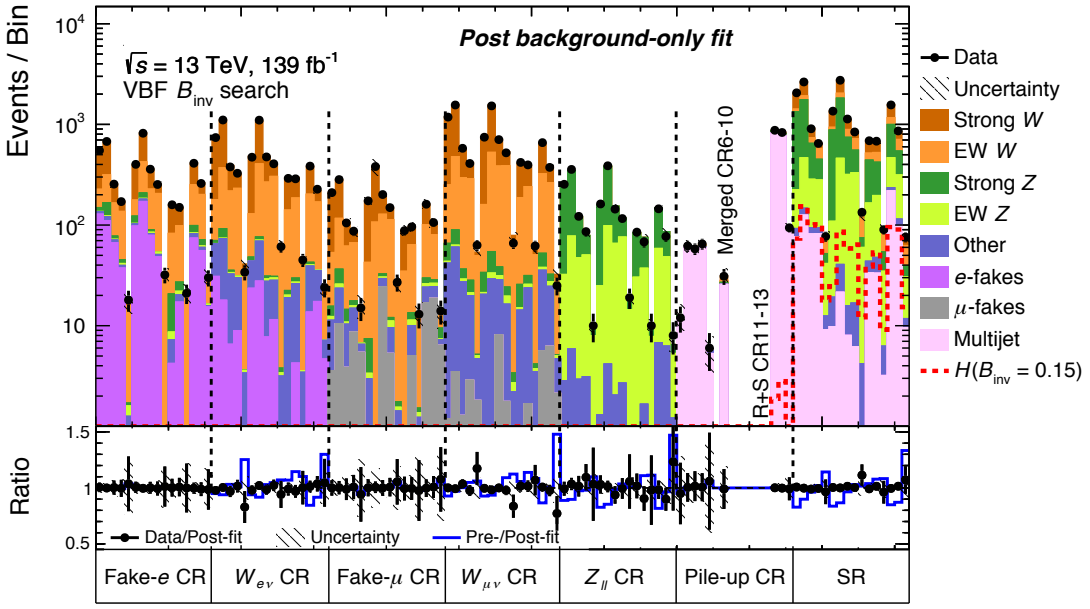

Figure 10.2: Post-fit distribution of all SR and CR bins for the background-only fit ($\mu = 0$). The signal is scaled to a branching ratio of 0.145.

- usage of modern ATLAS reconstruction techniques and object identification working points for leptons and jets such as the usage of PFlow jets including a forward jet pile-up tagging
- improved CR event selection with increased acceptance
- optimised SR event selection down to $E_{\mathrm{T}}^{\mathrm{miss}}$ values of 160 GeV and m_{jj} values of 0.8 TeV
- optimised SR binning scheme by dividing the inclusive SR into sixteen subregions with different signal sensitivity by binning in m_{jj}, $E_{\mathrm{T}}^{\mathrm{miss}}$, n_{jet} and $\Delta\phi_{\mathrm{jj}}$.

The different improvements are grouped and quantified in Figure 10.5.

Further, upper limits from the CONF note result and the newest result including and excluding the NLO correlation scheme of W and Z+jets processes are compared in Figure 10.6. This shows that the analysis is a huge improvement compared to the measurement from the 36 fb^{-1} analysis and is consistent with the CONF note result. The 139 fb^{-1} fit result excluding the Z/W correlation results in

$$\mathcal{B}_{\mathrm{inv}}^{\mathrm{no\,Z/W}} < 0.125 \left(0.11^{+0.028}_{-0.046}\right) \text{ at } 95\,\% \text{ CL},$$

with a small observed excess of 0.34 σ. The result is compatible with the CONF note result and the small excess originates from the newly added low $E_{\mathrm{T}}^{\mathrm{miss}}$ SR bins 14–16 in which a small excess in the SR is observed in a CR-only fit. The expected limit improves to 10 % when including the Z/W correlation since this fit model is less affected from statistical uncertainties of the Z CR. Including the Z/W correlation results in a slightly worse but statistically compatible observed upper limit (15 %) compared to the uncorrelated case (12.5 %), the difference is 0.68 σ. The reasons for this is twofold. First, the NLO correction factors for the EWK Z+jets processes, which are dominant in the high m_{jj} SR regime, are smaller than one which affects that the total pre-fit background estimate is roughly 0.5 σ lower. Second, three sources of uncertainties are treated uncorrelated between the two fit setups, namely the normalisation factors β_Z, theory uncertainties related to the NLO reweighting and statistical uncertainties from the $Z \to ll$ CR. The different treatment of uncertainties, the Z/W NLO correction and the independent normalisation factors for Z and W+jets processes, giving the fit more flexibility, explain the

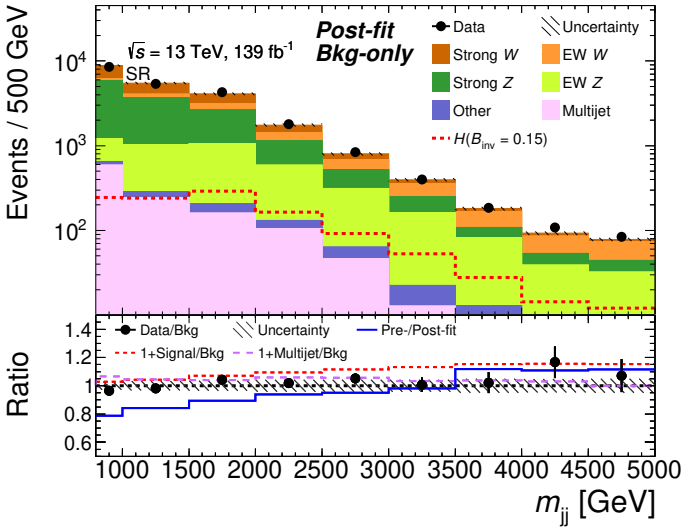

Figure 10.3: Post-fit distribution of m_{jj} in the inclusive SR. In addition to the ratio of data and background events, the lower panels show the ratio of the background expectation pre- and post-fit.

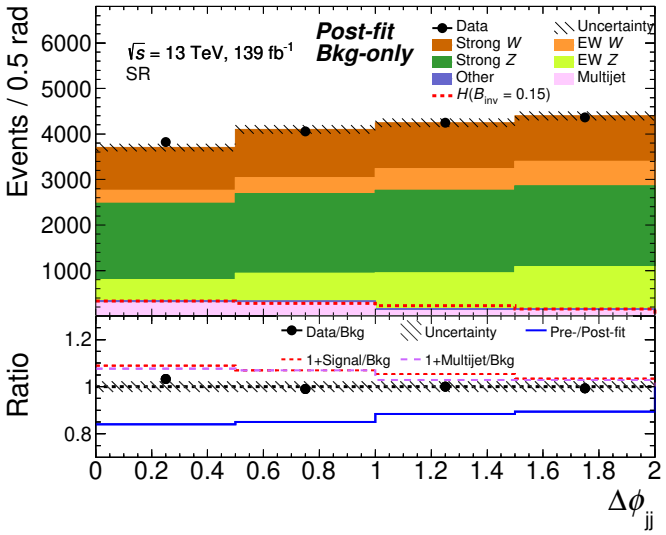

Figure 10.4: Post-fit distribution of $\Delta\phi_{jj}$ in the inclusive SR. In addition to the ratio of data and background events, the lower panels show the ratio of the background expectation pre- and post-fit.

slightly smaller observed limit in the uncorrelated case.

10.2 Interpretation

The profile likelihood fit results in an upper limit on the invisible branching fraction $\mathcal{B}_{inv}$ of the Higgs boson. The main interpretations of this result in terms of Higgs portal models are related to properties of the final state dark matter candidates (WIMPs) and the mediator:

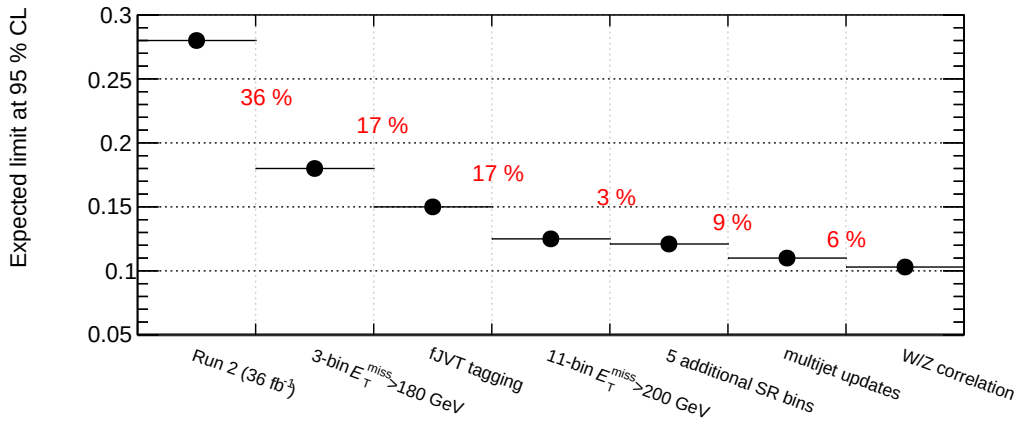

Figure 10.5: Evolution of the expected upper limit on $\mathcal{B}_{\text{inv}}$ with different analysis improvements compared to the 36 fb^{-1} analysis [1]. The red numbers represent the relative improvement with respect to the previous step. The second bin includes improvements of lepton identification WPs, increased acceptances in CRs and SR and increased MC statistics and is the configuration as close as possible to the previous result. The next two bins include the addition of fJVT pile-up tagging and an improved SR selection and binning scheme, respectively. The selection and binning scheme is further improved with the addition of a low $E_{\text{T}}^{\text{miss}}$ SR (160–200 GeV) and a finer binning of the $n_{\text{jet}} = 3, 4$ SR bin. The last two bins include the improvements of the multijet modelling with RnS and the pile-up CR and the NLO correlation scheme of W and Z+jets processes.

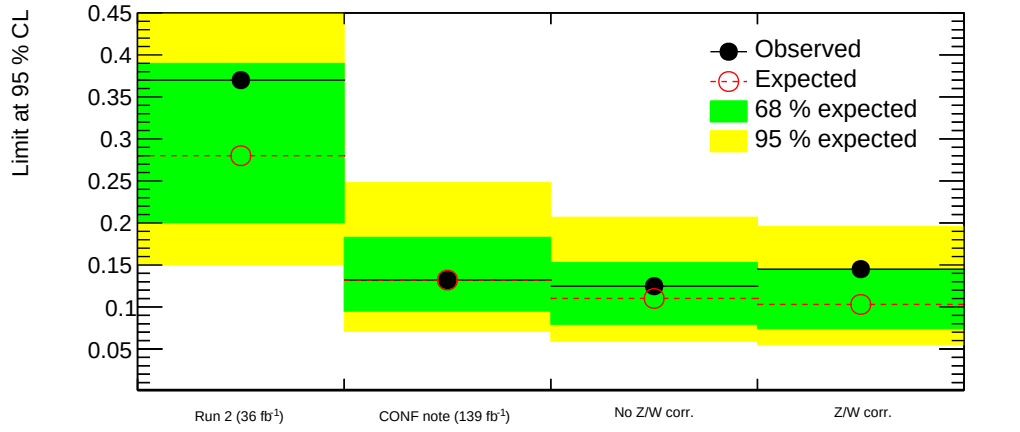

Figure 10.6: Comparison of the expected and observed limits from the 36 fb^{-1} analysis [1], the preliminary full Run II CONF note result [3] as well as the full Run II configuration excluding and including the NLO Z/W boson correction.

Table 10.1: Post-fit event yields of data, signal and backgrounds in the SR for each bin with $\mu = 0$. The uncertainties on the backgrounds (Bkg) are derived by the fit and take into account the correlations of the background uncertainties.

	$n_{\text{jet}} = 2, \lvert\Delta\phi_{\text{jj}}\rvert < 1, m_{\text{jj}}$ bins				
	0.8–1.0 TeV	1.0–1.5 TeV	1.5–2.0 TeV	2.0–3.5 TeV	>3.5 TeV
Process	Bin 1	Bin 2	Bin 3	Bin 4	Bin 5
Z strong	1 110 ± 57	1 289 ± 79	362 ± 41	169 ± 29	10.6 ± 3.4
Z EWK	132 ± 27	318 ± 69	190 ± 32	186 ± 27	28.9 ± 4.8
W strong	632 ± 41	735 ± 77	179 ± 24	82 ± 19	2.6 ± 1.8
W EWK	78 ± 16	157 ± 33	90 ± 16	120 ± 17	25.2 ± 4.4
Multijet	76 ± 49	124 ± 41	81 ± 25	82 ± 27	9.1 ± 4.4
Other	15.6 ± 2.8	21.4 ± 3.3	12.5 ± 2.3	11.6 ± 2.8	3.4 ± 1.0
Total Bkg	2 044 ± 43	2 646 ± 48	915 ± 28	650 ± 23	79.8 ± 7.1
H ($\mathcal{B}_{\text{inv}} = 0.15$)	74 ± 11	154 ± 16	98.9 ± 9.9	102 ± 11	17.9 ± 2.7
Data	2059	2640	905	647	77
Data/Bkg	1.01 ± 0.03	1.00 ± 0.03	0.99 ± 0.04	1.00 ± 0.05	0.97 ± 0.14
β_V	1.18 ± 0.23	1.07 ± 0.21	1.01 ± 0.15	0.97 ± 0.12	0.88 ± 0.12
	$n_{\text{jet}} = 2, 1 < \lvert\Delta\phi_{\text{jj}}\rvert < 2, m_{\text{jj}}$ bins				
	0.8–1.0 TeV	1.0–1.5 TeV	1.5–2.0 TeV	2.0–3.5 TeV	>3.5 TeV
Process	Bin 6	Bin 7	Bin 8	Bin 9	Bin 10
Z strong	768 ± 39	1 357 ± 80	424 ± 50	222 ± 39	14.5 ± 4.8
Z EWK	89 ± 19	418 ± 77	301 ± 45	313 ± 38	55.5 ± 6.1
W strong	416 ± 39	715 ± 63	228 ± 29	121 ± 34	4.3 ± 1.4
W EWK	56 ± 13	215 ± 41	145 ± 24	165 ± 21	41.8 ± 5.3
Multijet	9.8 ± 5.3	21 ± 12	8.0 ± 4.4	6.2 ± 3.5	0.5 ± 0.3
Other	9.4 ± 1.6	19.1 ± 3.1	7.8 ± 1.4	10.6 ± 2.5	3.7 ± 1.2
Total Bkg	1 348 ± 35	2 745 ± 49	1 115 ± 29	838 ± 26	120.3 ± 8.4
H ($\mathcal{B}_{\text{inv}} = 0.15$)	24.9 ± 3.0	86.4 ± 7.1	58.4 ± 4.7	64.2 ± 5.9	12.2 ± 1.7
Data	1354	2745	1131	841	134
Data/Bkg	1.00 ± 0.04	1.00 ± 0.03	1.01 ± 0.04	1.00 ± 0.05	1.11 ± 0.12
β_V	1.20 ± 0.24	1.14 ± 0.20	0.99 ± 0.12	0.94 ± 0.11	0.96 ± 0.12

- an upper limit on the WIMP-nucleon cross section $\sigma_{\text{WIMP-nucleon}}$ as a function of the WIMP mass
- an upper limit on $\sigma_{\text{SM}}^{\text{VBF}} \cdot \mathcal{B}_{\text{inv}}$ as function of the mediator mass.

The upper limit on $\mathcal{B}_{\text{inv}}$ can be compared to the direct dark matter detection experiments DarkSide-50 [90], PandaX-4T [256] and Cresst [257], which search in a laboratory directly for a recoil of an atomic nucleus scattering off a WIMP candidate. In direct detection measurements, the limit boundaries are set at 90 % CL instead 95 % CL as usual in collider searches. The measured 90 % CL for the SM Higgs boson ($m_{\text{H}} = 125\,\text{GeV}$) is calculated, resulting in 0.127 (0.087), and translated into an upper bound on the scattering cross section of nucleons and WIMPs. For this, the correlation between $\mathcal{B}_{\text{inv}}$ and the WIMP-nucleon cross section is evaluated in an EFT framework with a BSM physics scale at $O(1)\,\text{TeV} \gg m_H$. As described in Section 2.2.3 and in Equation 2.43, for WIMP masses $m_\chi < m_H/2$, the spin-independent scattering cross section for WIMPs and the nucleon can be described with

$$\sigma_{\text{WIMP-nucleon}} \sim \frac{f^2 \lambda_{HXX}^2 \mu}{m_H^4}, \tag{10.2}$$

with the reduced mass $\mu = m_n m_\chi/(m_n + m_\chi)$, nucleon mass $m_n = 0.939\,\text{GeV}$, mediator mass m_H, nucleon form factors f [86] and coupling constants λ_{HXX} [258]. Since both the WIMP-nucleon cross section as well as the $\mathcal{B}_{\text{inv}}$ are proportional to the Higgs boson-WIMP coupling λ_{HXX}^2, the invisible Higgs boson decay width can be related to the WIMP-nucleon cross section by $\Gamma_{\text{inv}} = r \cdot \sigma_{\text{WIMP-nucleon}}$, where r depends according to Equation 10.2 only on the WIMP mass and some SM parameters [84]. From the definition of the branching

Table 10.2: Post-fit event yields of data, signal and backgrounds in the SR for each bin with $\mu = 0$. The uncertainties on the backgrounds (Bkg) are derived by the fit and take into account the correlations of the background uncertainties.

	$3 \leq n_{\text{jet}} \leq 4$, m_{jj} bins			160 GeV $< E_{\text{T}}^{\text{miss}} <$ 200 GeV, m_{jj} bins		
	1.5–2.0 TeV	2.0–3.5 TeV	>3.5 TeV	1.5–2.0 TeV	2.0–3.5 TeV	>3.5 TeV
Process	Bin 11	Bin 12	Bin 13	Bin 14	Bin 15	Bin 16
Z strong	275 ± 41	224 ± 44	19.3 ± 6.7	530 ± 47	228 ± 32	8.4 ± 3.5
Z EWK	121 ± 39	148 ± 44	28.4 ± 6.0	230 ± 38	199 ± 28	18.7 ± 4.0
W strong	178 ± 30	147 ± 30	10.0 ± 3.8	404 ± 52	143 ± 29	8.6 ± 3.9
W EWK	76 ± 19	104 ± 23	29.7 ± 5.4	169 ± 29	164 ± 23	23.6 ± 5.6
Multijet	33 ± 21	33 ± 15	3.2 ± 2.4	218 ± 61	97 ± 32	9.6 ± 3.5
Other	10.2 ± 1.8	14.4 ± 2.8	3.0 ± 0.9	15.8 ± 2.6	16.8 ± 3.6	2.2 ± 0.8
Total Bkg	694 ± 25	671 ± 23	93.6 ± 8.2	1 568 ± 38	848 ± 27	71.0 ± 7.3
H ($\mathcal{B}_{\text{inv}} = 0.15$)	38.7 ± 6.2	54.9 ± 8.0	9.2 ± 2.4	95.6 ± 9.6	90.3 ± 7.8	15.3 ± 3.2
Data	688	681	90	1561	861	76
Data/Bkg	0.99 ± 0.05	1.01 ± 0.05	0.96 ± 0.13	1.00 ± 0.03	1.01 ± 0.05	1.07 ± 0.16
β_V	0.98 ± 0.23	0.84 ± 0.16	0.92 ± 0.14	1.22 ± 0.19	1.06 ± 0.14	0.64 ± 0.11

Table 10.3: 95 % CL limits on the invisible SM Higgs boson branching ratio $\mathcal{B}_{\text{inv}}$ for 139 fb^{-1} data collected at $\sqrt{s} = 13$ TeV.

Observed	Expected	$+1\sigma$	-1σ	$+2\sigma$	-2σ
0.145	0.103	0.144	0.075	0.196	0.055

Table 10.4: Relative impact for different sources of uncertainties on the 95 % CL expected upper limit for $\mathcal{B}_{\text{inv}}$. The third column shows the individual contributions on the upper limit uncertainty band. The "V+jets data statistics" is the uncertainty originating from limited statistics from the W and Z+jets CRs. The "Other" category contains sources from $E_{\text{T}}^{\text{miss}}$, luminosity, pile-up and a diboson uncertainty in the Z boson CR.

Source	Limit change (Δ %)	Impact on $\pm 1\sigma$
V+jets data statistics	9.4	0.015
Data statistics	8.7	0.022
MC statistics	3.8	0.010
Lepton fakes	6.5	0.014
Leptons exp.	5.3	0.011
Multijet	5.0	0.014
JER	4.2	0.011
Other	2.8	0.010
JES	2.1	0.008
V+jets theory	4.2	0.012
Signal theory	0.6	0009

fraction follows

$$\mathcal{B}_{\text{inv}} = \frac{\sigma_{\text{WIMP-nucleon}}}{\frac{\Gamma_{\text{SM}}}{r} + \sigma_{\text{WIMP-nucleon}}}, \tag{10.3}$$

with the full SM Higgs boson decay width Γ_{SM}. Therefore an upper bound on $\mathcal{B}_{\text{inv}}$ can be translated into an upper bound on $\sigma_{\text{WIMP-nucleon}}$. Due to the different WIMP mass dependencies of the effective Lagrangians introduced in Equation 2.40, the upper limits as a function of the WIMP mass depend on the spin-nature of the dark matter candidates, so that the weakest bound is expected in the scalar case [83].

The result is shown in Figure 10.7. The excluded cross section values in the WIMP mass range between 1 GeV and 60 GeV depend on the spin and mass of the WIMP hypothesis. For the scalar WIMP hypothesis, cross sections in the range $[3 \cdot 10^{-43}, 6 \cdot 10^{-46}]$ cm^2 are excluded. In the Majorana fermion WIMP model, the cross

section exclusion ranges from $4 \cdot 10^{-47}$ to 10^{-45} cm^2, while for the EFT vector interpretation the excluded cross sections range from $4 \cdot 10^{-45}$ to 10^{-50} cm^2. As described in Section 2.2.3, models for UV complete vector-like WIMP scenarios extended with a dark scalar Higgs boson of mass m_2 [87–89] can be introduced. Due to unspecific model parameters corresponding to a wide range in $\sigma_{\text{WIMP-nucleon}}$, typically worst and best-case scenarios are shown. Weaker (stronger) limits are obtained if the singlet-like scalar is lighter (heavier) than the SM Higgs boson.

The LHC results are complementary to those from direct detection experiments [90, 93, 259, 260]. While the LHC has a low sensitivity for large WIMP masses $m_\chi \geq O(100\,\text{GeV})$, direct searches reach in this range a higher sensitivity. In contrast, the LHC has a higher sensitivity in the low WIMP mass range. This is expected since the LHC apparatus has in principle no limitations for the production of particles with low masses, which is in contrast to direct detection experiments in which the recoil energies produced in the interactions of light dark matter particles with atomic nuclei is below the sensitivity threshold. For example, their low mass sensitivity is limited due to a background neutrino floor, which is created by atmospheric or solar neutrinos scattering off the target nuclei and thus fake a WIMP signal [261]. The neutrino floor for elastic neutrino-nucleus scattering is also displayed in Figure 10.7 and assumes Germanium as target material for the whole WIMP mass range [262, 263]. In addition, the various direct detection experiments differ in used technology and materials, e.g. of the target nuclei, and thus also in their sensitivity for different masses. As expected from kinematics, it is further observed that the LHC sensitivity is stronger (weaker) at low WIMP masses, i.e. in the limit $m_\chi \ll m_H$, for Majorana (scalar) WIMPs. Further, the sensitivity gets worse for WIMP masses close to $m_H/2$. The sensitivity boundary at $m_H/2$ corresponds to the on-shell requirement of the WIMP candidates produced in SM Higgs boson decays.

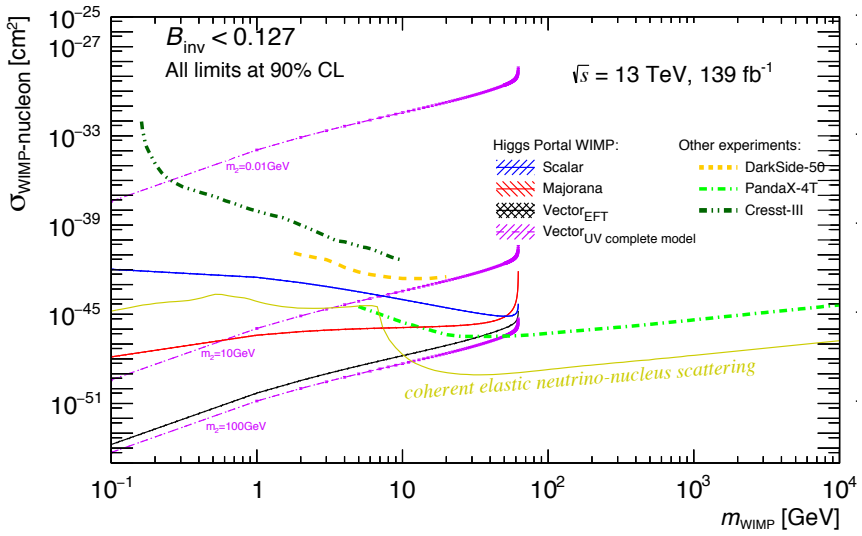

Figure 10.7: Resulting 90 % upper limit on the spin-independent WIMP-nucleon cross section obtained by interpreting the observed upper limit on $\mathcal{B}_{\text{inv}}$ in terms of Higgs portal models as function of the WIMP mass m_{WIMP}. Regions above each line are excluded. Its evident that the presented LHC search interpreted in Higgs portal models is complementary to direct dark matter searches.

Other hypothetical massive scalar bosons, as motivated by two Higgs doublet models or SUSY theories, are tested as alternative mediators to the dark sector. For this interpretation alternative signals are generated similar to the nominal VBF Higgs boson production but using a different Higgs boson mass and excluding the EWK NLO correction from HAWK of the nominal sample. The assumptions for this interpretation are that the new mediators couple to weak vector bosons and can be produced in VBF. However, since the production cross sections of these new mediators are unknown, upper limits are not set on the branching fraction but on the

product of production cross section σ^{VBF} and invisible branching ratio $\mathcal{B}_{\text{inv}}$. The nominal analysis fit is repeated by replacing the nominal SM Higgs boson of mass m_H with the new mediator of mass m_H. The resulting 95 % CL upper limits on cross section $\sigma_{\text{SM}}^{\text{VBF}}$ times invisible branching ratio $\mathcal{B}_{\text{inv}}$ are shown in Figure 10.8. The upper limits on the cross section times branching fraction range from 1.0 pb for scalar bosons with mass of 50 GeV to 0.1 pb at a scalar boson mass of 2 TeV. No re-optimisation of the analysis is performed for the BSM scenarios, i.e. for the whole mass range the analysis selections and categorisations are the same as for the nominal search though very heavy mediators ($m_H > 1$ TeV) have different m_{jj} shapes as the SM Higgs boson. This is visualised in Figure 10.9 for a selection of $E_{\text{T}}^{\text{miss}} > 150$ GeV, leading jet $p_{\text{T}} > 80$ GeV, subleading jet $p_{\text{T}} > 50$ GeV, $\Delta\eta_{\text{jj}} > 3.5$, $m_{\text{jj}} > 0.8$ TeV, $\Delta\phi_{\text{jj}} < 2$, $\eta_0 \cdot \eta_1 < 0$ and the $E_{\text{T}}^{\text{miss}}$ trigger is applied. Especially the m_{jj} and $\Delta\eta_{\text{jj}}$ shape show a signficant impact on the shape from varying the Higgs boson mass due to the t-channel VBF scattering kinematics with large quark four-momentum exchange. The ggF SM Higgs boson signal is also displayed which especially shows a different $\Delta\phi_{\text{jj}}$ signature than the VBF processes due to the typical collinear splitting of jets which originate mostly from initial state radiation. Given these kinematic arguments, the measured upper limits improve with increasing mediator mass due to the increasing accumulation of signal events at larger values of m_{jj}, while the background event yields remain small at high m_{jj} values.

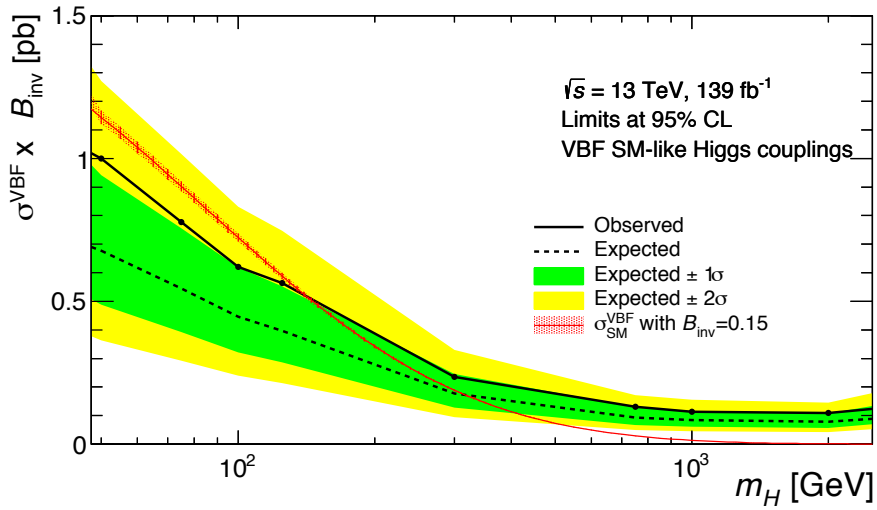

Figure 10.8: Resulting 95 % CL upper limit on cross section times $\sigma_{\text{SM}}^{\text{VBF}}$ times invisible branching ratio $\mathcal{B}_{\text{inv}}$ as function of the mass of a heavy scalar mediator particle. The red line shows the upper limit on $\sigma \cdot \mathcal{B}_{\text{inv}}$ which would be obtained for the observed limit of $\mathcal{B}_{\text{inv}} = 0.15$.

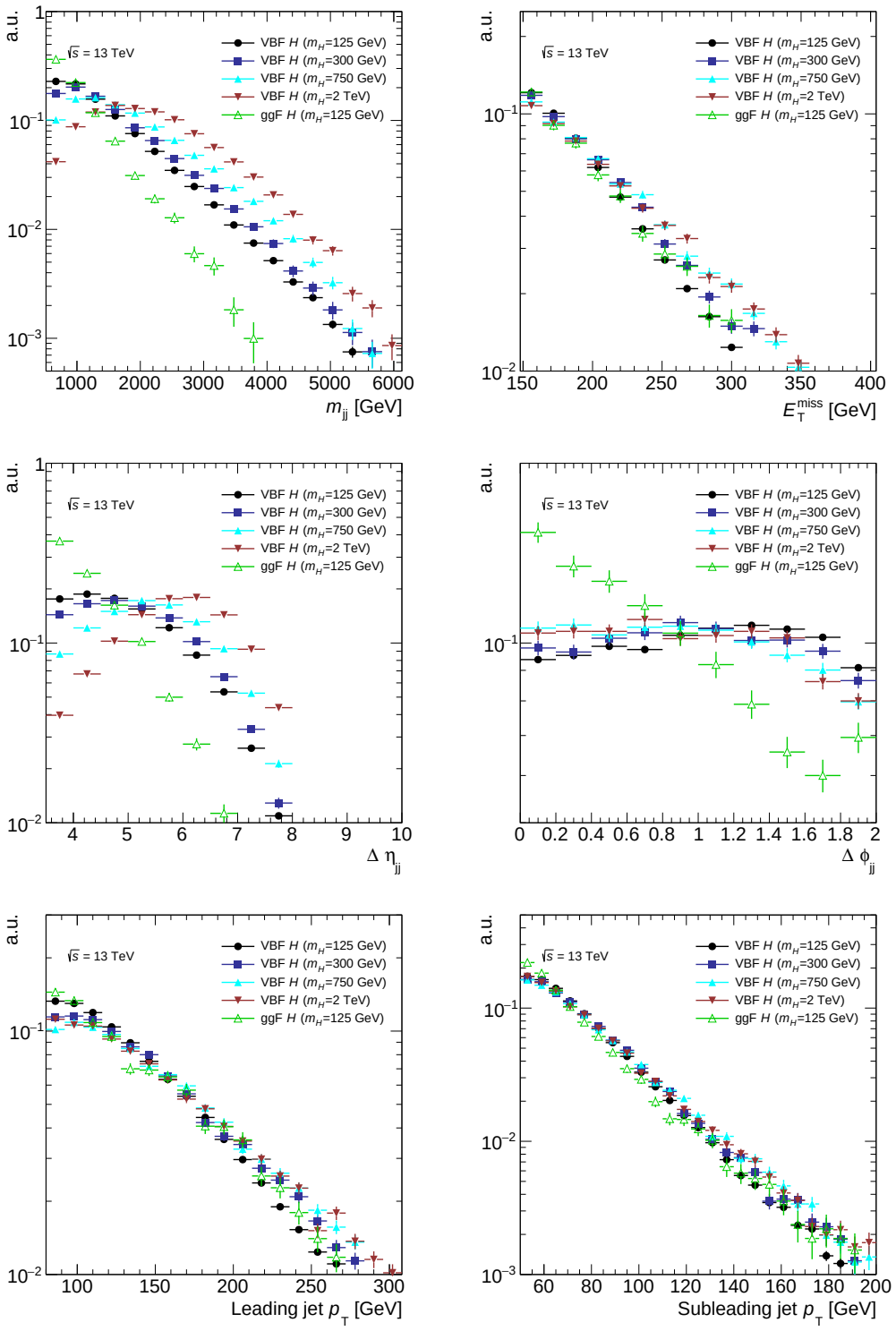

Figure 10.9: Shape of the dijet invariant mass m_{jj}, E_T^{miss}, $\Delta\eta_{jj}$, $\Delta\phi_{jj}$, leading and subleading jet p_T for VBF Higgs boson signals with different Higgs boson masses. For reference also the ggF SM Higgs boson signal is shown. The histograms are normalised to unity.

CHAPTER 11

Summary and Outlook

11.1 Summary

While there is overwhelming observational evidence for the existence of dark matter from astrophysical measurements, the standard model of particle physics cannot explain its particle nature, which is one of the biggest unanswered question in modern physics. A variety of complementary measurements targets this question, amongst others the ATLAS experiment at CERN.

A search for dark matter candidates in invisibly decaying Higgs bosons is presented using the full Run II data set corresponding to a luminosity of 139 fb^{-1} collected with the ATLAS experiment at the LHC at a center-of-mass energy of $\sqrt{s} = 13\,\text{TeV}$. The search is motivated by Higgs portal models which describe a coupling of dark matter particles, mostly assumed in form of WIMPs, to the Higgs boson. The analysis targets Higgs bosons produced in vector boson fusion, allowing for effective background rejection and thus for a high sensitivity for a BSM signal, and aims for setting an upper limit on the invisible Higgs boson branching fraction which is 0.12 % from $H \to ZZ \to 4\nu$ processes according to the standard model.

The key objects in the final state for this dark matter search are particle flow jets, for which the absolute Monte Carlo-based energy and η calibration is presented, indicating that for the first time in ATLAS a jet calibration with good closure down to p_{T} values of 10–15 GeV is possible, especially in the central detector region.

Higgs boson production in vector boson fusion combined with an invisible decay mode characterised by a large amount of $E_{\text{T}}^{\text{miss}}$ in the final state is a very challenging topology. To cope with the data-taking conditions in Run II, significant improvements of the analysis with respect to previous analyses were implemented: An improvement of the signal acceptance and background rejection in the SR, new and improved background estimation strategies for V+jets and multijet processes, increased Monte Carlo statistics for V+jets processes with fast filtering algorithms and a refined event categorisation in the signal region considering a changing fraction of signal as function of m_{jj}, $E_{\text{T}}^{\text{miss}}$, n_{jet} as well as $\Delta\phi_{\text{jj}}$.

The dominant and important background processes in the signal region arise from V+jets and multijet processes. A special focus in this thesis is the estimation of the multijet background, which is a small but relevant background due to its increasing importance with the current data-taking conditions at the LHC characterised by a high pile-up activity. The development and improvement of the RnS technique is a cornerstone of the analysis, allowing in a combination with a second, fully independent and new method, the pile-up CR technique, for a sensible multijet background estimate. Essentially, RnS is a sampling technique similar to the well-established jet smearing method, providing high-statistic multijet predictions with full event kinematics in extreme phase spaces which are currently not sufficiently covered with conventional Monte Carlo simulations. The clue of the new version of RnS is the categorisation of the multijet background into two different contributions:

- the HS-only topology, caused by hard-scatter jet mis-measurements
- the HS+PU topology, originating from the combinatorial mixing of hard-scatter and pile-up jets, which is for example caused by a failed pile-up tagging.

The RnS technique works with inclusive data (data-driven RnS) or simulated samples (MC-based RnS) as input. For the full Run II analysis, the MC-based RnS prediction is used as the benchmark RnS multijet background estimate and the difference to the data-driven RnS prediction is utilised as a systematic uncertainty covering data-simulation differences. Overall, the RnS technique shows a good performance and the possibility to significantly increase the effective statistics of the multijet prediction compared to pure MC samples. The invention of an independent handling of hard-scatter and pile-up jets is crucial also for future LHC data taking periods with busy pile-up conditions and the basis for future usages of RnS.

The statistical procedure for extracting the signal strength μ from the collected data follows a frequentist statistics approach with the CL_s method using a profile maximum likelihood fit. No signal excess over the background-only model is found. The observed (expected) limit at 95 % CL is 0.145 (0.103), which is the best ever measured limit for invisibly decaying Higgs bosons so far. Leading uncertainties are data and Monte Carlo statistics, the multijet background modelling and jet measurements.

The observed limit is interpreted with Higgs portal models in terms of the WIMP-nucleon cross section allowing for a comparison with direct detection experiments, which are complementary to this collider search in terms of the sensitivity as a function of the WIMP mass. This shows that for Higgs portal models, where the dark matter candidates are expected with masses $< m_H/2$, the LHC with the ATLAS and CMS detectors is at present one of the most sensitive dark matter detection experiments. Further, upper limits on potential heavier or lighter mediators than the SM Higgs boson are set as a function of the mediator mass.

11.2 Outlook

In future dark matter searches in the vector boson fusion Higgs boson to invisible channel different refinements of the analysis are possible. The sensitivity of the analysis will be increased by a better detector and reconstruction performance. However, higher pile-up conditions, e.g. in Run III or especially at the HL-LHC, can have an opposite effects on the sensitivity. First, more data collected at the LHC will allow for setting stronger limits on various BSM scenarios. In this context, the usage of additional ATLAS triggers such as VBF topological triggers can provide additional statistics. Similar, larger Monte Carlo productions can reduce the statistical uncertainties caused by limited sample size in simulation. Various analysis selection and object reconstruction improvements can enhance the sensitivity of the analysis in the future. The key objects in this analysis are PFlow jets for which improved reconstruction techniques, calibrations and pile-up tagging methods, corresponding to reduced jet energy scale and resolution as well as $E_{\mathrm{T}}^{\mathrm{miss}}$ systematic uncertainties, can significantly improve the analysis. Also, a more efficient primary vertex reconstruction can improve the analysis. Currently, in events with one (two) forward jet (jets) with a vector boson fusion topology and large $E_{\mathrm{T}}^{\mathrm{miss}}$, the vertex is 40 % (50 %) of the time wrongly identified, which in turn amongst others biases the pile-up jet tagging. Furthermore, the discrimination of signal and background events can benefit from an improved discrimination of quark- and gluon-initiated jets. In the signal process, the two tagging jets are quark-initiated, while for the irreducible $Z \rightarrow \nu\nu$ background one or two tagging jets from the vector boson fusion process can be gluon-initiated. Since gluon-initiated jets tend to have larger particle multiplicity and emerge in wider jets, a discrimination with respect to quark-initiated jets is possible [264]. Although it has been shown that the analysis cannot benefit from the application of machine learning techniques, since the presented cut-based analysis seems to be well optimised for the given background modelling and analysis strategy, the situation may be different in the future and must be evaluated again. In terms of the interpretation of the result, the sensitivity with respect to other massive mediators can be improved with an optimised event selection and a revised analysis binning for heavier mediator masses. Furthermore, the analysis uses the RECAST framework [265]. It is designed to reuse background estimates, systematic uncertainties and

the data to test alternative signal models in the future, e.g. fifth force, dark energy [266–268] or dark photon models [269] within an automatic analysis software workflow, allowing for a efficient collaboration between theorists and experimental physicists as well as a long-term preservation of the analysis.

While the presented VBF+$E_{\mathrm{T}}^{\mathrm{miss}}$ analysis is the most sensitive individual channel for invisible Higgs boson decays, the overall sensitivity can be further improved with a statistical combination of the analysis with other direct Higgs boson to invisible searches using the full Run II data, which are the VBF+$E_{\mathrm{T}}^{\mathrm{miss}}$ +γ, mono-Z($\ell\ell$), $t\bar{t}$ + $E_{\mathrm{T}}^{\mathrm{miss}}$, mono-jet and mono-$V$(had) analyses, anticipating an observed and expected limit on $\mathcal{B}_{\mathrm{inv}}$ below 10 % [270].

The HL-LHC will provide a significant improved detector [271]. The upgrade to the HL-LHC already started in 2018. An increase in luminosity will be achieved by increasing the number of protons per bunch and reducing the beam size with new quadrupole magnets. The proposed run time of the HL-LHC is 10 years with an instantaneous luminosity of $\sim 8 \cdot 10^{34}\,\mathrm{cm}^{-2}\mathrm{s}^{-1}$, giving in sum 3 ab^{-1}. The major challenge is the highly increased pile-up activity for which many of the subdetectors must be replaced with modern, state-of-the art techniques. For example, the ID will be replaced by a full-silicon tracker (ITk) with an extended η-coverage. The accompanying improvement in the pile-up tagging requires a reoptimisation of the third jet veto as used in the full Run II analysis which is sensitive to wrongly-tagged hard-scatter jets with $p_{\mathrm{T}} > 25\,\mathrm{GeV}$. Especially the multijet background, and more specifically the HS+PU topology, is sensitive to a third jet veto. In this context also proposed high-granularity timing detector [272] can help to identify pile-up jets and thus to reject multijet background events. Prospects of the VBF+$E_{\mathrm{T}}^{\mathrm{miss}}$ search for the HL-LHC are promising but show that pile-up jets, especially in the forward detector region, cause a significant challenge in a VBF topology. For this, a new approach for the generation of pile-up events provides the possibility to enhance the statistics of the multijet prediction in extreme phase spaces and helps to better estimate the combinatorial background, which will become more important at future hadron colliders. The approach of this new technique is to not only generate the hard-scatter process in p_{T}-slices but also the subleading interaction, i.e. the leading pile-up interaction [273].

Beside the upgrades of the LHC machine, a future collider is under planning. Before deciding on a strategy, physics arguments and political boundary conditions need to be addressed. Important questions from the physics side, in particular in context of a proposed Higgs boson factory, are which particles should be collided, i.e. a hadron collider or an e^+e^--collider, and the technology of the accelerator, i.e. linear or circular. All these possibilities have pros and cons amongst others with regard to synchrotron radiation, center-of-mass energies, luminosities, costs, electron polarisations and particle identification efficiencies. Four famous candidates are the International Linear Collider (ILC) [274], the Compact Linear Collider (CLIC) [275], the Future Circular Collider (Fcc-ee) [276] and the Circular Electron Positron Collider (CEPC) [277]. The ILC is a proposed linear electron-positron collider providing collision energies up to 1 TeV, proposed to be build in Japan with a length of $30 - 50\,\mathrm{km}$. CLIC is also a proposed linear e^+e^- collider providing collision energies in the TeV-range with a proposed length of $11 - 50\,\mathrm{km}$. If the CLIC will be realised, it will be build at CERN. FCC-ee and CEPC are circular colliders, proposed to be built at CERN or in China, respectively, with a focus on Higgs boson production. Whichever collider is built as follow-up to the LHC, the future of experimental particle physics remains exciting and searches for the dark sector are just at a start.

Bibliography

[1] ATLAS Collaboration,
Search for invisible Higgs boson decays in vector boson fusion at $\sqrt{s} = 13$ *TeV with the ATLAS detector*,
Phys. Lett. B **793** (2018) 499.

[2] P. Rivadeneira Bracho, *Search for invisible Higgs boson decays with vector boson fusion signatures with the ATLAS detector using an integrated luminosity of 139* fb^{-1} *(to be published soon)*,
Universität Hamburg, 2022.

[3] ATLAS Collaboration, *Search for invisible Higgs boson decays with vector boson fusion signatures with the ATLAS detector using an integrated luminosity of 139* fb^{-1}, tech. rep., CERN, 2020.

[4] ATLAS Collaboration,
Search for invisibly decaying Higgs bosons with the VBF+MET signature (to be published soon),
(2021).

[5] A. Einstein, *Zur Elektrodynamik bewegter Körper*, Annalen der Physik **322** (1905) 891.

[6] S. L. Glashow, *Partial Symmetries of Weak Interactions*, Nucl. Phys. **22** (1961) 579.

[7] S. Weinberg, *A Model of Leptons*, Phys. Rev. Lett. **19** (21 1967) 1264.

[8] A. Salam, *Weak and Electromagnetic Interactions*, Nobel Symposium **8** (1968).

[9] S. L. Glashow, J. Iliopoulos and L. Maiani, *Weak Interactions with Lepton-Hadron Symmetry*,
Phys. Rev. D **2** (1970) 1285.

[10] H. Georgi and S. L. Glashow, *Unified Weak and Electromagnetic Interactions without Neutral Currents*,
Phys. Rev. Lett. **28** (1972) 1494.

[11] W. R. Hamilton, *On a General Method in Dynamics; by which the Study of the Motions of all free Systems of attracting or repelling Points is reduced to the Search and Differentiation of one central Relation, or characteristic Function*,
Philosophical Transactions of the Royal Society, part II for 1834 (1834) 247.

[12] W. R. Hamilton, *Second Essay on a General Method in Dynamics*,
Philosophical Transactions of the Royal Society, part I for 1835 (1835) 95.

[13] R. P. Feynman, *Principles of least action in quantum mechanics*, 1942.

[14] V. Fock, *Konfigurationsraum und zweite Quantelung*, Zeitschrift fur Physik **75** (1932) 622.

[15] W. Pauli, *Über den Zusammenhang des Abschlusses der Elektronengruppen im Atom mit der Komplexstruktur der Spektren*, Zeitschrift fur Physik **31** (1925) 765.

[16] A. Purcell, *Go on a particle quest at the first CERN webfest. Le premier webfest du CERN se lance à la conquête des particules*, (2012) 10.

[17] J. C. Maxwell, *A dynamical theory of the electromagnetic field*, Phil. Trans. R. Soc. **155** (1865) 459.

[18] P. A. M. Dirac, *The Quantum Theory of the Electron*,
Proceedings of the Royal Society of London **117** (1928) 610.

[19] M. Gell-Mann, *A Schematic Model of Baryons and Mesons*, Phys. Lett. **8** (1964) 214.

[20] G. Zweig, *An SU_3 model for strong interaction symmetry and its breaking; Version 2*, (1964) 80 p.

[21] H. D. Politzer, *Reliable Perturbative Results for Strong Interactions*, Phys. Rev. Lett. **30** (1973) 1346.

[22] H. D. Politzer, *Asymptotic Freedom: An Approach to Strong Interactions*, Phys. Rept. **14** (1974) 129.

[23] D. J. Gross and F. Wilczek, *Asymptotically Free Gauge Theories*, Phys. Rev. D **8** (1973) 3633.

[24] TASSO, *Evidence for Planar Events in e^+e^- Annihilation at High-Energies*, Phys. Lett. B **86** (1979) 243.

[25] D. P. Barber et al., *Discovery of Three Jet Events and a Test of Quantum Chromodynamics at PETRA Energies*, Phys. Rev. Lett. **43** (1979) 830.

[26] C. S. Wu et al., *Experimental Test of Parity Conservation in Beta Decay*, Phys. Rev. **105** (4 1957) 1413.

[27] J. H. Christenson et al., *Evidence for the 2π Decay of the K_2^0 Meson*, Phys. Rev. Lett. **13** (4 1964) 138.

[28] M. Kobayashi and T. Maskawa, *CP-Violation in the Renormalizable Theory of Weak Interaction*, Progress of Theoretical Physics **49** (1973) 652.

[29] N. Cabibbo, *Unitary Symmetry and Leptonic Decays*, Phys. Rev. Lett. **10** (12 1963) 531.

[30] UA1, *Physics results of the UA1 collaboration at the CERN proton-antiproton collider*, eConf **C840723** (1984) 634.

[31] Particle Data Group, *Review of Particle Physics*, PTEP **2020** (2020) 083C01.

[32] S. van der Meer, *Stochastic cooling theory and devices*, (1978).

[33] G. 't Hooft, *Renormalization of massless Yang-Mills fields*, Nuclear Physics B **33** (1971) 173.

[34] G. 't Hooft, *Renormalizable Lagrangians for massive Yang-Mills fields*, Nuclear Physics B **35** (1971) 167.

[35] A. Castro, *Top Quark Mass Measurements in ATLAS and CMS*, 2019.

[36] F. Englert and R. Brout, *Broken Symmetry and the Mass of Gauge Vector Mesons*, Phys. Rev. Lett. **13** (1964) 321.

[37] P. W. Higgs, *Broken Symmetries, Massless Particles and Gauge Fields*, Phys. Lett. **12** (1964) 132.

[38] G. S. Guralnik, C. R. Hagen and T. W. B. Kibble, *Global Conservation Laws and Massless Particles*, Phys. Rev. Lett. **13** (1964) 585.

[39] Y. Nambu, *Quasi-Particles and Gauge Invariance in the Theory of Superconductivity*, Phys. Rev. **117** (3 1960) 648.

[40] J. Goldstone, *Field Theories with Superconductor Solutions*, Nuovo Cim. **19** (1961) 154.

[41] ATLAS Collaboration, *Observation of a new particle in the search for the Standard Model Higgs boson with the ATLAS detector at the LHC*, Phys. Lett. **B716** (2012) 1.

[42] CMS Collaboration, *Observation of a new boson at a mass of 125 GeV with the CMS experiment at the LHC*, Phys. Lett. **B716** (2012) 30.

[43] Particle Data Group, *Review of Particle Physics*, Chin. Phys. C **40** (2016) 100001.

[44] LEP Collaboration, *Search for the standard model Higgs boson at LEP*, Phys. Lett. B **565** (2003) 61.

[45] CDF Collaboration, *Combined Search for the Standard Model Higgs Boson Decaying to abb^-Pair Using the Full CDF Data Set*, Physical Review Letters **109** (2012).

[46] D0 Collaboration, *Combined Search for the Standard Model Higgs Boson Decaying to $b\bar{b}$ Using the D0 Run II Data Set*, Physical Review Letters **109** (2012).

[47] C. N. Yang, *Selection Rules for the Dematerialization of a Particle into Two Photons*, Phys. Rev. **77** (2 1950) 242.

[48] ATLAS Collaboration, *Test of CP invariance in vector-boson fusion production of the Higgs boson in the $H \to \tau\tau$ channel in proton−proton collisions at $\sqrt{s}$ = 13 TeV with the ATLAS detector*, Phys. Lett. B **805** (2020) 135426.

[49] B. Odom et al., *New Measurement of the Electron Magnetic Moment Using a One-Electron Quantum Cyclotron*, Physical Review Letters **97** (2006).

[50] A. D. Sakharov, *Violation of CP Invariance, C Asymmetry, and Baryon Asymmetry of the Universe*, Pisma Zh. Eksp. Teor. Fiz. **5** (1967) 32.

[51] T2K Collaboration, *Constraint on the matter-antimatter symmetry-violating phase in neutrino oscillations*, Nature **580** (2020) 339.

[52] R. D. Peccei and H. Quinn, *CP Conservation in the Presence of Pseudoparticles*, Physical Review Letters - PHYS REV LETT **38** (1977) 1440.

[53] Fermilab Collaboration, *Measurement of the Positive Muon Anomalous Magnetic Moment to 0.46 ppm*, Physical Review Letters **126** (2021).

[54] G. W. Bennett et al., *Final report of the E821 muon anomalous magnetic moment measurement at BNL*, Physical Review D **73** (2006).

[55] Super-Kamiokande Collaboration, *Evidence for Oscillation of Atmospheric Neutrinos*, Phys. Rev. Lett. **81** (8 1998) 1562.

[56] Z. Maki, M. Nakagawa and S. Sakata, *Remarks on the Unified Model of Elementary Particles*, Progress of Theoretical Physics **28** (1962) 870.

[57] T. Kaluza, *Zum Unitätsproblem der Physik*, Sitzungsberichte der Königlich Preußischen Akademie der Wissenschaften (Berlin (1921) 966.

[58] O. Klein, *Quantentheorie und fünfdimensionale Relativitätstheorie*, Zeitschrift fur Physik **37** (1926) 895.

[59] ATLAS Collaboration, *Search for TeV-scale gravity signatures in high-mass final states with leptons and jets with the ATLAS detector at s=13 TeV*, Physics Letters B **760** (2016) 520.

[60] P. A. R. Ade et al., *Planck2015 results*, Astronomy & Astrophysics **594** (2016) A13.

[61] F. Zwicky, *Die Rotverschiebung von extragalaktischen Nebeln*, Helvetica Physica Acta **6** (1933) 110.

[62] F. Zwicky, *On the Masses of Nebulae and of Clusters of Nebulae*, The Astrophysical Journal **86** (1937) 217.

[63] S. Smith, *The Mass of the Virgo Cluster*, The Astrophysical Journal **83** (1936).

[64] E. Holmberg, *A Study of Double and Multiple Galaxies Together with Inquiries into some General Metagalactic Problems*, Annals of the Observatory of Lund **6** (1937).

[65] V. C. Rubin and J. Ford W. K., *Rotation of the Andromeda Nebula from a Spectroscopic Survey of Emission Regions*, Astrophysical Journal **159** (1970) 379.

[66] K. G. Begeman, A. H. Broeils and R. H. Sanders, *Extended rotation curves of spiral galaxies: dark haloes and modified dynamics*, Monthly Notices of the Royal Astronomical Society **249** (1991) 523.

[67] M. S. Roberts and R. N. Whitehurst, *The rotation curve and geometry of M31 at large galactocentric distances.*, The Astrophysical Journal **201** (1975) 327.

[68] D. Clowe et al., *A Direct Empirical Proof of the Existence of Dark Matter*, The Astrophysical Journal **648** (2006) L109.

[69] K. G. Begeman, A. H. Broeils and R. H. Sanders, *Extended rotation curves of spiral galaxies: dark haloes and modified dynamics.*, Monthly Notices of the Royal Astronomical Society **249** (1991) 523.

[70] G. F. Smoot et al., *Structure in the COBE Differential Microwave Radiometer First-Year Maps*, The Astrophysical Journal **396** (1992).

[71] Planck Collaboration, *Planck 2015 results. XIII. Cosmological parameters*, Astron. Astrophys. **594** (2016) A13.

[72] E. Komatsu et al., *Five-Year Wilkinson Microwave Anisotropy Probe Observations: Cosmological Interpretation*, The Astrophysical Journal Supplement Series **180** (2009) 330.

[73] A. A. Penzias and R. W. Wilson, *A Measurement of Excess Antenna Temperature at 4080 Mc/s.*, The Astrophysical Journal **142** (1965) 419.

[74] D. J. Fixsen, *The Temperature of the Comsic Microwave Background*, The Astrophysical Journal **707** (2009) 916, ISSN: 1538-4357.

[75] J. Silk, *Cosmic Black-Body Radiation and Galaxy Formation*, The Astrophysical Journal **151** (1968) 459.

[76] R. K. Sachs and A. M. Wolfe, *Perturbations of a Cosmological Model and Angular Variations of the Microwave Background*, The Astrophysical Journal **147** (1967) 73.

[77] M. Kamionkowski, "WIMP and axion dark matter", *ICTP Summer School in High-Energy Physics and Cosmology*, 1997.

[78] M. Milgrom, *A modification of the Newtonian dynamics as a possible alternative to the hidden mass hypothesis.*, The Astrophysical Journey **270** (1983) 365.

[79] J. D. Bekenstein, *Relativistic gravitation theory for the MOND paradigm*, Phys. Rev. D **70** (2004) 083509.

[80] A. Deur, *An explanation for dark matter and dark energy consistent with the Standard Model of particle physics and General Relativity*, Eur. Phys. J. C **79** (2019) 883.

[81] J. Abdallah et al., *Simplified models for dark matter searches at the LHC*, Physics of the Dark Universe **9-10** (2015) 8.

[82] A. Djouadi et al., *Implications of LHC searches for Higgs–portal dark matter*, Phys. Lett. B **709** (2012) 65.

[83] A. Djouadi et al., *Direct detection of Higgs–portal dark matter at the LHC*, The European Physical Journal C **73** (2013).

[84] G. Arcadi, A. Djouadi and M. Raidal, *Dark Matter through the Higgs portal*, Phys. Rept. **842** (2020) 1.

[85] D. Choudhury and D. P. Roy, *Signatures of an invisibly decaying Higgs particle at LHC*, Phys. Lett. B **322** (1994) 368.

[86] QCDSF Collaboration, *A lattice study of the strangeness content of the nucleon*, Prog. Part. Nucl. Phys. **67** (2012) 467.

[87] S. Baek, P. Ko and W. Park, *Invisible Higgs decay width vs. dark matter direct detection cross section in Higgs portal dark matter models*, Physics Letters B (2014).

[88] G. Arcadi, A. Djouadi and M. Kado,
The Higgs-portal for vector dark matter and the effective field theory approach: A reappraisal,
Physics Letters B **805** (2020).

[89] M. Zaazoua et al., *Higgs portal vector dark matter interpretation: review of Effective Field Theory approach and ultraviolet complete models*, (2021).

[90] P. Agnes et al., *Low-Mass Dark Matter Search with the DarkSide-50 Experiment*,
Physical Review Letters **121** (2018).

[91] PandaX-4T Collraboration, *Dark matter direct search sensitivity of the PandaX-4T experiment*,
Science China Physics, Mechanics and Astronomy **62** (2018).

[92] C. Collaboration, *Probing low WIMP masses with the next generation of CRESST detector*, (2015).

[93] E. Aprile et al., *Dark Matter Search Results from a One Ton-Year Exposure of XENON1T*,
Physical Review Letters **121** (2018).

[94] Fermi LAT Collaboration,
Search for gamma-ray spectral lines with the Fermi Large Area Telescope and dark matter implications,
Physical Review D **88** (2013).

[95] AMS Collaboration, *Search for dark matter with the AMS experiment*,
AIP Conf. Proc. **878** (2006) 118, ed. by C. Munoz and G. Yepes.

[96] R. Bähre et al., *Any light particle search II —Technical Design Report*, JINST **8** (2013) T09001.

[97] P. W. Graham et al., *Experimental Searches for the Axion and Axion-Like Particles*,
Ann. Rev. Nucl. Part. Sci. **65** (2015) 485.

[98] D. Abercrombie et al., *Dark Matter Benchmark Models for Early LHC Run-2 Searches: Report of the ATLAS/CMS Dark Matter Forum*, Phys. Dark Univ. **27** (2020) 100371, ed. by A. Boveia et al.

[99] E. Mobs, *The CERN accelerator complex - 2019. Complexe des accélérateurs du CERN - 2019*, (2019).

[100] ALICE Collaboration, *The ALICE experiment at the CERN LHC*, JINST **3** (2008) S08002.

[101] ATLAS Collaboration, *The ATLAS Experiment at the CERN Large Hadron Collider*,
JINST **3** (2008) S08003.

[102] LHCb Collaboration, *The LHCb Detector at the LHC*, JINST **3** (2008) S08005.

[103] ATLAS Collaboration, *Observation of a new particle in the search for the Standard Model Higgs boson with the ATLAS detector at the LHC*, Physics Letters B **716** (2012) 1.

[104] CMS Collaboration,
Observation of a new boson at a mass of 125 GeV with the CMS experiment at the LHC,
Physics Letters B **716** (2012) 30.

[105] G. Apollinari et al.,
High-Luminosity Large Hadron Collider (HL-LHC): Technical Design Report V. 0.1,
CERN Yellow Reports: Monographs, CERN, 2017.

[106] ATLAS Collaboration, *Studies of the performance of the ATLAS detector using cosmic-ray muons*,
Eur. Phys. J. C **71** (2011) 1593.

[107] ATLAS Collaboration, *ATLAS Insertable B-Layer Technical Design Report*,
CERN-LHCC-2010-013. ATLAS-TDR-19, 2010.

[108] V. Ginzburg and I. Frank,
Radiation of a uniformly moving electron due to its transition from one medium into another,
J. Phys. (USSR) **9** (1945) 353.

[109] ATLAS Collaboration, *Alignment of the ATLAS Inner Detector and its Performance in 2012*,
ATLAS-CONF-2014-047, CERN, 2014.

[110] ATLAS Collaboration, *Alignment of the ATLAS Inner Detector in Run-2*, Eur. Phys. J. C **80** (2020) 1194.

[111] ATLAS Collaboration, *Performance of the reconstruction of large impact parameter tracks in the inner detector of ATLAS*, ATL-PHYS-PUB-2017-014, 2017.

[112] ATLAS Collaboration, *Jet energy scale and resolution measured in proton-proton collisions at $\sqrt{s}$ = 13 TeV with the ATLAS detector*, (2020).

[113] ATLAS Collaboration, *ATLAS detector and physics performance: Technical Design Report, 1*, Technical Design Report ATLAS, CERN, 1999.

[114] *ATLAS liquid-argon calorimeter: Technical Design Report*, Technical Design Report ATLAS, CERN, 1996.

[115] ATLAS Collaboration, *Energy calibration of the ATLAS Liquid Argon Forward Calorimeter*, Journal of Instrumentation **3** (2008) P02002.

[116] ATLAS Collaboration, *ATLAS muon spectrometer: Technical Design Report*, Technical Design Report, CERN, 1997.

[117] J. Pequenao, "Computer generated image of the ATLAS Muons subsystem", 2008.

[118] ATLAS Collaboration, *ATLAS high-level trigger, data-acquisition and controls: Technical Design Report*, Technical Design Report ATLAS, CERN, 2003.

[119] ATLAS Collaboration, *ATLAS computing: Technical design report*, (2005), ed. by G. Duckeck et al.

[120] ATLAS Collaboration, *Performance of the ATLAS Trigger System in 2015*, Eur. Phys. J. C **77** (2017) 317.

[121] S. Mandelstam, *Determination of the Pion-Nucleon Scattering Amplitude from Dispersion Relations and Unitarity. General Theory*, Phys. Rev. **112** (4 1958) 1344.

[122] ATLAS Collaboration, *The new LUCID-2 detector for luminosity measurement and monitoring in ATLAS*, JINST **13** (2018) P07017.

[123] S. van der Meer, *Calibration of the effective beam height in the ISR*, CERN-ISR-PO-68-31. ISR-PO-68-31, CERN, 1968.

[124] ATLAS Collaboration, *Luminosity determination in pp collisions at $\sqrt{s}$ = 13 TeV using the ATLAS detector at the LHC*, ATLAS-CONF-2019-021, CERN, 2019.

[125] V. Gribov and L. Lipatov, *Deep inelastic ep scattering in perturbation theory*, Sov. Phys. JETP **15** (1972) 438.

[126] G. Altarelli and G. Parisi, *Asymptotic freedom in parton language*, Nuclear Physics B. **126** (1977) 298.

[127] Y. L. Dokshitzer, *Calculation of the Structure Functions for Deep Inelastic Scattering and e^+e^- Annihilation by Perturbation Theory in Quantum Chromodynamics*, Sov. Phys. JETP **46** (1977) 641.

[128] ATLAS Collaboration, *Identification and rejection of pile-up jets at high pseudorapidity with the ATLAS detector*, The European Physical Journal C **77** (2017).

[129] G. Soyez, *Pileup mitigation at the LHC: A theorist's view*, Phys. Rept. **803** (2019) 1.

[130] ATLAS Collaboration, *ATLAS data quality operations and performance for 2015–2018 data-taking*, JINST **15** (2020) P04003.

[131] ATLAS Collaboration, *Performance of the ATLAS trigger system in 2015*, The European Physical Journal C **77** (2017).

[132] T. Cornelissen et al., *The new ATLAS track reconstruction (NEWT)*, Journal of Physics: Conference Series **119** (2008) 032014.

[133] ATLAS Collaboration, *Reconstruction of primary vertices at the ATLAS experiment in Run 1 proton–proton collisions at the LHC*, Eur. Phys. J. C **77** (2017) 332.

[134] ATLAS Collaboration, *The secondary vertex finding algorithm with the ATLAS detector*, tech. rep., CERN, 2017.

[135] ATLAS Collaborations, *Topological cell clustering in the ATLAS calorimeters and its performance in LHC Run 1*, Eur. Phys. J. C **77** (2017) 490.

[136] J. J. Thomson, *XL. Cathode Rays*, The London, Edinburgh, and Dublin Philosophical Magazine and Journal of Science **44** (1897) 293.

[137] ATLAS Collaboration, *Electron and photon reconstruction and performance in ATLAS using a dynamical, topological cell clustering-based approach*, (2017).

[138] ATLAS Collaboration, *Electron reconstruction and identification in the ATLAS experiment using the 2015 and 2016 LHC proton-proton collision data at $\sqrt{s} = 13$ TeV*, Eur. Phys. J. C **79** (2019) 639.

[139] W. Lampl et al., *Calorimeter Clustering Algorithms: Description and Performance*, ATL-LARG-PUB-2008-002. ATL-COM-LARG-2008-003, CERN, 2008.

[140] ATLAS Collaboration, *Photon identification in 2015 ATLAS data*, ATL-PHYS-PUB-2016-014, CERN, 2016.

[141] G. Aad et al., *Electron and photon performance measurements with the ATLAS detector using the 2015–2017 LHC proton-proton collision data*, Journal of Instrumentation **14** (2019) P12006.

[142] ATLAS Collaboration, *Muon reconstruction and identification efficiency in ATLAS using the full Run 2 pp collision data set at $\sqrt{s} = 13$ TeV*, 2020.

[143] ATLAS Collaboration, *Muon identification and performance in the ATLAS experiment*, CERN, 2018.

[144] ATLAS Collaboration, *Muon reconstruction performance of the ATLAS detector in proton–proton collision data at $\sqrt{s} =$13 TeV*, Eur. Phys. J. C **76** (2016) 292.

[145] ATLAS Collaboration, *Muon reconstruction and identification efficiency in ATLAS using the full Run 2 pp collision data set at $\sqrt{s} = 13$ TeV*, CERN, 2020.

[146] CDF Collaboration, *Observation of Top Quark Production in pp Collisions with the Collider Detector at Fermilab*, Physical Review Letters **74** (1995) 2626.

[147] D0 Collaboration, *Observation of the Top Quark*, Physical Review Letters **74** (1995) 2632.

[148] B. Andersson et al., *Parton fragmentation and string dynamics*, Phys. Rep. **97** (1983) 31.

[149] B. Webber, *A QCD model for jet fragmentation including soft gluon interference*, Nuclear Physics B **238** (1984) 492.

[150] G. P. Salam, *Towards Jetography*, Eur. Phys. J. C **67** (2010) 637.

[151] J. E. Huth et al., "Toward a standardization of jet definitions", *1990 DPF Summer Study on High-energy Physics: Research Directions for the Decade (Snowmass 90)*, 1990 134.

[152] T. Lee and M. Nauenberg, *Degenerate Systems and Mass Singularities*, Physical Review D **133** (1964).

[153] T. Kinoshita, *Mass Singularities of Feynman Amplitudes*, Journal of Mathematical Physics **3** (1962) 650.

[154] G. Sterman and S. Weinberg, *Jets from Quantum Chromodynamics*, Phys. Rev. Lett. **39** (23 1977) 1436.

[155] M. Wobisch and T. Wengler,
"Hadronization corrections to jet cross-sections in deep inelastic scattering",
Workshop on Monte Carlo Generators for HERA Physics (Plenary Starting Meeting), 1998 270.

[156] M. Cacciari, G. P. Salam and G. Soyez, *The anti-k_t jet clustering algorithm*, JHEP **04** (2008) 063.

[157] L. Asquith et al., *Performance of Jet Algorithms in the ATLAS Detector*, ATL-PHYS-INT-2010-129, CERN, 2010.

[158] ATLAS Collaboration, *Constituent-level pile-up mitigation techniques in ATLAS*,
ATLAS-CONF-2017-065, CERN, 2017.

[159] M. Cacciari et al., *The catchment area of jets*, Journal of High Energy Physics **2008** (2008) 005.

[160] ATLAS Collaboration, *Optimisation of the ATLAS b-tagging performance for the 2016 LHC Run*,
ATL-PHYS-PUB-2016-012, 2016.

[161] ATLAS Collaboration, *ATLAS b-jet identification performance and efficiency measurement with $t\bar{t}$ events in pp collisions at $\sqrt{s}$ = 13 TeV*, The European Physical Journal C **79** (2019).

[162] ATLAS Collaboration, *Tagging and suppression of pileup jets with the ATLAS detector*,
ATLAS-CONF-2014-018, CERN, 2014.

[163] ATLAS Collaboration, *Forward jet vertex tagging using the particle flow algorithm*,
ATL-PHYS-PUB-2019-026, CERN, 2019.

[164] ATLAS Collaboration, *Performance of missing transverse momentum reconstruction with the ATLAS detector using proton-proton collisions at $\sqrt{s}$ = 13 TeV*, Eur. Phys. J. C **78** (2018) 903. 66 p.

[165] ATLAS Collaboration, *Determination of jet calibration and energy resolution in proton-proton collisions at $\sqrt{s}$ = 8 TeV using the ATLAS detector*, 2019.

[166] ATLAS Collaboration, *Pile-up subtraction and suppression for jets in ATLAS*, (2013).

[167] ATLAS Collaboration, *Performance of pile-up mitigation techniques for jets in pp collisions at $\sqrt{s}$ = 8 TeV using the ATLAS detector*, Eur. Phys. J. C **76** (2016) 581.

[168] ATLAS Collaboration,
Jet energy measurement with the ATLAS detector in proton-proton collisions at $\sqrt{s}$ = 7 TeV,
Eur. Phys. J. C **73** (2013).

[169] ATLAS Collaboration,
Generalized Numerical Inversion: A Neural Network Approach to Jet Calibration,
ATL-PHYS-PUB-2018-013, CERN, 2018.

[170] A. Cukierman and B. Nachman, *Mathematical Properties of Numerical Inversion for Jet Calibrations*,
Nucl. Instrum. Meth. A **858** (2017) 1.

[171] ATLAS Collaboration, *TeV-scale jet energy calibration using multijet events including close-by jet effects at the ATLAS experiment*, ATLAS-CONF-2013-003, CERN, 2013.

[172] T. Sjöstrand et al., *An introduction to PYTHIA 8.2*, Comput. Phys. Commun. **191** (2015) 159.

[173] ATLAS Collaboration, *Multijet simulation for 13 TeV ATLAS Analyses*, ATL-PHYS-PUB-2019-017,
CERN, 2019.

[174] C. Runge, *Über empirische Funktionen und die Interpolation zwischen äquidistanten Ordinaten*,
Zeitschrift für Mathematik und Physik **46** (1901) 224.

[175] D. E. Groom, *Energy flow in a hadronic cascade: Application to hadron calorimetry*,
Nucl. Instrum. Meth. A **572** (1990) 633.

[176] T. A. Gabriel et al., *Energy dependence of hadronic activity*, Nucl. Instrum. Meth. A **338** (1993) 336.

[177] C. de Boor, *Subroutine package for calculating with B-splines*, Techn. Rep. **LA-4728-MS** (1971) 109.

[178] ATLAS Collaboration, *Constraints on new phenomena via Higgs boson couplings and invisible decays with the ATLAS detector*, Journal of High Energy Physics **2015** (2015).

[179] ATLAS and CMS Collaboration,
Measurements of the Higgs boson production and decay rates and constraints on its couplings from a combined ATLAS and CMS analysis of the LHC pp collision data at $\sqrt{s}$ = 7 *and 8 TeV*,
Journal of High Energy Physics **2016** (2016).

[180] M. Ciccolini, A. Denner and S. Dittmaier,
Electroweak and QCD corrections to Higgs production via vector-boson fusion at the CERN LHC,
Physical Review D **77** (2008).

[181] "Searches for invisible Higgs bosons: Preliminary combined results using LEP data collected at energies up to 209-GeV", *2001 Europhysics Conference on High Energy Physics*, 2001.

[182] ATLAS Collaboration, *Search for invisible decays of a Higgs boson using vector-boson fusion in pp collisions at* $\sqrt{s}$ = 8 *TeV with the ATLAS detector*, JHEP **01** (2016) 172.

[183] ATLAS Collaboration,
Combination of searches for invisible Higgs boson decays with the ATLAS experiment,
Phys. Rev. Lett. **122** (2019) 231801.

[184] ATLAS Collaboration, *Search for dark matter in association with an energetic photon in pp collisions at* $\sqrt{s}$ = *13 TeV with the ATLAS detector*, (2020).

[185] ATLAS Collaboration, *Search for dark matter produced in association with a single top quark in* $\sqrt{s}$ = 13 *TeV pp collisions with the ATLAS detector*, (2020).

[186] ATLAS Collaboration, *Search for dark matter and other new phenomena in events with an energetic jet and large missing transverse momentum using the ATLAS detector*,
Journal of High Energy Physics **2018** (2018).

[187] ATLAS Collaboration, *Search for dark matter in events with missing transverse momentum and a Higgs boson decaying into two photons in pp collisions at* $\sqrt{s}$ = 13 *TeV with the ATLAS detector*, (2021).

[188] ATLAS Collaboration, *Search for invisible decays of the Higgs boson produced in association with a hadronically decaying vector boson in pp collisions at* $\sqrt{s}$ = *8 TeV with the ATLAS detector*,
Eur. Phys. J. C **75** (2015) 337.

[189] ATLAS Collaboration,
Search for Invisible Decays of a Higgs Boson Produced in Association with a Z Boson in ATLAS,
Phys. Rev. Lett. **112** (2014) 201802.

[190] CMS Collaboration, *Search for invisible decays of Higgs bosons in the vector boson fusion and associated ZH production modes*, Eur. Phys. J. C **74** (2014) 2980.

[191] ATLAS Collaboration, *Constraints on off-shell Higgs boson production and the Higgs boson total width in* $ZZ \to 4l$ *and* $ZZ \to 2l2\nu$ *final states with the ATLAS detector*,
Physics Letters B **786** (2018) 223.

[192] CMS Collaboration, *Search for new physics in events with a leptonically decaying Z boson and a large transverse momentum imbalance in proton–proton collisions at* $\sqrt{s}$ = 13 *TeV*,
The European Physical Journal C **78** (2018).

[193] CMS Collaboration,
First constraints on invisible Higgs boson decays using $\mathrm{t\bar{t}H}$ *production at* $\sqrt{s}$ = 13 TeV,
CMS-PAS-HIG-18-008, CERN, 2019.

[194] CMS Collaboration,
Combined measurements of Higgs boson couplings in proton–proton collisions at $\sqrt{s} = 13$ *TeV*,
The European Physical Journal C **79** (2019).

[195] ATLAS Collaboration, *Performance of the missing transverse momentum triggers for the ATLAS detector during Run 2 data taking*, ATL-COM-DAQ-2019-129, CERN, 2019.

[196] ATLAS Collaboration, *Performance of the missing transverse momentum triggers for the ATLAS detector during Run-2 data taking*, Journal of High Energy Physics **2020** (2020).

[197] ATLAS Collaboration, *Performance of the ATLAS muon triggers in Run 2*, JINST **15** (2020) P09015.

[198] ATLAS Collaboration, *Performance of electron and photon triggers in ATLAS during LHC Run 2*, The European Physical Journal C **80** (2020).

[199] M. R. Whalley, D. Bourilkov and R. C. Group,
"The Les Houches accord PDFs (LHAPDF) and LHAGLUE",
HERA and the LHC: A Workshop on the Implications of HERA and LHC Physics (Startup Meeting, CERN, 26-27 March 2004; Midterm Meeting, CERN, 11-13 October 2004), 2005 575.

[200] S. Höche, "Introduction to parton-shower event generators", *Theoretical Advanced Study Institute in Elementary Particle Physics: Journeys Through the Precision Frontier: Amplitudes for Colliders*, 2015 235.

[201] S. Agostinelli et al., *GEANT4 – a simulation toolkit*, Nucl. Instrum. Meth. A **506** (2003) 250.

[202] K. Hamilton, P. Nason and G. Zanderighi,
Finite quark-mass effects in the NNLOPS POWHEG+MiNLO Higgs generator, JHEP **05** (2015) 140.

[203] J. Butterworth et al., *PDF4LHC recommendations for LHC Run II*, J. Phys. G **43** (2016) 023001.

[204] A. Denner et al., *HAWK 2.0: A Monte Carlo program for Higgs production in vector-boson fusion and Higgs strahlung at hadron colliders*, Comput. Phys. Commun. **195** (2015) 161.

[205] ATLAS Collaboration, *ATLAS simulation of boson plus jets processes in Run 2*, CERN, 2017.

[206] ATLAS Collaboration, *Multi-Boson Simulation for 13 TeV ATLAS Analyses*, CERN, 2017.

[207] E. Bothmann et al., *Event Generation with Sherpa 2.2*, (2019).

[208] NNPDF Collaboration, *Parton distributions for the LHC Run II*, JHEP **04** (2015) 040.

[209] T. Gleisberg and S. Höche, *Comix, a new matrix element generator*, JHEP **12** (2008) 039.

[210] F. Cascioli, P. Maierhofer and S. Pozzorini, *Scattering Amplitudes with Open Loops*,
Phys. Rev. Lett. **108** (2012) 111601.

[211] A. Denner, S. Dittmaier and L. Hofer,
Collier: A fortran-based complex one-loop library in extended regularizations,
Comput. Phys. Commun. **212** (2017) 220.

[212] M. Cacciari, "FastJet: A Code for fast k_t clustering, and more", *Deep inelastic scattering. Proceedings, 14th International Workshop, DIS 2006, Tsukuba, Japan, April 20-24, 2006*, 2006 487.

[213] J. Bellm et al., *Herwig 7.0/Herwig++ 3.0 release note*, Eur. Phys. J. C **76** (2016) 196.

[214] ATLAS Collaboration, *ATLAS Pythia 8 tunes to* 7 *TeV data*, ATL-PHYS-PUB-2014-021, 2014.

[215] R. Zuo, *Using Higgs Boson to search for dark matter with the ATLAS detector*,
University of Chicago, 2020.

[216] M. M. Perego, *Search for new physics produced via Vector Boson Fusion in final states with large missing transverse momentum with the ATLAS detector*, Universite Paris-Saclay, 2018.

[217] V. Kitali, *Search for invisible decays of the Higgs boson produced in vector-boson fusion in final states with jets and large missing transverse energy with the ATLAS detector*, Universität Hamburg, 2020.

[218] W. K. Balunas,
A Search for Nothing: Dark Matter and Invisible Decays of the Higgs Boson at the ATLAS Detector, University of Pennsylvania, 2018.

[219] A. Steinhebel, *Much Ado About Nothing: Searches for Higgs Boson Decays to Invisible Particles*, University of Oregon, 2021.

[220] *Characterisation and mitigation of beam-induced backgrounds observed in the ATLAS detector during the 2011 proton-proton run*, Journal of Instrumentation **8** (2013) P07004.

[221] ATLAS Collaboration,
Selection of jets produced in 13TeV proton-proton collisions with the ATLAS detector, tech. rep., CERN, 2015.

[222] ATLAS Collaboration, *Observation of electroweak production of two jets in association with an isolated photon and missing transverse momentum, and search for a Higgs boson decaying into invisible particles at 13 TeV with the ATLAS detector*, (2021).

[223] ATLAS Collaboration, *Search for new phenomena with top quark pairs in final states with one lepton, jets, and missing transverse momentum in pp collisions at $\sqrt{s}$= 13 TeV with the ATLAS detector*, (2020).

[224] ATLAS Collaboration, *ATLAS event showing signature of dark-matter searches using the Higgs boson*, (2015).

[225] ATLAS Collaboration,
Search for invisible Higgs boson decays in vector boson fusion at $\sqrt{s}$ = 13 TeV with the ATLAS detector, Phys. Lett. (2018).

[226] J. Neundorf, *A Novel Estimate of the Multijet background in a Search for Dark Matter Produced in Association with Top Quarks in the ATLAS experiment*, Masterarbeit: Universität Hamburg, 2019 62.

[227] X. Lou, *Search for Dark Matter Produced in Association with Heavy Standard Model Particles at $\sqrt{s}$ = 13 TeV with the ATLAS Detector at the LHC*, Universität Hamburg, 2020.

[228] S. A. Koay, *A Search for Dark Matter Production with Jets and Missing Momentum Signature in Proton-Proton Collisions at 7 TeV*, UC, Santa Barbara, 2011.

[229] CMS Collaboration,
Search for New Physics with Jets and Missing Transverse Momentum in pp collisions at $\sqrt{s}$ = 7 TeV, JHEP **08** (2011) 155.

[230] CMS Collaboration, *Search for supersymmetry in all-hadronic events with missing energy*, CMS-PAS-SUS-11-004, CERN, 2011.

[231] K. Goebel, *Probing supersymmetry based on precise jet measurements at the CMS experiment*, Universität Hamburg, 2014.

[232] S. L. Bein, *Targeting the Minimal Supersymmetric Standard Model with the CMS Experiment*, Florida State U., 2016.

[233] M. Schroeder, *Quality of Jet Measurements and Impact on a Search for New Physics at CMS*, Universität Hamburg, 2012.

[234] M. Niedziela,
Precise jet measurements and search for supersymmetric particles with the CMS experiment, Universität Hamburg, 2018.

[235] ATLAS Collaboration, *Expected performance of the ATLAS experiment: detector, trigger and physics*, CERN, 2009.

[236] ATLAS Collaboration, *Using Event Weights to account for differences in Instantaneous Luminosity and Trigger Prescale in Monte Carlo and Data*, (2015).

[237] J. E. Sundermann and T. Goepfert, *KinFitter - A Kinematic Fit with Constraints*, ATL-COM-SOFT-2009-014, CERN, 2009.

[238] R. J. Barlow and C. Beeston, *Fitting using finite Monte Carlo samples*, Comput. Phys. Commun. **77** (1993) 219.

[239] B. Efron, *Bootstrap Methods: Another Look at the Jackknife*, Ann. Statist. **7** (1979) 1.

[240] ATLAS Collaboration, *Evaluating statistical uncertainties and correlations using the bootstrap method*, tech. rep., CERN, 2021.

[241] A. Nappi, *A pitfall in the use of extended likelihood for fitting fractions of pure samples in a mixed sample*, Computer Physics Communications **180** (2009) 269.

[242] ATLAS Collaboration, *Measurement of the W-boson mass in pp collisions at $\sqrt{s}$ = 7 TeV with the ATLAS detector*, The European Physical Journal C **78** (2018).

[243] J. M. Lindert et al., *Precise predictions for V+jets dark matter backgrounds*, The European Physical Journal C **77** (2017).

[244] J. Lindert et al., *V+jets prescriptions for VBF+MET (to be published soon)*, (2021).

[245] C. Bierlich et al., *Robust Independent Validation of Experiment and Theory: Rivet version 3*, SciPost Physics **8** (2020).

[246] G. Cowan et al., *Asymptotic formulae for likelihood-based tests of new physics*, Eur. Phys. J. C **71** (2011) 1554, Erratum: Eur. Phys. J. C **73** (2013) 2501.

[247] J. Neyman and E. S. Pearson, *On the Problem of the Most Efficient Tests of Statistical Hypotheses*, Philosophical Transactions of the Royal Society of London Series A **231** (1933) 289.

[248] S. S. Wilks, *The Large-Sample Distribution of the Likelihood Ratio for Testing Composite Hypotheses*, The Annals of Mathematical Statistics **9** (1938) 60.

[249] A. L. Read, *Presentation of search results: The CL_s technique*, Journal of Physics G: Nuclear and Particle Physics **28** (2002) 2693.

[250] M. Baak et al., *HistFitter software framework for statistical data analysis*, Eur. Phys. J. C **75** (2015) 153.

[251] L. Moneta et al., *The RooStats Project*, 2011.

[252] S. Catani et al., *QCD Matrix Elements + Parton Showers*, JHEP **11** (2001) 063.

[253] J. Bellm et al., *Parton-shower uncertainties with Herwig 7: benchmarks at leading order*, The European Physical Journal C **76** (2016).

[254] LHC Higgs Cross Section Working Group, *Handbook of LHC Higgs Cross Sections: 4. Deciphering the Nature of the Higgs Sector*, CERN Yellow Reports: Monographs, 2016.

[255] I. W. Stewart and F. J. Tackmann, *Theory uncertainties for Higgs mass and other searches using jet bins*, Phys. Rev. D **85** (2012) 034011.

[256] PandaX-4T Collaboration, *Dark Matter Search Results from the PandaX-4T Commissioning Run*, (2021).

[257] CRESST Collaboration, *First results from the CRESST-III low-mass dark matter program*, Phys. Rev. D **100** (2019) 102002.

[258] G. Busoni et al., *Recommendations on presenting LHC searches for missing transverse energy signals using simplified s-channel models of dark matter*, Phys. Dark Univ. **27** (2020) 100365, ed. by A. Boveia et al.

[259] LUX, *Results from a search for dark matter in the complete LUX exposure*, Phys. Rev. Lett. **118** (2017) 021303.

[260] X. Cui et al., *Dark Matter Results from 54-Ton-Day Exposure of PandaX-II Experiment*, Physical Review Letters **119** (2017).

[261] C. Boehm et al., *How high is the neutrino floor?*, Journal of Cosmology and Astroparticle Physics **2019** (2019).

[262] J. Billard, L. Strigari and E. Figueroa-Feliciano, *Implication of neutrino backgrounds on the reach of next generation dark matter direct detection experiments*, Phys. Rev. D **89** (2014) 023524.

[263] F. Ruppin et al., *Complementarity of dark matter detectors in light of the neutrino background*, Phys. Rev. D **90** (2014) 083510.

[264] ATLAS Collaboration, *Quark versus Gluon Jet Tagging Using Charged Particle Multiplicity with the ATLAS Detector*, tech. rep., CERN, 2017.

[265] K. Cranmer and I. Yavin, *RECAST — extending the impact of existing analyses*, Journal of High Energy Physics **2011** (2011).

[266] G. W. Horndeski, *Second-order scalar-tensor field equations in a four-dimensional space*, Int. J. Theor. Phys. **10** (1974) 363.

[267] C. Burrage et al., *Fifth forces, Higgs portals and broken scale invariance*, Journal of Cosmology and Astroparticle Physics **2018** (2018) 036.

[268] P. Brax et al., *LHC signatures of scalar dark energy*, Physical Review D **94** (2016).

[269] S. Biswas et al., *Dark-photon searches via Higgs-boson production at the LHC*, Physical Review D **93** (2016).

[270] ATLAS Collaboration, *Combination of searches for invisible Higgs boson decays with the ATLAS experiment*, tech. rep., CERN, 2020.

[271] ATLAS Collaboration, *Expected performance of the ATLAS detector at the High-Luminosity LHC*, tech. rep., CERN, 2019.

[272] ATLAS Collaboration, *A High-Granularity Timing Detector (HGTD) in ATLAS: Performance at the HL-LHC*, tech. rep., CERN, 2018.

[273] C. Sander and A. Linss, *A new approach to simulate events with hard pileup activity: Multijet background estimation for VBF+MET search for invisible Higgs decays*, tech. rep., CERN, 2021.

[274] T. Behnke et al., *The International Linear Collider Technical Design Report*, tech. rep., 2013.

[275] L. Linssen et al., *Physics and Detectors at CLIC: CLIC Conceptual Design Report*, (2012).

[276] M. Benedikt, A. Blondel, O. Brunner et al., *FCC-ee: The Lepton Collider: Future Circular Collider Conceptual Design Report Volume 2. Future Circular Collider*, tech. rep., CERN, 2018.

[277] CEPC Study Group Collaboration, *CEPC Conceptual Design Report: Volume 2 - Physics & Detector*, tech. rep., 2018.

[278] ATLAS Collaboration, *Jet energy resolution and selection efficiency relative to track jets from in-situ techniques with the ATLAS Detector Using Proton-Proton Collisions at a Center of Mass Energy sqrts = 7 TeV*, ATLAS-CONF-2010-054, CERN, 2010.

[279] C. J. Clopper and E. S. Pearson, *The Use of Confidence or Fiducial Limits Illustrated in the Case of the Binominal*, Biometrika **26** (1934) 404.

APPENDIX A

Additional Information On Rebalance And Smear

The appendix includes additional studies and information related to the RnS technique and the multijet background in the VBF + $E_{\mathrm{T}}^{\mathrm{miss}}$ phase space.

A.1 Jet Kinematics in the VBF + $E_{\mathrm{T}}^{\mathrm{miss}}$ Phase Space

Several studies are performed to understand and validate the kinematics and (expected) correlations of jet and event variables using the RnS prediction, see Chapter 7, where the focus is on correlations and dependencies of m_{jj}, $E_{\mathrm{T}}^{\mathrm{miss}}$, $\Delta\phi_{\mathrm{jj}}$ and (sub-)leading jet p_{T}. For the interpretation it should be considered that $E_{\mathrm{T}}^{\mathrm{miss}}$ dependent cuts of fJVT and $H_{\mathrm{T}}^{\mathrm{miss}}$ are applied. The Figures A.1-A.4 are created with the full MC-based RnS prediction corresponding to 139 fb^{-1} and show two selections, a low $E_{\mathrm{T}}^{\mathrm{miss}}$ CR as defined in Table 7.5 and the inclusive dijet SR. Note that the z-axis uses an arbitrary colour scheme which is not matching the event yield.

The observations and explanations are:

- Leading and subleading jet p_{T} show an anti-correlation in the dijet SRs. The higher the leading jet p_{T}, the lower the subleading jet p_{T} can be in order to produce a sufficient amount of $E_{\mathrm{T}}^{\mathrm{miss}} > 200\,\mathrm{GeV}$.

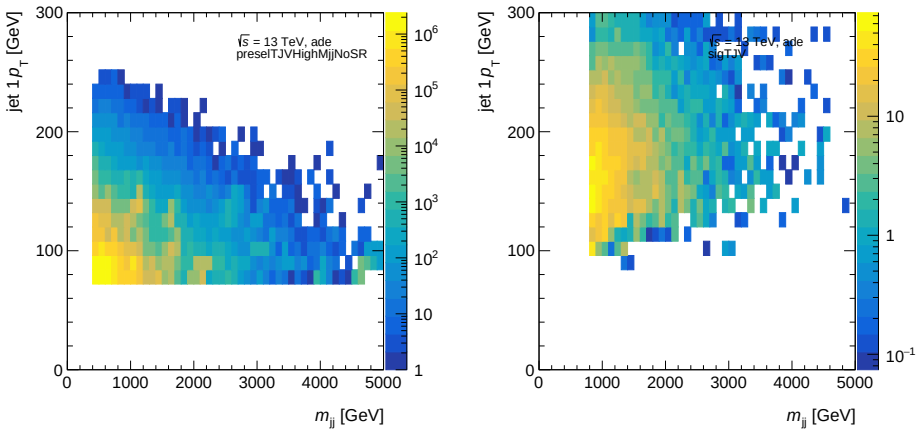

Figure A.1: Correlation of leading jet p_{T} and m_{jj} of multijet events predicted by RnS in the MJ CR (left) and dijet SR (right).

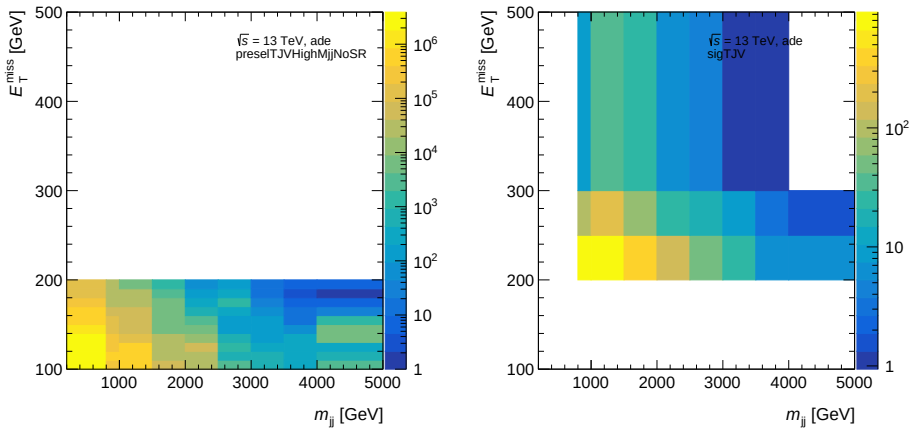

Figure A.2: Correlation of $E_{\mathrm{T}}^{\mathrm{miss}}$ and m_{jj} of multijet events predicted by RnS in the MJ CR (left) and dijet SR (right).

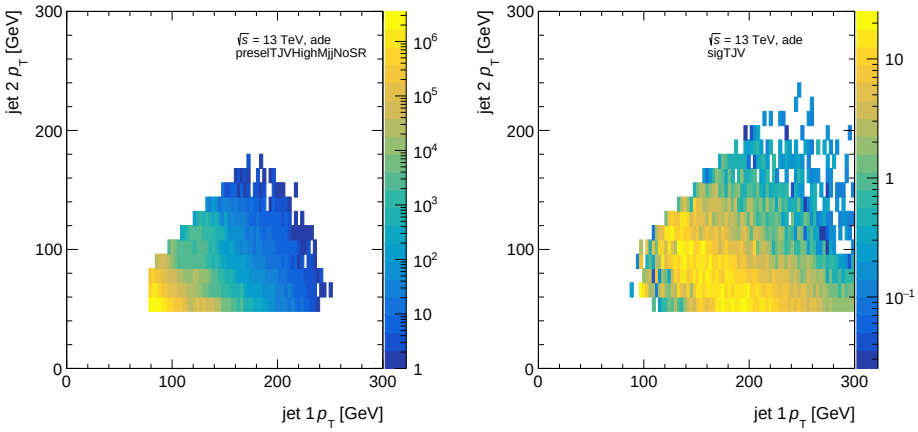

Figure A.3: Correlation of leading jet p_{T} and subleading jet p_{T} of multijet events predicted by RnS in the MJ CR (left) and dijet SR (right).

For that reason, the anti-correlation is not pronounced in the low $E_{\mathrm{T}}^{\mathrm{miss}}$ CRs with $E_{\mathrm{T}}^{\mathrm{miss}}$ conditions of $E_{\mathrm{T}}^{\mathrm{miss}} > 100\,\mathrm{GeV}$. The sharp upper border in Figure A.3 is not a kinematic effect rather it follows from the definition that the leading jet p_{T} is larger than the second leading jet p_{T}. The argumentation is not valid for topologies with more than two jets, where $E_{\mathrm{T}}^{\mathrm{miss}}$ can be enhanced or reduced by additional jet activity. Especially, if the additional jets stem from final state radiation and are roughly aligned with one of the two leadings jets.

- The amount of $E_{\mathrm{T}}^{\mathrm{miss}}$ which is produced by a dijet event strongly depends on $\Delta\phi_{\mathrm{jj}}$. The lower $\Delta\phi_{\mathrm{jj}}$, the higher the $E_{\mathrm{T}}^{\mathrm{miss}}$ produced for fixed jet leading and subleading jet p_{T}. As before, the arguments only hold for dijet topologies.
- As shown in Figure A.1, in the dijet SR, the leading jet p_{T} correlates with m_{jj} as expected. This is not the dominant effect in the low $E_{\mathrm{T}}^{\mathrm{miss}}$ CRs, where high m_{jj} values are produced primarily with softer leading jets. This is a clear sign that large m_{jj} values are driven by large $\Delta\eta_{\mathrm{jj}}$ values rather than high p_{T} jets.
- $E_{\mathrm{T}}^{\mathrm{miss}}$ values of $> 200\,\mathrm{GeV}$ are mainly produced with leading jets with $p_{\mathrm{T}} > 100\,\mathrm{GeV}$.
- $E_{\mathrm{T}}^{\mathrm{miss}}$ and m_{jj} are not independent as shown in Figure A.2. For increasing $E_{\mathrm{T}}^{\mathrm{miss}}$ between 150 and 200 GeV, the mean value of the m_{jj} distribution is shifted to higher values.

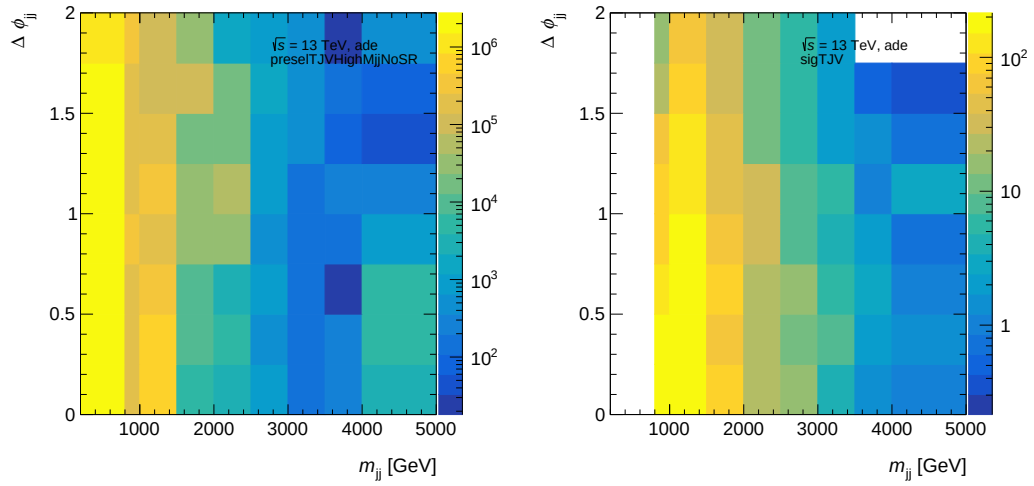

Figure A.4: Correlation of $\Delta\phi_{jj}$ and m_{jj} of multijet events predicted by RnS in the MJ CR (left) and dijet SR (right).

- m_{jj} and $\Delta\eta_{jj}$ are by definition highly correlated, especially in the VBF phase space
- As already observed in Section 8.2.3 and shown in Figure A.4, larger values of $\Delta\phi_{jj}$ tend to correspond to larger values of m_{jj}. This effect can be explained with a correlation of leading jet p_T and E_T^{miss}. Assume two jets with fixed p_T and assume similar shapes in $\Delta\eta_{jj}$ for high and low $\Delta\phi_{jj}$. For low $\Delta\phi_{jj}$ values, the E_T^{miss} produced by this event is larger compared to high values of $\Delta\phi_{jj}$. To produce a significant amount of E_T^{miss}, e.g. $E_T^{miss} > 200\,\text{GeV}$, the jets need to have larger p_T in the low $\Delta\phi_{jj}$ case than in the high $\Delta\phi_{jj}$ case. The larger values of jet momenta directly correlate to larger values of m_{jj}. Thus, a shift to larger m_{jj} values is expected when moving from low $\Delta\phi_{jj}$ to high $\Delta\phi_{jj}$ values. A lack in this argumentation is that is assumes equal $\Delta\eta_{jj}$ shapes for high and low $\Delta\phi_{jj}$.

A.2 Dijet Asymmetry and Tail Scaling Factors

The quality of the modelling of the jet response templates and their non-Gaussian tails are validated in a data-driven way [217, 233] using high-statistic dijet and multijet events. Alternatively, clean back-to-back γ+jet events similar to in situ jet calibration measurements could be used. In this case one would benefit from the high photon resolution, which is superior compared to the JER, one the other side the statistics would be lower. Therefore, the former approach is followed. The target of this study is to validate the jet response obtained from MC and to estimate systematic uncertainties associated with the Gaussian core and the non-Gaussian tails.

There is no jet response definition in data, since the definition of $\mathcal{R}$ includes truth-information, so the validation of the jet response tails in data is based on the dijet asymmetry $\mathcal{A}$, defined as

$$\mathcal{A} = \frac{p_{T,j_1} - p_{T,j_2}}{p_{T,j_1} + p_{T,j_2}}, \tag{A.1}$$

where the subscripts j_1 and j_2 refer to the leading- and subleading jet in an event. The concept of dijet asymmetry is well known from calibration strategies based on a tag-and-probe measurement. In general, the fraction of events in the tails of the jet response distribution $\mathcal{R}$ and asymmetry distributions $\mathcal{A}$ is expected to be similar. In case of clean dijet event with no further jets activity, i.e. that the two jets have similar resolutions with similar

p_{T} and $|\eta|$, the relative p_{T} resolution is given by

$$\frac{\sigma_{p_{\mathrm{T}}}}{p_{\mathrm{T}}} = \sqrt{2}\sigma_{\mathcal{A}}, \tag{A.2}$$

where $\sigma_{\mathcal{A}}$ is the width or 1-σ-interval of the dijet asymmetry distribution [278]. To reduce effects from the η-dependent JER, both jets are required to be in the same η-range. Since $\mathcal{A} > 0$ by definition, the dijet asymmetry cannot validate both the lower and upper tail independently. The following procedure is based on the assumption that the tails of $\mathcal{A}$ from data are related to tails of the JER from MC.

The selection of multijet events is a crucial part in the validation. There are two options: either selecting directly dijet events and sacrificing statistics (dijet approach) or using multijet events and potentially being biased by a non-negligible truth-level imbalance (multijet approach). The discussion follows first the multijet approach for the seek of argumentation. To account for a recoil of additional jet activity in multijet events, multijet events are selected followed by an extrapolation procedure to dijet events.

The parametrisation of any additional jet activity, which can break the momentum balance of the two leading jets and biases $\mathcal{A}$ to larger values, is done with an observable $\alpha_{||}$. $\alpha_{||}$ is defined as the projection of the third jet momentum onto the dijet axis of the two leading jets, shown in Figure A.5. The normalised dijet axis is in general defined as

$$\vec{p}_{\mathrm{dijet}} = \frac{\vec{p}_{\mathrm{T,j_1}} - \vec{p}_{\mathrm{T,j_2}}}{|\vec{p}_{\mathrm{T,j_1}} - \vec{p}_{\mathrm{T,j_2}}|}. \tag{A.3}$$

Based on this, $\alpha_{||}$ is computed as the scalar product of the third jet momentum $\vec{p}_{\mathrm{T,j3}}$ on the dijet axis $\vec{p}_{\mathrm{dijet}}$ normalised to the average momentum of the two leading jets via

$$\alpha_{||} = 2 \cdot \frac{\vec{p}_{\mathrm{dijet}} \cdot \vec{p}_{\mathrm{T,j3}}}{p_{\mathrm{T,j_1}} + p_{\mathrm{T,j_2}}}. \tag{A.4}$$

The dijet asymmetry $\mathcal{A}$ can be tested in bins of $\alpha_{||}$ where $\alpha_{||} \to 0$ mimics the dijet case.

However, the mean of the dijet asymmetry distribution $\mathcal{A}$ is shifted to larger values of α due to a particle level imbalance of multijet events, e.g. due to neutrinos in a third jet, which is a different effect than jet mis-measurements and not considered in Equation A.1. This is displayed in Figure A.6 and shows that the effect is in general important.

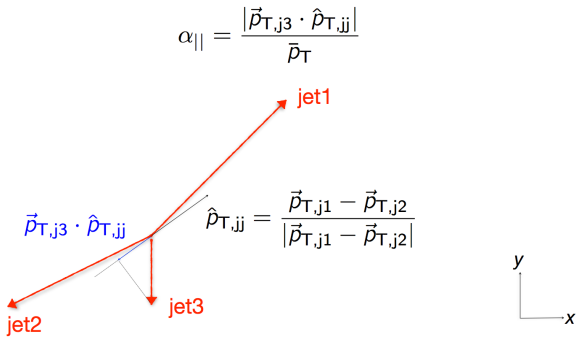

Figure A.5: Dijet axis and definition of $\alpha_{||}$.

In order to suppress these effects a different approach is used. The jet activity parametrisation is done with α, which is defined as

$$\alpha = \frac{|\vec{p}_{\mathrm{T,j3}}|}{\bar{p}_{\mathrm{T}}}, \tag{A.5}$$

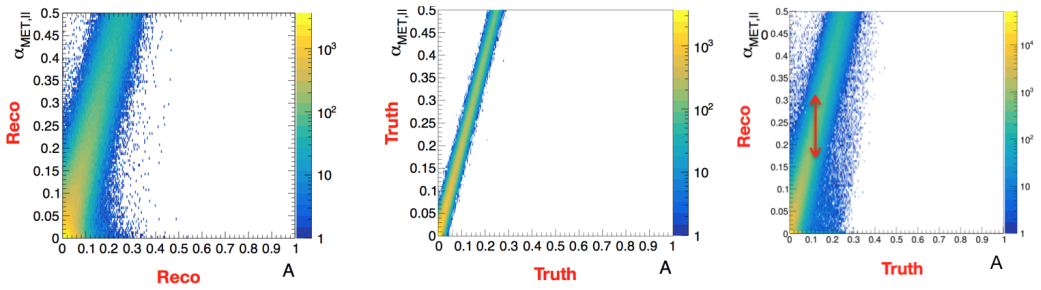

Figure A.6: Dijet asymmetry on reco (left) and truth-level (middle). The effect of the truth-level imbalance for an average energy of $E \in [1400, 1750]$ and $\eta \in [0, 1.3]$ is shown on the right in which $\alpha_{||}$ is calculated from reco jets in bins of the truth-level $\mathcal{A}$. Compared to the middle plot, the truth imbalance is migrating to other bins which results in a wider resolution.

with the average momentum of the two leading jets $\bar{p}_{\mathrm{T}}$. A very tight cut on α is set which effectively enforces $n_{\mathrm{jet}} = 2$ (note that in the case described above, α can be large, even if $\alpha_{||}$ is small). The asymmetries are determined in bins of average jet energy and in absolute values of η. The total fraction of events in the tail (tail fraction) is defined as

$$f_{\mathrm{tail,total}} = \frac{N_{\mathrm{tail}}}{N_{\mathrm{total}}}, \tag{A.6}$$

where N_{tail} is the total number of events in the tail of $\mathcal{R}$ and N_{total} the total number of events in $\mathcal{R}$. However, N_{tail} contains also events in tail which belong (according to a Gaussian fit) to the Gaussian core, denoted as $N_{\mathrm{core,tail}}$. This contribution is subtracted for the used definition of the tail fraction f_{tail}, i.e.

$$f_{\mathrm{tail}}(n) = \frac{N_{\mathrm{tail}} - N_{\mathrm{core,tail}}}{N_{\mathrm{total}}}, \tag{A.7}$$

where the tail, core and total number of events are more precisely defined as

$$N_{\mathrm{tail}} = N(\mathcal{A} > n\sigma) \tag{A.8}$$
$$N_{\mathrm{core,tail}} = N_{\mathrm{Gauss}}(\mathcal{A} > n\sigma) \tag{A.9}$$
$$N_{\mathrm{total}} = N(\mathcal{A} > 0) \tag{A.10}$$

Based on this, the asymmetry tail factor ρ_{tail} is defined as the dijet limit of the fraction of f_{tail} in data and simulation:

$$\rho_{\mathrm{tail}}(n) = \lim_{\alpha \to 0} \frac{f_{\mathrm{tail}^{\mathrm{data}}}(\alpha)}{f_{\mathrm{tail}^{\mathrm{MC}}}(\alpha)}. \tag{A.11}$$

Smaller or larger values of ρ_{tail} correspond to an under- or overestimation of the tails by simulation. The non-Gaussian tail correction factors ρ in bins of average energy and $|\eta|$ for $n = 3, 4, 5$ are shown in Table A.1. Apart from two ranges with large statistical uncertainties, no deviation larger than a factor of 2 is observed. Due to this relatively good agreement between data and simulation, the non-Gaussian tails are assumed to be well modeled by the MC simulation. Nevertheless, the non-Gaussian tails are varied by 50 % to get a conservative estimate of the related uncertainties.

A.3 Pile-up Tagging Probability via BDT

In ATLAS, the tagging of pile-up jets in the central detector region for $|\eta| < 2.4$ is based on JVT which effectively discriminates hard-scatter and pile-up jets. Within RnS, the tagging of pile-up jets must be done after passing

Table A.1: Tail scale factors ρ, defined as the ratio of the tail fraction in data and MC, in bins of average energy E and $|\eta|$ for JER σ-values of $n = 3, 4, 5$. In the forward region the event statistic is limited and thus only for a couple of energy ranges (with very low p_{T}) a measurement is possible.

E [GeV]	$\lvert\eta\rvert$	$\rho(3\sigma)$	$\rho(4\sigma)$	$\rho(5\sigma)$
100 . . . 190	0 – 1.3	0.93 ± 0.02	0.90 ± 0.05	0.90 ± 0.05
190 . . . 250	0 – 1.3	1.18 ± 0.04	1.18 ± 0.08	1.30 ± 0.17
250 . . . 400	0 – 1.3	1.06 ± 0.04	1.26 ± 0.10	1.33 ± 0.17
400 . . . 590	0 – 1.3	1.11 ± 0.04	1.14 ± 0.07	1.21 ± 0.09
590 . . . 820	0 – 1.3	1.22 ± 0.04	1.27 ± 0.07	1.32 ± 0.09
820 . . . 1090	0 – 1.3	1.25 ± 0.04	1.19 ± 0.07	1.40 ± 0.08
1090 . . . 1400	0 – 1.3	1.08 ± 0.05	1.32 ± 0.09	1.39 ± 0.12
1400 . . . 1750	0 – 1.3	1.27 ± 0.11	1.32 ± 0.16	1.35 ± 0.22
250 . . . 400	1.3 – 2.5	0.91 ± 0.02	0.83 ± 0.04	0.97 ± 0.16
400 . . . 590	1.3 – 2.5	1.06 ± 0.03	1.15 ± 0.06	1.27 ± 0.12
590 . . . 820	1.3 – 2.5	1.05 ± 0.06	1.12 ± 0.11	1.32 ± 0.26
820 . . . 1090	1.3 – 2.5	1.16 ± 0.10	1.33 ± 0.24	1.14 ± 0.38
1090 . . . 1400	1.3 – 2.5	1.49 ± 0.18	1.24 ± 0.22	1.21 ± 0.28
1400 . . . 1750	1.3 – 2.5	1.86 ± 0.22	1.94 ± 0.43	2.37 ± 0.97
250 . . . 400	> 2.5	1.31 ± 0.07	1.86 ± 0.21	4.13 ± 1.67
400 . . . 590	> 2.5	1.07 ± 0.03	1.28 ± 0.06	1.62 ± 0.15
590 . . . 820	> 2.5	0.82 ± 0.04	0.61 ± 0.05	0.66 ± 0.055

the jets through RnS since the jet kinematics can change. As described in Section 7.6, RnS uses a straight re-calculation of JVT based on the official multivariate Atlas algorithm implementation. As an alternative to the direct re-calculation of JVT, a machine learning based approach is developed to parametrise the pile-up removal probability. Historically, this approach was developed first but replaced for several reasons by the direct re-calculation as described in the Section 7.6. However, the BDT parametrisation approach might be relevant in the future, when EMTopo jets might no longer be available since the JVT re-calculation for PFlow jets is not directly possible due to the charged hadron subtraction inherent in the PFlow algorithm. Therefore, though not used in RnS for now, the BDT approach to determine the pile-up removal probability is described in the following. The pile-up removal probability must be clearly distinguished from the pile-up probability (i.e. the probability that a random jet is a pile-up jet) and the pile-up tagging efficiency (i.e. the efficiency that a pile-up jet is tagged as pile-up by JVT). The pile-up removal probability p_{PU} can be parametrised as a function of X via:

$$p_{\mathrm{PU}}(X) = \frac{n_{\text{PU-tagged}}(X)}{n_{\text{PU-tagged}}(X) + n_{\text{HS-tagged}}(X)}, \tag{A.12}$$

where $n_{\text{PU-tagged}}$ denotes the number of pile-up tagged jets and $n_{\text{HS-tagged}}$ the number of jets tagged as hard-scatter. For this study, a jet is treated as pile-up, if its JVT score is below 0.59, corresponding to the medium EMTopo JVT working point. A simple approach is to parametrise the pile-up removal probability p_{PU} as a function of jet p_{T} since pile-up jets tend to be low-energetic and hard-scatter to be high-energetic. However, this is only a rough estimate and it is known that there are more dependencies in the pile-up tagging, especially on track-related variables on which for example JVT is based. To combine these variables into a strong discriminator between hard-scatter jets and pile-up jets, a BDT is used. The training of the BDT is done using Pythia dijet MC samples with EMTopo small-R anti-k_t jets. The jets are splitted into a hard-scatter and a pile-up component via a geometrical truth-matching: reco jets are treated as hard-scatter if a truth jet is found around the jet in an area of $\Delta R < 0.15$, while a reco jet is treated as pile-up if no truth jet is found in the vicinity of $\Delta R < 0.3$. The BDT is implemented via the Tmva framework using adaptive boosting for training. The hard-scatter jets are treated

as "signal", while the pile-up jets are treated as "background". The training is performed with 10^5 events of the slices $JZ1W$, $JZ2W$ and $JZ3W$ from mc16a, whereby each event can contain several hard-scatter and pile-up jets. To remove any bias from a steeply falling jet p_{T} distribution, the p_{T} distribution is weighted to be flat so that the BDT is not driven mainly by p_{T}. Further, only jets with $p_{\mathrm{T}} < 60\,\mathrm{GeV}$ are used in the training since JVT is only applied for $p_{\mathrm{T}} < 60\,\mathrm{GeV}$. The used input jet and event variables are

- transverse momentum p_{T}
- pseudorapidity η
- azimuthal direction ϕ
- jet mass m_{jet}
- sum of track momenta associated to jet: $\sum_{i\in\mathrm{trk}} p_{\mathrm{T}}^{\mathrm{trk}}(PV_{\mathrm{all}})$
- sum of track momenta associated to jet which point to the PV_0: $\sum_{i\in\mathrm{trk}} p_{\mathrm{T}}^{\mathrm{trk}}(PV_0)$
- sum of track momenta associated to jet which point to the vertex of the jet: $\sum_{i\in\mathrm{trk}} p_{\mathrm{T}}^{\mathrm{trk}}(PV_{\mathrm{all}})$
- jet vertex fraction (JVF)
- vertex corresponding to the maximal value of JVF ($PV_i(\mathrm{max\ JVF})$)
- number of tracks associated to the jet n_{tracks}
- number of vertices in the event N_{Vtx}

Some of the input variables have just a minimal separation power between hard-scatter and pile-up jets. The distributions of the input variables of the BDT discriminator are shown in Figure A.7.

Figure A.8 shows the BDT distribution for signal and background and the parametrisation of the pile-up removal probability p_{PU} as a function of the BDT discriminator score. No sign of over-training is present since training and test data sets lead to statistical compatible distributions. The distribution of p_{PU} shows qualitatively the expected behaviour - p_{PU} tends to be large for pile-up jets (small BDT score) and small for hard-scatter jets (large BDT score). It is also worth noting that the pile-up removal probability shows a consistent performance for hard-scatter and pile-up jets which is a necessary condition for the usage of the method for assigning pile-up removal probabilities to unknown jets.

A similar method might be applicable also for pile-up tagging in the forward region for $|\eta| > 2.5$ (fJVT), for example using the $\Delta\phi$ information between pile-up tagged central jets and forward jets as input variables for the BDT discriminator. However, it is more challenging due to the complexity of the fJVT algorithm. Another drawback for the presented method and an even larger problem in case of fJVT is the difference in the pile-up tagging efficiencies in data and simulation. If the BDT parametrisation approach would be applied in an analysis, these uncertainties need to be carefully evaluated in addition to other systematic uncertainties inherent in this approach. In this regard, the re-calculation of JVT and fJVT within RnS based on the Atlas algorithm as described in Section 7.6 is chosen since it provides smaller uncertainties and consumes less computing power.

A.4 Trigger Efficiency Parametrisation

Since the two-dimensional $E_{\mathrm{T}}^{\mathrm{miss}}$ trigger efficiency emulation described in Section 7.8 considers only the dependence of the efficiency on the variables $H_{\mathrm{T}}^{\mathrm{miss}}$ and H_{T}, which are also correlated, and thus ignores other potential dependencies, a machine learning-based approach is studied to consider also the dependence of $\epsilon_{\mathrm{Trigger}}$ on various other variables, potentially providing a more reasonable estimation of $\epsilon_{\mathrm{Trigger}}$ and thus targeting smaller systematic uncertainties associated with it. A boosted decision tree (BDT) classification using adaptive boosting is trained and tested. The input for the BDT is single jet triggered data, where it is known if the $E_{\mathrm{T}}^{\mathrm{miss}}$-trigger would have fired or not. As a cross-check also MC Pythia dijet samples are used. In this section, signal is used as a synonym of $E_{\mathrm{T}}^{\mathrm{miss}}$ triggered data, while the term background is used to denote not $E_{\mathrm{T}}^{\mathrm{miss}}$ triggered data. The training uses the full available data statistics and so different number of events for signal and

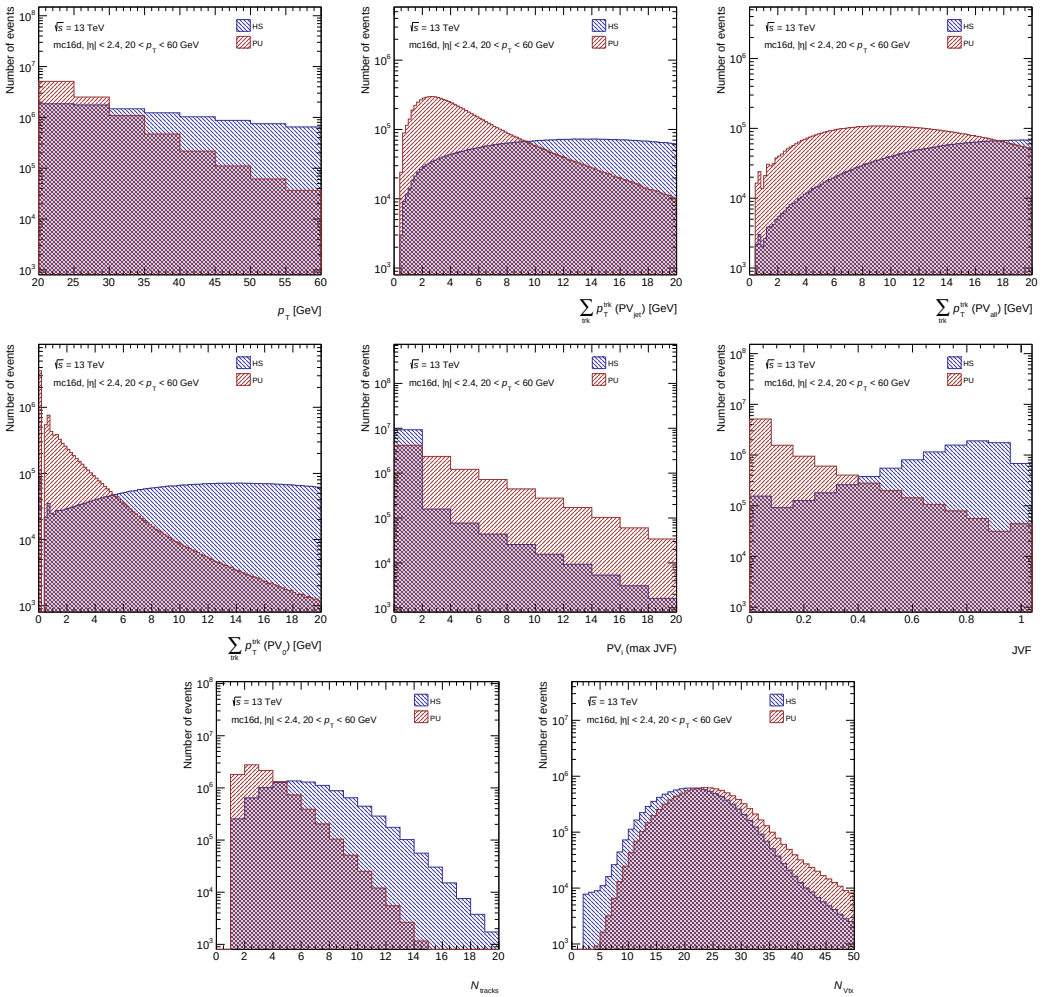

Figure A.7: Representative distributions of some input variables of the BDT discriminator used to determine the jet pile-up tagging probability.

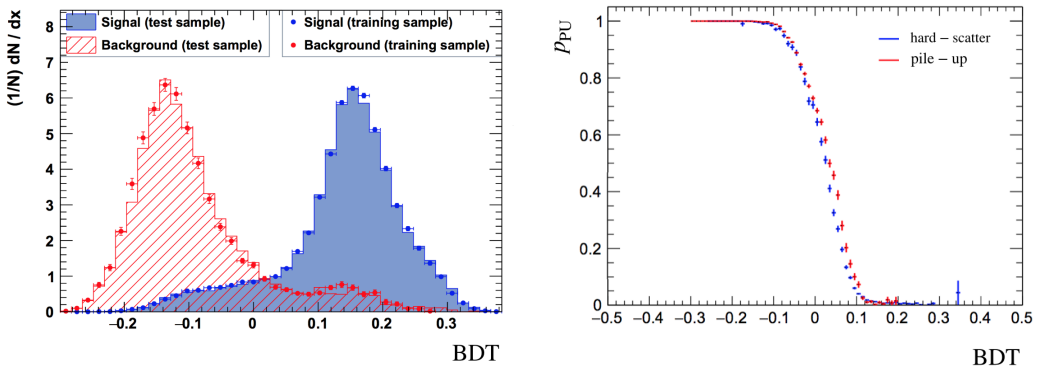

Figure A.8: Left: Distribution of the BDT discriminator for both the training and test data set. Hard-scatter jets are shown as signal in blue, pile-up jets as background in red. Right: Resulting distribution of the pile-up removal probability p_{PU} as a function of the BDT score. The distribution of p_{PU} has a similar shape for both hard-scatter and pile-up jets.

background are used. The internal weighting scheme of the BDT re-normalises the event weights in order to train on the same effective sample size for both signal and background. The input variables for the BDT training are chosen to be separating between $E_{\mathrm{T}}^{\mathrm{miss}}$-triggered and not $E_{\mathrm{T}}^{\mathrm{miss}}$-triggered data, where both contributions are triggered with the single jet monitoring trigger. These variables are a result of an optimisation process. Many different variables were also considered as potential BDT input variables, which turned out to be either highly correlated and/or not improving the BDT classification performance. The following set of variables is used to train the BDT:

- H_{T}
- $H_{\mathrm{T}}^{\mathrm{miss}}$
- m_{jj}
- $\Delta\phi_{\mathrm{jj}}$
- $H_{\mathrm{T}}^{\mathrm{miss}}/E_{\mathrm{T}}^{\mathrm{miss}}$
- $H_{\mathrm{T}}^{\mathrm{miss,\,soft}}/H_{\mathrm{T}}^{\mathrm{miss}}$
- $H_{\mathrm{T}}^{\mathrm{miss}}$/HLT threshold
- $H_{\mathrm{T}}^{\mathrm{miss}}$/L1 threshold

The two trigger-setup related variables, the high-level trigger (HLT) threshold and level-1 (L1) threshold, were raised during the data-taking periods from 2015 to 2018 and thus are sensitive to changes in the trigger efficiency in the different years. The used L1 thresholds are 0 and 50 GeV, the HLT thresholds range from 70 GeV to 110 GeV in steps of 10 GeV. It is favoured to use ratios of variables, e.g. $H_{\mathrm{T}}^{\mathrm{miss}}/E_{\mathrm{T}}^{\mathrm{miss}}$ to achieve an explicit scale independence of the input variables. A selection of potential input variables is shown in Figure A.9. To train the BDT classifier in a phase space which is relevant for the SRs and CRs a loose selection is applied on top of the selection described in Section 7.8:

- $\Delta\phi_{\mathrm{jj}} < 2$
- $m_{\mathrm{jj}} > 200$ GeV
- $E_{\mathrm{T}}^{\mathrm{miss}} > 100$ GeV
- $\Delta\eta_{\mathrm{jj}} > 3$

Tighter selection cuts are not possible since this would reduce the statistic of the single jet triggered data available in the BDT's training and testing phase dramatically. The trigger efficiency $\epsilon_{\mathrm{Trigger}}$ is defined in bins

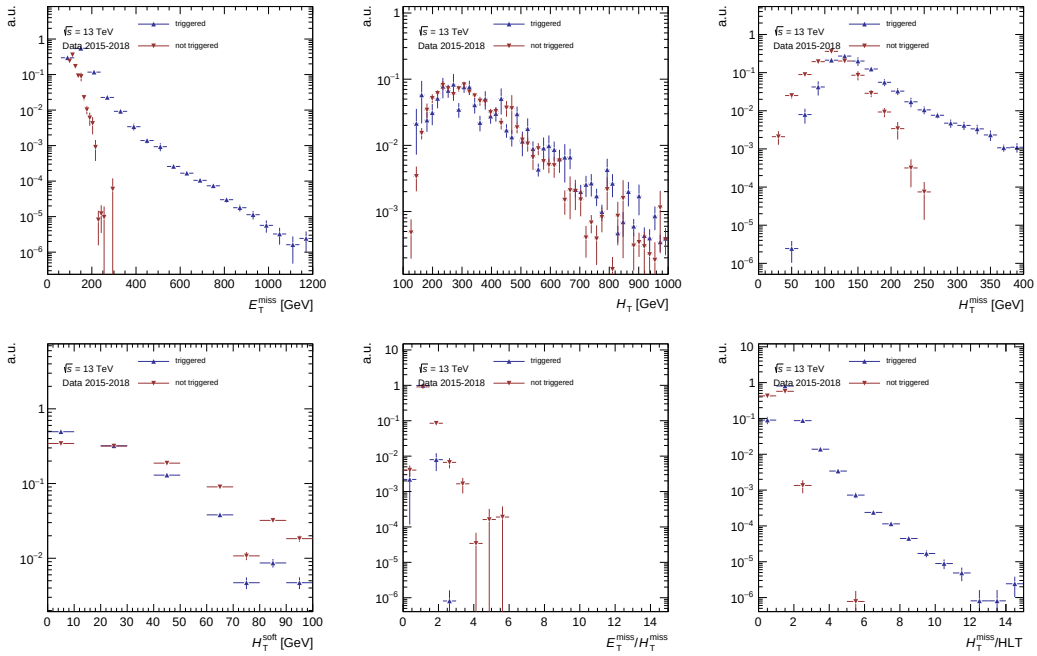

Figure A.9: Selection of variables used as input for the BDT training. Shown are the shapes (normalised histograms) for $E_{\mathrm{T}}^{\mathrm{miss}}$-triggered (red) and not $E_{\mathrm{T}}^{\mathrm{miss}}$-triggered data (blue) for combined data from 2015 to 2018.

of the BDT score as

$$\epsilon_{\mathrm{Trigger}}(\mathrm{BDT}) = \frac{N_{\mathrm{E_T^{miss}\ +\ single\ jet}}(\mathrm{BDT})}{N_{\mathrm{E_T^{miss}\ +\ single\ jet}}(\mathrm{BDT})) + N_{\mathrm{single\ jet}}(\mathrm{BDT})}, \tag{A.13}$$

where $N_{\mathrm{E_T^{miss}\ +\ single\ jet}}$ denotes the number of single jet and $E_{\mathrm{T}}^{\mathrm{miss}}$-triggered events and $N_{\mathrm{single\ jet}}$ of single jet but not $E_{\mathrm{T}}^{\mathrm{miss}}$-triggered events in each bin of the BDT classifier. The distribution of the BDT training classifier is shown in Figure A.10. As a test for overtraining, the test sample is superimposed. The uncertainty of the trigger efficiency as derived in Equation A.13 is calculated using the binomial error. The Clopper-Pearson interval [279] is used to calculate the binomial confidence intervals for the measured trigger efficiency. To correct for binning effects, a fit of a suited function $f(\mathrm{BDT}, \vec{p})$ as function of the BDT score and with free fit parameters $\vec{p} = (p_0, p_1, p_2)$, $p_i > 0$, is performed. The fit function must correctly fit the trigger turn-on feature, where the trigger efficiency is constant for small and larger BDT values. The fit function takes the form of a shifted error function as

$$f(\mathrm{BDT}, \vec{p}) = \frac{1}{2}\mathrm{erf}\left(\frac{\mathrm{BDT} - p_0}{p_1} + p_2\right), \tag{A.14}$$

with the Gauss error function erf defined by

$$\mathrm{erf}(x) = \frac{2}{\sqrt{\pi}} \int_0^x e^{-t^2} dt \tag{A.15}$$

for $x, t \in \mathbb{R}$. The quality of the fit is given by the ratio of χ^2 value and the number of degrees of freedom in the fit. The parametrised trigger efficiency with fit, see Equation A.14, are shown as well. As an alternative to the BDT approach to parametrise the $E_{\mathrm{T}}^{\mathrm{miss}}$ trigger efficiency, an artificial neural network (ANN) binary classifier is evaluated. In general an ANN learns to map inputs to outputs from training data in a stochastic gradient descent optimization algorithm which optimises weights between the layers of the ANN with a backpropagation of

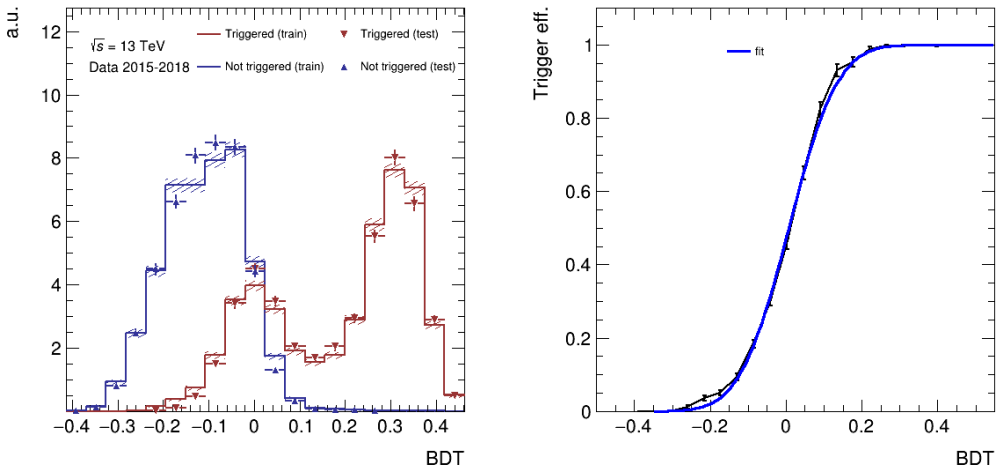

Figure A.10: BDT classifier distribution, over-training check and trigger efficiency parametrisation for combined data from 2015 to 2018.

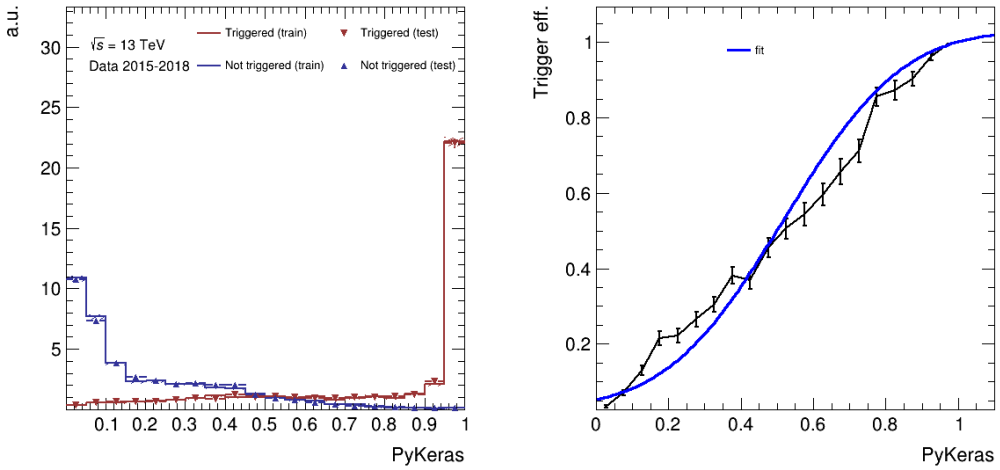

Figure A.11: ANN classifier distribution, over-training check and trigger efficiency parametrisation for combined data from 2015 to 2018.

error algorithm. The ANN is implemented via the Keras library ("PyKeras") interfacing the state-of-the-art TensorFlow machine learning library. Eight input nodes in the first layer with a rectified linear unit activation function and two nodes in the output layer with softmax activation are defined. The loss function of the stochastic gradient descent algorithm is categorical cross entropy. The resulting distribution of the ANN classifier and the trigger efficiency parametrisation after training are shown in Figure A.11. For completeness, the trigger efficiency is fitted with the same function as used for the BDT, though it is not a very suited function in that case. As a comparison of the ANN to the BDT classifier, a receiver operating characteristic (ROC) curve is shown in Figure A.12. The ANN and the BDT classifier based on the same input variables and data show a similar performance.

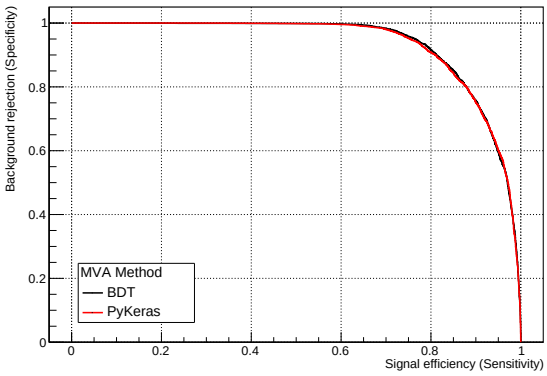

Figure A.12: ROC curve used for comparing the discrimination power of the ANN and the BDT classifier with respect to $E_{\mathrm{T}}^{\mathrm{miss}}$ triggered and not triggered data.

A.5 Monte-Carlo Closure Check

Closure tests in MC are used to validate the functionality of the MC-based RnS method. The drawback in MC closure test is the limited statistics in MC in a VBF phase space with high $E_{\mathrm{T}}^{\mathrm{miss}}$. For example, the number of events in th SR for 139 fb^{-1} is $O(10)$ with huge statistical uncertainties. Therefore, the MC closure test is performed in loose preselections. The MC-based RnS predictions for the HS-only and the HS+PU topology are normalised in $\Delta\phi_{\mathrm{jj}}$ in the respective regions. The preselection region is defined as the multijet CR as defined in Section 7.7 with the modification of $m_{\mathrm{jj}} > 0.2\,\mathrm{TeV}$, third-leading jet $p_{\mathrm{T}} > 0$ GeV and $E_{\mathrm{T}}^{\mathrm{miss}} > 100\,\mathrm{GeV}$. The closure plots are shown in Figure A.13. Overall the modelling is reasonable. The tail of the jet p_{T} distributions is too hard in the preselection but looks reasonable after applying a third jet veto.

A.6 Classical Rebalance And Smear

In this section the original version of RnS, similar as it was used in the first Run II paper corresponding to 36 fb^{-1} of data [1], is described and the performance of the method with the full Run II data set corresponding to 139 fb^{-1} of data is shown. Originally, RnS has been developed as a purely data-driven technique to estimate the multijet background in searches for new physics as an alternative to the widely used jet smearing. This version of RnS is called in this thesis “classical Rebalance and Smear" to distinguish it from the new data-driven and MC-based RnS developments. A detailed description of RnS is given in Chapter 7 and should be read first. This description shows also the limitation of the classical RnS method and serves as a natural motivation for developing more sophisticated versions of RnS. Further, it should be noted that new developments to increase the effective statistics of the multijet prediction, such as enhanced tail smearing or the azimuthal rotation, are incorporated as well in the presented classical RnS technique.

A.6.1 Input

The technique presented in the following can be used either with data or with simulated samples as input. It is well motivated to use RnS in a purely data-driven way, which was the original motivation for the development of this technique. Therefore, single jet triggered data from the data-taking years 2015 to 2018 is used as input for the classical RnS version. An un-prescaling as described in Section 7.2.2 is performed to correctly assign event weights on the prescaled single jet triggered data and to obtain a smooth p_{T}-distribution.

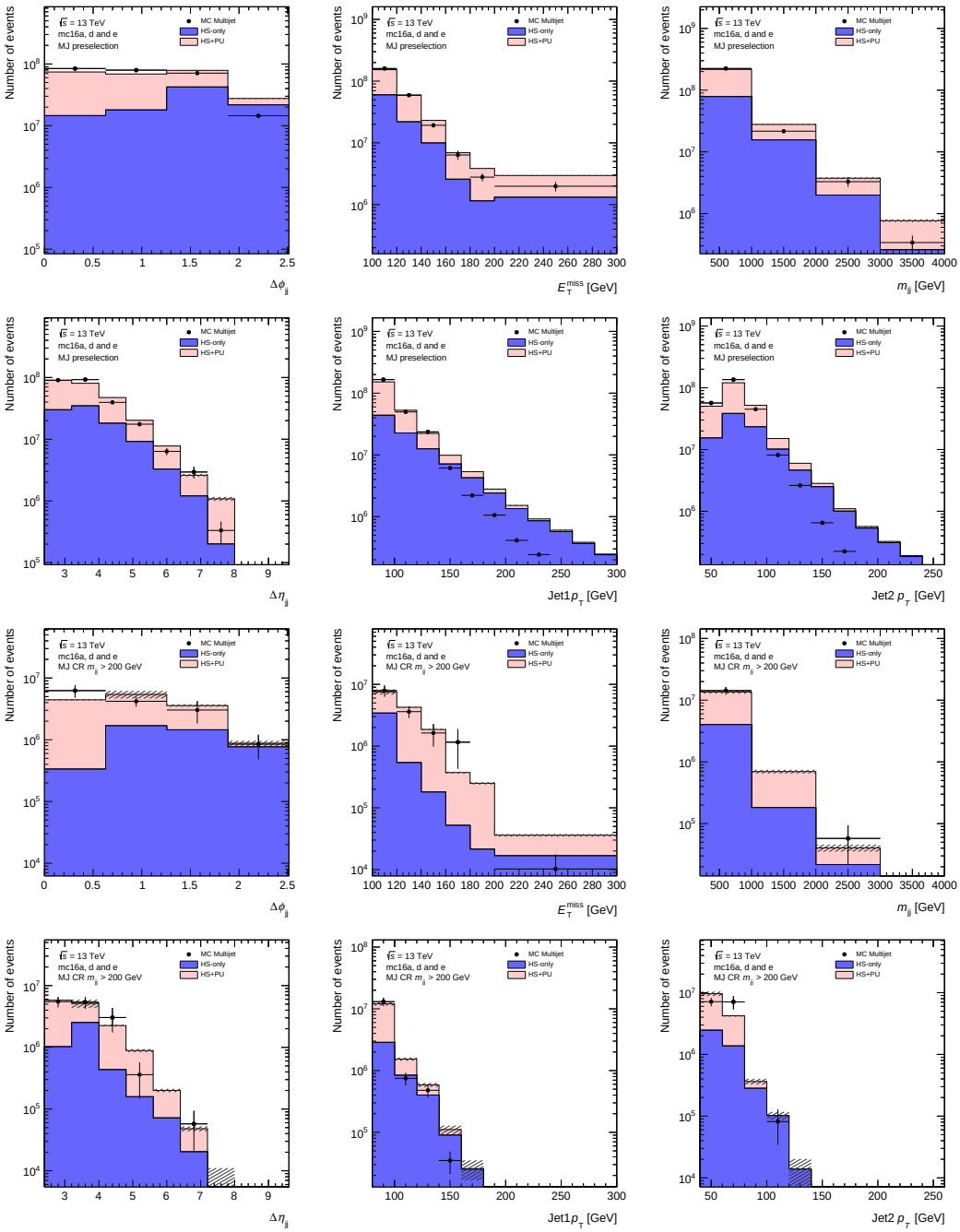

Figure A.13: MC closure test of the MC-based RnS multijet background prediction in an inclusive preselection and in a tighter preselection with third jet veto.

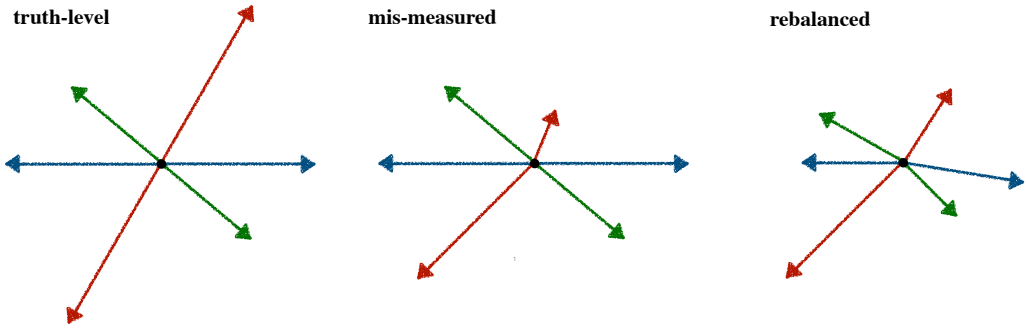

Figure A.14: Toy model of the inclusive rebalancing of hard-scatter and pile-up jets in an event. The truth-level transverse event plane is shown on the left. Three dijet events are shown - the hard-scatter jets (red) and two pile-up sub-events (blue and green). All three dijet events are balanced in p_{T} on truth-level. The sketch in the middle shows the reconstructed event. In this example only the hard-scatter jets are mis-measured. The figure on the right shows a potential result of the inclusive rebalancing where the full $H_{\mathrm{T}}^{\mathrm{miss}}$ in the event is compensated by an adjustment of all six jets in ϕ and p_{T}. This rebalancing results in an event in which none of the three dijet sub-events is balanced.

A.6.2 Seed Selection, Rebalancing and Smearing Strategy

In the classical RnS method, a very inclusive seed selection is applied to select data events without large amount of real $E_{\mathrm{T}}^{\mathrm{miss}}$, e.g. from heavy flavour decays. The seed event is summarised in Table A.2. To reject multijet

Table A.2: Seed event selection of the classical RnS technique.

Quantity	Cut	Description
n_{jet}	≥ 3	jet multiplicity
m_{jj}	$> 150\,\mathrm{GeV}$	invariant mass of the leading dijet system
$\Delta\eta_{\mathrm{jj}}$	> 2.4	$\lvert\eta_1 - \eta_2\rvert$ of the leading dijet system
$\Delta\phi_{\mathrm{jj}}$	< 2.6	azimuthal separation of the leading dijet system
$H_{\mathrm{T}}^{\mathrm{miss}}$ sig.	$< 5\,\sqrt{\mathrm{GeV}}$	$H_{\mathrm{T}}^{\mathrm{miss}}$ significance

events with real $E_{\mathrm{T}}^{\mathrm{miss}}$, a cut on the $H_{\mathrm{T}}^{\mathrm{miss}}$ significance can be applied, i.e.

$$H_{\mathrm{T}}^{\mathrm{miss}}\ \mathrm{sig.} = \frac{H_{\mathrm{T}}^{\mathrm{miss}}}{\sqrt{H_{\mathrm{T}}}} < 5\,\sqrt{\mathrm{GeV}}, \tag{A.16}$$

where all jets both hard-scatter and pile-up are included.

After the seed event selection, a rebalancing is performed. All jets in an event are rebalanced together. While the idea is simple, it has the drawback that pile-up events and hard-scatter events are not rebalanced independently. A p_{T} imbalance in the hard-scatter event may be balanced by a scaling of the pile-up jet in the kinematic rebalancing fit. This can cause problems as sketched in Figure A.14, e.g. a hard-scatter event may be balanced (i.e. perfectly measured at reco level) prior to the rebalancing but is then skewed in the fit which aims to rebalance the pile-up events, too, by modifying the hard-scatter jets.

After rebalancing, a jet smearing as described in Chapter 7 is performed. After the smearing, the pile-up tagging variables JVT and fJVT are re-calculated in order to correctly emulate the mixing of hard-scatter and pile-up jets and the production of fake $E_{\mathrm{T}}^{\mathrm{miss}}$ due to a failed pile-up tagging. Altough only a loose seed selection is applied, a residual normalisation in the MJ CR, defined in Section 7.7, is performed.

A.6.3 Closure Checks and Discussion

This section shows the closure plots of the classical RnS technique. The distributions and statistical uncertainties are obtained from a proper bootstrapping of the RnS output. The trigger efficiency is not applied for this closure test in single jet triggered data. The size of systematic uncertainties such as JER tail-up and JER core-up, see Section 7.9, are not evaluated for this approach.

Figure A.19 shows the RnS prediction in the variable N_{PV}. It is evident that the observed non-closure increases with N_{PV}, thus the method shows a worse performance with increasing pile-up conditions, which is understood according to Figure A.14. The classical RnS technique showed a reasonable performance in the first Run II VBF + $E_{\mathrm{T}}^{\mathrm{miss}}$ analysis based on 36 fb^{-1} of data from 2015/16 [1]. However, the method has conceptual problems due to the inclusive rebalancing of hard-scatter and pile-up jets, see Fig. A.14 which become more relevant for increasing pile-up conditions in the full Run II data set.

Due to the very loose seed event selection, the classic RnS technique gives also the correct normalisation of the multijet prediction since the seed selection only rejects events that are very unlikely to pass the analysis SR and CR selections. This is a strong advantage compared to jet smearing techniques and the new RnS techniques which obtain the background normalisation in dedicated control regions.

A.7 Truth Jet Smearing with Pile-Up Jets

Many analyses searching for BSM physics use a jet smearing technique to estimate the multijet background. For a DM search with jets from a VBF Higgs boson production (and thus much forward activity) and a large amount of $E_{\mathrm{T}}^{\mathrm{miss}}$ in the final state, the presence of pile-up jets is crucial to simulate the hard-scatter and pile-up mixing in multijet processes. In many applications of the jet smearing method, it is sufficient to smear the hard-scatter jets to enhance the statistics of the multijet prediction, while pile-up jets are not considered at all. To study the performance of a jet smearing approach in the presented analysis, modifications must be done to include pile-up jets in the jet smearing approach. This is the reason that a truth jet smearing is done and not a data-driven jet smearing.

The idea of this technique is closely related to the MC-based RnS approach. Therefore it is recommended to read Chapter 7 first.

The general approach of this truth jet smearing technique is to combine the truth hard-scatter jets, which are used in the jet smearing, and reco pile-up jets. A geometrical truth matching is used to identify the reco hard-scatter and pile-up jets. The reconstructed hard-scatter jets are replaced by the truth hard-scatter jets, while the reco pile-up jets serve as the pile-up events, which are freezed similar as in the MC-based RnS technique. A rebalancing is not needed in this approach since the hard-scatter event at truth level is already rebalanced up to the truth-level imbalance which simplifies the approach, as sketched in Figure A.20, and avoids inherit problems of the rebalancing step as discussed in Section 7.12.

A.7.1 Input

The input for this version of a jet smearing are simulated MC samples. The problem is that in almost all MC simulations, generated pile-up jets are not included to save computing time and disk space and thus only the reco information of pile-up events is introduced with simulated minimum bias events, which are overlayed to the hard-scatter event. Therefore, no truth pile-up information is available and reco information of pile-up jets must be used. In the following, it is described how the used jet collection is formed from a mixing of truth and reco jets.

The combination of matched truth jet and reco jet collections is non-trivial. For a better understanding of the procedure, its useful to distinguish four kinds of jets. The simulation provides truth-level jets and reconstructed jets. A truth-matching of truth and reco jets is performed, matching one reco and truth jet if possible. No jet is matched twice. Therefore, four kind of jets can be identified after the matching:

- matched truth jets
- unmatched truth jets
- matched reco jets
- unmatched reco jets

There is a variety of reasons why truth jets do not find a matching reco partner - the most obvious are that the corresponding reco jet is measured below the threshold of $p_{\mathrm{T}} = 20\,\mathrm{GeV}$ or that a truth jet is falsely reconstructed as two separate jets.

All truth jets form the hard-scatter event, while the pile-up jets are built from the not truth-matched reco jets (which are freezed in the jet smearing process). The matched reco jets (i.e. the reco hard-scatter jets) are dropped and not used in this method. As described before, the hard-scatter event is built from the truth jets. The first question here is: should it consists of both truth jets, the matched and unmatched, or only the matched truth jets?

If one chooses the first option, it is important to avoid a double-counting of unmatched reco and unmatched truth jets, e.g. in cases where the truth jet is reconstructed as two separate reco jets.

One potential solution is to introduce a quality criteria to account for these effects. It could be required that all truth jets abve a p_{T} threshold of 20 GeV are matched. The choice of this p_{T} threshold is ad hoc. Higher p_{T} threshold such as 25 GeV could also be discussed. In this version all truth jets would be smeared (independent of the matching) and only unmatched reco jets are treated as pile-up.

The second option, which shall be used, freezes unmatched truth jets, i.e. only matched truth jets are smeared. Unmatched truth jets are still treated as hard-scatter jets but not changed in the smearing. As before, unmatched reco jets are treated as pile-up, while matched reco jets are dropped.

Using the definition of the hard-scatter and pile-up jets allows for using the same HS-only and HS+PU topology definitions as in RnS, see Section 7.3.

A.7.2 Seed Selection and Jet Smearing

A seed event selection is used to select events which have the potential to end up in the SR or CRs. By this, a large amount of computing time can be saved. The seed selection is summarised in Table A.3.

Table A.3: Seed event selection of the truth jet smearing technique.

Quantity	Cut	Description
n_{HS}	≥ 2	number of hard-scatter jets
m_{jj}	$> 150\,\mathrm{GeV}$	invariant mass of the leading dijet system
$\Delta\eta_{\mathrm{jj}}$	> 2.4	$\lvert\eta_1 - \eta_2\rvert$ of the leading dijet system
$\Delta\phi_{\mathrm{jj}}$	< 2.6	azimuthal separation of the leading dijet system
p_{T}	$> 30\,\mathrm{GeV}$	leading jet p_{T}
$\langle p_{\mathrm{T}}\rangle / p_{\mathrm{T,j_1}}^{\mathrm{true}}$	$\in [0.6, 1.4]$	reject unphysical pile-up from simulation
$H_{\mathrm{T}}^{\mathrm{miss}}$(matched)	$< 35\,\mathrm{GeV}$	truth-matching quality

The truth jet smearing procedure follows the description in Section 7.5 using the same jet energy response maps as described in Section 7.4. All truth jets, even with $p_{\mathrm{T}} < 20\,\mathrm{GeV}$, are smeared multiple times to emulate the production of fake-$E_{\mathrm{T}}^{\mathrm{miss}}$ due to jet mis-measurements by the detector. The corresponding reco pile-up event is

then mixed to the corresponding smeared hard-scatter event. A proper bootstrapping as described in 7.9.1 is used to correctly handle the statistical uncertainty of the limited seed sample statstics as well as the various copies of pile-up events which are added to the smeared hard-scatter jet configurations.

In general the same systematic uncertainties as given in Section 7.9 are relevant for this technique but are not properly evaluated at this stage.

A.7.3 Closure Checks and Discussion

Closure plots for 2018 are shown in Figure A.21 in a MJ CR, summarised in Table A.4 using smeared mc16e Pythia samples. Overall, the performance is good and the predicted multijet shape corresponds to the observed single jet triggered data.

Table A.4: Definition of the MJ CR for the truth jet smearing.

Quantity	Cut
$E_{\mathrm{T}}^{\mathrm{miss}}$	$> 100\,\mathrm{GeV}$
$\Delta\phi_{\mathrm{jj}}$	< 2
$\Delta\eta_{\mathrm{jj}}$	> 2.5
m_{jj}	$> 200\,\mathrm{GeV}$
leading jet p_{T}	$> 80\,\mathrm{GeV}$
leading jet fJVT	< 0.2 if $E_{\mathrm{T}}^{\mathrm{miss}} < 200\,\mathrm{GeV}$, else < 0.5
subleading jet p_{T}	$> 50\,\mathrm{GeV}$
subleading jet fJVT	< 0.2 if $E_{\mathrm{T}}^{\mathrm{miss}} < 200\,\mathrm{GeV}$, else < 0.5
third-leading jet p_{T}	$< 25\,\mathrm{GeV}$
$H_{\mathrm{T}}^{\mathrm{miss}}$	≥ 0
$E_{\mathrm{T}}^{\mathrm{miss,soft}}$	$< 20\,\mathrm{GeV}$

The presented truth jet smearing technique is a new jet smearing approach based on the clever combination of truth-level and reco-level jets. This combination of jets makes it possible to perform a jet smearing under consideration of pile-up activity, which is crucial in VBF topologies. A big advantage compared to RnS is that a rebalancing with a kinematic fit is not needed since the hard-scatter event is at truth-level. Further, the freezing of pile-up jets makes the method stable and less sensitive to modelling problems of soft as well as pile-up jets caused for example by jet loss in the truth jet smearing.

A.8 RnS Comparisons

A comparison of important kinematic variables of the four different RnS version, namely the MC-based RnS, data-driven RnS, classical RnS and the truth jet smearing approach, in three different CRs based on a loose event selection is shown in Figures A.22-A.24. The MC-based and data-driven RnS techniques are described in Chapter 7, the truth jet smearing approach is described in Appendix A.7 and the classical RnS version in Appendix A.6. In addition, data minus non-multijet backgrounds and the raw Pythia MC samples are shown. The MJ CR is defined in Table 7.5. The MJ CR $m_{\mathrm{jj}} > 200\,\mathrm{GeV}$ is defined analogously but with a modified requirement of $m_{\mathrm{jj}} > 200\,\mathrm{GeV}$ instead $m_{\mathrm{jj}} > 400\,\mathrm{GeV}$. The preselection region is defined as the multijet CR as defined in Section 7.7 with the modification of $m_{\mathrm{jj}} > 0.2\,\mathrm{TeV}$, third-leading jet $p_{\mathrm{T}} > 0$ and $E_{\mathrm{T}}^{\mathrm{miss}} > 100\,\mathrm{GeV}$. The comparison is shown only for data from 2018 and simulation from the mc16e campaign. It is evident that the data and MC statistics is limited while the RnS predictions are increased in statistics.

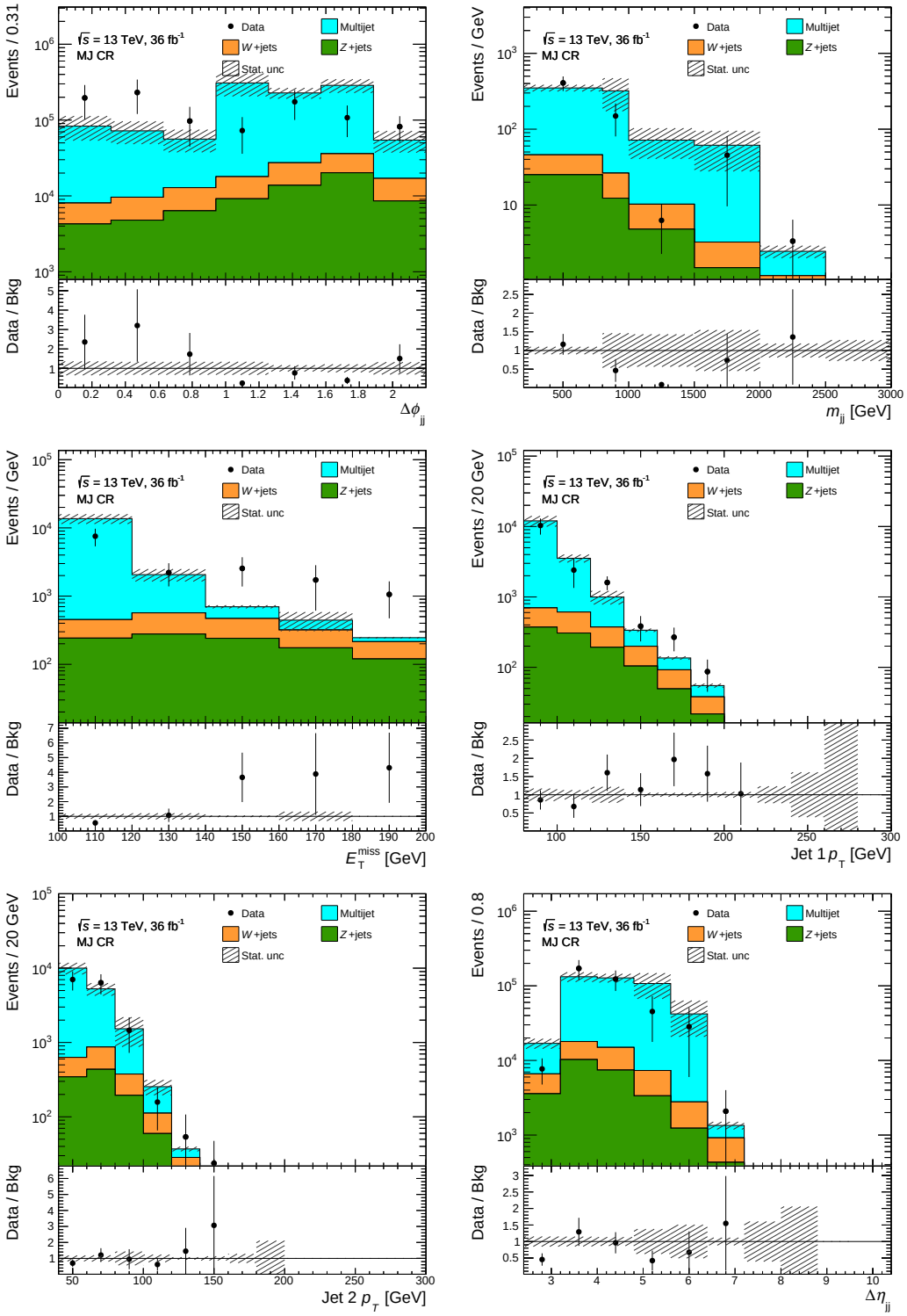

Figure A.15: Closure check of the classical RnS prediction in the MJ CR for data from 2015/16 corresponding to a luminosity of 36 fb^{-1}.

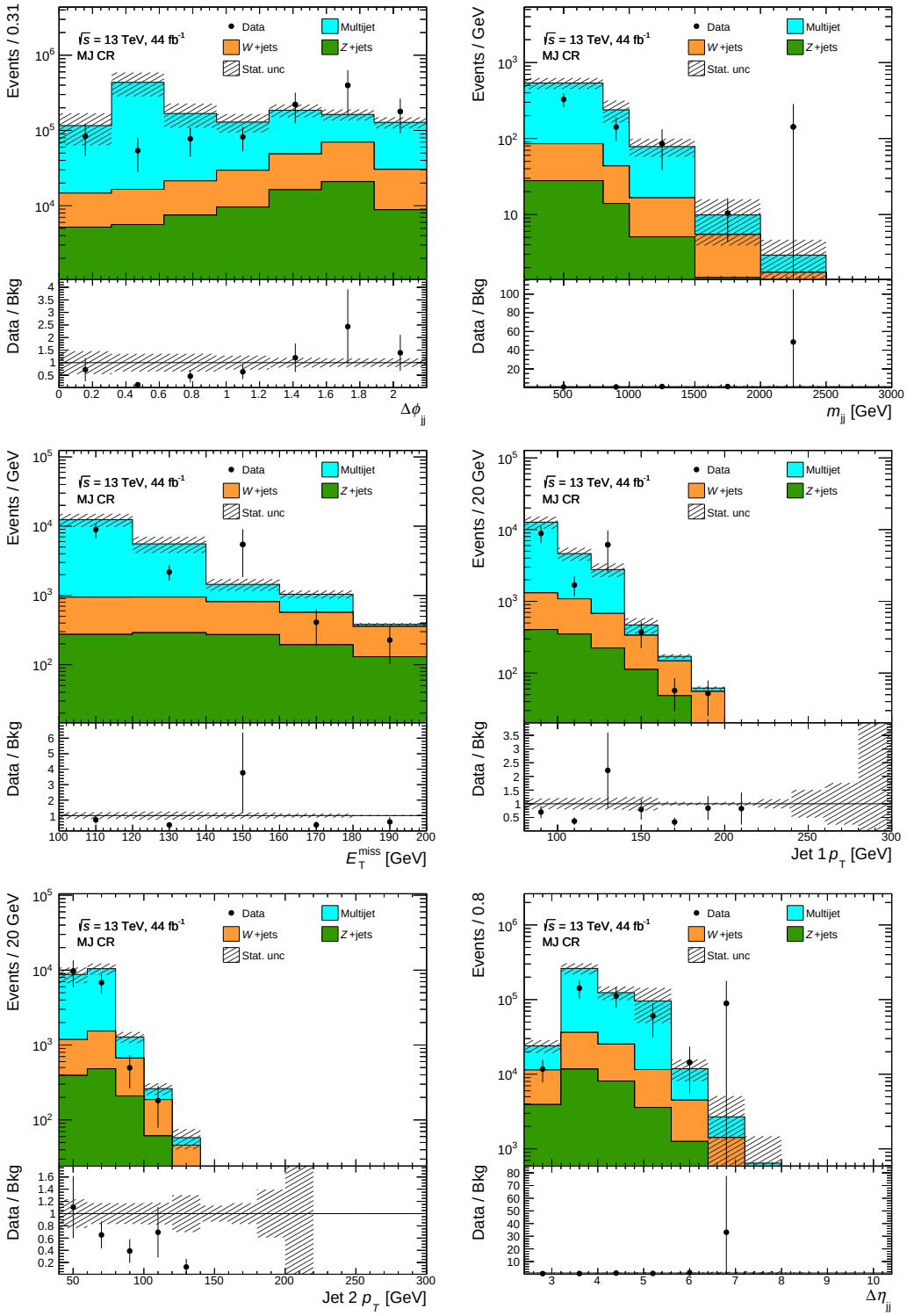

Figure A.16: Closure check of the classical RnS prediction in the MJ CR for data from 2017 corresponding to a luminosity of 44 fb^{-1}.

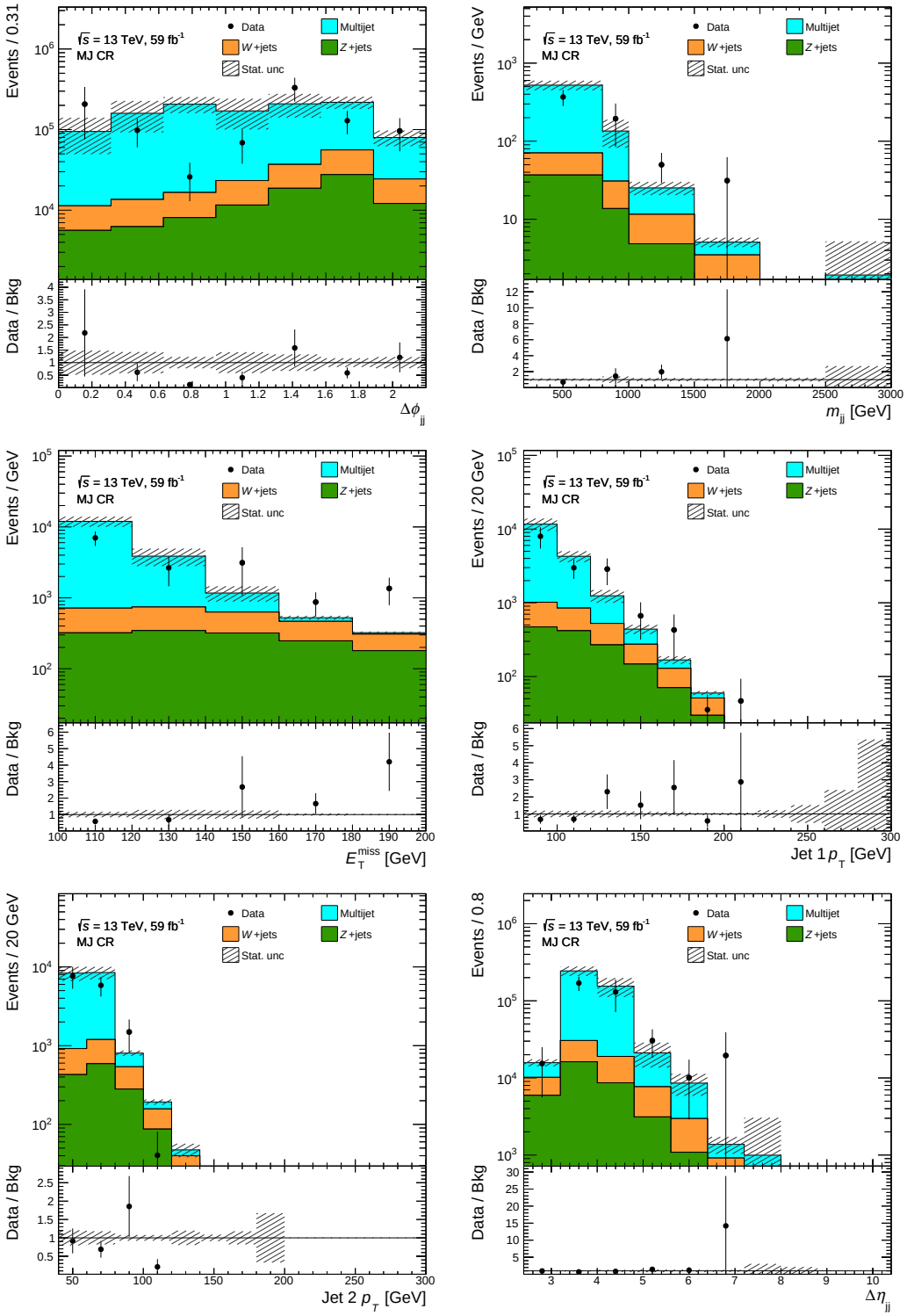

Figure A.17: Closure check of the classical RnS prediction in the MJ CR for data from 2018 corresponding to a luminosity of 59 fb^{-1}.

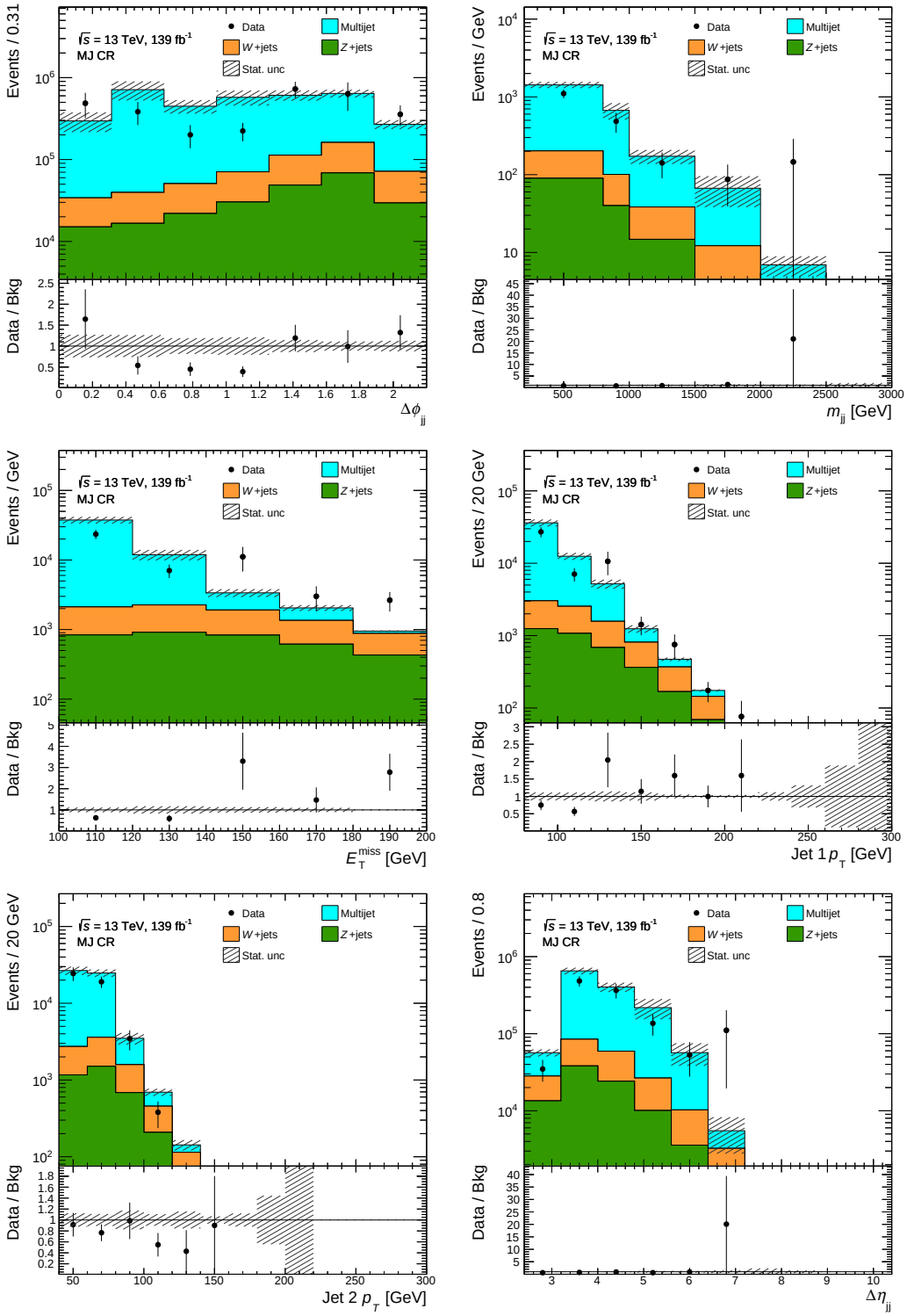

Figure A.18: Closure check of the classical RnS prediction in the MJ CR for data from 2015 to 2018 corresponding to a luminosity of 139 fb^{-1}.

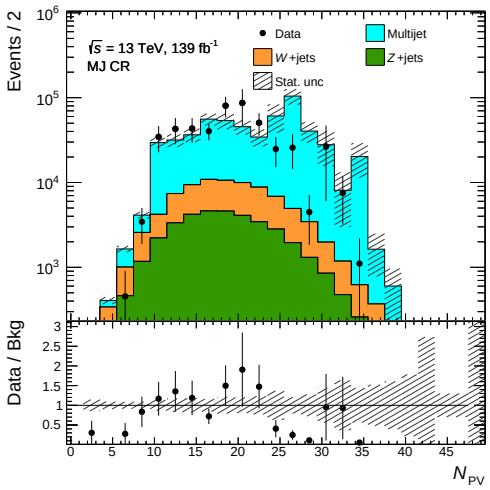

Figure A.19: Closure check of the classical RnS prediction in the MJ CR for data from 2015-2018 corresponding to a luminosity of 139 fb^{-1}.

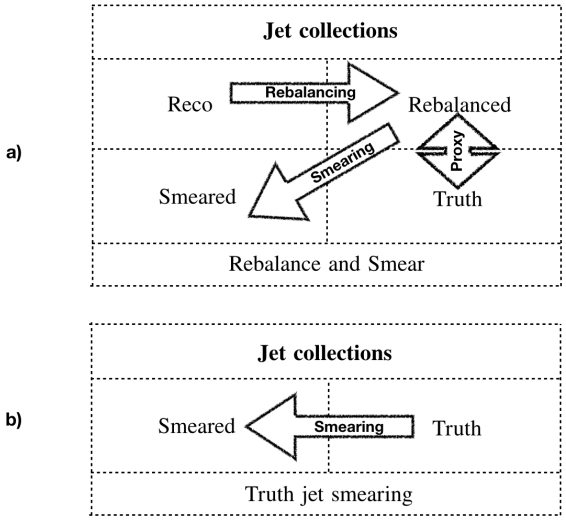

Figure A.20: Comparison of RnS (a) and a truth jet smearing (b) with respect to the involved jet collections.

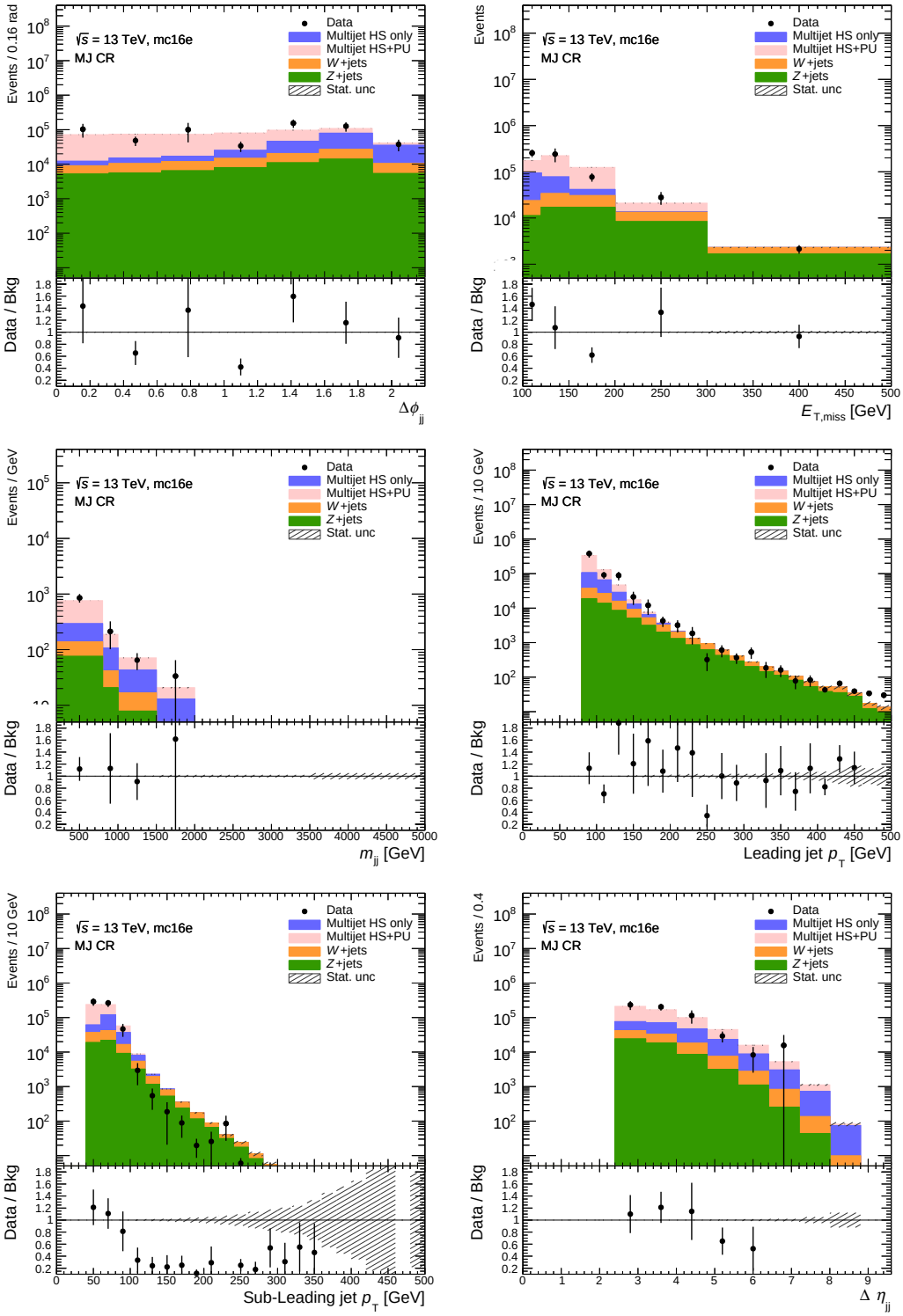

Figure A.21: Closure check of the truth jet smearing prediction in a MJ CR for mc16e and data from 2018. Shown are the variables $\Delta\phi_{\mathrm{jj}}$, $E_{\mathrm{T}}^{\mathrm{miss}}$, m_{jj}, leading and subleading jet p_{T} as well as $\Delta\eta_{\mathrm{jj}}$. The hashed uncertainty bands are statistical uncertainty only.

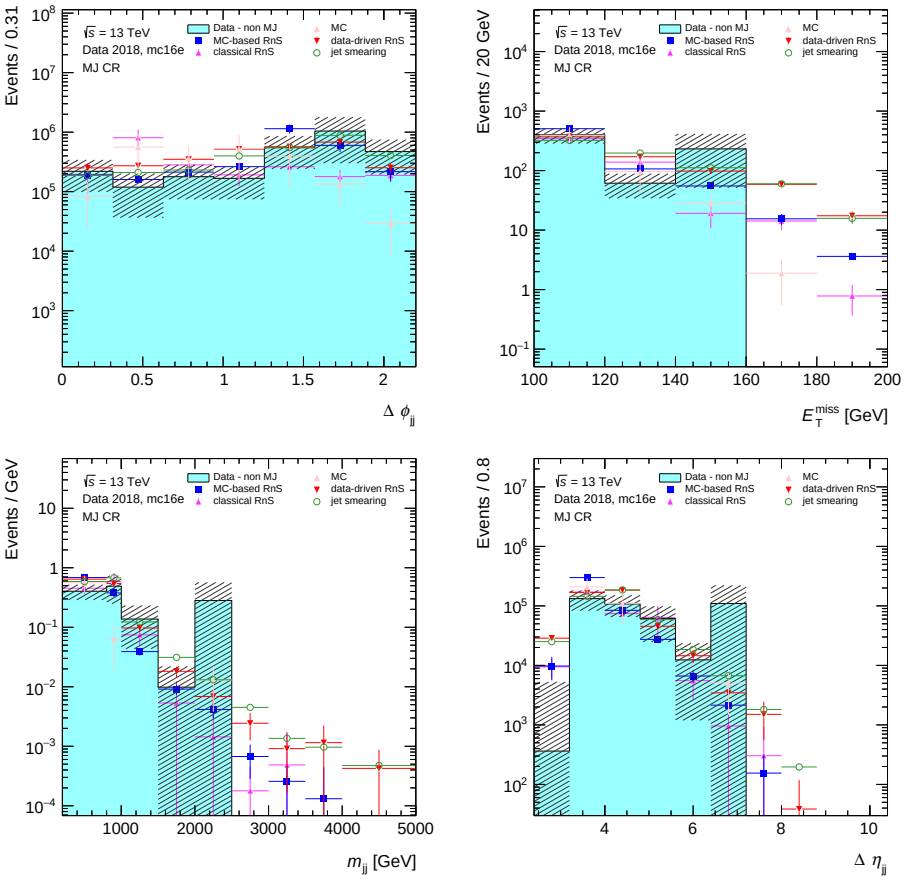

Figure A.22: Comparison of the four different RnS version (MC-based, data-driven, classical, truth jet smearing) in the MJ CR.

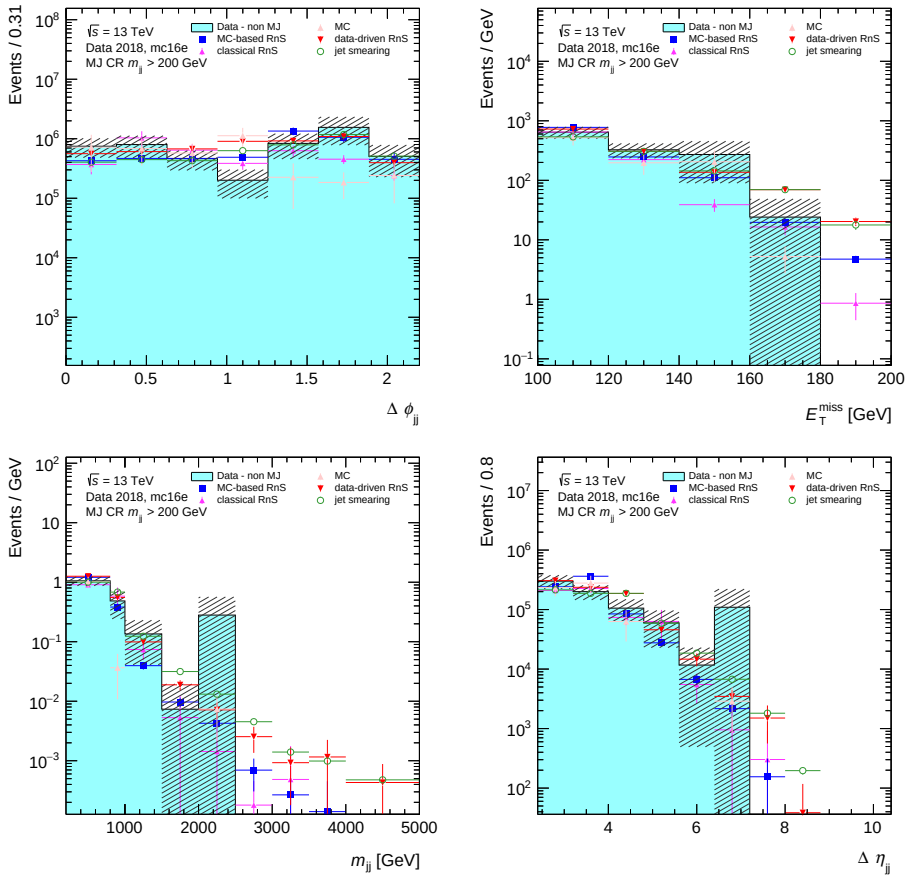

Figure A.23: Comparison of the four different RnS version (MC-based, data-driven, classical, truth jet smearing) in the MJ CR with $m_{jj} > 200\,\text{GeV}$.

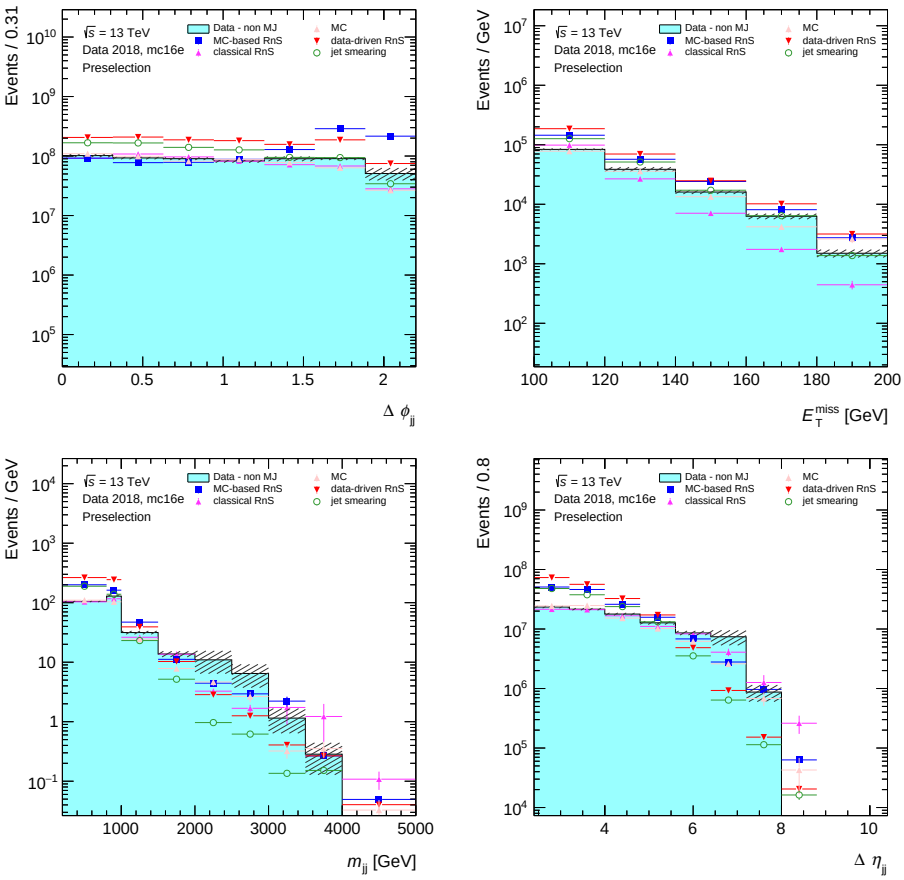

Figure A.24: Comparison of the four different RnS version (MC-based, data-driven, classical, truth jet smearing) in the preselection region.

List of Figures

List of Tables

Acknowledgements

Special thanks to Christian Sander who provided the best possible supervision and without whom this would not have been possible. Thanks for your support, expertise, trust and time.

Thanks to Johannes Haller for being a supportive and great second supervisor.

I also would like to thank DESY and the local ATLAS group for the great working environment, the nice infrastructure and the healthy working atmosphere, especially in times of pandemic. Thanks to Alicia, Ingrid, James, Janik, Jonas, Krisztian, Pablo, Othmane and Xuanhong.

Thanks to CERN, the ATLAS collaboration and in particular to Doug Schaefer, Jennifer Roloff, Chaowaroj Wanotayaroj and Michaela Quietsch-Maitland.

Eidesstattliche Versicherung

Hiermit versichere ich an Eides statt, die vorliegende Dissertationsschrift selbst verfasst und keine anderen als die angegebenen Hilfsmittel und Quellen benutzt zu haben.

Hamburg, den 18.10.2021

Arthur Linß